



International Journal of  
**Remote  
Sensing and  
Earth Sciences**

**Published by  
Indonesian National Institute of Aeronautics and Space  
(LAPAN)**

## **Editorial Committee Preface**

Dear IJReSES Readers,

We sincerely thank you for reading the International Journal of Remote Sensing and Earth Sciences Vol. 17 No 2, December 2020. In general, this journal is expected to enrich the serial publications on earth sciences. In particular this journal is aimed to present improvement in remote sensing studies and its applications on earth sciences. This journal also serves as the enrichment on earth sciences publication, not only in Indonesia and Asia but also worldwide.

This journal consists of papers discussing the particular interest in remote sensing field. Those papers are having remote sensing data for image processing, geosciences, oceanography, environment, disaster, mining activities, etc. A variety of topics are discussed in this seventeen edition. Briefly, the topics discussed in this edition are the studies of remote sensing data processing issues such as Fisheries production estimation, urban condition analysis, coral reef habitat, forest devegetation, total suspended solid, shoreline change, and bathymetri. There are some new methods, new analysis, and new novelties on this edition.

Finally, enjoy your reading of the IJRESES Vol. 17 No. 2 December 2020, and please refer this journal content for your next research and publication. For editorial team members and the journal secretariat, thank you very much for all big supports for this volume publication.

Editor-in-Chief,

Dr M. Rokhis Khomarudin.

**Editorial Committee Members**  
**INTERNATIONAL JOURNAL OF**  
**REMOTE SENSING AND EARTH SCIENCES**  
**Vol. 17 No. 2 December 2020**  
**P-ISSN 0216-6739; E-ISSN 2549-516X**

- Editor-in-Chief : **Dr. M. Rokhis Khomarudin**
- Peer Reviewers : **Prof. Dr. Ir. Nengah Suratijaya, M.Agr.**  
**Prof. Dr. Dewayany Sutrisno**  
**Prof. Dr. Ir. Dony Kushardhono, M.Eng.**  
**Dr. Widodo S. Pranowo**  
**Dr. Jonson Lumban-Gaol**  
**Dr. Ir. Baba Barus, M.Sc.**  
**Dr. Takahiro Osawa**  
**Dr. Ratih Dewanti**  
**Dr. Dede Dirgahayu**  
**Dr. Indah Prasasti, M.Si.**  
**Dr. Rahmat Arief**  
**Syarif Budhiman, S.Pi., M.Sc.**
- Secretariat : **Muhammad Bayu, S.Sos.**  
**Haris Benediktus, S.E.**  
**Lusiana Sulistianingsih, S.I.A.**  
**Ar Rasyiid Akbar, S.E.**

Contribution Paper to:

**IJReSES Secretariat**  
**Indonesian National Institute of Aeronautics and Space (LAPAN)**  
Jl. Kalisari No. 8, Pekayon, Pasar Rebo, Jakarta 13710, INDONESIA  
Telp. (021) 8710065, Fax. (021) 8722733  
[www.jurnal.lapan.go.id](http://www.jurnal.lapan.go.id)



Published by:  
**National Institute of Aeronautics and Space of Indonesia**  
**(LAPAN)**



**INTERNATIONAL JOURNAL OF  
REMOTE SENSING AND EARTH SCIENCES  
Vol. 17 No. 2 December 2020  
P-ISSN 0216-6739; E- ISSN 2549-516X  
Accreditation No. 30/E/KPT/2018**

**Contents**

Editorial Committee Preface .....	ii
Editorial Committee Members .....	iii
<b>VARIABILITY OF SEA SURFACE TEMPERATURE AT FISHERIES MANAGEMENT AREA 715 IN INDONESIA AND ITS RELATION TO THE MONSOON, ENSO AND FISHERY PRODUCTION</b>	
Komang Iwan Suniada .....	99
<b>DETECTION AND ANALYSIS OF SURFACE URBAN COOL ISLAND USING THERMAL INFRARED IMAGERY OF SALATIGA CITY, INDONESIA</b>	
Bayu Elwanto Bagus Dewantoro, Panji Mahyatar, Wafiq Nur Hayani.....	115
<b>MONITORING CHANGES IN CORAL REEF HABITAT COVER ON BERALAS PASIR ISLAND USING SPOT 4 AND SPOT 7 IMAGERY FROM 2011 AND 2018</b>	
Rosaria Ria Damai, Viv Djanat Prasita, Kuncoro Teguh Setiawan.....	127
<b>MULTITEMPORAL ANALYSIS FOR TROPHIC STATE MAPPING IN BATUR LAKE AT BALI PROVINCE BASED ON HIGH-RESOLUTION PLANETSCOPE IMAGERY</b>	
Rahma Nafila Fitri Sabrina, Sudaryatno Sudaryatno.....	149
<b>MONITORING MODEL OF LAND COVER CHANGE FOR THE INDICATION OF DEVEGETATION AND REVEGETATION USING SENTINEL-2</b>	
Samsul Arifin, Tatik Kartika, Dede Dirgahayu, and Gatot Nugroho.....	163
<b>INTERSEASONAL VARIABILITY IN THE ANALYSIS OF TOTAL SUSPENDED SOLIDS(TSS) IN SURABAYA COASTAL WATERS USING LANDSAT-8 SATELLITE DATA</b>	
Bela Karbela, Pingkan Mayestika Afgatiani, Ety Parwati.....	175
<b>A COMPARISON OF RAINFALL ESTIMATION USING HIMAWARI-8 SATELLITE DATA IN DIFFERENT INDONESIAN TOPOGRAPHIES</b>	
Nadine Ayasha.....	189
<b>SHORELINE CHANGES AFTER THE SUNDA STRAIT TSUNAMI ON THE COAST OF PANDEGLANG REGENCY, BANTEN</b>	
Fandi Dwi Julianto, Cahya Rizki Fathurohman, Salsabila Diyah Rahmawati, Taufiq Ihsanudin.....	201
<b>BATHYMETRIC EXTRACTION USING PLANETSCOPE IMAGERY (CASE STUDY: KEMUJAN ISLAND, CENTRAL JAVA)</b>	
Asih Sekar Sesama, Kuncoro Teguh Setiawan, Atriyon Julzarika.....	209
Instruction for Authors .....	
Index.....	

Published by:

**National Institute of Aeronautics and Space of Indonesia (LAPAN)**

**International Journal of  
Remote Sensing and Earth Sciences**

P-ISSN 0216 – 6739; E- ISSN 2549-516X

Vol. 17 No. 1 June 2020

Accreditation No. 30/E/KPT/2018

The abstract may be copied without permission or charge

ABSTRACT

**DETECTING THE SURFACE WATER AREA IN CIRATA DAM UPSTREAM CITARUM USING A WATER INDEX FROM SENTINEL-2/ Suwarsono Suwarsono, Fajar Yulianto, Hana Listi Fitriana, Udhi Catur Nugroho, Kusumaning Ayu Dyah Sukowati, Muhammad Rokhis Khomarudin**  
**IJRESES, 17 (1) 2020 : 1- 8**

This paper describes the detection of the surface water area in Cirata dam, upstream Citarum, using a water index derived from Sentinel-2. MSI Level 1C (MSIL1C) data from 16 November 2018 were extracted into a water index such as the NDWI (Normalized Difference Water Index) model of Gao (1996), McFeeters (1996), Roger and Kearney (2004), and Xu (2006). Water index were analyzed based on the presence of several objects (water, vegetation, soil, and built-up). The research resulted in the ability of each water index to separate water and non-water objects. The results conclude that the NDWI of McFeeters (1996) derived from Sentinel-2 MSI showed the best results in detecting the surface water area of the reservoir..

**Keywords:** *Surface water area, NDWI, Sentinel-2, Cirata dam, Upstream Citarum*

**ANALYSIS OF POTENTIAL FISHING ZONES IN COASTAL WATERS: A CASE STUDY OF NIAS ISLAND WATERS/ Anang Dwi Purwanto, Teguh Prayogo, Sartono Marpaung, Argo Galih Suhada**  
**IJRESES, 17 (1) 2020 : 9-24**

The need for information on potential fishing zones based on remote sensing satellite data (ZPPI) in coastal waters is increasing. This study aims to create an information model of such zones in coastal waters (coastal ZPPI). The image data used include GHRSSST, SNPP-VIIRS and MODIS-Aqua images acquired from September 1st-30th, 2018 and September 1st-30th, 2019, together with other supporting data. The coastal ZPPI information is based on the results of thermal front SST detection and overlaying this with chlorophyll-a. The method of determining the thermal front sea surface temperature (SST) used Single Image Edge Detection (SIED). The chlorophyll-a range used was in the mesotrophic area (0.2-0.5 mg/m<sup>3</sup>). Coastal ZPPI coordinates were determined using the polygon centre of mass, while the coastal ZPPI information generated was only for coastal areas with a radius of between 4-12 nautical miles and was divided into two criteria, namely High Potential (HP) and Low Potential (LP). The results show that the coastal ZPPI models were suitable to determine fishing locations around Nias Island. The percentage of coastal ZPPI information generated was around 90% information monthly. In September 2018, 27 days of information were produced, consisting of 11 HP sets of coastal ZPPI information and 16 sets of LP information, while in September 2019 it was possible to produce 29 days of such information, comprising 11 sets of HP coastal ZPPI information and 18 LP sets. The use of SST parameters of GHRSSST images and the addition of chlorophyll-a parameters to MODIS-Aqua images are very effective and efficient ways of supporting the provision of coastal ZPPI information in the waters of Nias Island and its surroundings.

**Keywords:** *Potential Fishing Zones, Coastal ZPPI, GHRSSST, Single Image Edge Detection (SIED), Nias Island*

**International Journal of  
Remote Sensing and Earth Sciences**

P-ISSN 0216 – 6739; E- ISSN 2549-516X  
Accreditation No. 30/E/KPT/2018

Vol. 17 No. 1 June 2020

The abstract may be copied without permission or charge

ABSTRACT

**ANALYSIS OF WATER PRODUCTIVITY IN THE BANDA SEA BASED ON REMOTE SENSING SATELLITE DATA/ Sartono Marpaung, Risky Faristyawan, Anang Dwi Purwanto, Wikanti Asriningrum, Argo Galih Suhada, Teguh Prayogo, Jansen Sitorus**  
IJRESES, 17 (1) 2020 : 25-34

This study examines the density of potential fishing zone (PFZ) points and chlorophyll-a concentration in the Banda Sea. The data used are those on chlorophyll-a from the Aqua MODIS satellite, PFZ points from ZAP and the monthly southern oscillation index. The methods used are single image edge detection, polygon center of mass, density function and a Hovmoller diagram. The result of the analysis show that productivity of chlorophyll-a in the Banda Sea is influenced by seasonal factors (dry season and wet season) and ENSO phenomena (El Niño and La Niña). High productivity of chlorophyll-a occurs during in the dry season with the peak in August, while low productivity occurs in the wet season and the transition period, with the lowest levels in April and December. The variability in chlorophyll-a production is influenced by the global El Niño and La Niña phenomena; production increases during El Niño and decreases during La Niña. Tuna conservation areas have as lower productivity of chlorophyll-a and PFZ point density compared to the northern and southern parts of the Banda Sea. High density PFZ point regions are associated with regions that have higher productivity of chlorophyll-a, namely the southern part of the Banda Sea, while low density PFZ point areas are associated with regions that have a low productivity of chlorophyll-a, namely tuna conservation areas. The effect of the El Niño phenomenon in increasing chlorophyll-a concentration is stronger in the southern part of study area than in the tuna conservation area. On the other hand, the effect of La Niña phenomenon in decreasing chlorophyll-a concentration is stronger in the tuna conservation area than in the southern and northern parts of the study area.

**Keywords:** *PFZ point, density, chlorophyll-a, water fertility, Hovmoller, Banda Sea*

**ASSESSMENT OF THE ACCURACY OF DEM FROM PANCHROMATIC PLEIADES IMAGERY (CASE STUDY: BANDUNG CITY. WEST JAVA)/ Rian Nurtyawan, Nadia fiscarina**  
IJRESES, 17 (1) 2020: 35-44

Pleiades satellite imagery is very high resolution. with 0.5 m spatial resolution in the panchromatic band and 2.5 m in the multispectral band. Digital elevation models (DEM) are digital models that represent the shape of the Earth's surface in three-dimensional (3D) form. The purpose of this study was to assess DEM accuracy from panchromatic Pleiades imagery. The process conducted was orthorectification using ground control points (GCPs) and the rational function model with rational polynomial coefficient (RFC) parameters. The DEM extraction process employed photogrammetric methods with different parallax concepts. Accuracy assessment was made using 35 independent check points (ICPs) with an RMSE accuracy of  $\pm 0.802$  m. The results of the Pleiades DEM image extraction were more accurate than the National DEM (DEMNAS) and SRTM DEM. Accuracy testing of DEMNAS results showed an RMSE of  $\pm 0.955$  m. while SRTM DEM accuracy was  $\pm 17.740$  m. Such DEM extraction from stereo Pleiades panchromatic images can be used as an element on base maps with a scale of 1: 5.000.

**Keywords:** *Pleiades, Digital Elevation Model, Stereo, Accuracy*

**International Journal of  
Remote Sensing and Earth Sciences**

P-ISSN 0216 – 6739; E- ISSN 2549-516X  
Accreditation No. 30/E/KPT/2018

Vol. 17 No. 1 June 2020

The abstract may be copied without permission or charge

ABSTRACT

**SPATIAL AND TEMPORAL ANALYSIS OF LAND SURFACE TEMPERATURE CHANGE ON NEW BRITAIN ISLAND/ Rafika Minati Devi, Tofan Agung Eka Prasetya, Diah Indriani**  
**IJRESES, 17 (1) 2020: 45-56**

Land Surface Temperature (LST) is a parameter to estimate the temperature of the Earth's surface and to detect climate change. Papua New Guinea is a tropical country with rainforests, the greatest proportion of which are located on the island of New Britain. Hectares of rainforests have been logged and deforested because of infrastructure construction. This study aims to investigate the change in land surface temperatures on the island from 2000 to 2019. The temperature data were taken from National Aeronautics and Space Administration (NASA) Terra satellites and were analysed using two statistical models: spatial and temporal. The spatial model used multivariate regression, while the temporal one used autoregression (AR). In this study, a cubic spline fitted curve was employed because this has the advantage of being smoother and providing good visuals. The results show that almost all the sub-regions of New Britain have experienced a significant increase in land surface temperature, with a Z value of 7.97 and a confidence interval (CI) of 0.264 – 0.437. The study only investigated land surface temperature change on New Britain Island using spatial and temporal analysis, so further analysis is needed which takes into account other variables such as vegetation and land cover, or which establishes correlations with other variables such as human health.

**Keywords:** *Land Surface Temperature, New Britain Island, Climate change, Cubic Spline*

**MAPPING BURNT AREAS USING THE SEMI-AUTOMATIC OBJECT-BASED IMAGE ANALYSIS METHOD/ Hana Listi Fitriana, Suwarsono Suwarsono, Eko Kusratmoko, Supriatna Supriatna**  
**IJRESES, 17 (1) 2020: 57-64**

Forest and land fires in Indonesia take place almost every year, particularly in the dry season and in Sumatra and Kalimantan. Such fires damage the ecosystem, and lower the quality of life of the community, especially in health, social and economic terms. To establish the location of forest and land fires, it is necessary to identify and analyse burnt areas. Information on these is necessary to determine the environmental damage caused, the impact on the environment, the carbon emissions produced, and the rehabilitation process needed. Identification methods of burnt land was made both visually and digitally by utilising satellite remote sensing data technology. Such data were chosen because they can identify objects quickly and precisely. Landsat 8 image data have many advantages: they can be easily obtained, the archives are long and they are visible to thermal wavelengths. By using a combination of visible, infrared and thermal channels through the semi-automatic object-based image analysis (OBIA) approach, the study aims to identify burnt areas in the geographical area of Indonesia. The research concludes that the semi-automatic OBIA approach based on the red, infrared and thermal spectral bands is a reliable and fast method for identifying burnt areas in regions of Sumatra and Kalimantan.

**Keywords:** *Burned area, Landsat 8, OBIA*

**International Journal of  
Remote Sensing and Earth Sciences**

P-ISSN 0216 – 6739; E- ISSN 2549-516X  
Accreditation No. 30/E/KPT/2018

Vol. 17 No. 1 June 2020

The abstract may be copied without permission or charge

ABSTRACT

**AN ENHANCEMENT TO THE QUANTITATIVE PRECIPITATION ESTIMATION USING RADAR-GAUGE MERGING/ Abdullah Ali, Gumilang Deranadyan, Iddam Hairuly Umam  
IJRESES, 17 (1) 2020: 65-74**

Quantitative Precipitation Estimation (QPE) is quite important information for the hydrology fields and has many advantages for many purposes. Its dense spatial and temporal resolution can be combined with the surface observation to enhance the accuracy of the estimation. This paper presents an enhancement to the QPE product from BMKG weather radar network at Surabaya by adjusting the estimation value from radar to the real data observation from rain gauge. A total of 58 rain gauge is used. The Mean Field Bias (MFB) method used to determine the correction factor through the difference between radar estimation and rain gauge observation value. The correction factor obtained at each gauge points are interpolated to the entire radar grid in a multiplicative adjustment. Radar-gauge merging results a significant improvement revealed by the decreasing of mean absolute error (MAE) about 40% and false alarm ratio (FAR) as well an increasing of possibility of detection (POD) more than 50% at any rain categories (light rain, moderate rain, heavy rain, and very heavy rain). This performance improvement is very beneficial for operational used in BMKG and other hydrological needs.

**Keywords:** *Quantitative Precipitation Estimation, radar-gauge merging, Mean Field Bias Method*

**OPTIMIZATION OF RICE FIELD CLASSIFICATION MODEL BASED ON THRESHOLD INDEX OF MULTITEMPORAL LANDSAT IMAGES /Dede Dirgahayu, Made Parsa, Sri Harini, Dony Kurhardono  
IJRESES, 17 (1) 2020: 75-84**

The development of rice land classification models in 2018 has shown that the phenology-based threshold of rice crops from the multi-temporal Landsat image index can be used to classify rice fields relatively well. The weakness of the models was the limitations of the research area, which was confined to the Subang region, West Java, so it is was deemed necessary to conduct further research in other areas. The objective of this study is to obtain optimal parameters of classification model of rice and land based on multi-temporal Landsat image indexes. The study was conducted in several districts of rice production centers in South Sulawesi and West Java (besides Subang). The threshold method was employed for the Landsat Image Enhanced Vegetation Index (EVI). Classification accuracy was calculated in two stages, the first using detailed scale reference information on rice field base, and the second using field data (from a survey). Based on the results of the analysis conducted on several models, the highest accuracy is generated by the three index parameter models (EVI\_min, EVI\_max, and EVI\_range) and adjustable threshold with 94.8% overall accuracy. Therefore this model was acceptable for used for nationally rice fields mapping.

**Keywords:** *multitemporal, EVI, threshold, optimizaton*

**International Journal of  
Remote Sensing and Earth Sciences**

P-ISSN 0216 – 6739; E- ISSN 2549-516X  
Accreditation No. 30/E/KPT/2018

Vol. 17 No. 1 June 2020

The abstract may be copied without permission or charge

ABSTRACT

**UTILISATION OF NASA - GFWD AND FIRMS SATELLITE DATA IN DETERMINING THE PROBABILITY OF HOTSPOTS USING THE FIRE WEATHER INDEX (FWI) IN OGAN KOMERING ILIR REGENCY, SOUTH SUMATRA/ Hermanto Asima Nainggolan, Desak Putu Okta Veanti, Dzikrullah Akbar  
IJRESES, 17 (1) 2020: 85-98**

Prevention and mitigation of forest and land fires have important roles considering its various negative impacts. Throughout 2018, in Ogan Komering Ilir District, 864 hectares of land burned. This data increased significantly compared to the burned area in the previous year. Lack of field meteorological observation is still a problem in solving the problem of forest fire in the region. Consequently, we utilize NASA - GFWD and FIRMS satellite data to analyze the hotspots probabilities in Ogan Komering Ilir District, South Sumatra. Conditional probability analysis will be used to find out the likelihood of hotspots based on FWI and FFMC from 2001 to 2016. More than 50 percent of hotspots appear during extreme FFMC class and high to extreme FWI class. The probability of hotspots for extreme FFMC class and extreme FWI class varied between 0.3 to 10.4 % and 0.1 to 3.8 % respectively. Meanwhile, fire-prone areas with the highest density of fires are in the sub-district of Tulung Selapan, and the safest region is the Cengal sub-district.

**Keywords:** *FWI, Hotspots, Forest Fires, Conditional Probability*

**International Journal of  
Remote Sensing and Earth Sciences**

P-ISSN 0216 – 6739; E- ISSN 2549-516X  
Accreditation No. 30/E/KPT/2018

Vol. 17 No. 2 December 2020

The abstract may be copied without permission or charge

ABSTRACT

**VARIABILITY OF SEA SURFACE TEMPERATURE AT FISHERIES MANAGEMENT AREA 715 IN INDONESIA AND ITS RELATION TO THE MONSOON, ENSO AND FISHERY PRODUCTION/ Komang Iwan Suniada IJRESES, 17 (2) 2020: 99-114**

Sea surface temperature (SST) is one of the important oceanographic and climate parameters. Its variability and anomalies often influence the environment and organisms, both in the oceans and on land. This study aims to identify the variability of SST and help the fisheries community to understand how climate phenomena such as ENSO and monsoonal phases (represented by wind speed) are related to SST and fishery production in Fisheries Management Area (FMA) 715. SST was measured at Parimo, which represents conditions in the western part of the area inside Tomini Bay, and at Bitung, which represents SST in the open ocean, with a more exposed geographical position. SST was derived from MODIS satellite imagery, downloaded from the oceancolor database (<https://oceancolor.gsfc.nasa.gov/>) with a 4 km spatial resolution, from January 2009 to December 2018. Wind speed data, historical El Niño or La Niña events, and fish production data were also used in the study. Pearson's correlation (Walpole, 1993) was used to test the relationship between SST variability or anomaly and ENSO and monsoons. The results show that the SST characteristics and variability of the Parimo and Bitung waters are very different, although they both lie in the same FMA 715. SST in Parimo waters is warmer, but with lower variability than in Bitung waters. SST in Parimo has a low correlation with ENSO ( $r=0.06$ ,  $n=66$ ), low correlation with wind speed ( $r=-0.29$ ,  $n=120$ ), with also a low correlation between SST anomaly and ENSO ( $r=0.05$ ,  $n=66$ ). SST in Bitung has a higher, but inverse, correlation with ENSO ( $r=-0.53$ ,  $n=66$ ), high correlation with wind speed ( $r=-0.60$ ,  $n=119$ ), with also a high correlation between SST anomaly and ENSO ( $r=-0.74$ ,  $n=66$ ). Unlike in other parts of Indonesia, fishery production in Parimo, or the western part inside Tomini Bay, is not affected by ENSO events.

Keywords: SST, FMA 715, ENSO, monsoon, Tomini Bay

**DETECTION AND ANALYSIS OF SURFACE URBAN COOL ISLAND USING THERMAL INFRARED IMAGERY OF SALATIGA CITY, INDONESIA/ Bayu Elwanto Bagus Dewantoro, Panji Mahyatar, Wafiq Nur Hayani IJRESES, 17 (2) 2020: 115-126**

The detection and monitoring of the dynamics of urban micro-climates needs to be performed effectively, efficiently, consistently and sustainably in an effort to improve urban resilience to such phenomena. Thermal remote sensing possesses surface thermal energy detection capabilities which can be converted into surface temperatures and utilised to analyse the urban micro-climate phenomenon over large areas, short periods of time, and at low cost. This paper studies the surface urban cool island (SUCI) effect, the reverse phenomenon of the surface urban heat island (SUHI) effect, in an effort to provide cities with resistance to the urban microclimate phenomenon. The study also aims to detect urban micro-climate phenomena, and to calculate the intensity and spatial distribution of SUCI. The methods used include quantitative-descriptive analysis of remote sensing data, including LST extraction, spectral transformation, multispectral classification for land cover mapping, and statistical analysis. The results show that the urban micro-climate phenomenon in the form of SUHI in the middle of the city of Salatiga is due to the high level of building density in the area experiencing the effect, which mostly has a normal surface temperature based on the calculation of the threshold, while the relative SUCI occurs at the edge of the city. SUCI intensity in Salatiga ranges between  $-6.71^{\circ}\text{C}$  and  $0^{\circ}\text{C}$  and is associated with vegetation.

Keywords: *Thermal Remote Sensing, Land Surface Temperature, Urban Microclimate, Surface Urban Cool Island*

**International Journal of  
Remote Sensing and Earth Sciences**

P-ISSN 0216 – 6739; E- ISSN 2549-516X

Vol. 17 No. 2 December 2020

Accreditation No. 30/E/KPT/2018

The abstract may be copied without permission or charge

ABSTRACT

**MONITORING CHANGES IN CORAL REEF HABITAT COVER ON BERALAS PASIR ISLAND USING SPOT 4 AND SPOT 7 IMAGERY FROM 2011 AND 2018/ Rosaria Ria Damai, Viv Djanat Prasita, Kuncoro Teguh Setiawan  
IJRESES, 17 (2) 2020: 127-148**

Beralas Pasir is part of the Regional Marine Conservation Area (KKLD), which was established by the Bintan Regency Government with Bintan Regent Decree No. 261 / VIII / 2007. Water tourism activities undertaken by tourists on the island have had an impact on the condition of the coral reefs, as have other factors, such as bauxite, granite and land sand mining activities around the island. This research aims to determine changes in the coral reef habitat cover and the condition of the coral reefs around Beralas Pasir Island with a remote sensing function, using SPOT 4 imagery acquired on June 1, 2011 and SPOT 7 imagery from April 5, 2020. Data collection of environmental parameters related to the coral reefs was also made. The image processing used the Lyzenga algorithm to simplify the image classification process. The percentage of coral live cover around the island ranges from 26% - 53%; this has experienced a significant change, from 67,560 hectares in 2011 to 38,338 hectares in 2018, a total decrease in the area of 29,222 hectares. Some of the natural factors found in the research which have caused damage to the reefs were *Drupella* snails, the abundance of *Caulerpa racemosa* algae, and sea urchins. The majority of the coral reef types consist of Non-Acupora: Coral Massive, Coral, Coral Foliose, Coral Encrusting, Acupora: Acupora Tabulate, Acupora Encrusting, and Acupora Digitate.

*Keywords: Monitoring, Coral Reefs, SPOT 4, SPOT 7, Beralas Pasir Island*

**MULTITEMPORAL ANALYSIS FOR TROPHIC STATE MAPPING IN BATUR LAKE AT BALI PROVINCE BASED ON HIGH-RESOLUTION PLANETSCOPE IMAGERY/ Rahma Nafila Fitri Sabrina, Sudaryatno Sudaryatno  
IJRESES, 17 (2) 2020: 149-162**

Remote sensing data for analyzing and evaluating trophic state ecosystem problems seen in Batur Lake is an approach that is suitable for water parameters that cannot be observed terrestrially. As the multitemporal spatial data used in this study were extensive, it was necessary to consider the effectiveness and efficiency of the processing and analysis, therefore R Studio was used as a data processing tool. The research aims to (1) map the trophic state of Batur Lake multitemporally using PlanetScope Imagery ; (2) assess the accuracy of the trophic state model and apply it to another temporal data as a Spatial Big Data; and (3) understand the trophic state impact on the water quality of Batur Lake based on physical factors and the lake's chemical concentration (sulfur concentration). The research shows that the trophic state of Batur Lake is in good condition, with an ultraoligotrophic state as the majority class, based on the mean Trophic State Index (TSI) value of 9.49. The standard errors of each trophic state parameter were 0.010 for total phosphor, 0.609 for chlorophyll-a, and 0.225 for Secchi Disk Transparency (SDT). The multitemporal model demonstrates that the correlation between the increase of trophic state and mass fish death cases in Batur Lake is existent.

*Keywords: Freshwater Lakes, Ultraoligotrophic, TSI Carlson, Sulfur Bursts, Remote Sensing*



**International Journal of  
Remote Sensing and Earth Sciences**

P-ISSN 0216 – 6739; E- ISSN 2549-516X  
Accreditation No. 30/E/KPT/2018

Vol. 17 No. 2 December 2020

The abstract may be copied without permission or charge

ABSTRACT

**MONITORING MODEL OF LAND COVER CHANGE FOR THE INDICATION OF DEVEGETATION AND REVEGETATION USING SENTINEL-2/ Samsul Arifin, Tatik Kartika, Dede Dirgahayu, and Gatot Nugroho  
IJRESES, 17 (2) 2020: 163-174**

Information on land cover change is very important for various purposes, including the monitoring of changes for environmental sustainability. The objective of this study is to create a monitoring model of land cover change for the indication of devegetation and revegetation using data from Sentinel-2 from 2017 to 2018 of the Brantas watershed. This is one of the priority watersheds in Indonesia, so it is necessary to observe changes in its environment, including land cover change. Such change can be detected using remote sensing data. The method used is a hybrid between Normalized Difference Vegetation Index (NDVI) and Normalized Burn Ratio (NBR) which aims to detect land changes with a focus on devegetation and revegetation by determining the threshold value for vegetation index ( $\Delta$ NDVI) and open land index ( $\Delta$ NBR). The study found that the best thresholds to detect revegetation were  $NDVI > 0.0309$  and  $NBR < 0.0176$  and to detect devegetation  $NDVI < - 0.0206$  and  $NBR > 0.0314$ . It is concluded that Sentinel-2 data can be used to monitor land changes indicating devegetation and revegetation with established NDVI and NBR threshold conditions.

*Keywords: Model, Monitoring. Land Cover, Sentinel-2, devegetation, revegetation*

**INTERSEASONAL VARIABILITY IN THE ANALYSIS OF TOTAL SUSPENDED SOLIDS(TSS) IN SURABAYA COASTAL WATERS USING LANDSAT-8 SATELLITE DATA/ Bela Karbela, Pingkan Mayestika Afgatiani, Ety Parwati  
IJRESES, 17 (2) 2020: 175-188**

The spatial and temporal capabilities of remote sensing data are very effective for monitoring the value of total suspended solids (TSS) in water using optical sensors. In this study, TSS observations were conducted in the west season, transition season 1, east season, and transition season 2 in 2018 and 2019. Landsat 8 image data were used, extracted into TSS values using a semi-analytic model developed in the Mahakam Delta, East Kalimantan, Indonesia. The TSS data obtained were then analysed for distribution patterns in each season. The sample points were randomly scattered throughout the study area. The TSS distribution pattern in the west season showed a high concentration spread over the coastal area to the off sea, while the pattern in the east season only showed a high concentration in the coastal areas. Transitional seasons 1 and 2 showed different patterns of TSS distribution in 2018 and 2019, with more varied values. The distribution of TSS is strongly influenced by the season. Observation of each cluster resulted in the conclusion that human activity and the rainfall rate can affect the concentration of TSS.

*Keywords: Rainfall Rate, Total Suspended Solids, Seasonal Total Suspended Solids, Surabaya*

**International Journal of  
Remote Sensing and Earth Sciences**

P-ISSN 0216 – 6739; E- ISSN 2549-516X  
Accreditation No. 30/E/KPT/2018

Vol. 17 No. 2 December 2020

The abstract may be copied without permission or charge

ABSTRACT

**A COMPARISON OF RAINFALL ESTIMATION USING HIMAWARI-8 SATELLITE DATA IN DIFFERENT INDONESIAN TOPOGRAPHIES/ Nadine Ayasha  
IJRESES, 17 (2) 2020: 189-200**

The Himawari-8 satellite can be used to derive precipitation data for rainfall estimation. This study aims to test several methods for such estimation employing the Himawari-8 satellite. The methods are compared in three regions with different topographies, namely Bukittinggi, Pontianak and Ambon. The rainfall estimation methods that are tested are auto estimator, IMSRA, non-linear relation and non-linear inversion approaches. Based on the determination of the statistical verification (RMSE, standard deviation and correlation coefficient) of the amount of rainfall, the best method in Bukittinggi and Pontianak was shown to be IMSRA, while for the Ambon region was the non-linear relations. The best methods from each research area were mapped using the Google Maps Application Programming Interface (API).

**Keywords:** *Rainfall Estimation, Himawari-8 Satellite, Google Maps API*

**SHORELINE CHANGES AFTER THE SUNDA STRAIT TSUNAMI ON THE COAST OF PANDEGLANG REGENCY, BANTEN/ Fandi Dwi Julianto, Cahya Rizki Fathurohman, Salsabila Diyah Rahmawati, Taufiq Ihsanudin  
IJRESES, 17 (2) 2020: 201-208**

The Sunda Strait tsunami occurred on the coast of west Banten and South Lampung at 22nd December 2018, resulting in 437 deaths, with 10 victims missing. The disaster had various impacts on the environment and ecosystem, with this area suffering the greatest effects from the disaster. The utilisation of remote sensing technology enables the monitoring of coastal areas in an effective and low-cost manner. Shoreline extraction using the Google Earth Engine, which is an open-source platform that facilitates the processing of a large number of data quickly. This study used Landsat-8 Surface Reflectance Tier 1 data that was geometrically and radiometrically corrected, with processing using the Modification of Normalized Difference Water Index (MNDWI) algorithm. The results show that 30.1% of the coastline in Pandeglang Regency occurred suffered abrasion, 20.2% suffered accretion, while 40.7% saw no change. The maximum abrasion of 130.2 meters occurred in the village of Tanjung Jaya. Moreover, the maximum shoreline accretion was 43.3 meters in the village of Panimbang Jaya. The average shoreline change in Pandeglang Regency was 3.9 meters.

**Keywords:** Landsat-8, Google Earth Engine, Abrasion, Tanjung Jaya, MNDWI

**International Journal of  
Remote Sensing and Earth Sciences**

P-ISSN 0216 – 6739; E- ISSN 2549-516X

Vol. 17 No. 2 December 2020

Accreditation No. 30/E/KPT/2018

The abstract may be copied without permission or charge

ABSTRACT

**BATHYMETRIC EXTRACTION USING PLANETSCOPE IMAGERY (CASE STUDY: KEMUJAN ISLAND, CENTRAL JAVA)/ Asih Sekar Sesama, Kuncoro Teguh Setiawan, Atriyon Julzarika IJRESES, 17 (2) 2020: 209-216**

Bathymetry refers to the depth of the seabed relative to the lowest water level. Depth information is essential for various studies of marine resource activities, for managing port facilities and facilities, supporting dredging operations, and predicting the flow of sediment from rivers into the sea. Bathymetric mapping using remote sensing offers a more flexible, efficient, and cost-effective method and covers a large area. This study aims to determine the ability of PlanetScope imagery to estimate and map bathymetry and to ascertain its accuracy using the Stumpf algorithm on the in-situ depth data. PlanetScope level 3B satellite imagery and tide-corrected survey data are employed ; satellite images are useful in high-precision bathymetry extraction. The bathymetric extraction method used the Stumpf algorithm. The research location was Kemujan Island, Karimunjawa Islands, Central Java. The selection of this region was based on its water characteristics, which have a reasonably high variation in depth. Based on the results of the data processing, it was found that the PlanetScope image data were able to estimate depths of up to 20 m. In the bathymetric results, the R2 accuracy value was 0.6952, the average RMSE value was 2.85 m, and the overall accuracy rate was 71.68%.

*Keywords: marine resources activity, Stumpf algorithm, Karimun Jawa Island, remote sensing, water characteristics*

# VARIABILITY OF SEA SURFACE TEMPERATURE IN FISHERIES MANAGEMENT AREA 715, INDONESIA AND ITS RELATION TO THE MONSOON, ENSO AND FISHERY PRODUCTION

Komang Iwan Suniada<sup>1\*</sup>

<sup>1</sup>Institute for Marine Research and Observation

Ministry of Marine Affairs and Fisheries

\*e-Mail: komang.suniada@kkp.go.id

Received: 7 July 2020; Revised: 24 August 2020; Approved: 31 August 2020

**Abstract.** Sea surface temperature (SST) is one of the important oceanographic and climate parameters. Its variability and anomalies often influence the environment and organisms, both in the oceans and on land. This study aims to identify the variability of SST and help the fisheries community to understand how climate phenomena such as ENSO and monsoonal phases (represented by wind speed) are related to SST and fishery production in Fisheries Management Area (FMA) 715. SST was measured at Parimo, which represents conditions in the western part of the area inside Tomini Bay, and at Bitung, which represents SST in the open ocean, with a more exposed geographical position. SST was derived from MODIS satellite imagery, downloaded from the oceancolor database (<https://oceancolor.gsfc.nasa.gov/>) with a 4 km spatial resolution, from January 2009 to December 2018. Wind speed data, historical El Niño or La Niña events, and fish production data were also used in the study. Pearson's correlation (Walpole, 1993) was used to test the relationship between SST variability or anomaly and ENSO and monsoons. The results show that the SST characteristics and variability of the Parimo and Bitung waters are very different, although they both lie in the same FMA 715. SST in Parimo waters is warmer, but with lower variability than in Bitung waters. SST in Parimo has a low correlation with ENSO ( $r=0.06$ ,  $n=66$ ), low correlation with wind speed ( $r=-0.29$ ,  $n=120$ ), with also a low correlation between SST anomaly and ENSO ( $r=0.05$ ,  $n=66$ ). SST in Bitung has a higher, but inverse, correlation with ENSO ( $r=-0.53$ ,  $n=66$ ), high correlation with wind speed ( $r=-0.60$ ,  $n=119$ ), with also a high correlation between SST anomaly and ENSO ( $r=-0.74$ ,  $n=66$ ). Unlike in other parts of Indonesia, fishery production in Parimo, or the western part inside Tomini Bay, is not affected by ENSO events.

Keywords: SST, FMA 715, ENSO, monsoon, Tomini Bay

## 1 INTRODUCTION

Sea surface temperature (SST) is one of the most important oceanographic and climate parameters (Kaplan et al., 1998; Corvianawatie et al., 2014; Davies and Cressie, 2016) since it plays the key role in regulating climate and its variability, together with several other atmospheric parameters including wind speed, air temperature, humidity and cloudiness (Deser et al., 2010). Variability in SST is influenced by both atmospheric and oceanic processes and

phenomena. Wind speed, air temperature, cloudiness and humidity are the dominant factors in the atmosphere which regulate SST dynamics, while heat transport by currents, vertical mixing and boundary layer depth are the dominant factors influencing SST variability which originate from the ocean. The widely recognised climatological phenomenon known as the El Niño Southern Oscillation (ENSO) clearly demonstrates how variability at the ocean surface,

especially SST in the tropical Pacific Ocean, corresponds to atmospheric variations, that will have an impact on weather conditions worldwide (Davies and Crissie, 2016). ENSO consists of two established events, El Niño (a warmer eastern tropical Pacific) and La Niña (a cooler eastern tropical Pacific). During the El Niño event, dry conditions increase and precipitation is lower in the Australia, Indonesia, New Guinea, Micronesia, Fiji, New Caledonia and Hawaii regions (Pui et al., 2012). During the La Niña event, SST in the western tropical Pacific Ocean is warmer than normal, and rainfall increases around Australia and Indonesia (Vitri and Marzuki, 2014). These conditions also correlate with the increasing number of tropical cyclones compared to normal climatology condition (Chand et al., 2013). The Oceanic Niño Index (ONI) is the standard measure of the ENSO phenomenon, using the combination of a part of the Niño 3 and Niño 4 regions, also known as the Niño 3.4 region. Five consecutive of three-month moving

average of SST anomalies within the Niño 3.4 region which are above (below) the threshold of +0.5 (-0.5), indicate the occurrence of the El Niño (La Niña) phenomenon (<https://www.ncdc.noaa.gov/teleconnections/enso/indicators/sst/>).

Beside ENSO, the Indonesian archipelago is influenced by the Asia Australia monsoonal system. Monsoon systems are fundamentally driven by solar position and radiation, which trigger pressure differences between the two continents. These differences generate different wind speeds and directions in Indonesia during such phases (Webster et al., 1999). In July, Australia is colder (higher pressure) than Asia (warmer, lower pressure), so the wind blows from Australia to Asia; this phase is known as the southeast monsoon. On the other hand, in January Asia is colder (higher pressure) than Australia (warmer, lower pressure), which means the wind direction is from Asia to Australia, in a phase known as the northwest monsoon.

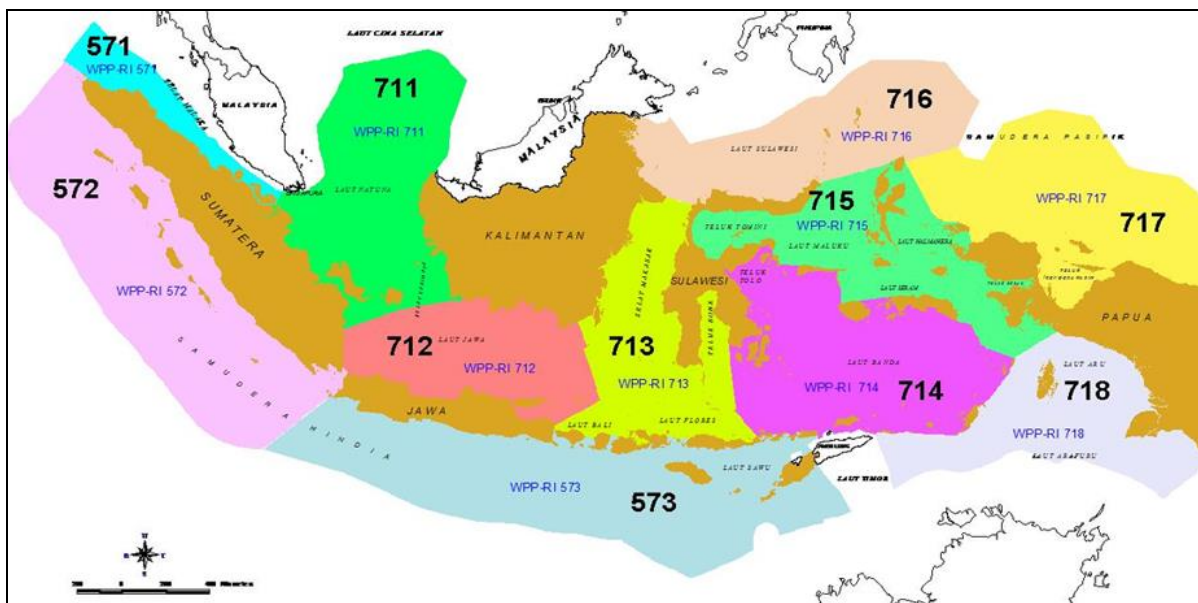


Figure 1-1: Fisheries Management Areas in Indonesia

The Indonesian archipelago, according to the Ministry of Marine Affairs and Fisheries regulation No. 18/PERMEN-KP/2014, is divided into 11 Fisheries Management Areas (FMAs), as shown in Figure 1-1. This classification was based on the resource characteristics and biophysical environment. An Ecosystem Approach to Fisheries Management (EAFM) was also used as a basis for developing the FMAs, with the management scope including the capture fisheries, marine culture, conservation, research, and fisheries development (Muawanah et al., 2018).

FMA 715 covers a large area from Tomini Bay, the Maluku Sea, Seram Sea, Halmahera Sea, to Berau Bay. The seabed topography of FMA 715 is very varied. It generally consists of oceanic deep waters, some area has a little coral bottom, especially around Tomini Bay, and rather shallow waters consisting of sand mud around Berau Bay. This varied topography leads to numerous fisheries resources within FMA 715. Tomini Bay is inhabited by many coral fish that can be caught throughout the year; shrimp resources are abundant in the muddy waters of Berau Bay; small pelagic fish resources are available in the shallow waters; while larger pelagic fish resources are available in the deeper waters. Other resources, such as lobster and squid, are also available in FMA 715 (Suman et al., 2014). Some water masses in FMA 715 are influenced by the Indonesian Through Flow (ITF), which carries water mass from the Pacific Ocean, entering Indonesia waters from the Sulawesi Sea through the Maluku Sea, Halmahera Sea and Seram Sea (Radjawane and Hadipoetranto, 2014). Other types of water mass characteristic in FMA 715 are semi-enclosed water such as Tomini Bay and Berau Bay.

Generally, climate phenomena including ENSO influence most SST around Indonesia, but only a minor information state about the ENSO effect on semi-enclosed water. In this study, the characteristics of semi-enclosed water SST in FMA 715 are represented by Parimo waters, which are located in the western part of Tomini Bay, while open ocean characteristics are represented by the area around Bitung waters. The objective of this study is to identify one of the oceanographic parameters (SST) and how climate phenomena such as ENSO and monsoonal processes are related to the variability of SST in Parimo and Bitung. The study also identifies the relationship between climate phenomena and fishery production within semi-enclosed water.

## 2 DATA AND METHOD

The main data used in the study were the monthly average SSTs derived from Moderate Resolution Imaging Spectroradiometer (MODIS) satellite images from January 2009 to December 2018. SST satellite data with a spatial resolution of 4 km were successfully downloaded from the oceancolor database (<https://oceancolor.gsfc.nasa.gov/>). A map of the monthly mean climatological SST was then created using QGIS software to show the spatial distribution of SST within FMA 715. To understand the variability, the SST data were extracted at two locations, one representing the variability at the western part inside Tomini bay (Parimo; 120.17°E and -0.76°S) and the other the SST variability in the open ocean (Bitung; 125.25°E and 1.38°N ) within FMA 715 (figure 2-1). Another important oceanic indicator is SST anomaly. In this study, the anomaly in Parimo and Bitung was calculated by subtracting the

monthly variation to its monthly mean data:

$$SSTA = SST_i - \overline{SST} \quad (2-1)$$

where SSTA is SST anomaly and  $\overline{SST}$  is SST monthly mean data

$$\overline{SST} = \frac{\sum_{i=1}^n SST_i}{n} \quad (2-2)$$

Wind speed data were downloaded from the Indonesian Agency of Meteorology, Climatology and Geophysics database center ([http://dataonline.bmkg.go.id/data\\_iklim](http://dataonline.bmkg.go.id/data_iklim)). This agency has many climate observation stations scattered throughout Indonesia, one of which is located in Bitung City (125.18°E and 1.44°N). In situ data from local observing stations were chosen for the study, since they can describe more realistic conditions compared to modelling data available online. Daily wind speed data from January 2009 to December 2018 were downloaded from that database centre, then processed into a monthly average using a simple mathematic equation. The monthly

average wind speed data are useful in describing their variability related to the monsoon.

The Oceanic Niño Index (ONI) is the standard measure of the ENSO phenomenon using a combination of part of the Niño 3 and Niño 4 regions, also known as the Niño 3.4 region. The occurrence of El Niño is indicating by SST anomaly with a value more than +0.5 for five consecutive months. While the occurrence of La Niña is indicating by the value of SST anomaly lower than -0.5. Historical El Niño or La Niña event data represented on the Oceanic Niño Index (ONI) are available at the Climate Prediction Center – National Weather Service website ([https://origin.cpc.ncep.noaa.gov/products/analysis\\_monitoring/ensostuff/ONI\\_v5.php](https://origin.cpc.ncep.noaa.gov/products/analysis_monitoring/ensostuff/ONI_v5.php)). ONI data from January 2009 to December 2018 are used in this study.

Fish production data recorded by the Parimo Marine and Fisheries Office provide information about dominant small or large pelagic fish caught inside the western side of Tomini Bay. This data series is also a useful indicator for describing fish production during El Niño or La Niña events.

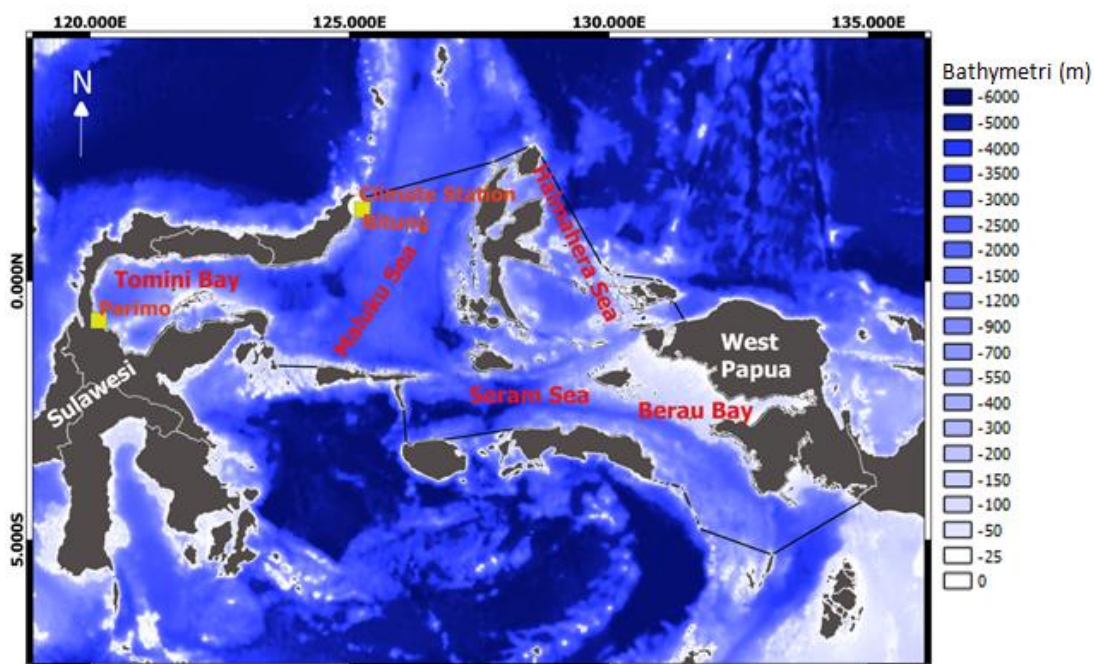


Figure 2-1: Study Area at FMA 715



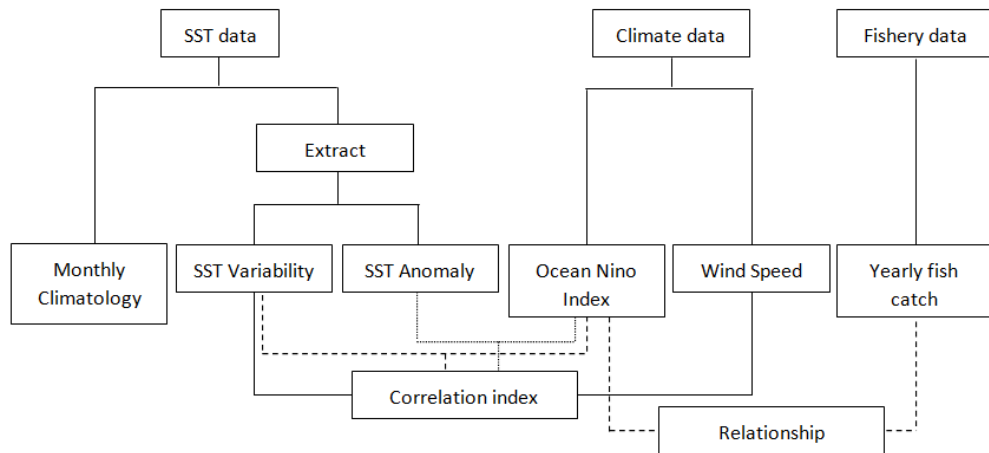


Figure 2-2: Block diagram of this study

Pearson’s correlation (Walpole, 1993) is used to test the relationship between SST variability or SST anomaly and the ENSO and monsoons, represented by wind speed.

A block diagram of the study is shown in Figure 2-2.

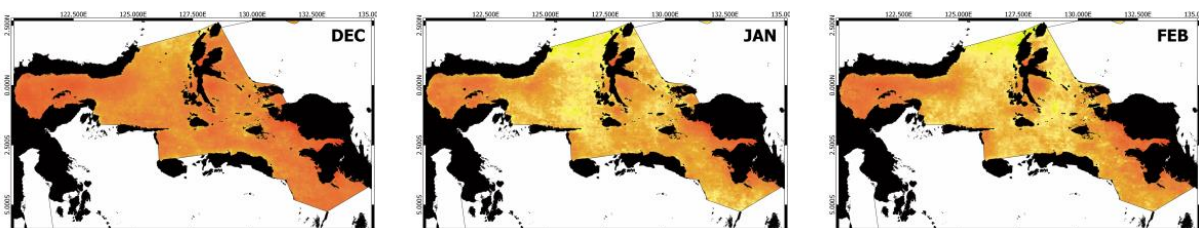
### 3 RESULTS

#### Map of Monthly Climatology SST Mean

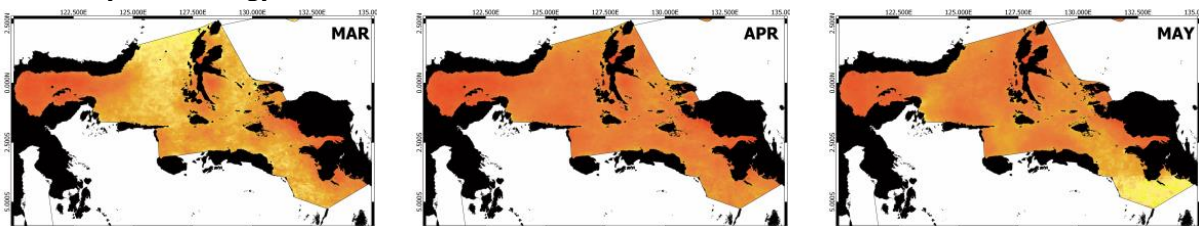
Evidence of the close relationship between SST and monsoonal systems

within FMA 715 is shown in Figure 3-1. Slightly cooler temperatures are found in some areas in FMA 715 during the boreal winter months (December to March). On the contrary, due to the southeast monsoon, cooler temperatures are found to the south of the equator from June to August. It is also shown that the variability of SST at Parimo, or the western part within Tomini Bay, is relatively stable, with only small SST variations compared to those near Bitung waters.

#### a. Monthly Climatology SST Mean from 2009 to 2018; Northwest Monsoon

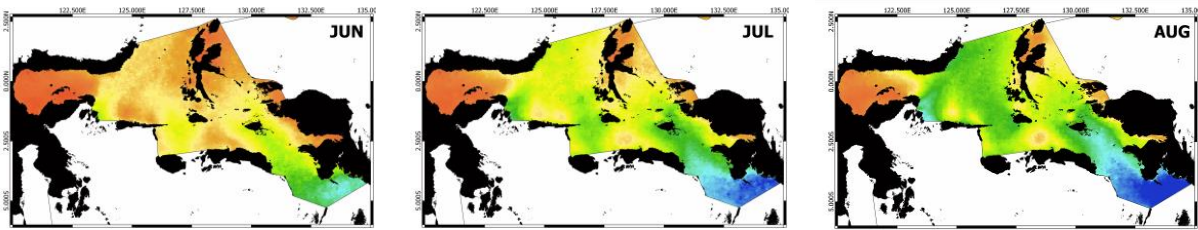


#### b. Monthly Climatology SST Mean from 2009 to 2018; Transition I





c. Monthly Climatology SST Mean from 2009 to 2018; Southeast Monsoon



d. Monthly Climatology SST Mean from 2009 to 2018; Transition II

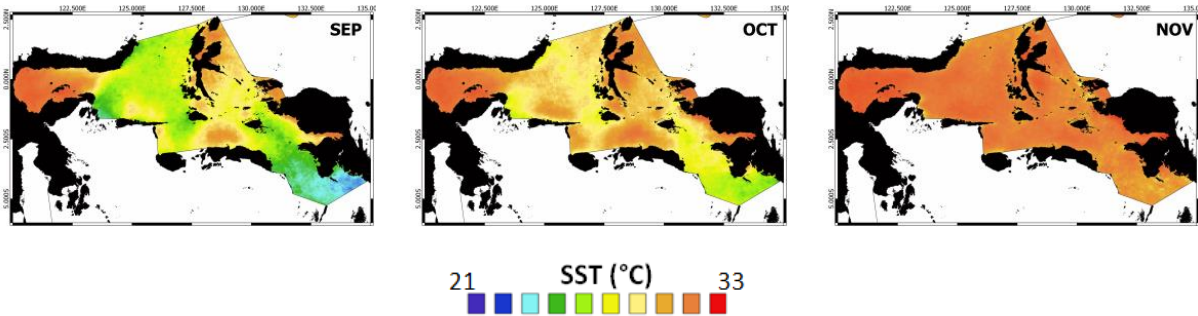


Figure 3-1: Monthly Climatology SST Mean from 2009 to 2018

*SST variability*

The mean SST value in Parimo waters during the period 2009 – 2018 is 30.68°C ( $\sigma = 0.51$ ,  $n = 120$ ), with a maximum value of 32.22°C in April 2010 and a minimum of 28.73°C in February 2015. The variability in monthly average SST shows that the maximum peak can be present in any month. For example, in 2009 the maximum peak was in October; in 2010, 2015 and 2017 it was in April; in 2011 in May; in 2012 in December; in 2013 in July; in 2014 and 2018 in March; and in 2016 the maximum SST peak occurred in June. Unlike the maximum peak, the minimum SST peak mostly occurs in January or February, except in 2012 when it was August. During the period 2009 – 2018, the mean SST value in Bitung waters was 29.34°C ( $\sigma = 0.87$ ,  $n = 119$ ), with a maximum value of 31.01°C in December 2016, and a minimum

value of 26.47°C in August 2015. The pattern of monthly variability in Bitung waters shows that the minimum SST peak is mostly found in July and August, although in 2010 it occurred in February. Similar to Parimo, the maximum peak in Bitung waters can also be found in several different months: in 2009 and 2018 it occurred in April; in 2010, 2014 and 2017 in November; in 2011 in February; in 2012 in March; in 2013 and 2015 in June; and in 2016 the maximum SST peak occurred in December. Figure 3-2 also shows that the SST in Parimo and Bitung waters have completely different characteristics. Most of the year, SST in Parimo tends to be higher than in Bitung. During the period 2009 – 2018, July, August, September and October 2015 were recorded as having the coolest SST in Bitung, with a minimum peak occurring in August.

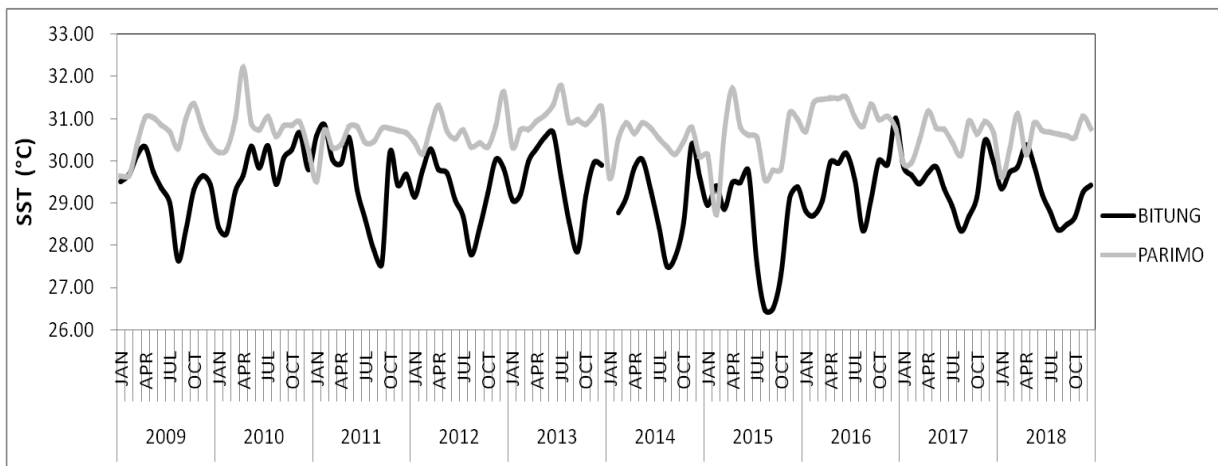


Figure 3-2: SST variability in Parimo and Bitung 2009 - 2018

The monthly climatological mean of SST at Parimo and Bitung waters is presented in Figure 3-3. This clearly shows that the two regions have different variability and surface temperatures. In Parimo, the lowest SST occurs in January (northwest monsoon), increasing in March and reaching its maximum in April (Transitional I). It then slightly cools in August (southeast monsoon), before slightly increasing again until November (Transitional II). In Bitung, SST tends to decrease during the northwest monsoon, especially in

January and February. It then starts to increase during Transition I, reaching a maximum in May. Entering the Southeast monsoon, SST starts to decrease and drops to a minimum in August. During Transition II, SST increases again, until a maximum value is reached in November. In general, Bitung waters are cooler than those of Parimo, and also the climatological variation of SST in Parimo is relatively small, with the value of 30.02°C - 31.11°C, compared to that of Bitung, with a variation of 28.04°C - 30.01°C.

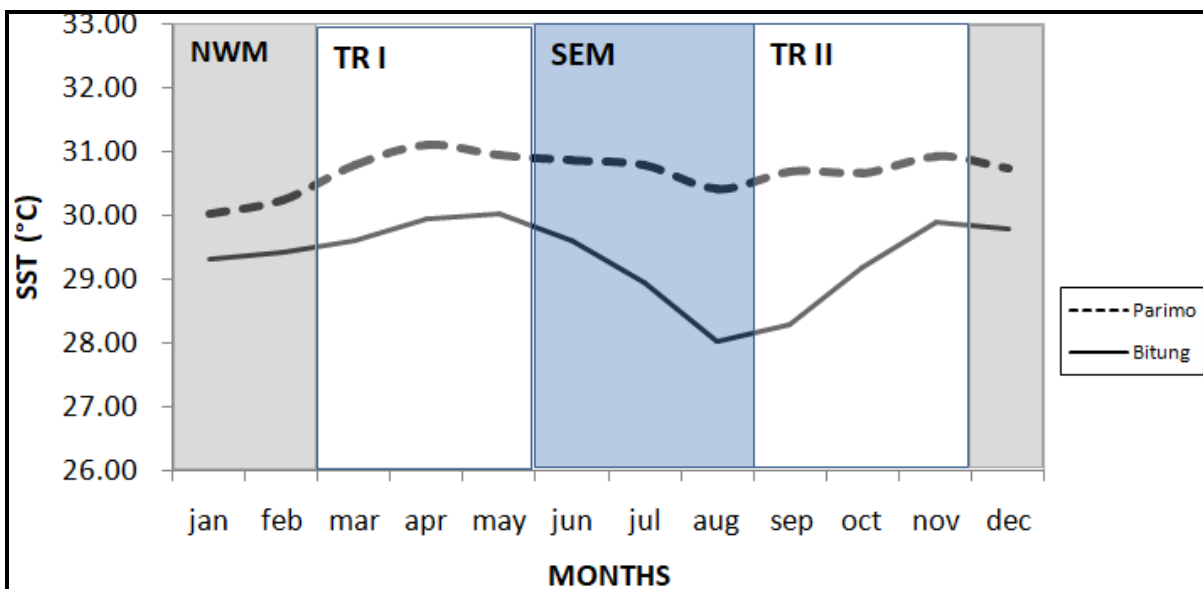


Figure 3-3. Climatology of SST in Parimo and Bitung 2009 - 2018 (NWM: Northwest Monsoon; TR I: Transition I; SEM: Southeast Monsoon; TR II: Transition II)

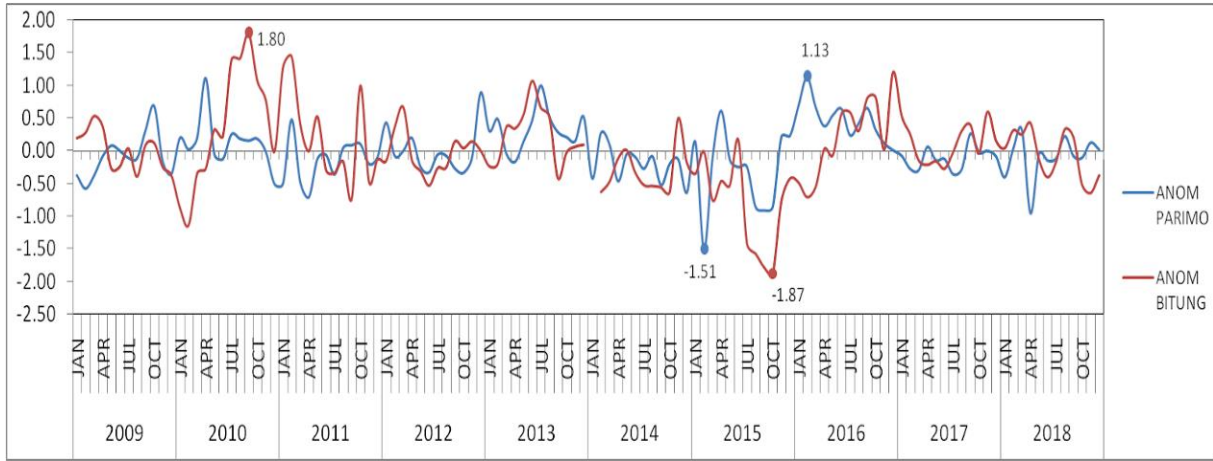


Figure3-4: SST anomaly in Parimo and Bitung 2009 – 2018

The SST anomaly in Parimo and Bitung is shown in Figure 3-4. This is calculated by subtracting the monthly variation to its monthly mean data. The highest positive anomaly in Parimo occurred in February 2016 at 1.13°C, with the lowest negative anomaly of -1.51°C in February 2015. In Bitung, the highest positive anomaly was in September 2010 at 1.80°C, and the lowest negative anomaly found in October 2015 with a value of -1.87°C.

SST anomaly is one of the important oceanic indicators, especially for coastal environments and organisms. Anomalous SST, either cool or warm, in the ecosystem can result in bacteria, algae or fish thriving or suffering. A warm SST anomaly in a certain period sends the signal that the coral reef may be in danger of bleaching.

*Wind Speed*

Differences in atmospheric pressure will generate wind, which is the movement of air from higher to lower pressure areas. The velocity of the air motion defines the strength of the wind. The mean value of wind speed at FMA 715 is 1.22 m/s ( $\sigma = 0.58$ ,  $n = 120$ ), with the strongest wind speed in January 2014 with a value of 2.48 m/s, while the weakest in July 2010. The monthly climatology mean of wind speed from 2009 to 2018 clearly shows the connexion between the speed and monsoonal systems (Figure 3-5). Low wind speeds tend to occur during Transition I and II periods, with higher speeds occurring during the northwest monsoon and the highest during the southeast monsoon.

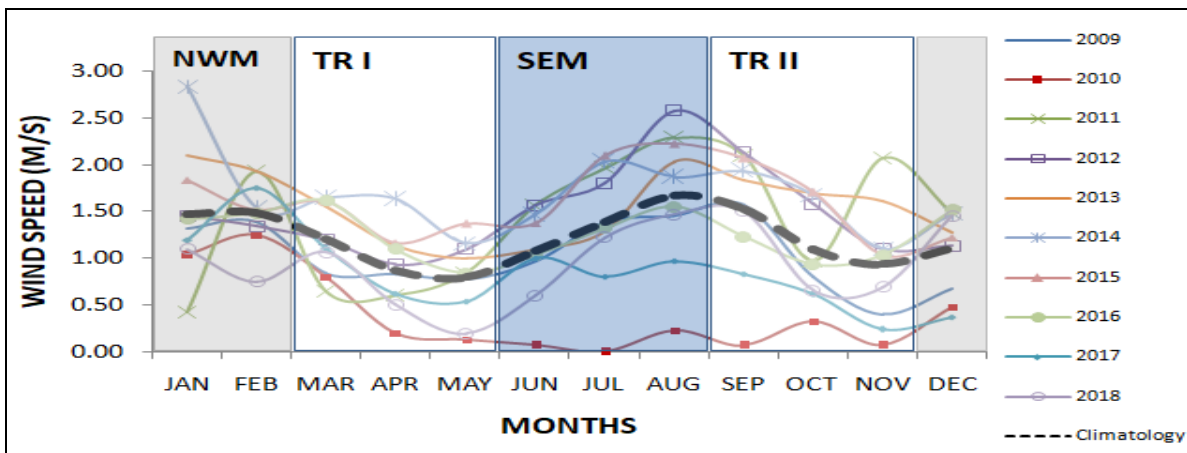


Figure 3-5. Variability and climatology of wind speed at FMA 715 2009 – 2018 (NWM: Northwest Monsoon; TR I: Transition I; SEM: Southeast Monsoon; TR II: Transition II)

*Oceanic Niño Index*

During the 2009 – 2018 period, several El Niño and La Niña events took place (Figure 3-6). The strongest El Niño started in November 2014 and lasted until May 2016, while the weakest and shortest period was observed between July 2009 and March 2010. From 2009 to 2018 several La Niña events also

occurred. The strongest La Niña started in June 2010 and lasted until May 2011, with other weaker and shorter periods taking place between July 2011 and March 2012, August 2012, August and December 2016, and October 2017 and March 2018. A long normal situation of SST anomaly also occurred between April 2012 and October 2014.

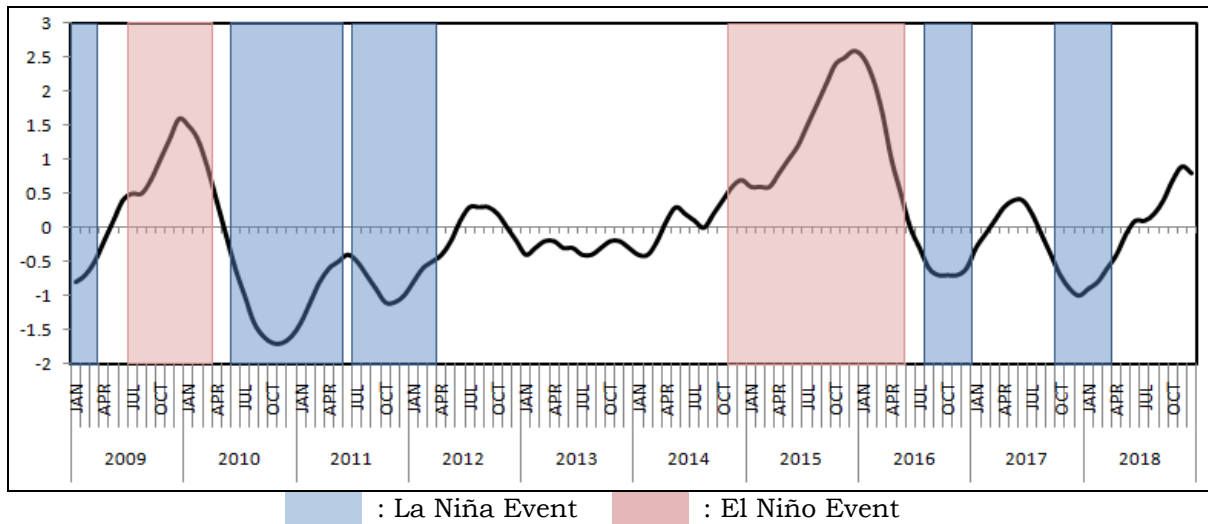


Figure 3-6. Oceanic Niño Index 2009 – 2018

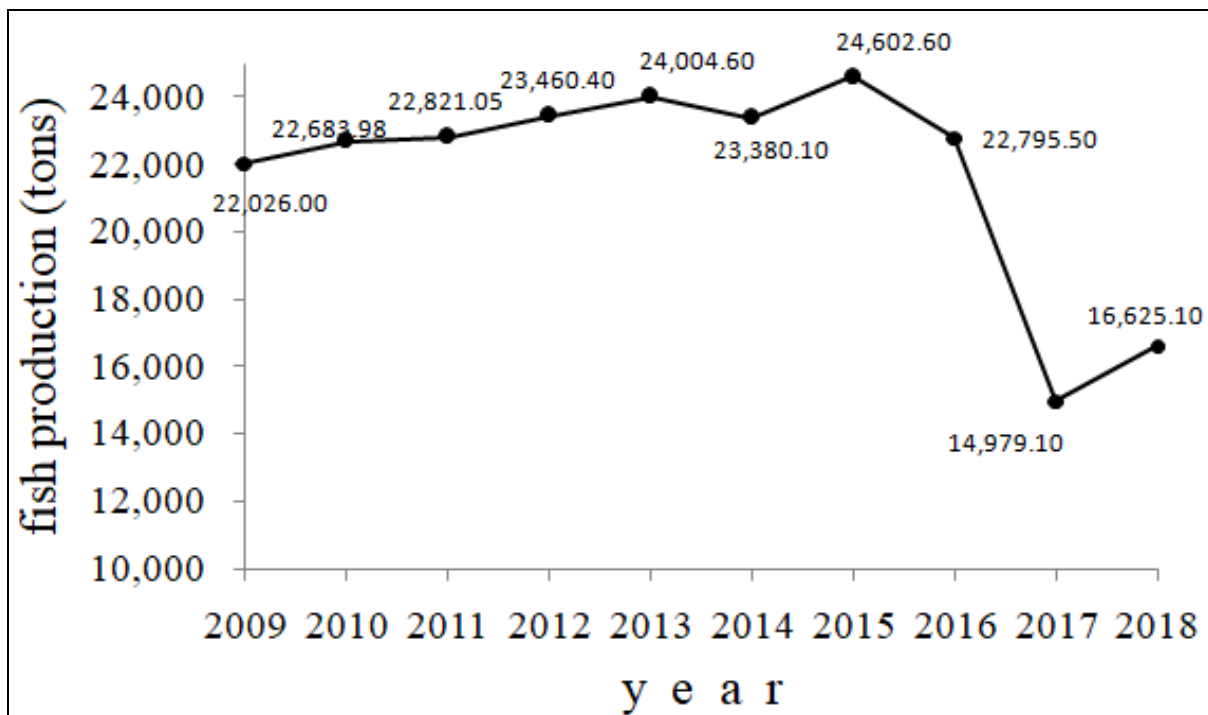


Figure 3-7: Overall fish production in the western part of Tomini Bay

*Yearly fish production in the western part of Tomini Bay*

Fishery data is very limited in this area, with no monthly production data available. Only yearly fish catch data based on fish species are available (Figure 10). Overall, based on these data, the highest fish production was recorded in 2015, with a total of 24,602 tons, while the lowest was recorded in 2017, with a total of 14,979 tons. Fish production for small pelagic fish in the western part of Tomini bay was dominated by Selar Kuning (*Selaroides leptolepis*), with a total catch in 2018 of 2,846 tons. This is consistent with Amri et al.'s (2006) findings. Production for large pelagic fish was dominated by Cakalang (*Katsuwonus pelamis*), with a total catch of around 3,273 tons in 2018.

During the strongest La Niña event in 2010, fish production tended to increase compared to previous years, with production showing a positive increasing trend until 2013. It then showed a slight decrease in 2014, which was considered to be a normal year. During the strong El Niño event in 2015,

fish production increased and reached a maximum peak, before significantly falling in 2016 and reaching a minimum level in 2017. The lowest fish production during the 2009-2018 period was also recorded in 2017. In 2018, when a La Niña event occurred at the beginning of the year, fish production showed a sign of improvement.

*Relationship between SST variability, ENSO and monsoons*

A correlation test between the monthly variation in SST or SST anomaly in Parimo and Bitung, with ONI conducted after only the months with El Niño or La Niña events were selected, as shown in the scattergraphs below (Figures 3-8 and 3-9). The results show that the correlation coefficient between SST and ENSO in Parimo is  $r = 0.06$  ( $n = 66$ ), indicating that SST variation in Parimo has a very weak correlation with ENSO. On the contrary, SST variation in Bitung has a strong but reverse relationship with ENSO, at  $r = -0.53$  ( $n = 66$ )

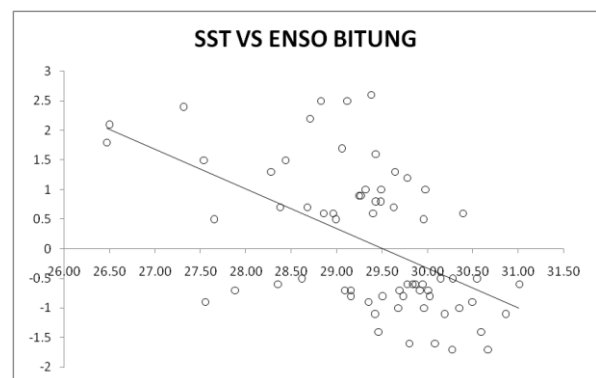
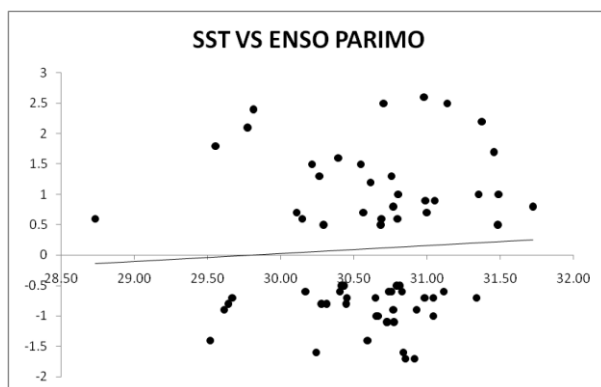


Figure 3-8: Scattergraph of relationship between SST and ENSO

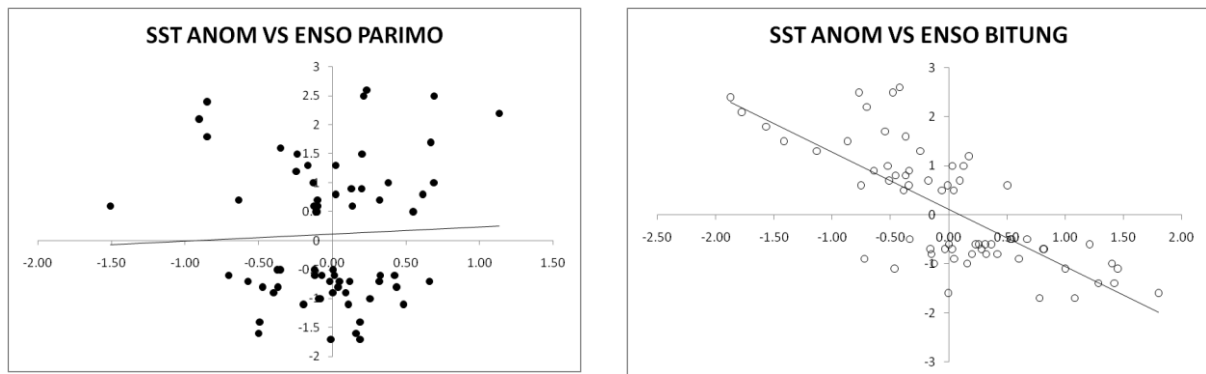


Figure 3-9: Scattergraph of relationship between SST anomaly and ENSO

The SST anomaly in Parimo also has a weak relationship with ENSO, at  $r = 0.05$  ( $n = 66$ ), but in Bitung the SST anomaly has a very strong, but reverse, relationship with ENSO, at  $r = -0.74$  ( $n = 66$ ).

Windspeed was also tested using a correlation test on the variation in SST in Parimo and Bitung in order to understand the relationship between monsoon systems, represented by wind speeds, and the variation in SST during the 2009 - 2018 period. The test shows that wind speed has a weak correlation, at  $r = -0.29$  ( $n = 120$ ), in Parimo, and a strong correlation, at  $r = -0.60$  ( $n = 119$ ) in Bitung.

#### 4 DISCUSSION

##### *SST variability in Parimo*

In general, the seasonal variability of SST in Indonesian waters is very varied and mostly affected by the monsoonal systems (Martono, 2016). Some areas, such as the Makassar Strait, Sulawesi Sea and the Halmahera Sea, experience only small variations, with warm SST over the years, which is similar to SST characteristics in Parimo. The variability of SST in FMA 715, especially around Tomini Bay, was examined over the period 2002 to 2003 (Amri et al., 2006), showing a similar pattern to the SST variability found in this study, which used SST satellite data from 2009 to 2018. The pattern of SST variability tends to be high during the

northwest monsoon and low during the southeast monsoon. In-situ measurements from 2002 to 2003 also showed that SST within Tomini Bay is higher than that at the mouth of the bay. Inside Tomini Bay, wind speed has a small and inverse correlation with the variability of SST ( $r = -0.29$ ), indicating the wind is not a dominant factor in SST variations. Another factor that might influence the SST variability inside Tomini Bay is tidal currents. Qu et al. (2005) state that in the Indonesian region these are very strong. The currents generate an intense ocean mix, which influences SST in numerous channels and basins in the archipelago. As well as wind speed, the ENSO event does not influence the variability in SST ( $r = 0.06$ ) inside Tomini Bay a situation which is also found in other parts of Indonesian waters. In Ambon Bay, Corvianawatie et al. (2014) argued that the monthly SST anomaly was not correlated with ENSO, but was strongly influenced by the local morphological conditions of the bay, which has the semi-enclosed basin characteristic.

##### *SST variability in Bitung*

The higher SST variation in Bitung waters is closely related to the upwelling indicator found in the northern (near Bitung) and southern part of the mouth of Tomini Bay (Amri et al., 2005). Some other areas in Indonesia have similar conditions, with a higher variation in

SST caused by the upwelling process, for example in the southern waters of Java, the Timor Sea, Arafura Sea and Banda Sea. Upwelling is a process caused by the stress of surface wind, which brings cooler and nutrient-rich water near to the surface. The geographical position of Bitung waters is more exposed than those of Parimo, which mean they are more influenced by the watermass from the Pacific throughflow. The Sulawesi Sea is the entrance for the cooler watermass from the Pacific ocean (Gordon, 2005) to Indonesia waters, including to the Maluku Sea and Halmahera Sea (Radjawane and Hadipoetranto, 2014). The cooler SST from the Pacific Ocean is suspected to be a key factor that causes the climatological SST in Bitung to be always lower than that in Parimo. Unlike within Tomini Bay, the variability in SST in Bitung waters is influenced by, and has a strong but reverse relationship with both wind speed ( $r = -0.60$ ) and ENSO events ( $r = -0.53$ ). The SST anomaly in Bitung also shows a strong inverse relationship with ENSO events ( $r = -0.74$ ).

#### *SST variability and monsoons in general*

By this study, the lowest SST anomaly ( $-1.87^{\circ}\text{C}$ ) was found during the strongest El Niño event, while the highest ( $1.80^{\circ}\text{C}$ ) was found during a La Niña event. SST variability in Indonesia is generally low compared to the tropical eastern Pacific, due to the lack of strong equatorial upwelling. The interannual variability in the eastern part of Indonesia, such as in Timor, Arafura and the Banda Sea, is less than  $2.0^{\circ}\text{C}$  (Qu et al., 2005). SST anomalies in Indonesia waters are also affected by the monsoonal systems and global climate change, such as the Indonesian Dipole and El Niño (Martono, 2016). Other

research has also found that wind speed is an important factor that influences SST variability and anomalies in other Indonesian waters, especially in the Makassar Strait (Nababan et al., 2016), the Java Sea and Jakarta Bay (Corvianawatie, 2019). The Asia-Australia monsoon which influences Indonesian waters is characterised by seasonal changes in wind speed/stress direction. The lowest wind speed/stress takes place in April, which is clearly the month of transition between the northwest and southeast monsoons. A characteristic of the southeast monsoon is the intensified easterly winds, which start in June and reach their peak in July and August, after which they begin to subside. October is a monsoon transition month, when winds are low within the internal Indonesian Sea. In December, the wind changes direction and reaches a maximum in January-February (Susanto et al., 2006).

#### *ENSO and fishery production*

An impact of El Niño across Indonesian waters is the increase in ocean productivity due to anomalous easterly wind stress, that generates strong upwelling in some parts of Indonesian waters (Susanto et al., 2006). Upwelling is characterised by nutrient-rich water, but cooler SST. This anomalous wind is believed to be a key factor in causing the lowest SST and SST anomaly in the 2009 to 2018 period. Elsewhere, for example in the South China Sea, Piton and Delcroix (2018) state that the variability in SST is also connected to upwelling due to wind stress curl or Ekman pumping during the El Niño phase. Indonesian waters respond differently to the ENSO event. In some areas, such as Sumatra, Java and the Banda Sea, productivity increases due to the stronger upwelling during the El Niño event. Higher productivity during



the El Niño phase is connected to fisheries production; for example, in the eastern Indian Ocean, the highest CPUE (Catch Per Unit Effort) of swordfish was found during an El Niño event (Setyadji and Amri, 2017); the highest tuna landings from the Indian Ocean have been recorded during El Niño years (Kumar et al., 2014); and skipjack catches in southeastern Java are also influenced by ENSO, with production increasing during El Niño events and declining during La Niña events (Handayani et al., 2019). In addition, the climate change that has intensified alongshore wind stress and accelerated coastal upwelling in the Bali Strait has likely increased sardine production (Gaol et al., 2012). In the western part of Tomini Bay, near Parimo waters, yearly catch data indicate that fish production has not been affected by ENSO events; yearly production may increase or decrease in any phase, during La Nina, El Niño or in normal conditions. Related to data on the decrease in fish production in 2017, Kadim et al. (2017) state that environmental degradation due to pollution might affect the abundance of the fish population around the western part of Tomini Bay. Another theory is that fish caught but unreported to the authorities may have been the reason for the decrease in fish production in 2017.

## 5 CONCLUSION

SST characteristics and variability in Parimo and Bitung waters are very different, although they are both located in the same FMA. SST in Parimo waters is warmer, but with lower variability compared to Bitung waters. Based on the mean climatology of SST, the minimum SST in Parimo occurs during the northwest monsoon, while in Bitung it is during the southeast monsoon. In Parimo, wind speed and ENSO events

have a weak relationship with SST variability. The opposite was found in Bitung, where wind speed and ENSO have a stronger relationship with SST variability. In other parts of Indonesian waters, El Niño and La Niña are connected with fishery production; production increases during the El Niño and decreases during La Niña. Unlike in other parts of Indonesia, fishery production in Parimo or the western part within Tomini Bay is not affected by ENSO events.

## ACKNOWLEDGMENTS

We would like to thank the head of IMRO and our fellow researchers for their support and collaboration during this work. We also thank the head of the Parimo Marine and Fisheries Office for sharing the fishery production data. Special thanks also to oceancolor website for providing MODIS Aqua time series satellite data.

## REFERENCE

- Amri, K., Suwarso, & Herlisman. (2005). Dugaan Upwelling Berdasarkan Analisis Komparatif Citra Sebaran Suhu Permukaan Laut dan Klorofil-a di Teluk Tomini [Alleged Upwelling Based on Comparative Analysis of Sea Surface Temperature and Chlorophyll-a Distribution in Tomini Bay]. *Indonesian Fisheries Research Journal*, 11(6), 57-71. (in Bahasa).
- Amri, K., Suwarso, & Awwaludin. (2006). Kondisi Hidrologis dan Kaitannya dengan Hasil Tangkapan Ikan Malalungis (*Decapterus macarellus*) di Perairan Teluk Tomini [Hydrological Conditions and their Relation to the Capture of Malalungis (*Decapterus macarellus*) in the Waters of Tomini Bay]. *Indonesian Fisheries Research Journal*, 12(3), (in Bahasa).
- Chand, S. S., K.J. Tory, J.L. McBride, M. C. Wheeler, R. A. Dare, & K. J. E. Walsh. (2013). The Different Impact of Positive-



- Neutral and Negative-Neutral ENSO Regime on Australian Tropical Cyclones. *Journal of Climate*, 26, 8008-8016.
- Corvianawatie, C., M. R. Putri, S. Y. Cahyarini, & W. M. Tattipata. (2014). Variability of Sea Surface Temperature and Sea Surface Salinity in the Ambon Bay and its Relation to ENSO/IOD and Monsoon. *Indonesian Journal of Geospatial*, 3(2), 1-8.
- Corvianawatie, C. (2019). Seasonal and Intra-Seasonal Variability of Sea Surface Temperature in Pari Island-Jakarta, Indonesia. *Jurnal Kelautan*, 12(1), 97-103.
- Davies, G. & N. Cressie. (2016). Analysis of Variability of Tropical Pacific Sea Surface Temperature. *Advances in Statistical Climatology, Meteorology and Oceanography – An International Open-Access Journal on Applied Statistics*, 2, 155-169.
- Deser, C., M. A. Alexander, S. Xie, & A. S. Phillips. (2010). Sea Surface Temperature Variability : Patterns and Mechanisms. *The Annual Review of Marine Science*, 2, 115-143.
- Gaol, J. L. & B. Nababan. (2012). *Climate Change Impact on Indonesian Fisheries*. World Meteorological Organization. Tudor Rose Publisher. Leicester, UK.
- Gordon, A. L. (2005). Oceanography of the Indonesian Seas and Their Throughflow. *Journal of Oceanography*, 18(4), 14-27.
- Handayani, C., A. H. Soepardjo, & E. Aldrian. (2018). Impact of a El-Nino Southern Oscillation (ENSO) to Fluctuation of Skipjack Catch Production in Southern East Java. *Journal of Physics : Conference Series*, 1217 012170, 1-5.
- Kadim, M. K., N. Pasingi, & A. R. Paramata. (2017). Kajian Kualitas Perairan Teluk Gorontalo dengan Menggunakan Metode STORET [Study of Waters Quality of the Gorontalo Bay using STORET Method]. *Depik, Journal of Aquatic, Coastal and Fisheries Sciences*, 6(3), 235-241. (in Bahasa)
- Kaplan, A., M. A. Cane, Y. Kushnir, A. C. Clement, M. B. Blumenthal, & B. Rajagopalan. (1998). Analyses of Global Sea Surface Temperature 1856-1991. *Journal of Geophysical Research*, 103(C9), 18,567-18,589.
- Kumar, P. S., G. N. Pillai, & U. Manjusha. (2014). El Nino Southern Oscillation (ENSO) Impact on Tuna Fisheries in Indian Ocean. SpringerPlus 2014 3:591, 1-13.
- Martono. (2016). Seasonal and Interannual Variations of Sea Surface Temperature in the Indonesian Waters. *Forum Geografi*, 30(2), 120-129.
- Muawanah, U., G. Yusuf, L. Adrianto, J. Kalthar, R. Pameroy, H. Abdullah, & T. Ruchimat. (2018). Review of National Laws and Regulation in Indonesia Relation to an Ecosystem Approach to Fisheries Management. *Marine Policy* 91, 150-160.
- Nababan, B., N. Rosyadi, D. Manurung, N. M. Natih, & R. Hakim. (2016). The Seasonal Variability of Sea Surface Temperature and Chlorophyll-a Concentration in the South of Makassar Strait. *Procedia Environmental Science* 33, 583-599.
- Piton, V. & T. Delcroix. (2018). Seasonal and Interannual (ENSO) Climate Variabilities and Trends in the South China Sea over the Last Three Decades. *Ocean Sci. Discuss.*, <https://doi.org/10.5194/os-2017-104>.
- Pui, A., A. Sharma, A. Santoso, & S. Westra. (2012). Impact of the El Nino-Southern Oscillation, Indian Ocean Dipole, and Southern Annual Mode on Daily to Subdaily Rainfall Characteristics in East Australia. *Journal of American Meteorology Society*, 140, 1665-1682.
- Qu, T., Y. Du, J. Strachan, G. Meyers, & J. Slings. (2005). Sea Surface Temperature and Its Variability in the Indoneisan Region. *Journal of Oceanography*, 18(4), 50-61.
- Radjawane, I.M. & P.P. Hadipoetranto. 2014. Water Masses Characteristics At The

- Sangihe Talaud Entry Passage Of Indonesian Throughflow Using Index Satal Data 2010. *Jurnal Ilmu dan Teknologi Kelautan Tropis*, 6(2), 525-536.
- Setyadji, B. & K. Amri. (2017). The Effect Of Climate Anomaly (ENSO And IOD) On The Distribution Of Swordfish (*Xiphias gladius*) In The Eastern Indian Ocean. *Journal Segara*, 13(1), 49-63.
- Suman, A., Wudianto, B. Sumiono, Badrudin, D. Nugroho, G.S. Merta, ... E. Rahmat. (2014). Potensi dan Tingkat Pemanfaatan Sumberdaya Ikan di Wilayah Pengelolaan Perikanan Republik Indonesia [Potential and Level of Utilization of Fish Resources in the Republic of Indonesia Fisheries Management Area]. Ref Publisher. Jakarta. (in bahasa).
- Susanto, R. D., T. S. Moore, & J. Marra. (2006). Ocean Color Variability in the Indonesian Seas during the SeaWiFS era. *An Electronic Journal of the Earth Sciences : Geochemistry, Geophysics, Geosystems*, 7(5), 1-16.
- Vitri, T. & Marzuki. (2014). Analysis of the Effect of El Nino Southern Oscillation (ENSO) on Rainfall in Koto Tabang, West Sumatera. *Andalas University Physics Journal*, 3(4), 214-221. (in Bahasa).
- Walpole, R.E. (1993). *Introduction to Statistics*. Jakarta: PT. Gramedia Pustaka Utama (in Bahasa).
- Webster, P. J., A. M. Moore, J. P. Loschnigg, & R. R. Leben. (1999). Coupled ocean-atmosphere dynamics in the Indian Ocean during 1997-98. *Nature*, 401, 356-360. doi:10.1038/43848



# DETECTION AND ANALYSIS OF SURFACE URBAN COOL ISLAND USING THERMAL INFRARED IMAGERY OF SALATIGA CITY, INDONESIA

Bayu Elwanto Bagus Dewantoro<sup>1\*</sup>, Panji Mahyatar<sup>1</sup>, Wafiq Nur Hayani<sup>1</sup>

<sup>1</sup>Department of Geographic Information Science, Faculty of Geography, Universitas Gadjah Mada, Yogyakarta, 55281, Indonesia

\*e-mail: bayuelwanto@mail.ugm.ac.id

Received: 13 August 2020; Revised: 10 November 2020; Accepted: 17 December 2020

**Abstract.** The detection and monitoring of the dynamics of urban micro-climates needs to be performed effectively, efficiently, consistently and sustainably in an effort to improve urban resilience to such phenomena. Thermal remote sensing possesses surface thermal energy detection capabilities which can be converted into surface temperatures and utilised to analyse the urban micro-climate phenomenon over large areas, short periods of time, and at low cost. This paper studies the surface urban cool island (SUCI) effect, the reverse phenomenon of the surface urban heat island (SUHI) effect, in an effort to provide cities with resistance to the urban microclimate phenomenon. The study also aims to detect urban micro-climate phenomena, and to calculate the intensity and spatial distribution of SUCI. The methods used include quantitative-descriptive analysis of remote sensing data, including LST extraction, spectral transformation, multispectral classification for land cover mapping, and statistical analysis. The results show that the urban micro-climate phenomenon in the form of SUHI in the middle of the city of Salatiga is due to the high level of building density in the area experiencing the effect, which mostly has a normal surface temperature based on the calculation of the threshold, while the relative SUCI occurs at the edge of the city. SUCI intensity in Salatiga ranges between  $-6.71^{\circ}\text{C}$  and  $0^{\circ}\text{C}$  and is associated with vegetation.

Keywords: *Thermal Remote Sensing, Land Surface Temperature, Urban Microclimate, Surface Urban Cool Island*

## 1 INTRODUCTION

The urbanization phenomenon has a significant impact on increases in surface temperature, meaning cities are vulnerable to changes in microclimate characteristics, which can lead to environmental problems (Wang et al., 2016; Huang & Wang, 2019). A microclimate is a climatic condition in the local atmospheric zone which exhibits differences to the surrounding environment (Chen et al., 1999; Ismangil et al., 2016). The change in microclimate is one of the types of pressure faced by cities, as it is related to the urban heat island (UHI), which is a phenomenon in which the temperature of

the urban area is higher than the surrounding rural areas (Xian & Crane, 2006; Mostofi & Hasanlou, 2017). UHI also has other negative impacts, such as changing air quality, effect on human health, and energy exchange (Lai & Cheng, 2009; Road et al., 2010; Stone et al., 2010; Tan et al., 2010; Skelhorn et al., 2016; Ng & Ren, 2017; Fawzi, 2017). It eventually also disrupts the comfort of life in urban areas.

In recent years, the study of micro-climate change has been much more focused on the UHI phenomenon. However, few studies have considered the urban cool island (UCI) effect, which is the opposite of UHI and is a phenomenon

whereby the air temperature in the countryside is higher than in the urban area (Yang et al., 2016). Several previous studies have suggested that UCI is effective for the microclimate mitigation, reducing rising air temperatures, and improving the comfort of urban areas (Cao et al., 2010; Kong, et al., 2014). Therefore, UCI can also be used to plan the provision of green open spaces and to improve the effectiveness of monitoring the dynamics of climate changes in an effort to improve cities' resilience to microclimate change.

Few studies on UCI have been conducted in Indonesia, especially in relation to the city of Salatiga. This was one of the cities in Central Java province which in 2020 was a pilot nationally and internationally for the integration of the development of green open spaces. The city managed to exceed the national target for the provision of green open space by 24%, of which 16.11% was combined green open space, with the remainder being sustainable development agricultural land. This condition makes Salatiga an interesting location for research on UCI, considering RTH has an influence on the surface temperature of cities.

Study of UCI is differentiated into two types: UCI surface and UCI water. The surface intensity of UCI, commonly abbreviated as SUCI, can be gauged directly from the land surface temperature (LST) value of data extraction recorded by infrared thermal sensor satellite remote sensing. LST is an energy beam of ground level objects successfully recorded by sensors (Li et al., 2013; Alhawiti, 2016). On the other hand, UCI water requires different data to LST, namely the air temperature, usually obtained from measurements in the field or from station climatology. Remote sensing applications for SUCI/UCI research are almost the same as those for SUHI/UHI research, mostly

employing cover/land use as one of its variants. For example, Reisi et al. (2019) examined the effect of LULC (landuse/landcover) changes on LST in Isfahan City, Iran, from 1985 to 2017, using Landsat 5 and 7 ETM imagery. However, the results in their study did not further assess SUCI/UCI intensity. The study of such intensity has been more detailed in previous years. For instance, Li and Dai (2011) measured UCI intensity based on the boundary line changes of several cities in Hunan, China in 1989, 2001 and 2006. Their results showed that the difference in the city boundary line affected UCI intensity up to a maximum of  $> 2$  °C. In addition, the negative correlation between NDVI and UCI intensity was also established by Li and Dai (2011), even though the coefficient of the correlation decreased from 0.845 to 0.606. The results of their study is shown only in table form and are not visualized spatially in the form of maps, so the spatial distribution is unknown.

The association between UCI and green open space was examined by Chen et al. (2014) in Beijing, China, whose research results showed the influence of urban RTH spatial patterns on UCI, and that these were stronger during winter. The pattern size and combination of RTH vegetation also influenced UCI. More complex research was conducted by Rasul et al. (2015), who examined the influence of LST on SUCI in the dry season using several spectral transformations, which included wetness, brightness, the greenness index, NDBI and NDVI. Their results show that the brightness index was a very influential factor in the LST, while the wetness index was the second factor. In addition, the LST with NDBI had a strong positive correlation, whereas NDVI-based LST had a negative correlation.

The purpose of this SUCI research in the city of Salatiga using the remote sensing approach is (1) to, establish the

spatial distribution of SUCI intensity; and (2) to calculate this intensity.

## 2 MATERIALS AND METHODOLOGY

### 2.1 Location and Data

The research site was located in Salatiga City, Central Java province, Indonesia, with coordinates of between  $07^{\circ}17' - 07^{\circ}17'23''$  S and  $110^{\circ}27'57'' - 110^{\circ}32'05''$  E. The city is completely bordered by Semarang Regency, Central Java province. It has a total area of 56.78 km<sup>2</sup>, of which 24% is green open space (see Figure 2-1).

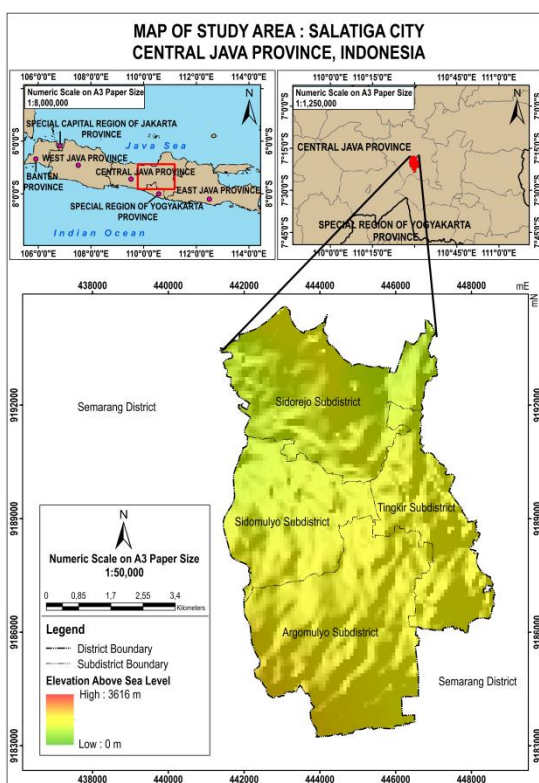


Figure 2-1: Location of Study Area

The imagery used in the research was obtained from Landsat 8 OLI/TIRS with a resolution of 30 m (*pixel resampling from Earth Engine Dataset*) with a recording date of 16 November 2019, and Sentinel 2A MSI with a resolution of 10 m, with a recording date of 19 November 2019. The selection of the dates was based on the availability of data with minimum cloud cover to produce objective analysis. The Landsat 8 OLI Thermal Infrared Sensor (TIRS) was

employed for the Land Surface Temperature (LST) estimation used for Surface Urban Cool Island (SUCI) analysis, and data with 1-7 multispectral bands used for the creation of the vegetation index transformation. Sentinel 2A MSI images were used for the classification of land cover in the study area.

Landsat 8 and Sentinel 2A were not used for comparison analysis. Landsat 8 focused on thermal imagery analysis covering LST to SUCI, while land cover from Sentinel 2A was only used to observe SUCI spatial distribution of certain land cover classes. Sentinel 2A was selected for land cover classification with the aim of improving its accuracy.

### 2.2 Radiometric and Geometric Correction

Landsat 8 OLI/TIRS Imagery and Sentinel 2A MSI were atmospherically corrected to surface reflectance (*bottom-of-atmosphere*). The atmospheric corrected imagery from Landsat 8 OLI/TIRS was used for spectral transformation purposes, while Sentinel 2A MSI was used for the multispectral classification of land cover. The image products used were also geometrically corrected, so it was only necessary to make an overview check to ensure the geometric position of both the images was precise and relevant to be processed based on the 1:25,000 scale Rupabumi Indonesia map of Salatiga City. The imagery used is available on the Google Earth Engine (GEE) platform

### 2.3 Land Surface Temperature Extraction

Land Surface Temperature (LST) extraction was performed on the Google Earth Engine using the Single Channel Algorithm (SCA) method, based on its ease of accessibility, efficiency and effectiveness in data acquisition.

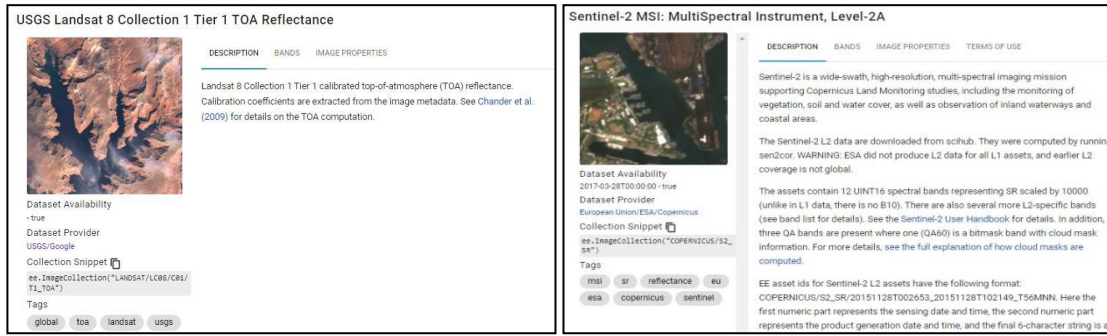


Figure 2-2: Image Metadata Collection in Google Earth Engine  
 Source: <https://developers.google.com/earth-engine/datasets>

The extraction was performed on the Landsat 8 TIRS imagery using thermal channel Band 10. According to Loyd (2017), cited in Fawzi (2017), band 10 has a thermal accuracy of  $\sim \pm 1$  Kelvin for simple LST estimation at the urban scale or greater. The thermal imagery acquired from GEE was already a brightness temperature ( $T_{rad}$ ) as a result of the calibration of at-sensor spectral radiance ( $L\lambda$ ).

The brightness temperature of the extraction used Kelvin units to facilitate the analysis; the conversion of the units to Celsius ( $^{\circ}C$ ) was made with the following formula:

$$T_{celsius} = T - 273.15 \quad (2-1)$$

where:

- $T_{celsius}$  = temperature in Celsius ( $^{\circ}C$ )
- $T$  = temperature in Kelvin (K)

The extraction of surface temperature needs to be made through the emissivity correction process to obtain accurate values (Fawzi, 2017). One method for the correction of emissivity is use of the vegetation index NDVI (Salih et al., 2018; Bahi et al., 2016; Fawzi, 2017). The formula used to compose the NDVI in Landsat 8 OLI is as follows:

$$NDVI = \frac{(B5 - B4)}{(B5 + B4)} \quad (2-2)$$

where:

- B5 = NIR Band
- B4 = Red Band

An emissivity correction method using NDVI requires the values of vegetation and soil emissivity. Referring to Fawzi (2017), the vegetation values in the measurement results were in the range of  $\epsilon_v = 0.980 - 0.990$ , while for soil emissivity in the range of  $\epsilon_s = 0.950 - 0.970$ . The calculation of the surface emissivity value to be used in the LST estimation refers to the following formulas (Salih et al., 2018; Li & Norford 2016; Sobrino et al., 2008; Valor, 1996):

$$\epsilon = \epsilon_v P_v + \epsilon_s (1 - P_v) + d\epsilon \quad (2-3)$$

where:

- $\epsilon$  = land surface emissivity
- $\epsilon_v$  = emissivity of vegetation
- $\epsilon_s$  = emissivity of soil
- $P_v$  = proportion of vegetation
- $d\epsilon$  = surface roughness

$$P_v = \left( \frac{NDVI - NDVI_s}{NDVI_v - NDVI_s} \right)^2 \quad (2-4)$$

where:

- $P_v$  = proportion of vegetation
- $NDVI_s$  = spectral value of soil in NDVI
- $NDVI_v$  = spectral value of vegetation in NDVI

The last phase of the LST extraction process involves inclusion of all the necessary variables in the following equation (Salih et al., 2018):

$$LST = \frac{T_{rad}}{\left( 1 + \left( \frac{T_{rad}}{p} \right) \ln \epsilon \right)} \quad (2-5)$$

where:

- LST = land surface temperature (°C)
- T<sub>rad</sub> = brightness temperature (°C)
- P = constant of 1.488 x 10<sup>-2</sup>
- ε = surface emissivity

#### 2.4 Detection of Area Indicated by Surface Urban Heat and Cool Island (SUHI/SUCI)

Initial detection and identification of surface urban heat and cool island (SUHI/SUCI) can be made visually by observing the LST distribution patterns, but for the purpose of mitigation and planning of areas related to urban microclimate phenomena it is necessary that heat and cool islands are accommodated in quantitative form. Lima and Lopes (2017) used the following formula for early detection of areas indicated as SUHI/SUCI:

$$\Delta T_{\mu-r} = T_{\mu} - T_r \quad (2-6)$$

where:

- ΔT<sub>μ-r</sub> = LST difference in the area indicated by SUHI (°C)
- T<sub>μ</sub> = LST difference in urban area (°C)
- T<sub>r</sub> = LST difference in nonurban area (°C)

$$\Delta T_{r-\mu} = T_r - T_{\mu} \quad (2-7)$$

where:

- ΔT<sub>r-μ</sub> = LST difference in the area indicated by SUCI (°C)
- T<sub>μ</sub> = LST difference in urban area (°C)
- T<sub>r</sub> = LST difference in non-urban area (°C)

Equation (6) was used to identify the surface temperature of the area indicated by the SUHI phenomenon, while equation (7) was used to identify the surface temperature in the area indicated by SUCI. These equations are simple one to ascertain the surface temperature difference in the early detection of the

SUHI/SUCI phenomena ; it needs a formula to find the SUHI/SUCI intensity to obtain the surface temperature threshold as the basis for the analysis.

Research conducted by Ma et al. (2010) used a more specific formula related to determining the surface temperature threshold in the SUHI/SUCI phenomena, as follows:

$$T_{suhi} > \mu_{ori} + 0,5\alpha_{ori} \quad (2-8)$$

where:

- T<sub>suhi</sub> = LST in the area indicated by SUHI (°C)
- μ<sub>ori</sub> = average of LST in the original thermal image (°C)
- α<sub>ori</sub> = standard deviation in the original thermal image

Equation (8) was used to obtain a surface temperature threshold on an indicated area of SUHI.

$$0 < T_{norm} \leq \mu_{ori} + 0,5\alpha_{ori} \quad (2-9)$$

where:

- T<sub>norm</sub> = LST in normal condition (°C)
- μ<sub>ori</sub> = average of LST in the original thermal image (°C)
- α<sub>ori</sub> = standard deviation in the original thermal image

Equation (9) was used to obtain the surface temperature threshold in regions not indicated as SUHI. The area that is included in this surface temperature range has not been identified as SUCI because it still has the potential to become an area with normal surface temperature, or a SUCI indication area.

The determination of the SUCI surface temperature threshold requires statistical surface temperatures in areas with normal conditions to determine the distribution of surface temperature values and central tendencies. Equations that can be reduced to acquire threshold values in the SUCI-indicated areas are as follows:



$$T_{Suci} < \mu_{norm} + 0,5\alpha_{norm} \quad (2-10)$$

where:

$T_{suci}$  = LST in the area indicated by SUCI (°C)

$\mu_{norm}$  = average of LST in the original thermal image with normal condition (°C)

$\alpha_{norm}$  = standard deviation in thermal image with normal condition

Table 2-1: Average, StDev and Threshold Values of SUHI, Normal and SUCI

	Average	StDev
Toriginal (°C)	30.09	4.68
Tnormal (°C)	27.21	3.02
SUHI Threshold (°C)	T > 32.43	
Normal Threshold (°C)	28.72 ≤ T ≤ 32.43	
SUCI Threshold (°C)	T < 28.72	

## 2.5 Measuring Surface Urban Cool Island (SUCI) Intensity

The value of the surface temperature threshold was obtained as the basis for the spatial measurement of SUCI intensity. This intensity was obtained by using a modified equation from Fawzi's (2017) study, as follows:

$$SUCI_{in} = T_{suci} - (\mu_{norm} + 0,5\alpha_{norm}) \quad (2-11)$$

where:

$SUCI_{in}$  = SUCI Intensity (°C)

$T_{suci}$  = LST in the area indicated by SUCI (°C)

$\mu_{norm}$  = average of LST in the original thermal image in normal conditions (°C)

$\alpha_{norm}$  = standard deviation in the original thermal image in normal conditions

## 2.6 Land Cover Classification and Accuracy Assessment

Land cover classification was performed using the supervised

classification method with the maximum likelihood algorithm. The classification was divided into three class: bare land, built up areas and vegetation. This algorithm was selected based on its good performance in land cover classification based on probability calculation or the maximum probability of each sample group (Danoedoro, 2012).

The accuracy assessment of the land cover map was made using a confusion matrix and kappa coefficient. Sampling for the assessment was made using the cross-validation method, which was performed by different people so the results were more objective. This was also because of the small number of land cover classes with many different characteristics. The sampling method used in the accuracy assessment was stratified random sampling, with a total sample of 22,686 pixels divided into 15,886 model samples and 6,800 accuracy samples.

## 3 RESULTS AND DISCUSSION

### 3.1 Spatial Distribution of LST and Land Cover in Salatiga City

The results of the processing of the Landsat 8 TIRS thermal imagery indicates that the surface temperature is high enough in the central area of Salatiga that for it to be visually identified against the LST distribution pattern. The distribution of LST is quite high between 30°C - 37°C, concentrated in the middle of the city, which is influenced by the densely built-up area. This increases the emissivity of the surface, which is recorded by the thermal infrared sensor as a higher surface temperature than that in the surrounding area. The built-up area spatial pattern also affects the surface temperature distribution, as shown in the image in this figure.

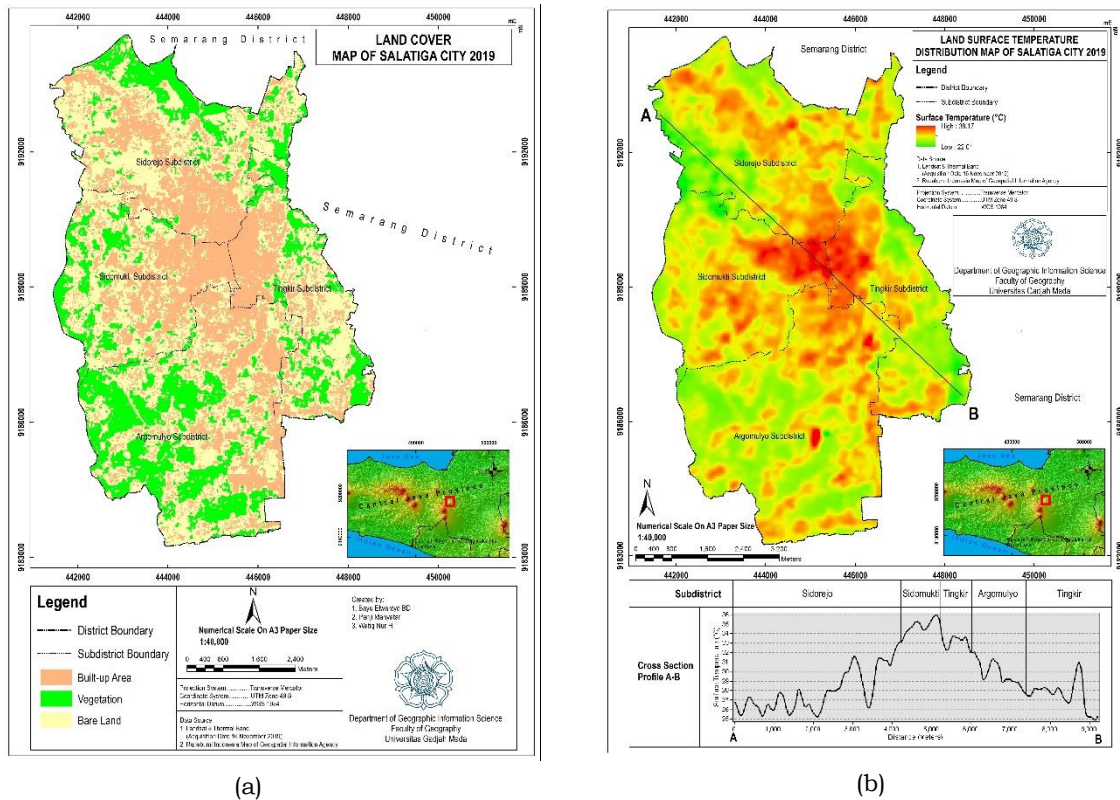


Figure 3-1: Land cover (a) and LST (b) on map of Salatiga City

The patterns of the LST values are quite high in the central part of the city, where the land cover is dominated by built-up areas, while the edge of the city tends to have a lower surface temperature, with a dominance of vegetation. This shows that there is a difference in the thermal energy emitted from the built-up area and the area with vegetation, as seen in Figure 3-1.

### 3.2 Detection of SUHI Area, Normal Condition and SUCI

The detection process of the area indicated by SUHI, the normal condition and SUCI is based on the equations used and the threshold value of the surface temperature. The results of the processing indicate that the potential occurrence of SUHI is in areas with a surface temperature of  $>32.43^{\circ}\text{C}$ , which are distributed in the center of the city, while the surface temperatures in normal conditions are in the range of  $28.72^{\circ}\text{C}$  -  $32.43^{\circ}\text{C}$ , and are spread around the region with potential SUHI.

Indications of SUCI were detected on the edge of the city, with a surface temperature of  $<28.72^{\circ}\text{C}$ . These indications have a pattern that tends to group on the city edge, with land cover in the form of vegetation and some bare land. SUCI intensity measurements were taken to obtain specific information related to SUCI.

Based on the measurement results, SUCI intensity was divided into five classes : very high ( $-6.71^{\circ}\text{C}$  -  $-5.37^{\circ}\text{C}$ ); high ( $-5.36^{\circ}\text{C}$  -  $-4.03^{\circ}\text{C}$ ); medium ( $-4.02^{\circ}\text{C}$  -  $-2.68^{\circ}\text{C}$ ); low ( $-2.67^{\circ}\text{C}$  -  $-1.34^{\circ}\text{C}$ ); and very low ( $-1.33^{\circ}\text{C}$  -  $0^{\circ}\text{C}$ ). The intensity shows the SUCI effect that occurs in related areas. It is very high, signifying that the area has a greater SUCI effect than the surrounding area, with a difference in the value of the surface temperature of between  $-6.71^{\circ}\text{C}$  to  $-5.37^{\circ}\text{C}$ . The dominance of land cover in areas of high intensity value in the form of vegetation with varying levels of greenish.

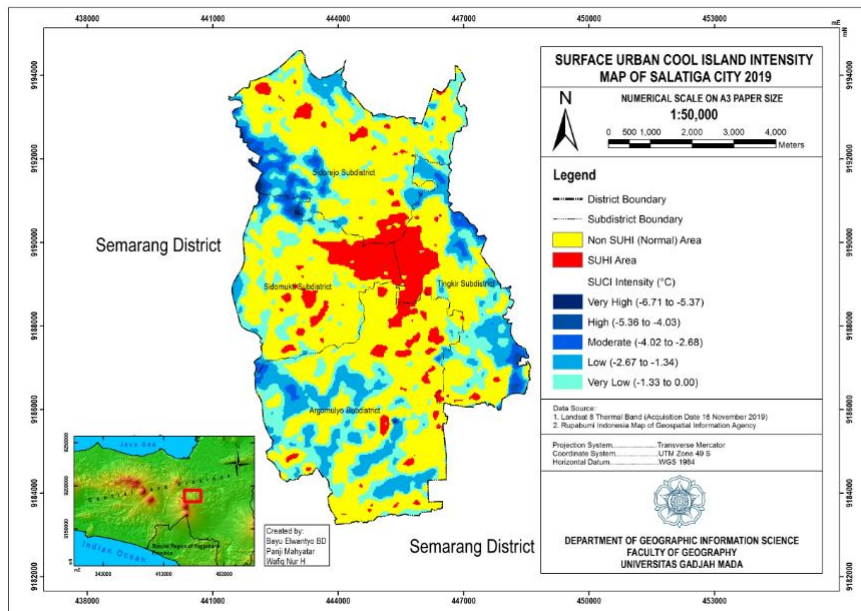


Figure 3-2: SUCI Intensity Map of Salatiga City

Table 3-1: Accuracy Assessment of Land Cover Map  
Ground Truth (Pixels)

		Vegetation	Built up Area	Bare land	Total row	User Accuracy (%)
Tentative Map	Vegetation	1932	100	256	2288	84.44
	Built up Area	224	1957	34	2215	88.35
	Bare land	140	117	2040	2297	88.81
	Total column	2296	2174	2330	6800	
	Producer Accuracy (%)	84.15	90.02	87.55		
	Overall Accuracy (%)	87.19				

### 3.3 Accuracy Assessment of the Land Cover Map

The land cover map accuracy test was conducted using a confusion matrix and kappa coefficient. The accuracy assessment results show good accuracy with the kappa coefficient, in the very good agreement category. The accuracy assessment results can be seen in Table 3-1.

### 3.4 Accuracy Assessment of Land Surface Temperature (LST)

Some researchers suggest that the accuracy test and validation of that surface temperature should be conducted a maximum of 3-4 hours after recording (for addition, Sabins, 2007, cited in Fawzi, 2017), even though the surface temperature is very dynamic, even in seconds. Ideally, an accuracy test should

be made simultaneously when the satellite is recording the area, but this is very difficult to achieve.

There is also the option to make comparisons of two thermal infrared sensors that record the same area, but due to data source limitations, this is also difficult to do. Studies on surface temperature accuracy tests need to be reviewed in relation to the extraction process. Accuracy testing of remote sensing imagery is made only on the results of both visual and digital interpretation; for example, on the interpretation of land cover/land use. Land cover/land use is a hybrid variable that needs to be tested, while the biophysical variables that make up the hybrid variable are sets of pixel values that do not need to be tested (Danoedoro, 2012).

Table 3-2: Calibration constant of Landsat 8 TIRS Band 10

Temperature (K)	TIRS Band10 Change in Response (K)	
	Feb 11, 2013 – Mar 1, 2015	Mar 2, 2015 - Present
240 (extrapolated)	-0.11	2.73
273	0.08	1.05
285	0.14	0.60
300	0.20	0.12
320 (extrapolated)	0.27	-0.42

Source: <https://www.usgs.gov/core-science-systems/nli/landsat/landsat-8-oli-and-tirs-calibration-notice>

Related to this issue, land surface temperature is a biophysical variable derived from inversions in physics equations, so there is no need to test its accuracy as long as the equations are used correctly according to established procedure. Another example of a biophysical variable is the pixel value in the images of the NDVI vegetation index transformation results. This value does not need to be tested because it is a biophysical variable derived from an equation, and a variable used as interpretation material to compose the hybrid variable. When accuracy tests are made on land surface temperature (LST), these are performed to test the thermal infrared sensor used in terms of its accuracy in relation to the actual temperature in the field, and not to test the land surface temperature (LST) itself (Danoedoro, 2012).

Based on these issues, the United States Geological Survey has routinely calibrated the TIRS sensors attached to Landsat 8, with the results shown in Table 3-2.

Based on Table 3-2, the accuracy of the TIRS sensor in Landsat 8 Band 10 is an average of 0.466 K. This shows that the analysis using land surface temperature data derived using Landsat 8 TIRS Band 10 has an estimated value of 0.466 K warmer than the original condition.

#### 4 CONCLUSION

The phenomenon of SUHI in Salatiga was detected in the centre of the city, which was surrounded by areas with normal surface temperature based on the threshold value, while SUCI was distributed on the edge of the city, with an intensity  $-6.71^{\circ}\text{C}$  to  $0^{\circ}\text{C}$ , and was associated with vegetation.

#### ACKNOWLEDGEMENTS

The authors would like to thank the United States Geological Survey for providing free-access data. We also would like to express our gratitude to the reviewer and editorial team.

#### AUTHOR CONTRIBUTIONS

Detection and Analysis of Surface Urban Cool Island Using Thermal Infrared Imagery of Salatiga City, Indonesia. Lead Author: Bayu Elwantyo Bagus Dewantoro, Co-Author: Panji Mahyatar and Wafiq Nur Hayani. Author contributions are as follows:

1. Bayu Elwantyo Bagus Dewantoro: Thermal image processing, map layouting, and results analysis
2. Panji Mahyatar: Provision and processing of optical imagery
3. Wafiq Nur Hayani: Provision of introductions and prepare draft manuscripts

## REFERENCES

- Adachi, S.A., Kimura, F., Kusaka, H., Inoue, T., & Ueda, H. (2012). Comparison of the impact of global climate changes and urbanization on summertime future climate in the Tokyo metropolitan area. *American Meteorological Society*, 7, 1441-1454, <https://doi.org/10.1175/JAMC-D-11-0137.1>.
- Alhawiti, R. H., & Mitsova, D. (2016). Using Landsat-8 Data to Explore The Correlation Between Urban Heat Island and Urban Land Uses. *IJRET: International Journal of Research in Engineering and Technology*, 5(3), 457-466.
- Bahi, H., Hassan, R., Ahmed, B., Ute, F., & Dieter, S. (2016). Effects of Urbanization and Seasonal Cycle on the Surface Urban Heat Island Patterns in the Coastal Growing Cities: A Case Study of Casablanca, Morocco. *Remote Sensing*, 8(829), 1-26. doi:10.3390/rs8100829.
- Cao, X., Onishi, A., Chen, J., & Imura, H. (2010). Quantifying the Cool Island Intensity of Urban Parks Using ASTER and IKONOS Data. *Landscape and Urban Planning*, 96(4), 224-231.
- Chen, A., Yao, X. A., Sun, R., & Chen, L. (2014). Effect of Urban Green Patterns on Surface Urban Cool Islands and Its Seasonal Variations. *Urban Forestry & Urban Greening*, 13(4), 646-654. <https://doi.org/10.1016/j.ufug.2014.07.006>.
- Chen, J., Saunders, S.C., Crow T.R., Naiman, R.J., Brosofske, K.D., Mroz G.D., Brookshire, B.L., & Franklin, J.F. (1999). Microclimate in forest Ecosystem and Landscape Ecology: Variations in local climate can be used to monitor and compare the effects of different management regimes. *BioScience*, 49(4), 288-297.
- Danoedoro, P. (2012). *Pengantar penginderaan jauh digital [Introduction to digital remote sensing]*. Yogyakarta: Andi.
- Fawzi, N. I. (2017). Mengukur urban heat island menggunakan penginderaan jauh, kasus di Kota Yogyakarta [Measuring urban heat island using remote sensing, a case in Yogyakarta City]. *Majalah Ilmiah Globè*, 19(2), 195-206.
- Goggins, W.B., Chan, E.Y.Y., Ng, E., Ren, C., & Chen, L., (2012). Effect modification of the association between short-term meteorological factors and mortality by urban heat islands in Hong Kong. *PLOS ONE*, 7(6), 1 - 6. <https://doi.org/10.1371/journal.pone.0038551>.
- Huang, X., & Wang, Y. (2019). Investigating The Effects of 3D Urban Morphology on The Surface Urban Heat Island Effect in Urban Functional Zones by Using High-Resolution Remote Sensing Data: A Case Study of Wuhan, Central China. *ISPRS Journal of Photogrammetry and Remote Sensing*, 152, 119-131. <https://doi.org/10.1016/j.isprsjprs.2019.04.010>.
- Ismangil, D., Wiegant, D., Hagos, E., Steenbergen, F.V., Kool, M., Sambalino, F., Castelli, G., Bresci, E., & Hagos F. (2016). Managing the Microclimate. Spate Irrigation Network Foundation.
- Kong, F., Yin, H., Wang, C., Cavan, G., & James, P. (2014). A Satellite Image-Based Analysis of Factors Contributing to The Green-Space Cool Island Intensity on A City Scale. *Urban Forestry & Urban Greening*, 13(4), 846-853. <http://dx.doi.org/10.1016/j.ufug.2014.09.009>.
- Lai, L.W., & Cheng, W.L. (2009). Air Quality Influenced by Urban Heat Island Coupled with Synoptic Weather Patterns. *Science of the Total Environment*, 407(8), 2724-2733.
- Li, S., Mo, H., & Dai, Y. (2011). Spatio-Temporal Pattern of Urban Cool Island Intensity and Its Eco-environmental Response in Chang-Zhu-Tan Urban Agglomeration. *Communications in Information Science and Management Engineering*, 1(9), 1-6.
- Li, X.X., & Norford, L.K.. (2016). Evaluation of cool roof and vegetations in mitigating

- urban heat island in a tropical city, Singapore. *Urban Climate*, 16, 59–74.
- Li, Z-L, Tang, B-H, Wu, H., Ren, H., Yan, G., Wan, Z., Trigo, I.F., & Sobrino, J.A. (2013). Satellite-Derived Land Surface Temperature: Current Status and Perspectives. *Remote Sensing of the Environment*, 131, 14-37. <http://dx.doi.org/10.1016/j.rse.2012.12.008>.
- Lima, A. E., & Lopes, A. (2017). The urban heat island effect and the role of vegetation to address the negative impact of local climate changes in a small Brazilian City. *Atmosphere Multidisciplinary Digital Publishing Institute* 8(2), 1-14
- Loyd, C.. (2017). Landsat 8 bands. Landsat Science. Available at: <https://landsat.gsfc.nasa.gov/landsat-8/landsat-8-bands/>. Accessed 19 June 2020.
- Ma, Y., Kuang, Y., & Huang, N. (2010). Coupling urbanization analyses for studying urban thermal environment and its interplay with biophysical parameters based on tm/etm+ imagery. *International Journal of Applied Earth Observation and Geoinformation* 12(2): 110–118.
- Mostofi, N., & Hasanlou, M. (2017). Feature Selection of Various Land Cover Indices for Monitoring Surface Heat Island in Tehran City Using Landsat 8 Imagery. *Journal of Environmental Engineering and Landscape*, 25(3), 1-10. <http://dx.doi.org/10.3846/16486897.2016.1223084>.
- Ng, E., & Ren, C. (2017). China's Adaptation to Climate & Urban Climatic Changes: A Critical Review. *Urban Climate*, 23, 352 – 372. <https://doi.org/10.1016/j.uclim.2017.07.006>.
- Rasul, A., Balzter, H., & Smith, C. (2015). Spatial Variation of The Daytime Surface Urban Cool Island During The Dry Season in Erbil, Iraqi Kurdistan, from Landsat 8. *Urban Climate*, 14(2), 176-186. <http://dx.doi.org/10.1016/j.uclim.2015.09.001>.
- Reisi, M., Nadoushan, M. A., & Aye, L. (2019). Remote Sensing for Urban Heat and Cool Islands Evaluation in Semi-Arid Areas. *Global Journal of Environmental Science and Management*, 5(3), 319-330. doi: 10.22034/gjesm.2019.03.05.
- Kershaw, T., Sanderson, M., Coley, D., Eames, M. (2010). Estimation of The Urban Heat Island for UK Climate Change Projections. *Building Services Engineering Research and Technology*, 31(3), 251–263.
- Sabins, F. F. (2007). *Remote Sensing: Principles and Interpretation 3rd Edition*. Illinois: Waveland Press.
- Salih, M. M., Jasim, O. Z., Hassoon, K. I., & Abdalkadhum, A. J. (2018). Land surface temperature retrieval from Landsat-8 thermal infrared sensor data and validation with infrared thermometer camera. *International Journal of Engineering and Technology*, 7(4.2), 608 – 612, doi: 10.14419/ijet.v7i4.20.27402.
- Skelhorn, C. P., Lindley, S. & Levermore, G. (2016). Urban Greening and the UHI: Seasonal Trade-Offs in Heating and Cooling Energy Consumption in Manchester, UK. *Urban Climate*, 23, available at: <https://doi.org/10.1016/j.uclim.2017.02.010>.
- Stone, B., Hess, J.J., & Frumkin, H. (2010). Urban Form and Extreme Heat Events: Are Sprawling Cities More Vulnerable to Climate Change than Compact Cities? *Environmental Health Perspectives*, 118(10), 1425–1428.
- Sobrino, J. A., Jimenez-Munoz, J. C., Soria, G., Romaguera, M., Guanter, L., Plaza, A., & Martinez, P. (2008). Land surface emissivity retrieval from different VNIR and TIR sensors. *IEEE Transactions on Geoscience and Remote Sensing* 46, 316 – 327.
- Tan, J., Zheng, Y., Tang, X., Guo, C., Li, L., Song, G., Zhen, X., Yuan, D., Kalkstein, A.J., & Li, F. (2010). The Urban Heat Island and

- Its Impact on Heat Waves and Human Health in Shanghai. *International Journal of Biometeorology*, 54(1), 75–84.
- Tran, H., Uchihama, D., Ochi, S., & Yasuoka, Y., (2006), Assessment with satellite data of the urban heat island effects in Asian mega cities. *International Journal of Applied Earth Observation and Geoinformation* 8(1), 34-48. <https://doi.org/10.1016/j.jag.2005.05.003>.
- Valor, E., & Caselles, V. (1996). Mapping land surface emissivity from NDVI: Application to European, African, and South American areas. *Remote Sensing of Environment* 57(3), 167–184.
- Wang, Y., Chen, L., & Kubota, J. (2016). The Relationship Between Urbanization, Energy Use and Carbon Emissions: Evidence from A Panel of Association of Southeast Asian Nations (ASEAN) Countries. *Journal of Cleaner Production*, 112, 1368–1374.
- Xian, G., & Crane, M. (2006). An Analysis of Urban Thermal Characteristics and Associated Land Cover in Tampa Bay and Las Vegas Using Landsat satellite Data. *Remote Sensing of Environment* 104(2), 147–156. <https://doi.org/10.1016/j.rse.2005.09.023>
- Yang, X., Li, Y., Luo, Z., & Chan, P. W. (2016). The Urban Cool Island Phenomenon in A High-Rise High-Density and Its Mechanism. *International Journal of Climatology*, 37(2), 890–904. <https://doi.org/10.1002/joc.4747>.

# MONITORING CHANGES IN CORAL REEF HABITAT COVER ON BERALAS PASIR ISLAND USING SPOT 4 AND SPOT 7 IMAGERY FROM 2011 AND 2018

Rosaria Damai<sup>1\*</sup>, Viv Djanat Prasita<sup>1</sup>, Kuncoro Teguh Setiawan<sup>2</sup>

<sup>1</sup>Universitas Hang Tuah Surabaya

<sup>2</sup>Remote Sensing Applications Center–National Institute of Aeronautics and Space (LAPAN)

\*e-mail: rosadamai2@gmail.com

Received: 26 September 2020; Revised: 16 December 2020; Approved: 21 December 2020

**Abstract.** Beralas Pasir is part of the Regional Marine Conservation Area (KKLD), which was established by the Bintan Regency Government with Bintan Regent Decree No. 261 / VIII / 2007. Water tourism activities undertaken by tourists on the island have had an impact on the condition of the coral reefs, as have other factors, such as bauxite, granite and land sand mining activities around the island. This research aims to determine changes in the coral reef habitat cover and the condition of the coral reefs around Beralas Pasir Island with a remote sensing function, using SPOT 4 imagery acquired on June 1, 2011 and SPOT 7 imagery from April 5, 2020. Data collection of environmental parameters related to the coral reefs was also made. The image processing used the Lyzenga algorithm to simplify the image classification process. The percentage of coral live cover around the island ranges from 26% - 53%; this has experienced a significant change, from 67,560 hectares in 2011 to 38,338 hectares in 2018, a total decrease in the area of 29,222 hectares. Some of the natural factors found in the research which have caused damage to the reefs were *Drupella* snails, the abundance of *Caulerpa racemosa* algae, and sea urchins. The majority of the coral reef types consist of Non-Acropora: *Coral Massive*, *Coral*, *Coral Foliose*, *Coral Encrusting*, *Acropora*: *Acropora Tabulate*, *Acropora Encrusting*, and *Acropora Digitate*.

Keywords: *Monitoring, Coral Reefs, SPOT 4, SPOT 7, Beralas Pasir Island.*

## 1 INTRODUCTION

The coast of Bintan Regency has a coral reef area of 17,394.83 hectares (DKP, 2007 as cited in Adriman et al., 2013). There was 14 families and 78 type of coral in bad to moderate condition (Giyanto et al., 2017). Since 2006, the coastal area of Bintan Regency has been determined by the government to be one of the locations for the Coral Reef Rehabilitation and Management Program (COREMAP) (Adriman et al., 2013). Beralas Pasir Island is one of 3000 large and small islands in Bintan Regency, Riau Islands Province, and is a marine tourism area known as the “private islands”. The island is part of Gunung Kijang District, which is one of the two

sub-districts where COREMAP is being implemented. In addition, Beralas Pasir Island is a Regional Marine Conservation Area (KKLD,) which was established by the Bintan Regency Government with the Bintan Regent Decree No. 261 / VIII / 2007. The island has an area of around 6 hectares (Lumbantoruan, 2017).

Environmental conditions on the island are influenced by seasonal winds and include currents, some of which are quite complex as a result of the interaction between various fixed and seasonal currents, and other factors such as the water topography and coastlines. Moreover, tides also affect the movement of various chemical pollutants, such as oil pollution. The geographical position of



Beralas Pasir Island, which is part of Bintan, is at the confluence of the Indian Ocean through the Malacca Strait and the Pacific Ocean through the South China Sea, causing the Riau Islands waters to experience tidal currents with an alternating pattern (Lumbantoruan, 2017). The weather on Beralas Pasir Island is influenced by the monsoons, which change direction according to the position of the sun to the earth, meaning the climate on the island is wet tropical, with the highest rainfall in September to February (Lumbantoruan, 2017), and with an average monthly temperature of 24.8 °C (Lumbantoruan, 2017). Land elevation above sea level is around 10 m, and the topography of the Beralas Pasir Island is a sloping base with a sand substrate (Lumbantoruan, 2017).

The island was previously uninhabited, but in September 2015 PT. Indo Bintan Trijaya opened it to the public as a tourist destination. The number of activities undertaken by tourists in the sea waters of around the island have an impact on the condition of the coral reefs. Another factor which is a reason for the study is the influence of bauxite mining, which together with the development of the resorts on the coast, has an impact on changes in the coral reef cover. CRITC Bintan (2009) as cited in Adriman et al., (2013) reported a decrease in live coral cover in the East Bintan Marine Protected Area (KKLD), allegedly the result of bauxite, granite and land sand mining activities. Based on the problems mentioned above, this research was conducted to monitor changes in the coral reef cover on Beralas Pasir Island using remote sensing methods in 2011 with SPOT 4 images and comparing them to ones from 2018 from SPOT 7, together with the conducting of ground truths in the field using a confusion matrix accuracy test. Irawan et al. (2017) and

Azka et al. (2019) previously conducted research on changes in coral reef areas utilising remote sensing and the water column correction method using the Lyzenga algorithm, together with Landsat imagery. Remote sensing is a method that is often used in research both on land and at sea as it can facilitate large scale research, such as studies of one island or several islands at the same time.

## 2 MATERIALS AND METHODOLOGY

### 2.1 Research Location and Time

The research was conducted from March to May 2020, with steps including the preparation stage, field survey and field data collection on Beralas Pasir Island, Riau Islands Province. The field data processing was conducted at the Hydro-Oceanography Laboratory, Hang Tuah University, Surabaya and that of the satellite imagery at the Remote Sensing Utilization Center, LAPAN. The tools used for the study were a secchidisc, roller meter, thermometer, underwater camera, underwater paper, floating ball, salinometer and a laptop for the image data processing, as well as ErMapper 7.1, ENVI 5.3, ArcGIS 0.3 and CPCe 4.1 software. The research materials can be seen in Table 2-1.

Table 2-1: Research Materials

Type of Data	Date of Acquisition
SPOT 4	June 6, 2011
SPOT 7	April 5, 2018

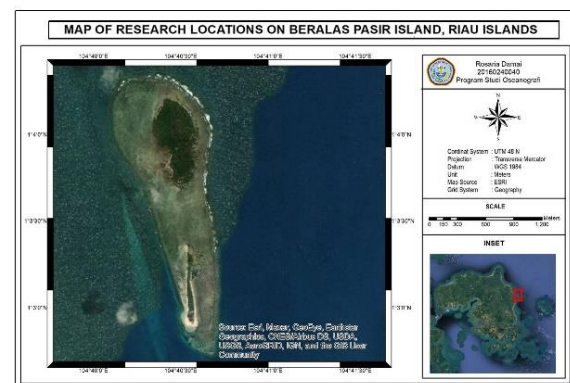


Figure 2-1: Research Location

## 2.2 Standardization of Data

### 2.2.1 Ground Truths

Field validity checks were performed to establish the condition of coral cover and the environmental conditions, in accordance with the conditions in the field. Determination of the data collection points was made using the purposive sampling method.

#### a. Retrieval of coral reef data

Retrieval of coral reef data with a size of 9 m x 9 m was made from ten points spread across locations around the island. The 9 m x 9 m data size aimed to be a sample point for the SPOT 7 image pixels, representing a resolution of 6 m x 6 m for each pixel, with the remaining size used for errors. There were 30 sampling points for the reclass and accuracy tests, ten comprising details of data on coral reefs, ten on seagrass, and ten on sand. The coral reef data were then processed using CPCe 4.1 software.

#### b. Environmental Parameters

Environmental parameter data were collected to observe the limiting factors for coral reef growth. Some of the parameters used in the study were temperature, brightness, salinity and current velocity.

### 2.2.2 Image processing

The image processing can be seen in the flow chart shown in figure 2-2.

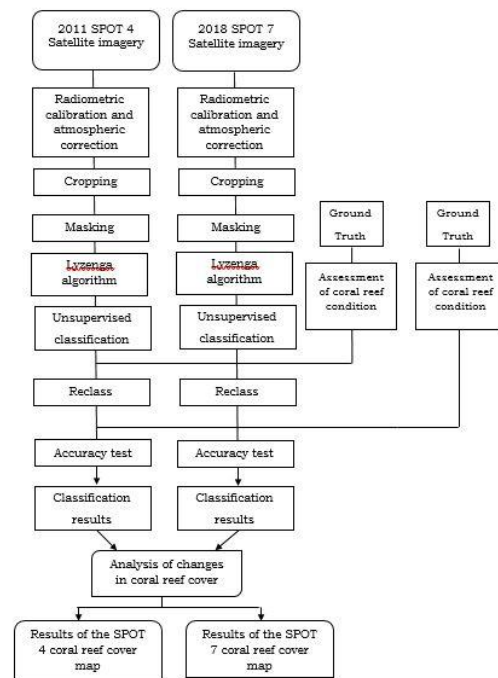


Figure 2-2: Flow Chart

#### 1. Radiometric Calibration

Radiometric calibration is a satellite image processing process that aims to convert data in images that are generally stored in the form of a digital number (DN) into radiance (LTOA) or reflectance ( $\rho$ TOA), which can be in the form of brightness temperature for Thermal Infrared (Jaelani, 2017).

#### 2. Atmospheric Correction

The method used to eliminate atmospheric effects is the histogram adjustment method (Chavez et al., 1988).

#### 3. Image Cropping

The satellite images obtained had a wide coverage, so it was necessary to cut the image to the required research area.

4. Masking

The separation stage between land and water/ocean was performed to make it easier to analyse the ocean as the main object, by entering the formula if (I1 / I2) > 0.7 then 255 else I2.

5. Lyzenga's Algorithm

The Lyzenga algorithm is a step taken in water column correction which is applied to satellite images to eliminate the influence of water columns:

$$Y = Ln(TM1) + (Ki/Kj * Ln(TM2)) \quad (2-1)$$

Where:

Y = image extracted from the bottom of the water

TM1 = digital number on Band TM1

TM2 = digital number on Band TM2

Ki/Kj = attenuation coefficient value

6. Unsupervised Classification

Image classification in this research was made using unsupervised classification with the ISODATA (Iterative Self-Organizing Data Analysis Technique) method for images from 2011 and 2018.

Classification is a clustering algorithm that allows the number of clusters to be adjusted automatically based on the iteration process performed (Rahmawan et al., 2020).

7. Reclass

Reclass is the stage of improving the unsupervised classification so that it matches the actual situation with the help of field data to match the image results with the actual field conditions.

8. Accuracy Test

A classification accuracy test was performed to test the accuracy of the usage map generated from the digital classification process, with test samples from the results of the ground truth. The sample used as the training area and that used for the accuracy test was not the same sample; that for the accuracy test was taken from a different place so that its accuracy was more acceptable. The method used to test the accuracy of image classification was a configuration, or error matrix (Jensen, 2005 as cited in Wulansari 2017). This matrix can be seen in Table 2-2.

Table 2-2: Error Matrix

	Reference Data							Total Row
	PL I	PL II	PL III	PL IV	PL V	PL VI	PL VII	
PL I	A	a	b	c	D	e	f	Σ row 1
PL II	g	B	h	i	J	k	l	Σ row 2
PL III	m	n	C	o	P	q	r	Σ row 3
PL IV	s	t	u	D	V	w	x	Σ row 4
PL V	y	z	a'	b'	E	c'	d'	Σ row 5
PL VI	e'	f	g'	h'	I'	F	j'	Σ row 6
PL VII	k'	l'	m'	n'	o'	p'	G	Σ row 7
Total column	Σ row 1	Σ row 2	Σ row 3	Σ row 4	Σ row 5	Σ row 6	Σ row 7	Σ total column/row
	1	2	3	4	5	6	7	

Confusion matrix analysis (Banko, 1998) employs the following equation:

$$K = \frac{\text{number of rows and columns}}{\text{sum of all data}} \times 100\% \quad (2-2)$$

9. Coral Reef Assessment

The condition of coral reefs is based on the percentage cover of live coral (rock coral) and other living components, together with dead coral, as shown in the Table 2-3.

Table 2-3: Category of Coral Reef Cover Condition (English et al., 1997 as cited in Raazy, 2018).

Coral Reef Cover (%)	Condition Category
00 - 25	Bad
26 - 50	Moderate
51 - 75	Good
76 - 100	Best

10. Calculation of Coral Reef Area

The area and changes can be seen from image data that have been processed and converted to .shp, as shown in the attribute table in ArcGIS 10.3 software. Calculation of the area of and change in coral reefs is made in hectares (ha).

2.2.3 Environmental Parameter Data Analysis

1 Visibility

The visibility value is calculated by taking the percentage value of the strap length when the Secchi disc is still visible or not visible at all, which is then converted into a percent brightness value. The following formula is used:

$$\frac{\text{visibility (m)}}{\text{depth (m)}} \times 100\% \quad (2-3)$$

2 Current Velocity

The current velocity measured in

the field can be calculated using the formula:

$$\text{Rated current velocity, } v = s / t \quad (2-4)$$

where

s = length of the current floating ball (m)

t = current time (seconds)

3 RESULTS AND DISCUSSION

3.1 Pre-processing results of SPOT 4 and SPOT 7 imagery of Beralas Pasir Island

3.1.1 Radiometric Calibration

The results of the radiometric calibration are image data initially in the form of a digital number (DN), which is then converted into radiance (LTOA). The results of the radiometric calibration are shown in Figure 3-1.

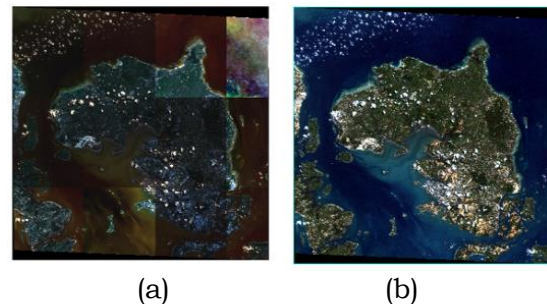


Figure 3-1: (a) before radiometric calibration; (b) after radiometric calibration

3.1.2 Atmospheric Correction

The method used to eliminate the effects of the atmosphere is the histogram shift method (histogram adjustment); the approach commonly used is dark object subtraction (DOS). The digital number (DN) in an image if there is no atmospheric influence, then the minimum pixel value is zero and the maximum value is one or less (Chavez et al., 1988). If the minimum DN pixel in the image histogram is not equal to zero, this indicates a disturbance from atmospheric impact. The results of the atmospheric correction are shown in Tables 3-1 and 3-2.

Table 3-1: Digital numbers of SPOT 7 before atmospheric correction

Band	Min	Max	Mean	St.Dev
Band 1	0	4095	225.15	172.98
Band 2	0	4095	418.28	135.23
Band 3	0	4095	539.42	98.55
Band 4	0	4095	254.57	424.09

Table 3-2: Digital numbers of SPOT 7 after atmospheric correction

Band	Min	Max	Mean	StDev
Band 1	0.0	0.0045	0.0006	0.0002
Band 2	0.0	0.0039	0.0004	0.0002
Band 3	0.0	0.0036	0.0002	0.0002
Band 4	0.0	0.0024	0.0003	0.0003

### 3.1.3 Image Cropping

After atmospheric correction, the imagery is cropped cut according to the location required to be observed. The results of the cropping can be seen in Figure 3-2.

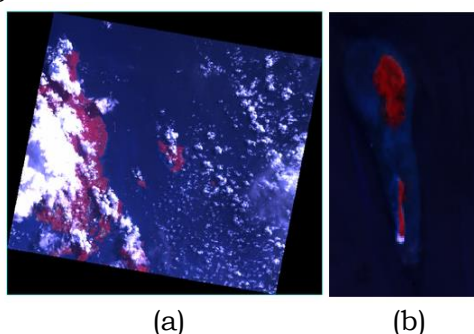


Figure 3-2: (a) SPOT 4 image before cropping; (b) image after cropping

### 3.1.4 Masking

Separation is made of land from ocean, in order for all land values to become 255 so as not to disturb the value

of the marine waters during the next process. The results of the masking are shown in Figure 3-3.

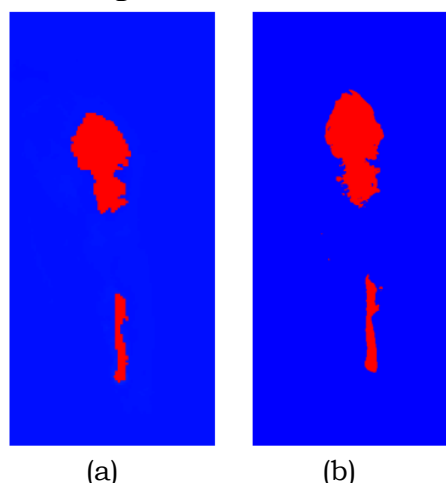


Figure 3-3: (a) Masking SPOT 4, (b) Masking SPOT 7

## 3.2 Results of SPOT 4 and SPOT 7 Image Data Processing from Beralas Pasir Island

### 3.2.1 Lyzenga's Algorithm

The application of the Lyzenga algorithm uses SPOT 4 green and red channels, and SPOT 7 blue and red channels. The value of the  $K_i/K_j$  coefficient is obtained by creating a training area of 30 regions in the image which have homogeneous colours in the coral reef area. The results of the calculation of the creation of the area are shown in Tables 3-3 and 3-4. The results of the Lyzenga algorithm can be seen in Figure 3-4.

Table 3-3: 2011 SPOT 4 Results of calculation create region

a	0.96277804
$K_i/K_j$	0.925556078

Table 3-4: 2018 SPOT 7 Result of calculation create region

a	0.32264807
$K_i/K_j$	0.64529615



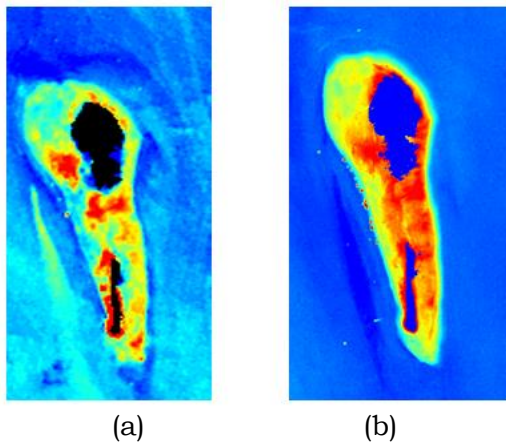


Figure 3-4: Results of the application of the Lyzenga algorithm: (a) SPOT 4 image from 2011; (b) SPOT 7 image from 2018

### 3.2.2 Image Classification

The results of the classification of the images of the coral reefs around Beralas Pasir Island using SPOT 4 and the ISODATA classification method resulted in ten classes. In the next class processing step, the SPOT 4 2011 image is not reclassified using field data, but instead the reclassification process refers to the shallow water object key when conducting ground truth, with the help of Google Earth to observe the condition of Beralas Pasir Island in 2011. The results of the classification can be seen in Figure 3-5.

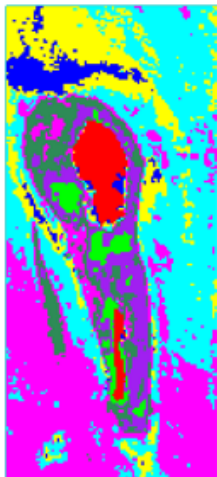


Figure 3-5: Unsupervised classification results of SPOT 4

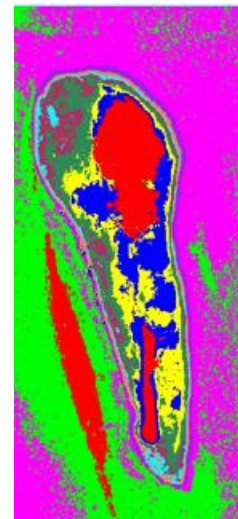


Image 3-6: Unsupervised classification results of SPOT 7

The results of the SPOT 7 image classification using the ISODATA method produced ten classes. Each class represented the characteristics of aquatic objects. Then for the SPOT 7 image after being classified into 10 classes, the next process was the reclassification process to improve the results so they match the ground truth data. The results of the classification can be seen in Figure 3-6.

### 3.2.3 Reclassification

Recolouring was performed to match the results of the images with the ground truth data that had been obtained, which were divided into five classes: coral reefs, seagrass, sand, land and sea. Each class was assigned a different colour to make it easier to recognise each water object. The coral ground truth location can be seen in Figure 3-7. Table 3-5 shows the details of the station for the reclassification process, consisting of the coral reef, seagrass and sand reclassification points.

Table 3-5: Station coordinate points for the 2018 SPOT 7 reclassification.

Station	Habitat Cover	Coordinate point	
		X	Y
1	Coral Reefs	117995.00 m N	463096.00 m E
2	Coral Reefs	118127.00 m N	464138.00 m E
4	Coral Reefs	116059.00 m N	463850.00 m E
10	Coral Reefs	115533.00 m N	464114.00 m E
2	Seagrass	116348.00 m N	463814.00 m E
4	Seagrass	116488.00 m N	463814.00 m E
7	Seagrass	116242.00 m N	464026.00 m E
10	Seagrass	115809.00 m N	464028.00 m E
1	Sand	115924.27 m N	463875.43 m E
4	Sand	115841.73 m N	463985.96 m E
5	Sand	115874.70 m N	463903.59 m E
8	Sand	116085.97 m N	463880.55 m E

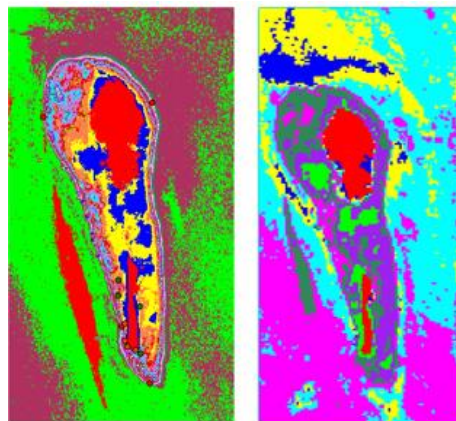


(a)

(b)

(c)

Figure 3-7: Coral ground truth location points for reclassification of SPOT 7 Figure: (a) coral reef; (b) seagrass; (c) sand (source: Google Earth)



(a)

(b)

Figure 3-8: (a) unsupervised SPOT 7 classification results; (b) unsupervised SPOT 4 classification results

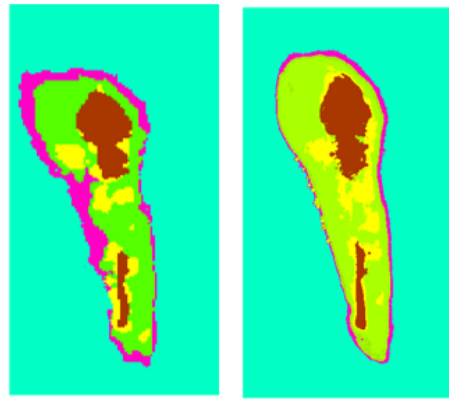


Figure 3-9: Reclassification Results: (a) SPOT 4 in 2011 (b) SPOT 7 in 2018

Table 3-6: Confusion Matrix Accuracy Test.

Image Classification Results	Information on Ground Truth Results				
	Class	Coral	Seagrass	Sand	Total
Coral		5	0	0	5
Seagrass		1	5	1	7
Sand		0	1	5	6
Total		6	6	6	18
Accuracy					83.3%

Figure 3-8 shows the results of the classification process, after which a reclassification process was conducted to correct classes not in accordance with the conditions in the field. Figure 3-9 shows the results of the reclassification process, which comprise five classes: coral reef, seagrass, ocean, land and sand.

### 3.2.4 Accuracy Test

Based on the results of the accuracy test shown in Table 3-6, the test value from the confusion matrix method is 83.333%. In remote sensing, the results of the accuracy tests are divided into 3 classes, namely if  $K > 80\%$ , the accuracy value is very strong (strong agreement); if  $K = 40\% - 80\%$  the value is moderate (moderate agreement); and if  $K < 40\%$  the value is not good (poor

agreement) (Jensen, 2005). The level of research accuracy therefore falls into the very strong category). Table 3-7 shows the details of the stations for the accuracy tests, consisting of the accuracy test points of the coral reefs, seagrass and sand.

### 3.2.5 Calculation of the Coral Reef Area

Based on the results of the processing of the 2011 and 2018 images, which were tested for accuracy with ground truth data, there are differences in the areas of all types of Beralas Pasir Island habitat cover, as shown in Table 3-8. Maps of the condition of the coral reef areas around the island can be seen in Figure 3-10 - 3-12.



Table 3-7: Station coordinate points for the 2018 SPOT 7 accuracy test.

Station	Habitat Cover	Coordinate Point	
		X	Y
3	Coral	115720.00 m N	463872.00 m E
5	Coral	116139.00 m N	463805.00 m E
6	Coral	116217.00 m N	463783.00 m E
7	Coral	116415.00 m N	463726.00 m E
8	Coral	116488.00 m N	463702.00 m E
9	Coral	116571.00 m N	463675.00 m E
1	Seagrass	116150.00 m N	463872.00 m E
3	Seagrass	116397.00 m N	463820.00 m E
5	Seagrass	116569.00 m N	463782.00 m E
6	Seagrass	116334.09 m N	464000.95 m E
8	Seagrass	116021.00 m N	464103.00 m E
9	Seagrass	115909.00 m N	464071.00 m E
2	Sand	115990.21 m N	463885.14 m E
3	Sand	115876.73 m N	464016.33 m E
6	Sand	115846.35 m N	463925.67 m E
7	Sand	116034.62 m N	463894.05 m E
9	Sand	115905.24 m N	463877.89 m E
10	Sand	115968.39 m N	463883.50 m E

Table 3-8: Difference in the findings on coral reefs cover in 2011 and 2018.

Substrate	Substrate area (ha)		Area Difference (ha)
	2011	2018	
Sand	27.48	25.62	-1.85
Seagrass	85.52	189.93	104.41
Coral	67.56	38.33	-29.22
Total	180.56	253.90	73.34

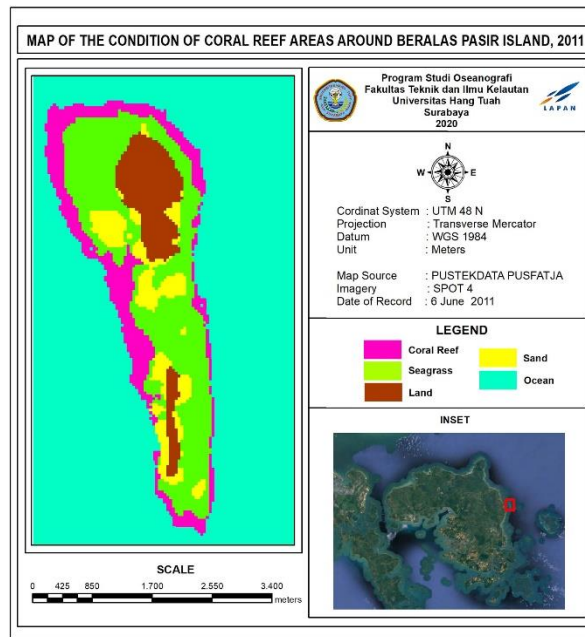


Figure 3-10: Map of the Condition of Coral Reef Areas around Beralas Pasir Island, 2011

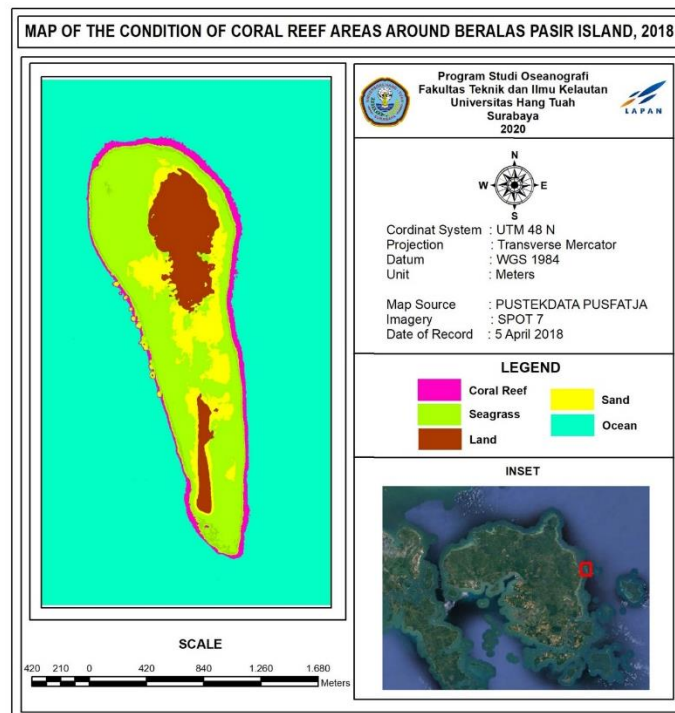


Figure 3-11: Map of the Condition of Coral Reef Areas around Beralas Pasir Island, 2018

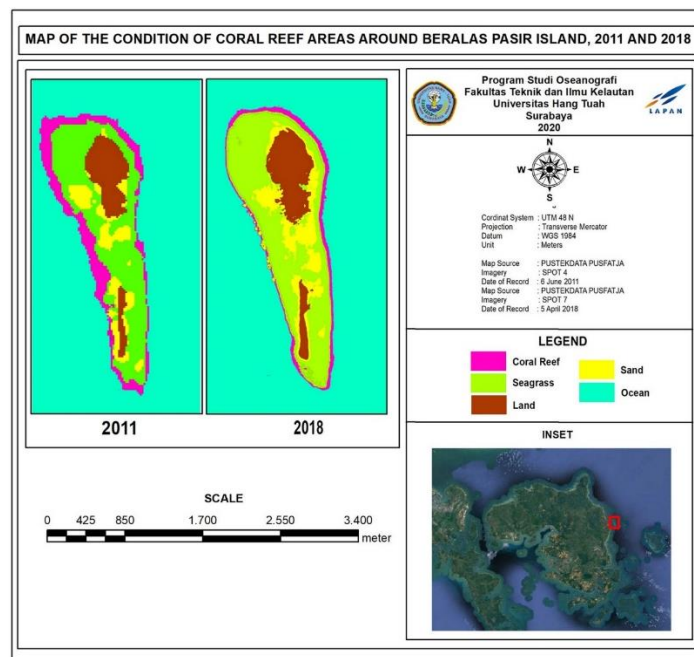


Figure 3-12: Map of the Condition of Coral Reef Areas around Beralas Pasir Island, 2011 and 2018

### 3.3 Results of the Field Data Retrieval

#### 3.3.1 Water Conditions around Beralas Pasir Island

The condition of marine waters is also a component that affects the life, condition and growth of coral reefs. Some of the environmental parameter data taken for coral reefs in this study include

salinity, visibility, temperature and current velocity, as shown in Table 3-8. Beralas Pasir Island is unique in its ocean currents. To the south of the island, the currents have different directions. Those to the west are in a southwesterly direction, while to the east they are northerly.

Table 3-9: Water Parameter Data around Beralas Pasir Island.

Station	Salinity (‰)	Depth (m)	Visibility (m/%)	Temp. (°C)	Cur.Vel (m/s)
1	35	6.8	6.8 (100%)	30.8	0.12
2	35	4	4 (100%)	30.4	0.53
3	35	2.5	2.5 (100%)	30.3	0.53
4	35	1.2	1.2 (100%)	30.9	0.12
5	35	1.4	1.4 (100%)	30.9	0.12
6	35	2	2 (100%)	30.7	0.12
7	35	4	4 (100%)	31.8	0.12
8	35	4.2	4.2 (100%)	30.9	0.12
9	35	1.5	1.5 (100%)	30.6	0.53
10	35	6.5	6.5 (100%)	30.5	0.53

#### 3.3.2 Coral Reef Condition around Beralas Pasir Island

Coral reef assessment was made by entering photos of coral reef condition documented under water into the CPCe

4.1 software. The results of the assessment from the software could then be opened in Microsoft Excel. Coral reef cover can be seen in Figure 3-13.

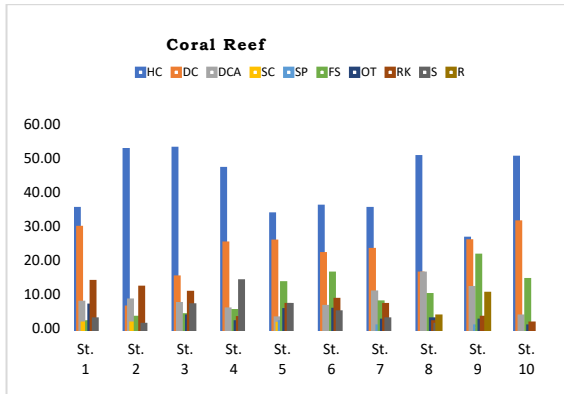


Figure 3-13: Coral reef cover around Beralas Pasir Island

**1. Station 1**

Station 1 was located to the northwest of the island, at a depth of 6.8 metres, with a sloping topographical condition of the sea floor. The percentage of habitat cover is shown in Figure 3-14.

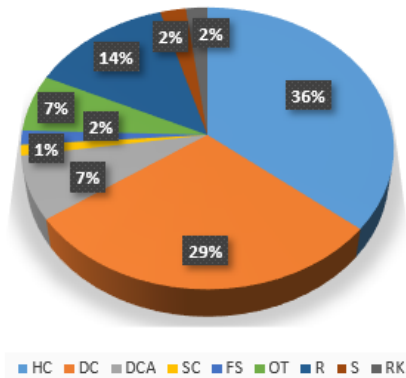


Figure 3-14: Percentage of coral reef cover at station 1

Its "medium" category indicates that its condition of coral reef is neither good nor bad. According to information from the manager of the Sand Island tourist area, the location of Station 1 is often used as a place for fishing, and many boats pass to taking tourists around the island to see the scenery. The percentage of the diversity of coral reef species at the station can be seen in Table 3-10.

Table 3-10: Percentage of diversity of coral reef species at station 1.

Species	(%)
<b>Acropora</b>	
Acropora Digitate (ACD)	0.41
Acropora Tabulate (ACT)	2.86
<b>Non-Acropora</b>	
Coral Encrusting (CE)	1.22
Coral Foliose (CF)	21.63
Coral Massive (CM)	2.45
Coral Mushroom (CMR)	2.86
Coral Submassive (CS)	4.49

It can be seen that the type of coral reef that is most abundant at station 1 is non-Acropora coral foliose (sheet), at 21.63%, while the least abundant is Acropora digitate (fingers), at 0.41%. An image of coral foliose is shown in Figure 3-15.



Figure 3-15: Most abundant coral species at station 1: non-Acropora coral foliose (Source: private collection, P. Beralas Pasir)

**2. Station 2**

Station 2 was to the northeast of the island, at a depth of 4 metres, with the topography of the seabed sloping from the coastline 200 metres into the open sea. Based on the results of the ground truth data collection, the percentage of coral reef cover at station 2 is 52%, which is in

the "good" category. Based on a statement by the manager of the Beralas Pasir Island tourist area, the location of station 2 is rarely used for snorkeling, diving, canoeing or other water tourism by tourists. The percentage of habitat cover at station 2 is shown in Figure 3-16.

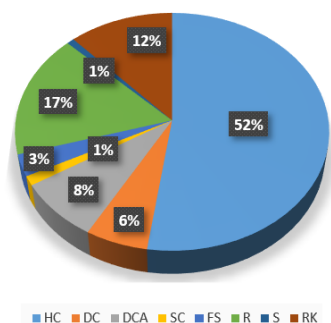


Figure 3-16: Percentage of coral reef cover at station 2

Based on literature regarding the sea conditions around Beralas Pasir Island, station 2 is in a location with quite strong currents and high waves, with a current circulation coming from the Natuna Sea. The percentage of diversity at station 2 is shown in Table 3-11.

Table 3-11: Percentage of diversity of coral reef species at station 2

Species	(%)
<b>Acropora</b>	
Acropora Branching (ACB)	5.06
Acropora Digitate (ACD)	1.27
Acropora Encrusting (ACE)	2.95
Acropora Tabulate (ACT)	10.55
<b>Non-Acropora</b>	
Coral Branching (CB)	0.84
Coral Encrusting (CE)	1.69
Coral Foliose (CF)	4.22
Coral Massive (CM)	16.88
Coral Submassive (CS)	8.86

It can be seen that the type of coral reef that is most abundant at station 2 is non-Acropora coral massive (solid), at 16.88%, and the least abundant Acropora digitate (fingers), at 1.27%. An image of coral massive is shown in Figure 3-17.



Figure 3-17: Most abundant coral species at station 2: non-Acropora coral massive (Source: private collection, P. Beralas Pasir)

### 3. Station 3

Station 3 was located to the south of the island, at a depth of 2.5 metres, with the topography of the seabed sloping from the coastline 150 metres into the open sea. The percentage habitat cover at the station is shown in Image 3-18.

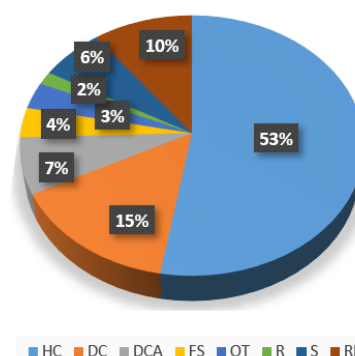


Figure 3-18: Percentage of coral reef cover at station 3

Based on the results of the ground truth data collection, the percentage of live coral cover at station 3 is 53%, which is in the "good" category.

Based on a statement by the manager of the Beralas Pasir Island tourist area, the location of station 3 is rarely used as a location for snorkeling or diving by tourists because it is in a location that has fairly strong currents, coming from the east of the island, circulating to the south, and originating in the Natuna Sea. The percentage of diversity at the station is shown in Table 3-12.



Table 3-12: Percentage of coral reef species diversity at station 3.

Species	(%)
<b>Acropora</b>	
Acropora Encrusting (ACE)	2.47
Acropora Tabulate (ACT)	10.29
<b>Non-Acropora</b>	
Coral Encrusting (CE)	2.88
Coral Foliose (CF)	7.82
Coral Massive (CM)	17.28
Coral Mushroom (CMR)	0.41
Coral Submassive (CS)	11.52

It can be seen that the type of coral reef that is most abundant at station 3 is non-Acropora coral massive (solid), with a percentage of 17.28%, with the least abundant being non-Acropora coral mushroom (mushroom), at 0.41%. An image of coral massive is shown in Figure 3-19.



Figure 3-19: Most abundant coral species at station 3: non-Acropora coral massive (Source: private collection, P. Beralas Pasir)

**4. Station 4**

Station 4 was located to the west of Beralas Pasir Island, at a depth of 1.2 metres, with the topography of the sea floor sloping from the coastline 120 metres into the open sea. The percentage habitat cover at the station is shown in Figure 3-20.

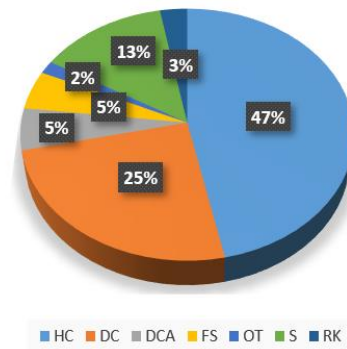


Figure 3-20: Percentage of coral reef cover at station 4

Based on the results of the field data collection, the percentage of live coral reef cover at station 4 is 47%, which is in the "medium" category.

The manager of the Beralas Pasir Island tourist area stated that the location of the station was the main spot for snorkeling and diving by tourists as it had weak currents, it was not too deep, and its location is not too far from the island. In addition, the various types of coral made the station the main tourist location of the island. The percentage of diversity at station 4 is shown in Table 3-13.

Table 3-13: Percentage of coral reefs species diversity at station 4.

Species	(%)
<b>Acropora</b>	
Acropora Encrusting (ACE)	1.24
Acropora Tabulate (ACT)	6.61
<b>Non-Acropora</b>	
Coral Encrusting (CE)	0.41
Coral Foliose (CF)	1.65
Coral Massive (CM)	23.97
Coral Submassive (CS)	12.81

It can be seen that the type of coral reef that is most abundant at station 4 is non-Acropora coral massive (solid), with a

percentage of 23.97%, while the least abundant type is non-Acropora coral encrusting (creeping), at 0.41%. An image of coral massive is shown in Figure 3-21.



Figure 3-21: Most abundant coral species at station 4: non-Acropora coral massive (Source: private collection, P. Beralas Pasir)

### 5. Station 5

Station 5 was located to the west of Beralas Pasir Island; this station had a depth of 1.4 metres, with a wide topography of the seabed from the coastline, up to 130 metres into the open sea. The percentage habitat cover at station 5 is shown in Figure 3-22.

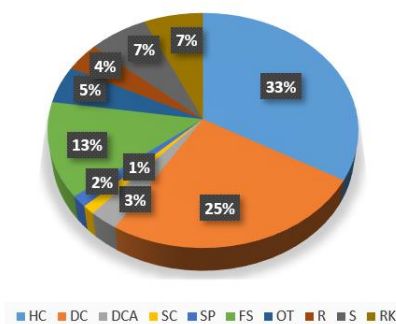


Figure 3-22: Percentage of coral reef cover at station 5

From the results of the ground truth data collection, the percentage of live coral reef cover at the station is 33%, which is in the "medium" category, so it can be said that the condition is quite good. The manager of the Sand Island tourist area said that the location of station 5 was often used for snorkeling, diving, playing kanau or other water

tourism by tourists, as it has calm currents, the water is not too deep, it is located near to Beralas Pasir Island and various types of coral can be found there. The percentage of diversity at station 5 is shown in Table 3-14.

Table 3-14: Percentage of coral reef species diversity at station 5.

Species	(%)
<b>Acropora</b>	
Acropora Digitate (ACD)	3.17
Acropora Submassive (ACS)	5.56
Acropora Tabulate (ACT)	10.71
<b>Non-Acropora</b>	
Coral Encrusting (CE)	4.76
Coral Foliose (CF)	0.79
Coral Massive (CM)	7.14
Coral Mushroom (CMR)	0.4
Coral Submassive (CS)	0.79

It can be seen that the type of coral reef that is most abundant at station 5 is Acropora tabulate (table) coral, with a percentage of 10.71%, while the least abundant type is non-Acropora coral mushroom (mushroom), with a percentage of 0.40%. An image of Acropora tabulate is shown in Figure 3-23.



Figure 3-23: Most abundant coral species at station 5: Acropora tabulate (Source: private collection, P. Beralas Pasir)

### 6. Station 6

Station 6 was located to the west of Beralas Pasir Island, with a sea floor depth of 1.4 metres from the coastline to 170 metres into the open sea. From the results of the ground truth data

collection, the percentage of live coral cover here was 32%, in the "medium" category. The percentage of habitat cover is shown in Figure 3-24.

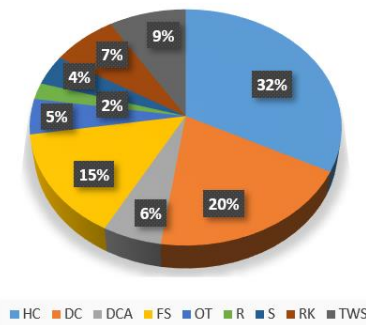


Figure 3-24: Percentage of coral reef cover at station 6

The manager of the Beralas Pasir Island tourist area stated that the location of station 6 was a spot often used for snorkeling, diving, playing kanau or other water tourism by tourists, because the water is calm and not too deep and its location is not too far from Beralas Pasir island and various types of coral near the station. Natural factors that could cause damage to coral at station 6 or even kill it included drupella snails, which are coral reef-eating animals (Figure 3-25). The percentage of diversity at station 6 is shown in Table 3-15.

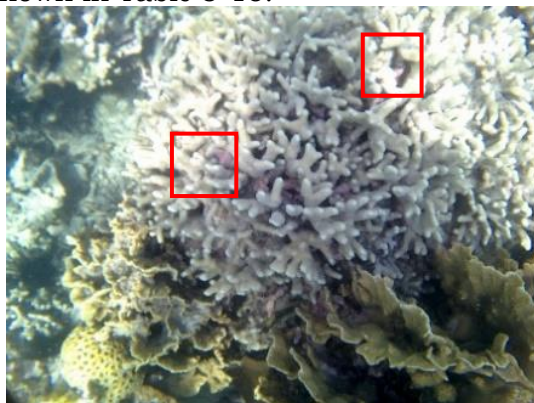


Figure 3-25: Coral-eating Drupella snails (source: private collection, Beralas Pasir Island)

Table 3-15: Percentage of coral reef species diversity at station 6.

Species	(%)
<b>Acropora</b>	
Acropora Digitate (ACD)	4.51
Acropora Encrusting (ACE)	0.82
Acropora Tabulate (ACT)	2.46
<b>Non-Acropora</b>	
Coral Branching (CB)	0.82
Coral Foliose (CF)	4.51
Coral Massive (CM)	13.9
Coral Mushroom (CMR)	0.82
Coral Submassive (CS)	7.79

The type of coral reef that is most abundant at station 6 is non-Acropora coral massive (solid), with a percentage of 13.93%, while the least abundant type is non-Acropora coral mushroom (mushroom), at 0.82% and Acropora encrusting (creeping), also at 0.82%. An image of coral massive is shown in Figure 3-26.



Figure 3-26: Most abundant coral species at station 6: non-Acropora coral massive (Source: private collection, Beralas Pasir Island)

### 7. Station 7

Station 7 was located to the west of the island, with a depth of 4 meters, and a seabed topography sloping from the coastline 230 metres into the open sea. Based on the results of the ground truth data collection, the percentage of live coral reef cover is 35%, which is in the "moderate" category, therefore, the condition is quite good. The percentage habitat cover is shown in Figure 3-27.



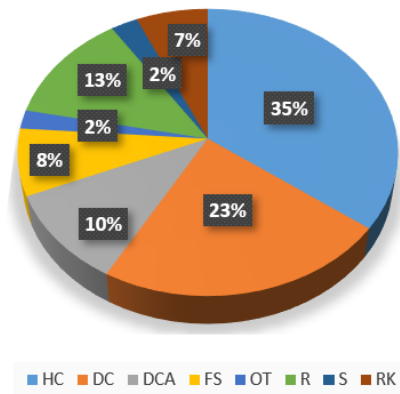


Figure 3-27: Percentage of coral reef cover at station 7

According to the manager of the Beralas Pasir Island tourist area, the location of station 7 is a location that is also often used for snorkeling, diving, playing kanau or other water tourism by tourists. The percentage of diversity at the station is shown in Table 3-16.

Table 3-16: Percentage of coral reef species diversity at station 7.

Species	(%)
<b>Acropora</b>	
Acropora Branching (ACB)	0.42
Acropora Digitate (ACD)	0.42
Acropora Encrusting (ACE)	2.08
Acropora Submassive (ACS)	0.83
Acropora Tabulate (ACT)	3.75
<b>Non-Acropora</b>	
Coral Encrusting (CE)	2.08
Coral Foliose (CF)	5.00
Coral Massive (CM)	16.6
Coral Mushroom (CMR)	0,42
Coral Submassive (CS)	3.33

The type of coral reef that is most abundant at station 7 is non-Acropora coral massive (solid), with a percentage of 16.67%, with the least abundant species, with a percentage of 0.42%, being non-Acropora coral mushroom (mushrooms),

Acropora branching (branching) and Acropora digitate (fingers). An image of coral massive is shown in Figure 3-28.



Figure 3-28: Most abundant coral species at station 7: non-Acropora coral massive (Source: private collection, Beralas Pasir Island)

### 8. Station 8

Station 8 was located to the west of Beralas Pasir Island, at a depth of 4.2 metres, with the topography of the seabed sloping from the coastline 250 meters into the open sea. Based on the results of the ground truth data collection, the percentage of live coral reef cover was 50%, which is in the "good" category. Percentage habitat cover at the station is shown in Figure 3-29, and the percentage of diversity in Table 3-17.

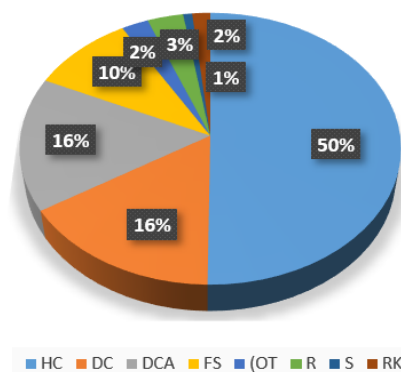


Figure 3-29: Percentage of coral reef cover at station 8

Table 3-17: Percentage of coral reef species diversity at station 8.

Species	(%)
<b>Acropora</b>	
Acropora Digitate (ACD)	1.26
Acropora Encrusting (ACE)	1.26
Acropora Tabulate (ACT)	5.44
<b>Non-Acropora</b>	
Coral Branching (CB)	16.74
Coral Massive (CM)	18.83
Coral Mushroom (CMR)	1.67

The type of coral reef that is most abundant at station 8 is non-Acropora coral massive (solid), with a percentage of 18.83%, and the least abundant species, with a percentage of 0.42%, are Acropora encrusting (creeping) and Acropora digitate (fingers). An image of coral massive is shown in Figure 3-30.



Figure 3-30: Most abundant coral species at station 8: non-Acropora coral massive (Source: private collection, Beralas Pasir Island)

**9. Station 9**

Station 9 was located to the west of Beralas Pasir Island, at a depth of 1.5 metres, with the topography of the seabed sloping from the coastline 250 metres into the open sea. From the ground truth data collection, the percentage of live coral reef

cover was 26%, in the "moderate" category, so it can be said that the condition is damaged. The percentage habitat cover at station 9 is shown in Figure 3-31.

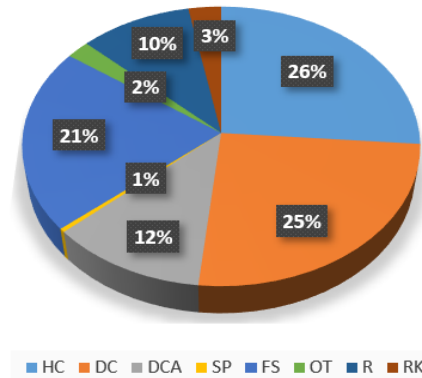


Figure 3-31: Percentage of coral reef cover at station 9

According to the manager of the Beralas Pasir Island tourist area, the location of station 9 is also often used for playing kanau or other water tourism by tourists because the water is calm and not too deep. The percentage of diversity at the station is shown in Table 3-18.

Table 3-18 Percentage of coral reef species diversity at station 9.

Species	(%)
<b>Acropora</b>	
Acropora Digitate (ACD)	0.83
Acropora Encrusting (ACE)	1.25
<b>Non-Acropora</b>	
Coral Foliose (CF)	8.75
Coral Massive (CM)	7.50
Coral Mushroom (CMR)	4.17
Coral Submassive (CS)	3.75

The type of coral reef that is most abundant at station 9 is non-Acropora coral foliose (sheet), at 8.75%, while the least abundant species, with a percentage of 0.42%. An image of coral foliose is shown in Figure 3-32.

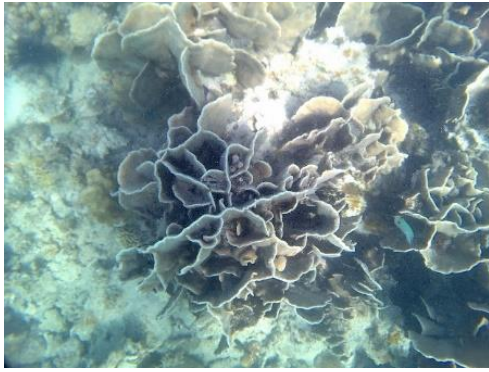


Figure 3-32: Most abundant coral species at station 9: non-Acropora coral foliose (Source: private collection, Beralas Pasir Island)

### 10. Station 10

Station 10 was located to the south of the island, with a depth of 6.5 metres and a sea floor topography sloping from the coastline 350 meters into the open sea. Based on the field data collection, the percentage of live coral reef cover at the station is 50% which is in the "good" category. The percentage of habitat cover is shown in Figure 3-33.

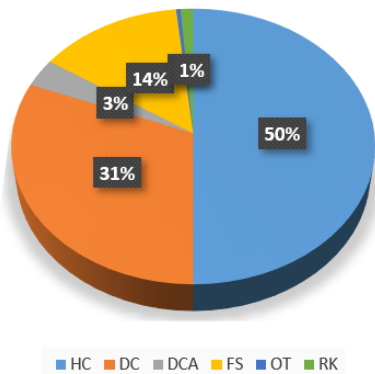


Figure 3-33: Percentage of coral reef cover at station 10

The manager of the Beralas Pasir Island tourist area said the location of station 10 was rarely used for snorkeling or diving by tourists because it had fairly strong currents originating from the east of the island in the Natuna Sea and circulating to the south. The percentage of diversity at station 9 is shown in Table 3-16. Several natural factors have caused damage to the coral reefs in this location, namely the drupella snail, which is a

coral-eating snail, and the algae *Caulerpa racemose*, which lives on coral reefs and can interfere with their growth (Figure 3-34). The percentage of diversity at station 10 is shown in Table 3-19.

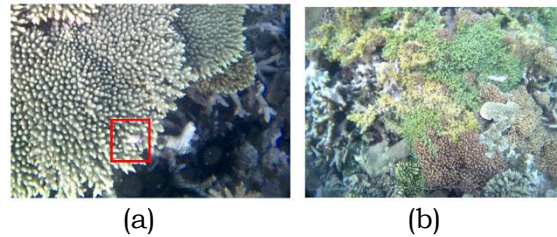


Figure 3-34: (a) coral-eating drupella snail; (b) algae *Caulerpa racemosa* living on the coral (Source: private collection, Beralas Pasir Island)

Table 3-19: Percentage of coral reef species diversity at station 10.

Species	(%)
<b>Acropora</b>	
Acropora Branching (ACB)	4.13
Acropora Digitate (ACD)	0.41
Acropora Encrusting (ACE)	2.07
Acropora Tabulate (ACT)	15.29
<b>Non-Acropora</b>	
Coral Foliose (CF)	2.89
Coral Massive (CM)	4.55
Coral Submassive (CS)	20.66

It can be seen that the type of coral reef that is mostly present at station 10 is non-Acropora coral submassive (dense-bumps), with a percentage of 20.66%, with the least abundant species, with a percentage of 0.42%. An image of coral submassive is shown in Figure 3-35.



Figure 3-35: Most abundant coral species at station 10: non-Acropora coral submassive (Source: private collection, Beralas Pasir Island)

### 3.4 Discussion

#### 1. Changes in the Coral Reef Area between 2011 and 2018

Based on the results of the monitoring research on changes in the area of coral reefs around Beralas Pasir Island using SPOT 4 and SPOT 7 imagery, it can be seen that they experienced a decrease. In 2011, using SPOT 4 images, it was established that the total area of coral reefs was 67,560 hectares, whereas in 2018, using SPOT 7 imagery, the total area of coral reefs was 38,338 hectares, a decline of 29,222 hectares.

#### 2. Condition of Coral Reef Habitat Cover

Based on the results of the research on the condition of coral reef cover around Beralas Pasir Island conducted by Andriaman et al. (2013), the percentage of live coral cover in 2010 was 62.38%, while Sidik et al., (2013) found that in 2013 the percentage of cover was 29-57%, while in 2020 this figure ranged from 26-53%, generally being in the medium category. In this study, the highest percentage of coral cover was at station 3, with a percentage of 53%, and the lowest at station 9, with a percentage of 26%. Based on all the research that has been conducted on Beralas Pasir Island, it can be seen that there has been a decrease in the habitat of living coral. According to our study, one of the factors that has caused this has been the disturbance of natural factors, namely drupella snails, an abundance of *Caulerpa racemose* algae, sea urchins, and the proliferation of seaweed types *Padina* sp. and *Halimeda* sp.

### 4 CONCLUSION

The conclusion from this is that there was a change in the area of coral reef cover between 2011 and 2018, with a fall of 29,222 hectares. The percentage of live coral cover across the stations ranged from 26-53% and was generally in the

medium category. The accuracy rate of the image classification results in the study is 83%, which is in the strong agreement category (strong).

### ACKNOWLEDGEMENTS

We are grateful to LAPAN's Remote Sensing Center, LAPAN Remote Sensing PUSTEKDATA, Ferdy Fitriando Hia, S.T, who accompanied, encouraged and helped me greatly when collecting the ground truth data, Mr. Firman, the tour guide who helped direct us to the research location, Berlas Pasir Island tourism manager Mr. Kewin, who gave permission to conduct research at the tourist sites.

### AUTHOR CONTRIBUTIONS

Monitoring Changes in Coral Reef Habitat Cover on Beralas Pasir Island Using Spot 4 and Spot 7 Imagery from 2011 and 2018. Lead Author: Rosaria Damai, Viv Djanat Prasita, Kuncoro Teguh Setiawan.

### REFERENCES

- Adriaman, A., Purbayanto, S., Budiharso, Damar, A. (2013). Pengaruh Sedimentasi terhadap Terumbu Karang di Kawasan Konservasi Laut Daerah Bintan Timur Kepulauan Riau (The Effect of Sedimentation on Coral Reef in the Marine Conservation Area of East Bintan, Riau Islands). *Berkala Perikanan Terubuk*, 41(1), 90-101.
- Azka, L.M., Mustafa, L.D., Mas'udia, PEM. (2019). Analisis Luasan Terumbu Karang Berdasarkan Pengolahan Data Citra Satelit Landsat 8 Menggunakan Algoritma Lyzenga (Analysis of the Area of Coral Reef based on Landsat 8 Satellite Image Data Processing Using the Algorithm Lyzenga). *Jurnal JARTEL*, 8(1), 13.
- Banko, G. (1998). A Review of Assessing the Accuracy of Classifications of Remotely Sensed Data and of Methods Including Remote Sensing Data in Forest. Austria:



- International Institute for Applied Systems Analysis.
- Pat S. Chavez Jr. (1988). An Improved Dark-Object Substraction Technique Atmosphere Scattering Correction of Multispectral Data. *Remote Sensing of Environment*, 24(3), 459-479.
- Giyanto, Manuputty, AEW., Abrar, M., Siringoringo, RM., Suharti, SR., Wibowo, K., dan Edrus, IN. (2014). Panduan Monitoring Kesehatan Terumbu Karang (Guidance for Monitoring Coral Reef Health). Jakarta: CRITC COREMAP LIPI.
- Giyanto, Abrar, M., Hadi, TA., Budiyanto, Hafiz, M., Salatalohy, A., Iswari, MY. (2017). Status Terumbu Karang Indonesia 2017 (The Status of Indonesia's Coral Reef 2017). COREMAP-CTI Pusat Penelitian Oseanografi-LIPI.
- Irawan, Sasmito, JB., Suprayogi, A. (2017). Pemetaan Sebaran Terumbu Karang dengan Metode Algoritma Lyzenga Secara Temporal Menggunakan Citra Landsat 5, 7 dan 8 (Mapping the Distribution of Coral Reef with the Lyzenga Algorithm Method temporally using Landsat 5, 7 and 8). *Jurnal Geodesi UNDIP*, 6(2), 56-61.
- Jaelani, L.M. (2017). PPT Kalibrasi Radiometrik (Radiometric Calibration). Surabaya. Departemen Teknik Geomatika - ITS.
- Januardi, R., Hartoko, A., Purnomo, P.W. (2016). Analisis Habitat dan Perubahan Luasan Terumbu Karang di Pulau Menjangan Besar, Kepulauan Karimunjawa Menggunakan Citra Satelit (Analysis of Habitat and Changes in the Area of Coral Reef on the Island of Menjangan Besar, Karimunjawa Islands using Satellite Imagery). *Management of Aquatic Resources* (MAQUARES), 5(2),302-310.
- Jensen, J.R. (2005). Introdoction Digital Image Processing: A Remote Sensing Perspective edition 3rd. University of California, California: Prentice Hall.
- Lumbantoruan, L.H. (2017). Kesesuaian dan Daya Dukung Sumberdaya Terumbu Karang untuk Pengembangan Wisata *Snorkeling* dan *Diving* di Pulau Beralas Pasir Desa Teluk Bakau Kabupaten Bintan (Suitability and Carrying Capacity of Coral Reef Resources dor the Development of Snorkeling and Diving Tours on Beralas Pasir Island, Teluk Bakau Village, Bintan Regency.
- Raazy, A.F. (2018). Monitoring Perubahan Tutupan Habitat Terumbu Karang Di Pulau Kapoposang Kepulauan Spermonde (Monitoring Changes in Coral Reef Habitat Cover in Kapoposang Island, Spermonde Islands. Skripsi. Makassar. Universitas Hassanudin.
- Rahmawan, AD., Pawestri, DA., Fakhriyah, RA., Pasha, HDS., Ferryandy, M., Sugandi, D., Ridwana, R., dan Somantri, L. (2020). Penggunaan Metode Unsupervised (ISO Data) untuk Mengkaji Kerapatan Vegetasi di Kecamatan Pangandaraan (The use of Unsupervised (ISO Data) method to Asses the Extent of Vegetation in Pangandaran). *Jurnal Pendidikan Geografi Undiksha*, 8(1), 1-11.
- Sidik, F., Tanjung, A., Elizal. (2013). The Coral Reef Condition In Beralas Pasir Island Waters of Gunung Kijang, Regency Bintan, Riau Island Province.
- Wulansari, H. (2017). Uji Akurasi Klasifikasi Penggunaan Lahan Dengan Menggunakan Metode Defuzzifikasi Maximum Likelihood Berbasis Citra Alos Avnir-2 (Test the Accuracy of Land Use USING Defuzzied Land in Accordance with the Image Based on ALOS Avnir-2).

# MULTITEMPORAL ANALYSIS FOR TROPHIC STATE MAPPING IN BATUR LAKE AT BALI PROVINCE BASED ON HIGH-RESOLUTION PLANETSCOPE IMAGERY

Rahma Nafila Fitri Sabrina<sup>1\*</sup> and Sudaryatno<sup>1</sup>

<sup>1</sup>Department of Geographic Information Science, Faculty of Geography, Universitas Gadjah Mada, Bulaksumur, Yogyakarta 55281, Phone. (0274) 6492340 Fax. (0274) 589595

\*e-mail: rahmanafilafs98@gmail.com

Received: 4 August 2020; Revised: 17 December 2020; Accepted: 21 December 2020

**Abstract.** Remote sensing data for analyzing and evaluating trophic state ecosystem problems seen in Batur Lake is an approach that is suitable for water parameters that cannot be observed terrestrially. As the multitemporal spatial data used in this study were extensive, it was necessary to consider the effectiveness and efficiency of the processing and analysis, therefore R Studio was used as a data processing tool. The research aims to (1) map the trophic state of Batur Lake multitemporally using PlanetScope Imagery ; (2) assess the accuracy of the trophic state model and apply it to another temporal data as a Spatial Big Data; and (3) understand the trophic state impact on the water quality of Batur Lake based on physical factors and the lake's chemical concentration (sulfur concentration). The research shows that the trophic state of Batur Lake is in good condition, with an ultraoligotrophic state as the majority class, based on the mean Trophic State Index (TSI) value of 9.49. The standard errors of each trophic state parameter were 0.010 for total phosphor, 0.609 for chlorophyll-a, and 0.225 for Secchi Disk Transparency (SDT). The multitemporal model demonstrates that the correlation between the increase of trophic state and mass fish death cases in Batur Lake is existent.

Keywords: *Freshwater Lakes, Ultraoligotrophic, TSI Carlson, Sulfur Bursts, Remote Sensing*

## 1 INTRODUCTION

Water is the most important source of life for all organisms on earth and is found in exceptionally large quantities. 70% of the earth's surface is covered by water, of which 97.2% is in the form of oceans/seawater, with 2.15% formed by glaciers and ice, 0.61% by groundwater, 0.009% by freshwater lakes, and the remaining 0.031% by inland seas, soil moisture, the atmosphere and rivers (Nace, 1967). Water is a resource that can be utilized by humans in various sectors, including tourism, agriculture, industry, the environment, and households. Approximately 80% of surface water was used in a home daily basis (NGWA, 2020).

One supply of freshwater is from lakes. At present, many lakes are

experiencing problems due to disruption to the catchment area, which causes the degradation of the lake such as siltation (sedimentation), lake narrowing, growth in the intensity of water hyacinth, decreased water volume, increased lake water temperature, and a decrease in water quality. One of the lakes in Indonesia currently experiencing such ecosystem problems is Lake Batur, located in Kintamani, Bangli Regency, Bali Province. At The 1<sup>st</sup> Conference of National Lakes Indonesia (KNDI I) in 2009, it was declared that Lake Batur was one of the 15 National Priority Lakes (MoE, 2011), meaning the government needed to develop a policy to save it.

Because of the large area of the lake, the use of remote sensing data to analyze

and evaluate its ecosystem problems is a suitable research method that can take into account parameters around the lake that cannot be seen terrestrially. In addition, the method can also accelerate the research process because the required samples are determined according to their level of accuracy. In the studies by Z.Y. Avdan, Kaplan, Goncu, and U. Avdan (2019); Trisakti, Suwargana, and Parsa (2015); Marpaung, Faristyawan, Purwanto, Wikanti, Suhada, Prayogo, and Sitorus (2020); and Arief (2015); it can be seen that remote sensing images can also be used to extract several water quality parameters, for example, electrical conductivity (EC), total dissolved solids (TDS), water transparency, water turbidity, Dissolved Oxygen (DO) concentration, suspended particular matter (SPM) and chlorophyll-a. The expected benefits of this research are in establishing how to map the trophic state of Lake Batur multitemporally by extracting information from PlanetScope Remote Sensing imagery, ascertaining the trophic state effect on Lake Batur water quality conditions, and finding the accuracy level of trophic state modeling using R Studio as a processor for Spatial Big Data. In addition, the study is expected to be used as a reference for similar research in the future.

PlanetScope is high-resolution imagery with a 3 meter spatial resolution produced by Planet Labs Inc. The study used PlanetScope Ortho Scene Lake Batur regional images, covering a total of ten recording dates from 2020 to 2017. Mapping was made using the Carlson Trophic State Index (TSI) method, consisting of three trophic state parameters, namely total phosphorus, chlorophyll-a, and Secchi Disk Transparency (SDT). The model was

obtained from the results of the regression between the field data with pixel values of input band (single band images, band ratios, or Principle Component Analysis (PCA) bands) that have the highest correlation value. The models were performed to the image of the fieldworks time to gain the standard errors of each trophic state and then applied to nine other images using the R Studio application.

The mass fish mortality was the result of a complex process of organic matter accumulation both in the bottom and the water column. In the early stages, due to the accumulation of organic matter on the bottom of the waters, there is a formation of the large anaerobic layer (Garno et al., 1999), followed by the formation of toxic compounds such as  $H_2S$  and  $NH_3$ . Under certain conditions, there will be "turn over" which encourages the rise of a water column that does not contain oxygen (anaerobic) and threatens many fish in net cages (Lukman et al., 2013). This case of mass fish mortality could also be affected by the trophic state of the lake.

## **2 MATERIALS AND METHODOLOGY**

### **2.1 Location and Data**

Lake Batur is located in Kintamani District, Bangli Regency, Bali Province (Figure 2-1). It is in the old caldera of Mount Batur, an active volcano that is subject to the volcanic activity of the Pacific Ring of Fire. Lake Batur is located at Latitude  $8^{\circ}13'-8^{\circ}18'S$  and Longitude  $115^{\circ}22'-115^{\circ}26'E$ , with an elevation of 1,080m above sea level (Radiarta & Sagala, 2012). The area of Lake Batur is  $15.9km^2$ , with a maximum depth of 88m (World Lakes, 2005).

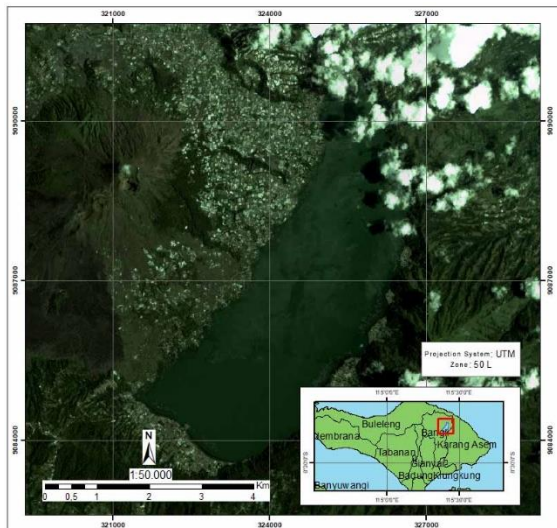


Figure 2-1: Research Location Map (ArcGIS Basemap)

The data used for the research were:

- a. Landuse vector data acquired in March 2018 on Bangli Regency and Karangasem Regency, Bali Province from InaGeoportal opensource,
- b. PlanetScope Lake Batur area 2020 image;
- c. PlanetScope imagery from 2017-2020 (recording dates 13 February 2020, 29 January 2020, 2 September 2019, 25 February 2019, 8 July 2019, 14 November 2018, 2 April 2018, 15 July 2017, 17 April 2017 and 13 March 2017);
- d. River flow vector data acquired in March 2018 on Bangli Regency and Karangasem Regency, Bali Province from InaGeoportal opensource;
- e. Lake Batur boundary vector data acquired from visual interpretation of PlanetScope imagery on January 2020;
- f. Field sample data, field checklist, and laboratory test results of total phosphorus and chlorophyll-a, acquired on 26 February 2020.

## 2.2 Data standardization

River and land use data were obtained from InaGeoportal opensource on Bangli Regency and Karangasem Regency, Bali Province. The river vector data used were in the form of line data, while land use vector data were in the form of polygon data. Lake Batur

boundary vector data were obtained by visual interpretation of the PlanetScope 2019 image of the NIR spectral band, assisted by true color composite from the on-screen digitization results using the ArcGIS software.

The Planet Scope imagery that was used as a reference in determining the sample points, standardized by mosaicking process, masking, and sunglint correction (an image correction process to reduce the error in image spectral values caused by wavy water surfaces as a result of tide or water current effects (Hedley et al., 2005)). In addition, processing with spectral band maths was conducted to obtain an index value that represented the level of each parameter determining the trophic state. The image mosaic process was performed to combine several scenes covering the study area. The process employed ENVI 5.1 software to produce image scenes that covered the entire Lake Batur area. Transformation of PlanetScope imagery to produce images with index values that represent the level of each parameter include SDT (Secchi Disk Transparency), chlorophyll-a content, and total phosphorus, refers to the regression results obtained by Musfiroh (2019), assuming that the resulting accuracy was in accordance with standards for being able to produce sample map.

## 2.3 Methods

The sample point was based on the results of the transformation of TSI with PlanetScope imagery in February 2020. The transect sampling method was used to determine the sample point at intervals of 1 km and covered the whole class of TSI transformation. Field activities were conducted to collect water samples of total phosphorus and chlorophyll-a for laboratory testing, as well as the measurement of in situ data such as SDT



and a dataset obtained with a water quality checker (WQC) tool.

The correlation test is a statistical technique used to test the presence or absence of a relationship, and the direction of the relationship, between two or more variables (Sami'an, 2008). The extent of the relationship between these variables is expressed as a correlation coefficient, with a value between -1, 0, and +1. A strong relationship is expressed by -1 and +1, whereas if each of the variables has no relationship at all, then the correlation coefficient is 0. The correlation sought in this study was the relationship between the independent variable, in the form of image pixel values, and the dependent variables, in the form of total phosphorus concentration, chlorophyll-a concentration, and SDT value. A correlation test for each parameter was performed using the bootstrap method in the IBM SPSS 24 application. This process used 14 sample models with four single PlanetScope spectral bands, 12 band ratios, and 16 Principal Component bands to be tested. The input spectral bands were considered significant and passed the correlation test if the lower and upper bootstrap values had values not equal to 0. If the bootstrap had a negative lower and a positive upper value, or otherwise, there was a possible relationship between the two variables with a determinant coefficient of 0, or no relationship at all, it could be determined that the input spectral band did not pass the correlation test.

Regression analysis aims to find the factors that might influence trophic state distribution. This study was conducted to produce a regression equation for each parameter, which was then used to model the estimated trophic state level of Lake Batur. The analysis was performed by

regressing every single input spectral band with the value of each independent variable (total phosphorus, chlorophyll-a, and SDT) value. The best regression of the input spectral band was then used to model the value of Carlson's TSI parameters.

The TSI value was calculated using an algorithm developed by Carlson (1977), which uses three parameters as its variables, namely the total values of phosphorus, chlorophyll-a, and water clarity. These were obtained from the results of the remote sensing data extraction recorded at the same time as the field activities in February 2020. The calculation results were then divided into seven classes according to the lake trophic state classification categories based on Carlson's Trophic State Index shown in Table 2-1.

Table 2-1: Lake Trophic State Classification

TSI Value	Trophic State
>30	Ultraligotrophic
30-40	Oligotrophic
40-50	Mesotrophic
50-60	Mild Eutrophic
60-70	Moderate Eutrophic
70-80	Heavy Eutrophic
>80	Hypereutrophic

Source: Laksitaningrum et al. (2017)

Accuracy tests were conducted based on RMSE (Root Mean Square Error) to assess the difference between the field data used for the regression and those that were not. The lower the RMSE value, the lower the deviation or shift in the value of each parameter. The RMSE value was obtained from the standard error estimation algorithm as follows:

$$\delta_{est} = \sqrt{\frac{\sum(Y - Y')^2}{N - 2}} \quad (2-1)$$

$\delta_{est}$  = Standard error of estimation

- Y = Field measurement results  
 Y' = Estimated results  
 N = Sample count

The multitemporal data modeling aimed to obtain Lake Batur trophic state information multitemporally using big data from nine recording dates of PlanetScope images, with modeling used for the field regression imagery. The R scripts used before PCA were used for image cropping processing, image masking, and band ratio calculations. R Studio processing after PCA was performed to model the image of the PCA results in order to obtain information on the distribution of trophic state parameters used for the Carlson TSI transformation. In this process, a CTSI classification plot image was obtained from the three parameters and the final result of Carlson TSI image processing.

The multitemporal analysis was made by taking into account the TSI value graph obtained from each sample point in the complete image of the trophic state modeling results using R Studio within a 3 year period of the PlanetScope image being acquired. The resulting graph was then analyzed by considering the incidence of sulfur bursts (dead fish masses) and drought cases that had occurred in Lake Batur based on information from media news.

### 3 RESULTS AND DISCUSSION

The Planet Scope imagery used consisted of a total of ten acquisition dates, 13 February and 29 January 2020; 2 September, 25 February, and 8 July 2019; 14 November and 2 April 2018; and 15 July, 17 April, and 13 March on 2017. The PlanetScope imagery acquired on 29 January 2020 was used for the TSI transformed pre-field image, and imagery acquired 13 February 2020 was used for mapping the trophic state was from 13 February 2020. The chosen imagery was

considered based on the availability of qualifying PlanetScope images with minimal cloud cover and area coverage completeness.

The distribution of the sample points using the transect sample method had interval distances between each sample of 1 km (Figure 3-1). Field testing including water sampling and collection of in-situ data was performed on February 26, 2020. A total of 20 samples were obtained, with a composition of 15 model samples and five validation samples. Water sampling was divided into two types, namely the total phosphorus sample and the chlorophyll-a sample. The sampling was conducted simultaneously at each predetermined sample point.

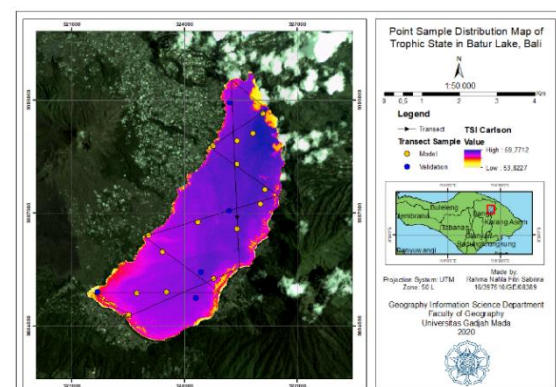


Figure 3-1: Map of Distribution of Final Field Sample Points for Lake Batur Trophic State (Data Processing, 2020)

Other in-situ water parameters obtained in the field activities besides SDT data were temperature, pH, salinity, TDS, and conductivity. The temperature of the water sample increased during sunny weather and around 12.00 when the sun was directly above, but decreased when it was rainy. Water pH tended to have a constant high value of around 8.5 and up to 8.8. Salinity, TDS, and conductivity value had an alteration quantity due to the precipitation during the fieldwork. Salinity content was very low at 1.1 to 1.3 ppt, with electrical conductivity ranging from 1776 to 1883  $\mu\text{S}/\text{cm}$  and TDS from 1.16 to 1.34 ppt.

Statistical analysis was performed so that the value and accuracy of the modeling could be accounted for. The analysis included a bootstrap test, correlation test, and regression test. Otherwise, Principal Component Analysis (PCA) process and band ratios statistical analysis is also applied to the images for analyzing the spectral pixel bands value in conjunction with each single PlanetScope Imagery band.

A description of the correlation for each parameter with pixel values that passed the bootstrap test can be seen in Tables 3-1 to 3-3. The PC number refers to the order of the PCA processing result.

Table 3-1: Correlation Test of Total Phosphorus

Band	Correlation	Bootstrap Value	
		Lower	Upper
PC3	0.530	0.047	0.857
PC7	-0.302	-0.623	-0.110
PC11	-0.311	-0.600	-0.149
PC14	-0.356	-0.672	-0.212

Source: Data Processing, 2020

Table 3-2: Correlation Test of Chlorophyll-a

Band	Correlation	Bootstrap Value	
		Lower	Upper
PC14	0.843	0.129	0.966

Source: Data Processing, 2020

Table 3-3: Correlation Test of Secchi Disk Transparency

Band	Correlation	Bootstrap Value	
		Lower	Upper
PC11	0.579	0.431	0.945
PC15	-0.342	0.896	-0.154

Source: Data Processing, 2020

Regression analysis was performed to determine the factors that might influence the distribution of the trophic state parameters. In this study, it was conducted to produce a regression model or equation for each parameter, which was then used to model the estimated trophic state class of Lake Batur. The analysis was made by regressing the input band (single band, band ratio, or PC band) with the value of each dependent variable (total phosphorus, chlorophyll-a, and SDT values).

Total phosphorus regression analysis was applied to the band that had the best (highest) correlation value, namely PC3. The coefficient determination ( $R^2$ ) was obtained from the scatter plot between the pixel value and the 14 total phosphorus values in the field. The  $R^2$  was equal to 0.281. This value was low, being strongly influenced by the overall phosphorus data, with the majority of the values being 0.01 mg/l. The formula obtained with the help of Microsoft Excel to make the model was  $y = 0.0004x + 0.018$ , where  $y$  is the total image of phosphorus transformed and  $x$  is the PC3 band. The minimum value of the image pixels was -0.193, and the maximum was 1.06, with an average value of 0.018. Noise or interference contained in the pixels, such as background images, pixels damaged by transformation, error correction, or noise that did originate from the initial PlanetScope imagery from both sensors and atmospheric effects, greatly affected the results of the transformation.

Chlorophyll-a regression analysis was applied to the spectral band that had the highest correlation value, namely PC14. A model that could represent the chlorophyll-a parameter with the independent variable was this band. The coefficient of determination resulting from the regression was 0.710. The combined coefficients that produced the model-making formula were  $y = 2143.145x + 0.767$ , where  $y$  is the image of the transformed chlorophyll-a and  $x$  the PC14 band. The minimum value of the image pixels was -31.67, with a maximum value of 135.90, and an average of 0.767.

SDT regression analysis was also applied to the spectral band that had the highest correlation value, namely PC11. The result of this regression analysis led to two models that could represent the SDT parameter, with the suitable variables being the PC11 and PC7 bands.

The first model of this regression had a coefficient of determination of 0.335, while that of the second was 0.703. The model used for mapping the distribution of SDT was that which had the highest coefficient value, namely the second. The combined coefficients that produced the formula for constructing the second model were  $y = 105.568x_1 + 459.664x_2 + 1.419$ , where  $y$  was the transformed image of *Secchi Disk*,  $x_1$  was the PC7 band, and  $x_2$  was the PC11 band. The minimum image pixel value was -248.79, the maximum 26.59, with an average value of 1.42.

Lake Batur trophic state mapping was performed to obtain information about the distribution of trophic state classes with the Carlson TSI index. The results of the total phosphorus distribution obtained from the previous modeling were converted using equation  $TSI-TP = 14.42 \times \ln [TP] + 4.15$ , where  $[TP]$  is the input spectral band resulting from the distribution of all the phosphorus parameters. The total trophic state in the overall Lake Batur area (Figure 3-2) shows that the lake was in the ultraoligotrophic class, which is characterized by a dark green shading shown in Figure 3-2 that almost covers the whole lake area. As for the locations shown in white, this indicates that in these areas the TSI value could not be visualized because it was not classified in the seven classes. The low TSI class of total phosphorus was proportional to the total value of phosphorus in Lake Batur, which was also relatively low, in the range of 0.01 mg/l to 0.082 mg/l. The maximum TSI value for total phosphorus was only 5.

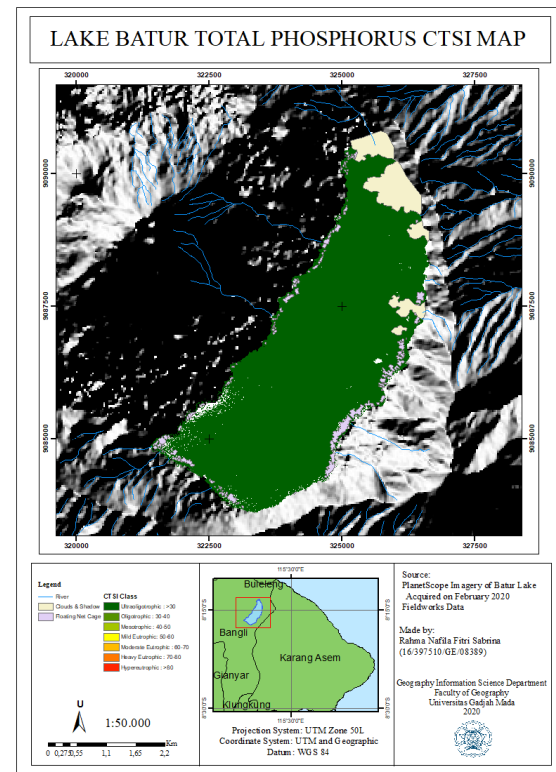


Figure 3-2: Map of Lake Batur Total Phosphorus CTSI (Data Processing, 2020)

The Lake Batur chlorophyll-a TSI class was dominated by the ultraoligotrophic and oligotrophic classes. The results of the chlorophyll-a distribution obtained from the previous modeling were converted using the equation  $TSI-Chl-a = 30.6 + 9.81 \times \ln [Chl-a]$ , where  $[Chl-a]$  is the input spectral band (resulting from the distribution of the chlorophyll-a parameter). The chlorophyll-a trophic state class as shown in Figure 3-3, at the edge of Lake Batur and in the middle of the lake, had a lower class compared to the edge of the lake. In the area where floating net cages were built, most of the water was in the oligotrophic CTSI class with a TSI value of 30-40, shown in green in Figure 3-3. The ultraoligotrophic class which had a TSI value of less than 30 was spread in the central and southern parts of the lake.

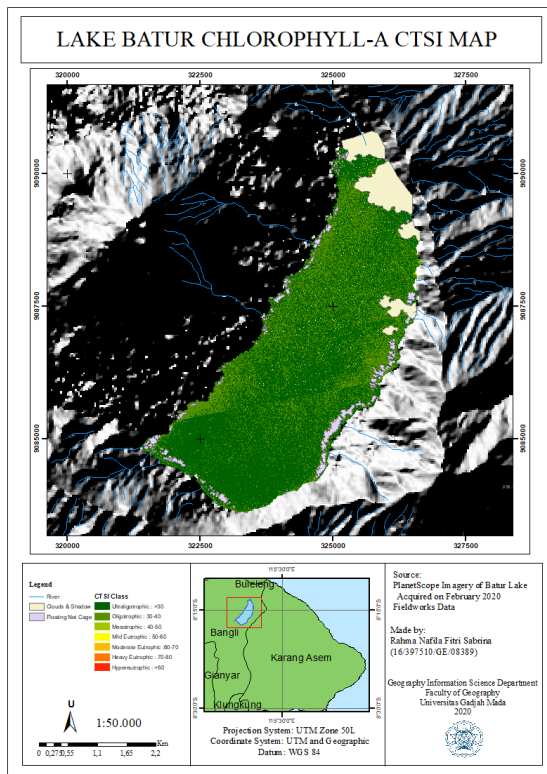


Figure 3-3: Map of Lake Batur Chlorophyll-a CTSI (Data Processing, 2020)

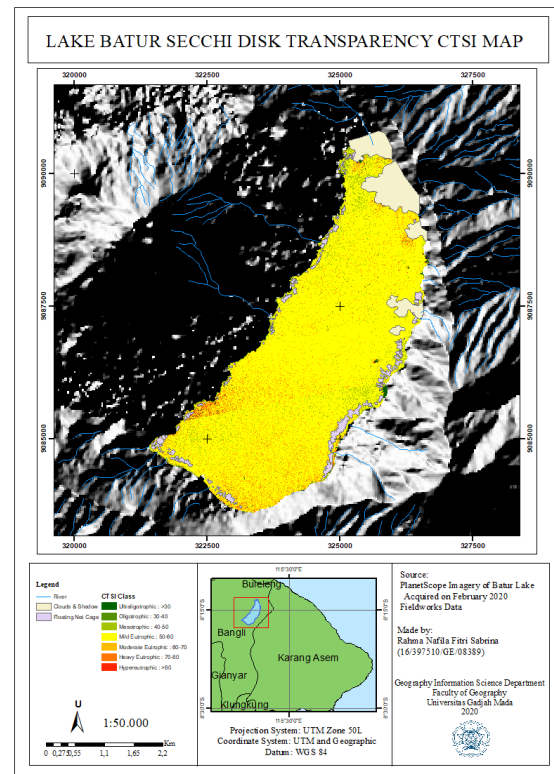


Figure 3-4: Map of Lake Batur Secchi Disk Transparency CTSI (Data Processing, 2020)

The results of the SDT parameter distribution obtained from the previous model were converted using equation  $TSI-SD = 60 - 14.41 \times \ln [\text{Secchi}]$ , where [Secchi] is the input band (layer input of the SDT parameter distribution results). The TSI of the SDT Lake Batur class (Figure 3-4) was dominated by mild eutrophic, moderate eutrophic, and mesotrophic classes. In the area where the floating net cages were built, the distribution of the trophic state was low, namely the mesotrophic class symbolized by light green pixels around the edge of the lake near the floating net cages in Songan A Village. As for classes that had high TSI values, such as moderate eutrophic and heavy eutrophic, these were scattered around the floating cages in the southwestern part of the lake. The varied distribution of SDT eutrophication classes spread throughout the lake shows that the presence of the floating net cages did not greatly affect the quality of the lake waters in terms of its SDT trophic state.

The results of the distribution of the trophic state class estimates with the Carlson TSI index were obtained by calculating the average of the three CTSI maps previously produced. Each layer was converted by using the Carlson TSI equation,  $TSI = [(TSI - TP) + (TSI - Chl a) + (TSI - SD)] / 3$ . The trophic state class with the Lake Batur TSI Carlson index was dominated by the ultraoligotrophic class, as shown in Figure 3-5. However, overall the condition of Lake Batur could be categorized as not experiencing eutrophication, with an ultraoligotrophic class area covering an area of 12.07 km<sup>2</sup> and an average TSI value of 9.49 (Figure 3-5). Even though this Carlson TSI class shows that lake water fertility was relatively low, if it were left continuously subject to human activity and high floating net cage production without any attempt to improve the quality of the water, this could lead to algae blooming, as occurred in Lake Maninjau (Yulianto, 2017).



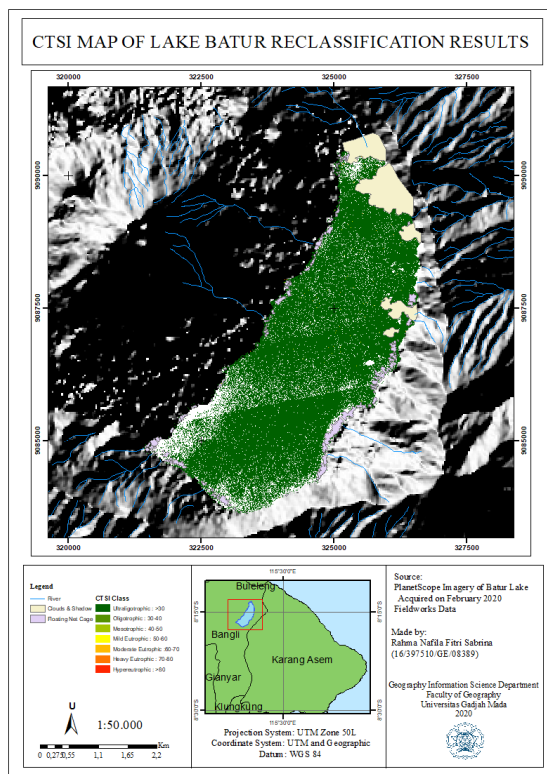


Figure 3-5: CTSI Map of Lake Batur Reclassification Results (Data Processing, 2020)

Accuracy assessment was conducted to assess the difference between the field data used for regression and the transformed images used for estimating the distribution of the trophic state parameters. The method used for this was based on RMSE (Root Mean Square Error).

The accuracy assessment for the parameters of total phosphorus was made by testing the image of the transformation of PC3 for modeling total phosphorus using three validation samples. The resulting standard error was 0.010, while the estimated value of the image (RMSE) had an error probability of 0.010 mg/l. The accuracy of this modeling had a maximum value of 76.97% and a minimum of -65.79%. This accuracy value showed a very large error, which exceeded the negative linear level of percent.

The accuracy test for the chlorophyll-a parameter was conducted by testing the image of the transformation of PC14 for modeling chlorophyll-a using

three validation samples. The resulting standard error was 0.609, while the estimated value of the image (RMSE) had an error probability of 0.609 mg/m<sup>3</sup>. The accuracy of this modeling had a maximum value of 47.74% and a minimum of -30.19%. This accuracy value also displayed a large error, as seen from the minimum value which exceeds a negative linear level and a maximum value that is still below 50%, but better than the accuracy of the total phosphorus parameter content.

Accuracy assessment for the SDT parameters was made by examining the image of the transformation results of PC7 and PC11 for modeling SDT using four validation samples. The resulting standard error was 0.224, while the estimated value of the image (RMSE) had an error probability of 0.609 mg/m<sup>3</sup>. The accuracy of this modeling had a maximum value of 83.34% and a minimum of 82.42%. This accuracy value shows a small error and very good accuracy, with the accuracy value exceeding 70%.

The multitemporal data modeling aimed to obtain Lake Batur trophic state information multitemporally using big data from nine PlanetScope Imagery acquisition dates and modeling used for the imagery of 13 February 2020. The model show the level trophic state of 1 to 7, where 1 was ultraoligotrophic, 2 was oligotrophic, 3 was mesotrophic, 4 was mild eutrophic, 5 was moderate eutrophic, 6 was heavy eutrophic, and 7 was hypereutrophic.

The value obtained of the distribution of the trophic state of the total phosphorus in Figure 3-6 was dominated by ultraoligotrophic classes, but with different distributions. This can be seen from the values shown in the legend, which only rise to class 1, with other areas unclassified. This trophic

state class was in the same class on all dates, but with different distributions.

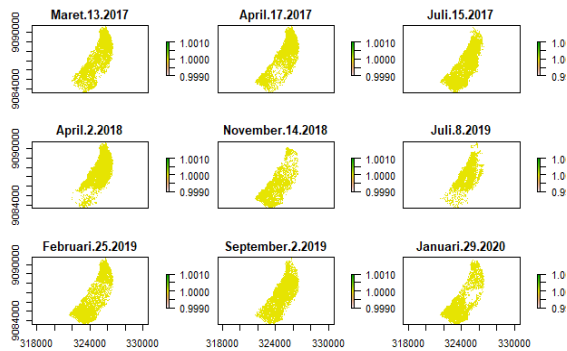


Figure 3-6: Plot Map Distribution of Total Phosphorus Trophic State (Data Processing, 2020)

The distribution values of the chlorophyll-a trophic state classes are dominated by ultraoligotrophic and oligotrophic classes. In Figure 3-7, it can be seen that the trophic state of the chlorophyll-a class was quite low in the trophic state class; i.e., in the ultraoligotrophic to mild eutrophic classes. This can be seen from the chlorophyll-a value, which tended to be low in the Lake Batur area. However, it is shown that in some parts of the lake there are signs of mild eutrophication. Figure 3-7 shows that the oligotrophic state displayed a spreading distribution over the whole lake during the wet season (Dec-Feb). On the other hand, in the dry season (May-Aug) the trophic state declined.

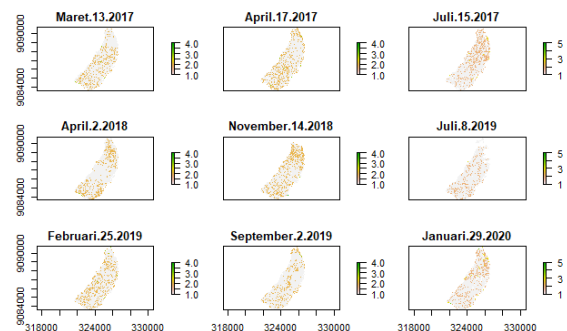


Figure 3-7: Plot Map Distribution of Chlorophyll-a Trophic State (Data Processing, 2020)

The distribution value of the TSI Carlson of SDT is dominated by mild eutrophic classes. In Figure 3-8, it can be

seen that the SDT trophic state class was at various levels, namely from the ultraoligotrophic class to the hypereutrophic class. However, in some locations there were some parts of the lake showed signs of severe eutrophication, and some were still in the mesotrophic class. The highest classes were generally located in the north, which could be due to the mining of sand in Songan A Village (Nada et al., 2017). The distribution of SDT trophic state classes on each recording date shows a high distribution, especially in July 2017, November 2018, July 2019, and January 2020. On the other hand, the lowest classes were in March 2017 and September 2019. Figure 3-8 shows that the ultraoligotrophic, oligotrophic, and to a low extent the mesotrophic states displayed a spreading distribution over a whole lake during the wet season (Dec-Feb). On the other hand, in the dry season (May-Aug) the trophic state increased into eutrophication.

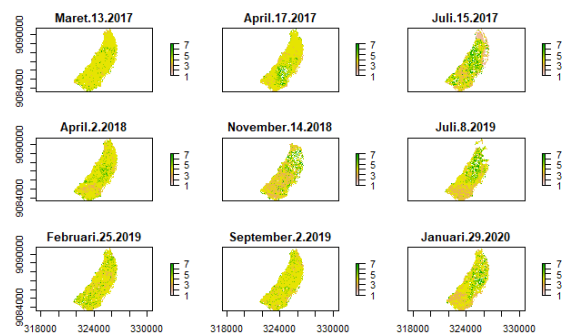


Figure 3-8: Plot Map Distribution of SDT Trophic State (Data Processing, 2020)

From Figure 3-9, it can be seen that Lake Batur was at various trophic state class levels, namely from the ultraoligotrophic class to the mild eutrophic class, but that in November 2018 and September 2019 it was in the lowest trophic state class, the oligotrophic. The distribution of Lake Batur trophic state classes on each recording date shows an increase in distribution in April 2017, July 2019, and January 2020,

whereas a decline occurred in November 2018 and September 2019. There was no difference between each season in the trophic state distribution of Batur Lake.

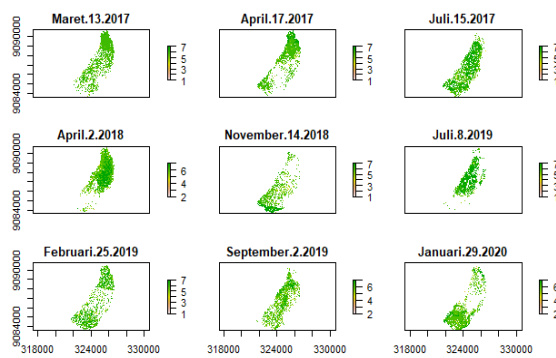


Figure 3-9: Plot Map Distribution Lake Batur Trophic State (Data Processing, 2020)

The CTSI graph in Figure 3-10 was produced from the data representation of the average TSI value of each mapped parameter, as well as the total TSI final results. There were fluctuations in the average trophic state index on each date within the three years from 1 March 2017 to 1 December 2019. The graph was then linked to events in Lake Batur, namely fish mortality and drought. Fish deaths occurred on 13 July 2019, 13 March 2018, 13 July 2017, and 7 February 2017, and took place almost every year, encouraged by the volcanic activity of Mount Batur, with sulfur bursts at the bottom of the lake. The use and management of land around the lake could also be a factor having a big impact on the problems of sedimentation and the mass death of fish, especially the high intensity of the use of organic fertilizers, resulting in very high sedimentation rates caused by runoff during the rainy season. Mass fish mortality is shown by dark blue vertical lines and the drought which occurred on 19 August 2019 is shown by a green vertical line.

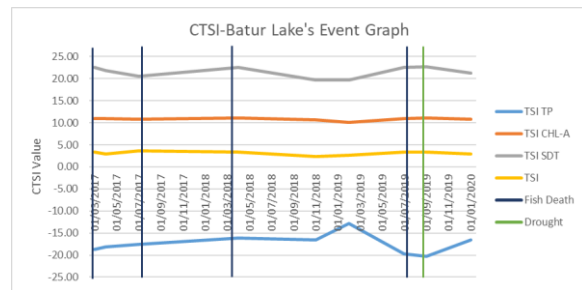


Figure 3-10: Graph of fluctuation in CTSI value affected by Lake Batur's Event (Data Processing, 2020)

The increase of the trophic state index was followed by a decline that occurred on dates of mass fish deaths. The fluctuation's line near the date of the mass fish mortality tends to show the peak of the trend. This can be seen that the peak approaches almost every line of the conjunction between the occurrence of sulfur bursts (mass fish deaths) and the CTSI values. This is comparable with the possibility of volcanic eruptions, which also increase the trophic state, or it could also be affected by poor handling of the floating net cages. The *Beggiatoa* bacteria which are generally located in fresh water and the mud layer of the lake when sulfide concentrations increase can oxidize the sulfur contained in the lake's bedrock in the form of sulfides, with the help of the nitrates stored in its vacuoles (Dodds & Whiles, 1958).

The increase in the TSI class also occurred during the lake drought event, when the peak of the chart trend was on the date of the drought. This may have occurred due to the presence of mixed sediments, which could increase the turbidity of the lake water when overflow occurred after the drought. The plants that were planted when the land width increased on the border of the lake could affect the levels of phosphorus from fertilizers and chlorophyll-a from the plants.

#### 4 CONCLUSION

Batur Lake trophic state classes were mapped with PlanetScope images in



February 2020, resulting in ultraoligotrophic trophic states, with an average TSI value of 9.49. TSI SDT achieved the highest accuracy, of 83.36%, while the highest accuracy of the parameters of total phosphorus and chlorophyll-a were -65.79% and 76.97% respectively. The increase in the trophic state of Batur Lake was triggered by sulphur bursts at the bottom of the lake as well as by bacteria that can oxidise sulfur using nitrate nutrients, facts based on the graph (Figure 3-10) of the relationship between mass dead fish (sulfur bursts) and drought, and the CTSI values in Lake Batur.

### ACKNOWLEDGEMENTS

The authors would like to thank Dr. Sudaryatno, M. Si., as the research adviser, and the contributors Dr. Pramaditya Wicaksono, S.Si, M.Sc. and Dr. Mohammad Pramono Hadi, M.Sc. for their suggestions which helped the research to be completed. We are grateful to the Department of Geographic Information Science, UGM, which supported the study. We would also like to thank the reviewers and Dr. M. Rokhis Khomarudin from the Indonesian National Institute of Aeronautics and Space (LAPAN) for their comments and suggestions for improving the paper.

### AUTHOR CONTRIBUTIONS

Multitemporal Analysis For Trophic State Mapping in Batur Lake at Bali Province Based on High-Resolution PlanetScope Imagery. Lead author: Rahma Nafila Fitri Sabrina, Co-Author: Sudaryatno.

### REFERENCES

Arief, M. (2015). Development of Dissolved Oxygen Concentration Extraction Model Using Landsat Data Case Study: Ringgung Coastal Waters. *International Journal of Remote Sensing and Earth Sciences* 12(1), 1-12.

- Avdan, Z.Y., Kaplan, G., Goncu, S., & Avdan, U. (2019) Monitoring the Water Quality of Small Water Bodies Using High-Resolution Remote Sensing Data. *International Journal of Geo-Information* 8(553), 1-12
- Carlson, R.E. (1977). A trophic state index for lakes. *Limnology and Oceanography* 22(2), 361-369.
- Dodds, W.K., & Whiles, M.R. (1958). *Freshwater Ecology: Concepts and Environmental Applications of Limnology* (2nd edition). London: Elsevier.
- Garno, Y.S. & Adibroto, T.A. (1999). Dampak Penggemukan Ikan di Badan Air Waduk Multiguna pada Kualitas Air dan Potensi Waduk [Impact of Fish Fattening in Water Body Multipurpose Reservoir on Water Quality and Reservoir Potential]. *Prosiding Semiloka Nasional Pengelolaan dan Pemanfaatan Danau dan Waduk*. IPB-Ditjen Pengairan - Men KLH. XVII: 1-10.
- Hedley, J.D., Harborne, A.R., Mumby, P.J. (2005). Simple and Robust Removal of Sun Glint for Mapping Shallow-Water Benthos. *International Journal of Remote Sensing* 26(10), 2107-2112.
- Laksitaningrum, K.W., Widyatmanti, W., & Gunawan, T. (2017). Applications of Landsat 8 OLI Image for Identification of Status Trophic Gajah Mungkur Wonogiri Reservoir, Central Java, Indonesia. *Majalah Ilmiah Globe* 19(2), 113-122
- Lukman, Sutrisno, & Hamdani, A. (2013). Pengamatan Pola Stratifikasi di Danau Maninjau Sebagai Potensi Tubo Belerang [Observation of Stratification Patterns in Lake Maninjau as Potential Tubo Sulfur]. *Jurnal Limnotek* 20(2), 129-140
- Marpaung, S., Faristyawan, R., Purwanto, A.D., Wikanti, A., Suhada, A.G., Prayogo, T., & Sitorus, J. (2020). Analysis of Water Productivity in the Banda Sea Based on Remote Sensing Satellite Data. *International Journal of Remote Sensing and Earth Sciences* 17(1), 25-34.

- MoE. (2011). Profile 15 Lake National Priorities 2010-2014. Ministry of Environment (In Indonesian).
- Musfiroh, Z. (2019). Aplikasi Citra PlanetScope untuk Pemetaan Status Trofik Waduk Cirata, Jawa Barat [The Application of Planetscope Imagery to Mapping Out The Trophic State of Cirata Reservoir, West Java]. Undergraduate Thesis, Universitas Gadjah Mada.
- Nace, R.L. (1967), *Are We Running Out of Water ?* U.S. Geological Survey, National Center, Reston.
- Nada, I.M., Suryatmaja, I.B., & Wiswasta, I.G.N.A. (2017). Community Based Lake Sedimentation Mitigation Model on Bali Island. *Jurnal Bumi Lestari* 17(2):100-117
- NGWA. (2020). *Groundwater- Information on Earth's Water*. <https://www.ngwa.org/what-is-groundwater/About-groundwater/information-on-earths-water>. Accessed 16 November 2020
- Radiarta, I.N, & Sagala, S.L. (2012) Spatial Model of Aquatic Fertility in Lake Batur, Bangli Regency, Bali Province with Geographic Information System Applications. *Journal of Aquaculture Research* 7(3), 499-508
- Sami'an. (2008). *SPSS Correlation & Regression*. Available via PDF.<https://fdokumen.com/document/spss-correlation-regresi-statistics-easurement-nbsp.pdf>.html of subordinate document. Accessed 28 November 2019
- Trisakti, B., Suwargana, N., & Parsa, I.M. (2015). Water Clarity Mapping in Kerinci and Tondano Lake Waters Using Landsat 8 Data. *International Journal of Remote Sensing and Earth Sciences* 12(2), 117–124.
- LakeNet. (2005). *Batur Lake*. Available via post. <http://www.worldlakes.org/lakedetails.asp?lakeid=10> of subordinate document. Accessed 23 June 2020.
- Yulianto, A. (2017). Kondisi Danau Maninjau Alami Eutrofikasi Berat [Lake Maninjau Conditions Severe Eutrophication]. Available via REPUBLIKA <https://republika.co.id/berita/nasional/daerah/17/02/05/okwcfw396-kondisi-danau-maninjau-alami-eutrofik-berat>. Accessed 20 June 2020



# MONITORING MODEL OF LAND COVER CHANGE FOR THE INDICATION OF DEVEGETATION AND REVEGETATION USING SENTINEL-2

Samsul Arifin<sup>1\*</sup>, Tatik Kartika<sup>1</sup>, Dede Dirgahayu<sup>1</sup>, and Gatot Nugroho<sup>1</sup>

<sup>1</sup>Remote Sensing Applications Center – National Institute of Aeronautics and Space (LAPAN)

\*e-mail: samsul\_lapan@yahoo.com

Received: 11 August 2020; Revised: 17 December 2020; Approved: 21 December 2020

**Abstract.** Information on land cover change is very important for various purposes, including the monitoring of changes for environmental sustainability. The objective of this study is to create a monitoring model of land cover change for the indication of devegetation and revegetation using data from Sentinel-2 from 2017 to 2018 of the Brantas watershed. This is one of the priority watersheds in Indonesia, so it is necessary to observe changes in its environment, including land cover change. Such change can be detected using remote sensing data. The method used is a hybrid between Normalized Difference Vegetation Index (NDVI) and Normalized Burn Ratio (NBR) which aims to detect land changes with a focus on devegetation and revegetation by determining the threshold value for vegetation index ( $\Delta$ NDVI) and open land index ( $\Delta$ NBR). The study found that the best thresholds to detect revegetation were  $\Delta$ NDVI > 0.0309 and  $\Delta$ NBR < 0.0176 and to detect devegetation  $\Delta$ NDVI < - 0.0206 and  $\Delta$ NBR > 0.0314. It is concluded that Sentinel-2 data can be used to monitor land changes indicating devegetation and revegetation with established NDVI and NBR threshold conditions.

Keywords: *Model, Monitoring, Land Cover, Sentinel-2, devegetation, revegetation*

## 1 INTRODUCTION

Geobiophysics is one of the parameters for determining the phenomenon of land surface change. It has been applied by several researchers using the vegetation index and open/burned land index from optical satellite data. The vegetation index describes the level of greenness of plants, using a mathematical combination of the red band and NIR (Near-Infrared) band (Lillesand & Kiefe, 1997). According to Ryan (1997), the calculation of the Normalized Difference Vegetation Index (NDVI) is based on the principle that green plants grow very effectively by absorbing radiation in the red spectrum region of Photosynthetic Active Radiation (PAR), and strongly reflect sunlight from the infrared region close to the range value indices -1 to 1. The vegetation index has been used in numerous studies on a global

scale of vegetation and to map drought, devegetation and deforestation (Horning, Juli. Robinson, Eleanor Sterling, Turner, and Spector, 2010; Kartika et al., 2018). Determination of the extraction of forest identification geobiophysical parameters can be made using the NDVI model with a threshold value with SATELIT LAPAN -3 data (Arifin, S., Kartika, T., & Carolita, I., 2019).

In general, NDVI with a combination of red and infrared specimens is an index that is widely used to identify signs of burning land (Chuvienco, E., Martin, M.P., & Palacios, A., 2002., 2002). In addition, there have been many developments in the method of identifying burnt land/forests through the single band method (Near IR, Mid IR, Spectral thermal temperature Brightness) and the ratio band vegetation index. Research on the detection of burnt land has been widely conducted globally

using low to medium resolution remote sensing satellite data, such as that from MODIS ( Martín M.P., & Díaz-Delgado R., 2002; Roy, D.P, Boschettm, L., & Triffm, S.N., 2002; Chuvieco et al., 2005); from NOAA-AVHRR (Barbosa, P.M., Pereira, J.M.C., & Grégoire, J. M., 1998); Nielsen, T.T., Mbow, C., & Kane R., 2002);; Nielsen et al., 2002); and from SPOT VEGETATION (Silva, J.M.N, Cadima, J.F.C.L., Pereira, J.M.C. M. Grégoire., 2004). This study aims to map mangrove density in Arakan village and to determine the best NDVI results from the band combination used (Philiani, I, Saputra, L, Harvianto, L., & Muzaki, A.A., 2016). However, it should be noted that low and medium resolution data cannot detect burnt areas of less than 25 ha well (Miettinen, 2007). NDVI, the Normalized Burn Ratio (NBR), Soil-adjusted Vegetation Index (SAVI), Modified Soil-Adjusted Vegetation Index (MSAVI), and multivariate component (Principle Component Analysis, Tasseled Cap-greenness, Tasseled Cap-wetness) (Escuin, 2007) will be compared by the calculation of field data using the Composite Burn Index (CBI) method. The results show that the NBR index using the Near Infrared (NIR) and Shortwave Infrared (SWIR) spectral has a high correlation with the field data (CBI), especially in forest vegetation, in comparison to other indices. NIR and SWIR radiation spectral are exceptionally good at separating burnt and unburned land. Decreases in the tree canopy and water content after changes due to fire can be represented well by the SWIR spectrum, which has increased reflection (Key & Benson 1999; Escuin et al., 2007).NBR can be used to identify burned areas using SPOT-4 (Parwati et al., 2012). According to the index theory, NBR would be optimal in quantifying fire severity. Although previous studies have reported a high correlation between fire severity as measured in the field and satellite-derived

NBR, our results provide no evidence for this (Roy et al., 2006). The formula is similar to a NDVI, except that it uses NIR and SWIR portions of the electromagnetic spectrum (Key & Benson, 1999). The TIRS band has a 100-metre spatial resolution but can be resampled to 30 metres for it to be used to identify burned scar areas. SWIR bands (TM bands 5 and 7 in Landsat 5 and 7 systems) as an NBR composite can be used to detect and map burnt areas. The Thermal Infrared Sensor (TIRS) algorithm which was used to detect fires and SWIR, which was used to detect water stress in vegetation and burned vegetation, will be seen in green, and both will become darker when burning takes place. This method modifies the dNBR (pre-NBR-post-NBR) composite (Indratmoko & Rizqihandar, 2019).

Based on several examples of studies on the utilization of NDVI and NBR geobiophysical information extracts, it is necessary to use this geobiophysical combination as a requirement for the devegetation and revegetation of land.

The objective of this study is to create a monitoring model of land cover change for the indication of devegetation and revegetation using Sentinel-2 data from 2017 to 2018. The definition of devegetation used is when there is a decrease in the appearance of the green level in the image (Aldrian & Sucahyono, 2013), while revegetation is shown by an increase in the appearance of the green level in the image at a certain location compared to the previous time.

## 2 MATERIALS AND METHODOLOGY

The Sentinel-2 satellite uses remote sensing technology that is easily obtained for analysis of spatial information. The satellite is a medium resolution type and has a temporal resolution of 5 days. Sentinel-2 is faster than Landsat, which has temporal resolution of 16 days. The data can be used to monitor land and

coastal cover. The Sentinel-2 Multi-spectral Instrument (MSI) has 13 spectral bands: four bands (Bands 2, 3, 4 and 8) with a resolution of 10m; six (Bands 5, 6, 7, 8a, 11 and 12) with a spatial resolution of 20m; and three (Bands 1, 9 and 10) with a spatial resolution of 60m. Sentinel-2 complements Landsat-7 and 8 and can also be used for other themes, such as spatial planning, agro/environmental monitoring, water resources, forests and vegetation, carbon resources, and global agricultural products (The European Space Agency, 2015)

The research location was the Brantas watershed in East Java Province (Figure 2-1). The data used in the study were Sentinel-2A multi-temporal data for 2017 and 2018 (Figure 2-2).

### 2.3 Sentinel Characteristics

Sentinel-2 is a European wide-swath, high-resolution, multi-spectral imaging mission. The full mission specification of the twin satellites, flying in the same orbit but phased at 180°, is

designed to give a high revisit frequency of 5 days at the Equator and with orbital swath width is 290 km.

#### 2.3.1 Sentinel-2 MSI

The Sentinel-2 Multi-spectral Instrument (MSI) measures the earth's reflected radiance in 13 spectral bands consisting of three levels of spatial resolution: four bands at 10 meters, six bands at 20 meters and three bands at 60 meters. Sentinel-2 is supporting Copernicus land monitoring studies with an imaging mission to monitor vegetation, soil and water cover, as well as to observe inland waterways and coastal areas. The data is designed to be modified and adapted by users interested in areas such as spatial planning and the monitoring of the agro-environment, water, forests and vegetation, land carbon and natural resources, and global crops.

The spatial resolution of Sentinel-2 depends on the spectral band, as shown in Table 2.1.

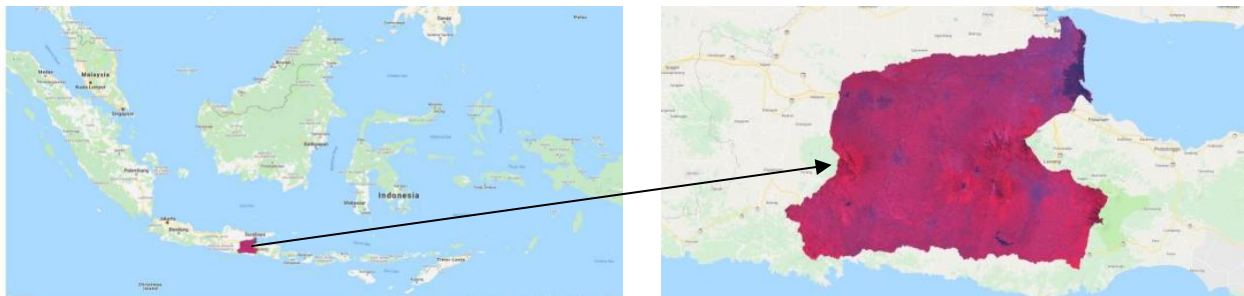


Figure 2-1: Research location: the Brantas Watershed in East Java

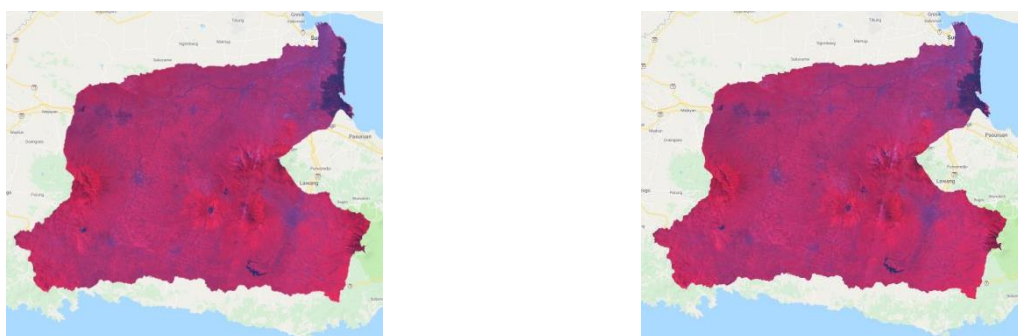


Figure 2-2: Sentinel-2 Data 2017-2018

Table 2-1. Spatial Resolution of Sentinel-2

Sentinel-2 Bands	Central Wavelength ( $\mu$ )	Resolution (m)
Band 1: Coastal Aerosol	0.443	60
Band 2: Blue	0.490	10
Band 3: Green	0.560	10
Band 4: Red	0.665	10
Band 5: Vegetation Red Edge	0.705	20
Band 6: Vegetation Red Edge	0.740	20
Band 7: Vegetation Red Edge	0.783	20
Band 8: NIR	0.842	10
Band 8A: Vegetation Red Edge	0.865	20
Band 9: Water Vapour	0.945	60
Band 10: SWIR-Cirrus	1.375	60
Band 11: SWIR	1.610	20
Band 12: SWIR	2.190	20

### 2.3.3 Normalized Difference Vegetation Index (NDVI)

The NDVI quantifies vegetation by measuring the difference between near-infrared (which vegetation strongly reflects) and red light (which vegetation absorbs). As shown below, NDVI uses the NIR and red channels in its formula:

$$NDVI = \frac{NIR - Red}{NIR + Red} \quad (2-1)$$

Healthy vegetation (chlorophyll) reflects more near-infrared (NIR) and green light compared to other wavelengths, but absorbs more red and blue light. Therefore, we see vegetation as green. If it were possible to see near-infrared, this would also show strong vegetation. The satellite sensors of Sentinel-2 both have the necessary NIR and red bands. The result of this formula generates a value between -1 and +1.

$$\Delta NDVI = NDVI_{t1} - NDVI_{t2} \quad (2-2)$$

where  $NDVI_{t1}$  is NDVI at the initial time and  $NDVI_{t2}$  is NDVI at the final time.

### 2.3.4 Normalized Burn Ratio (NBR)

The NBR is used to identify burned areas. The formula is similar to a NDVI, except that it uses near-infrared (NIR) and shortwave-infrared (SWIR) portions of the

electromagnetic spectrum (Key & Benson, 1999).

$$NBR = \frac{NIR - SWI}{NIR + SWIR} \quad (2-3)$$

$$\Delta NBR = NBR_{t1} - NBR_{t2} \quad (2-4)$$

where  $NBR_{t1}$  is NBR at the initial time and  $NBR_{t2}$  is NBR at the final time.

The NIR and SWIR parts of the electromagnetic spectrum are a powerful combination of bands for the index to use, given that vegetation is reflected strongly in the NIR region of the electromagnetic spectrum and weakly in the SWIR (see Figure 2-3).

Plants are reflected very strongly on the NIR spectrum, but weak on the SWIR spectrum, the combination of the NIR and SWIR spectra is excellent for identifying areas of burned land (wood / bark burnt) and soil / earth US Forest Service

The NBR index was originally developed for use with Landsat TM and ETM+ bands 4 and 7, but it will work with any multi-spectral sensor with an NIR band between 760-900 nm and a SWIR band between 2080-2350 nm. Therefore, this index can be used with both Landsat-8, MODIS and other multi (and hyper) spectral sensors.



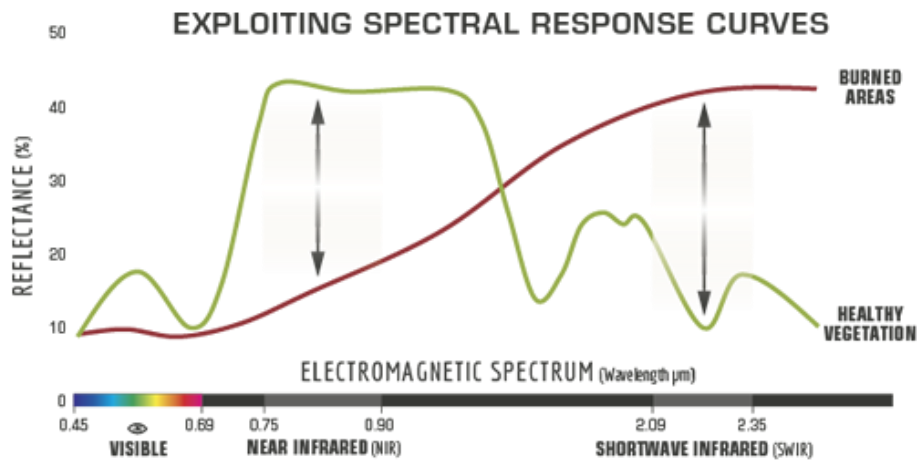


Figure 2-3: Exploiting Spectral Response Curves of Burned Areas with Healthy Vegetation  
Source: US Forest Service, 2017

Based on the USGS, NBR succeeded to level 2 derived from Landsat from Landsat 4–5 (TM), Landsat 7 (ETM +), and Landsat 8 (OLI) / (TIRS), so that it became a Level-2 Surface Reflectance product.

It is calculated as a ratio between the NIR and SWIR values in a traditional fashion  $(NIR - SWIR) / (NIR + SWIR)$ . In Landsat 4-7,  $NBR = (Band\ 4 - Band\ 7) / (Band\ 4 + Band\ 7)$ . In Landsat 8,  $NBR = (Band\ 5 - Band\ 7) / (Band\ 5 + Band\ 7)$ .

NBR is delivered as a single band product, specified as shown in the Table 2-2.

Table 2-2: Landsat Surface Reflectance-derived Normalized Burn Ratio (NBR) Specifications

Attribute	Value
Long Name	Normalized Burn Ratio
Short Name	LC8NBR, L7TNR, LT5NBR, or LT4NBR
File Name	*_sr_nbr.tif
Data Type	Signed 16-bit Integer
Units	Spectral Index (Band Ratio)
Valid Range	-10,000 – 10,000
Fill Value	-9999
Saturate Value	20,000
Scale Factor	*0.0001

Source : USGS Earth Resources Observation and Science (EROS) Center Science Processing Architecture (ESPA) On Demand Interface (ESPA).

### 2.3.5 Determination of the Threshold

In previous example, the threshold of NDVI and NBR single data was

ascertained visually by comparison between 2017 and 2018 using the trial and error

In previous studies that correlated between LAPAN, KLHK and WRI, the NDVI and NBR single data threshold was visually confirmed by comparison between 2017 and 2018 using trial and error. method. However, this research was conducted by observing changes in the vegetation index (NDVI) and in the open land index (NBR). Differences between NDVI and NBR between 2017 and 2018 were minimal as a threshold to identify indications of changes in land cover. This was determined by sampling the difference between the NDVI and NBR points.

To detect revegetation and devegetation, the threshold requirements of each index were used. Revegetation can be expressed using equation 5 and devegetation by equation 6.

$$\text{If } (NDVI > n \text{ and } NBR < m), \text{ then class 1} \quad (2-5)$$

$$\text{If } (NDVI < n \text{ and } NBR > m), \text{ then class 2} \quad (2-6)$$

where n is the NDVI threshold, m is the NBR threshold. The revegetation area (class 1) is based on the result of equation 2-5, and the revegetation area (class 2) is based on the result of equation 2-6.

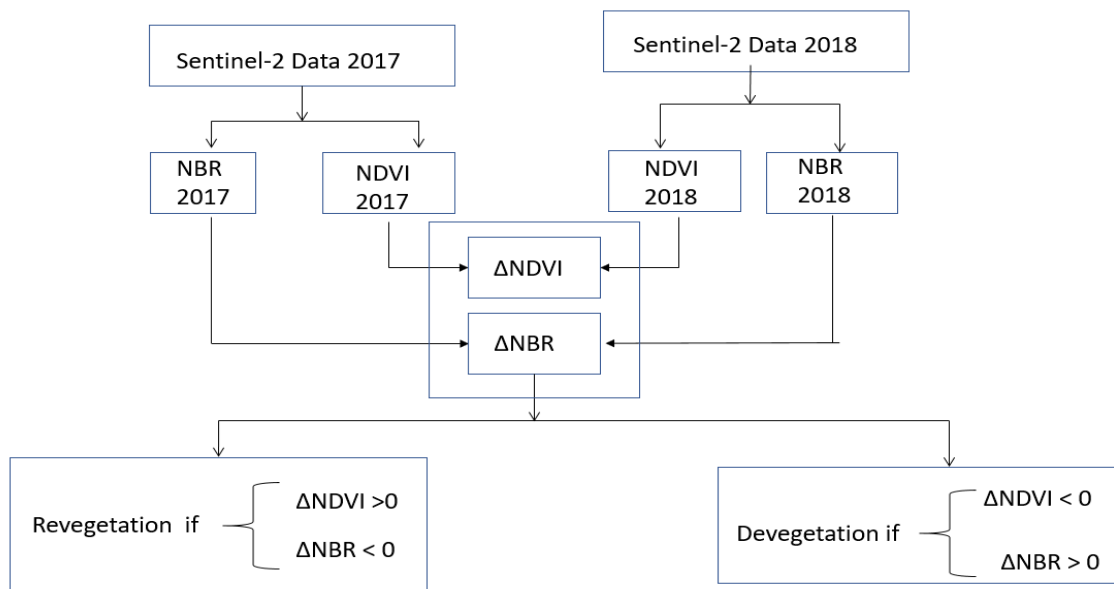


Figure 2-4: Flow diagram of the research development.

### 3 RESULTS AND DISCUSSION

The results from equations 1 and 3 are shown in Figures 3.1 and 3.2. Figure 3.1(a) shows the annual mean NDVI images for 2017, while 3.1(b) shows those for 2018 for the Brantas watershed. Figure 3.2(a) shows the annual mean NBR images for 2017 and 3.2(b) those for 2018. Visually, the NDVI and NBR imagery from 2017 and 2018 shows no changes in land cover. However, a digital assessment shows there is a change in land cover, indicated by a change in the NDVI and NBR values from 2017 to 2018. If the NDVI in 2018 is lower than that of 2017 and the NBR in 2018 is higher than that of 2017, then land cover is indicated to be devegetated; the sample data are shown in Figure 3.3. Conversely, if the value of NDVI in 2018 is higher than that of 2017 and if the NBR in 2018 is lower than that of 2017, then this indicates land cover revegetation, as shown in Figure 3-4. Figure 3-1 shows images of NDVI in

2017 and 2018, with an index value of -1 to 1. This value is depicted by the gradation of colour from light to dark, namely yellow, green and dark green, which shows the level of green of the vegetation.

Figure 3-2 shows NBR images from 2017 and 2018, with the NBR index value from -1 to 1, which shows the level of land openness. The light green colour indicates a greater level of land openness than that shown in dark green. Figure 3-3(a) shows an image of the results of the 2017 and 2018 NDVI change analysis. The level of vegetation change is divided into three classes based on the  $\Delta$ NDVI value interval, as shown in Table 3.2. Figure 3-3(b) shows an image of the results of the analysis of NBR changes in 2017 and 2018. The level of vegetation change is also divided into three classes based on the  $\Delta$ NBR value interval, as shown in Table 3.3.

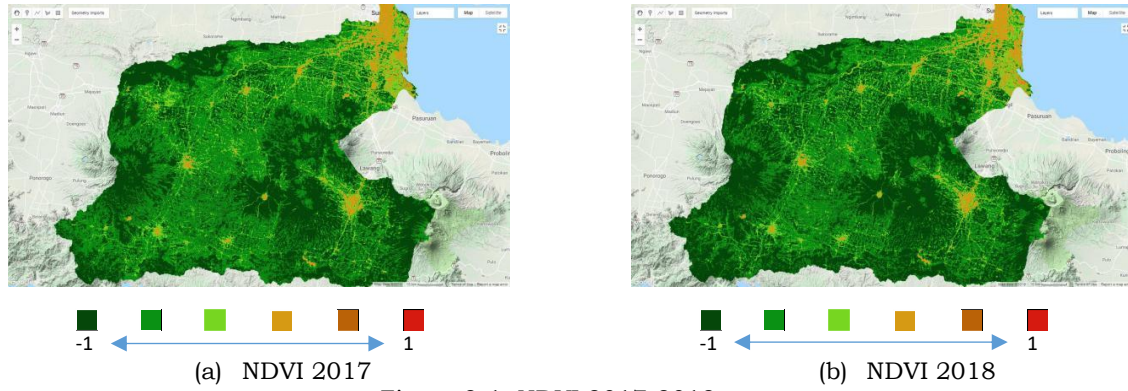


Figure 3-1: NDVI 2017-2018

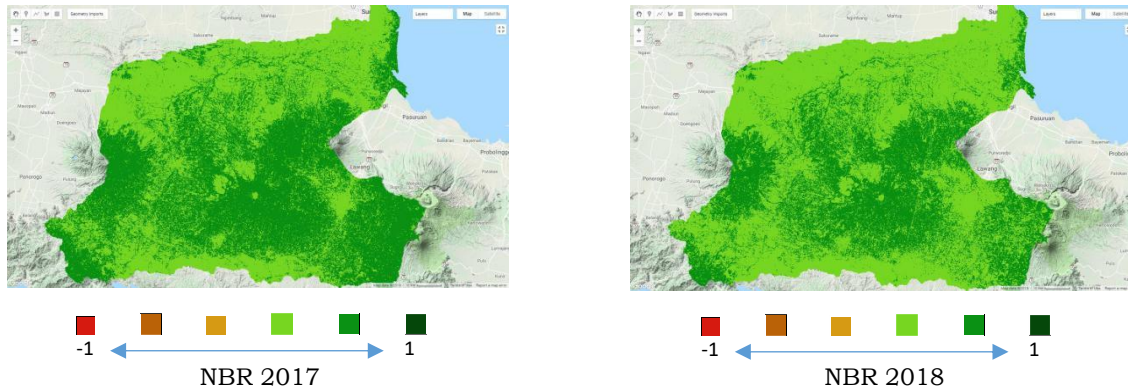


Figure 3-2: NBR 2017-2018

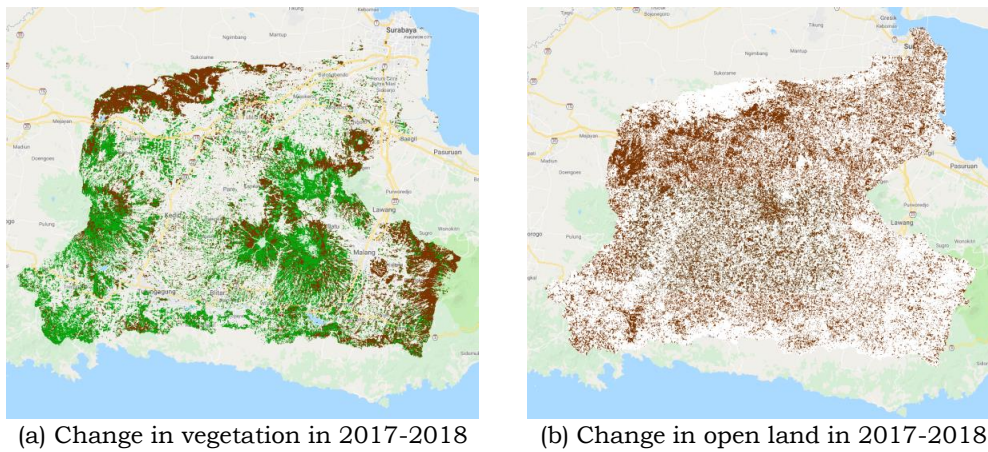


Figure 3-3: Change in vegetation and open land 2017-2018.

Table 3-2. NDVI 2017-2018 Changes







No	$\Delta$ NDVI (2017-2018)	NDVI Change	Colour
1	$>-1$	No Change	
2	-1 to 0	Small Change	
3	0 to 1	Large Change	

Table 3-3. NBR 2017-2018 Changes

No	$\Delta$ NBR (2017-2018)	NBR Change	Colour
1	$>-1$	No Change	
2	-1 to 0	Small Change	
3	0 to 1	Large Change	



Revegetation and devegetation areas were determined by application of the threshold of  $\Delta$  NDVI and  $\Delta$  NBR, obtained from several sample points which were visually experiencing changes, as shown in figures 3-3, 3-4 and 3-5 Example Revegetation and devegetation. The results of the sample points obtained by the threshold for identifying indications of revegetation and devegetation are shown in Figure 3-6.

The threshold obtained to determine the existence of revegetation was  $\Delta$ NDVI= 0.0309 and  $\Delta$ NBR= -0.0176, while  $\Delta$ NDVI= -0.0206 and  $\Delta$ NBR= 0.0314 was

the threshold for devegetation. Based on these calculations, the spatial information of revegetation and devegetation obtained is shown in Figure 3-6.

Spatial revegetation locations can be determined using the equation 5 algorithm, namely if  $\Delta$  NDVI > 0.0309 and  $\Delta$  NBR < 0.0176; and the spatial location of devegetation can also be determined using the equation 5 algorithm, namely if  $\Delta$  NDVI < - 0.0206 and  $\Delta$  NBR > 0.0314.

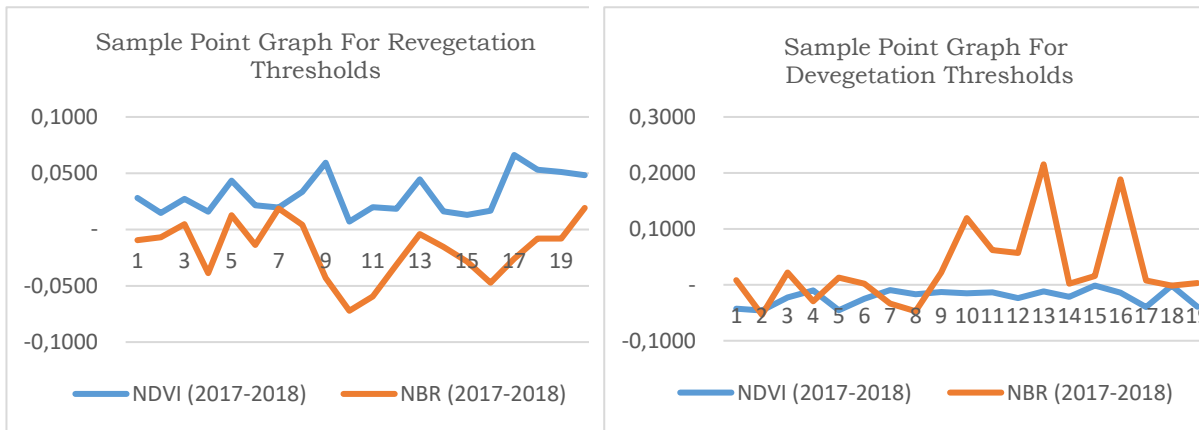
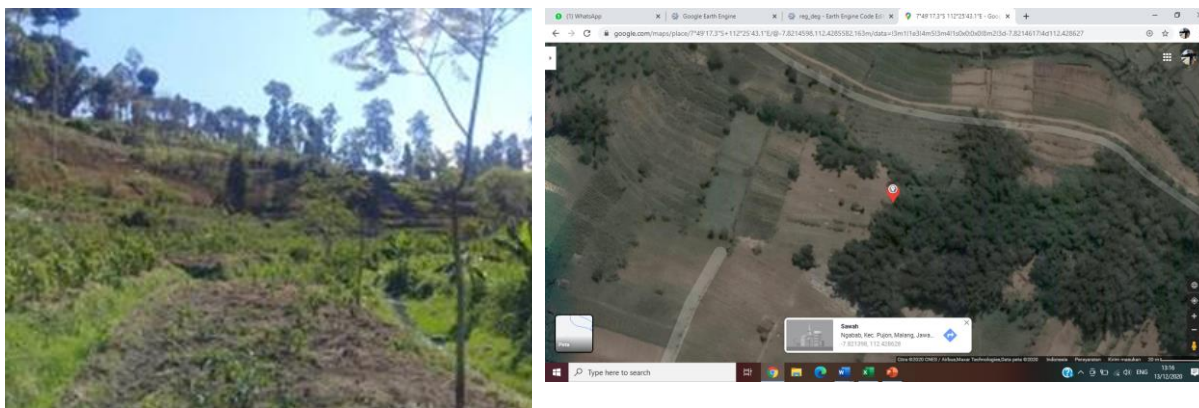
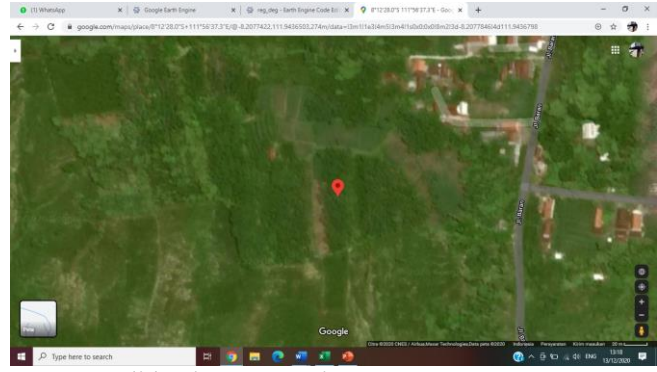


Figure 3-4: Graph of sample points for threshold determination



Devegetation, Malang,Pujon,Ngabab  
-7.8214617,112.428627



Revegetation Tulungagung,Kalidawir,Banyuurip  
-8.2077846,111.9436798

Figure 3-5: Revegetation and devegetation spatial information

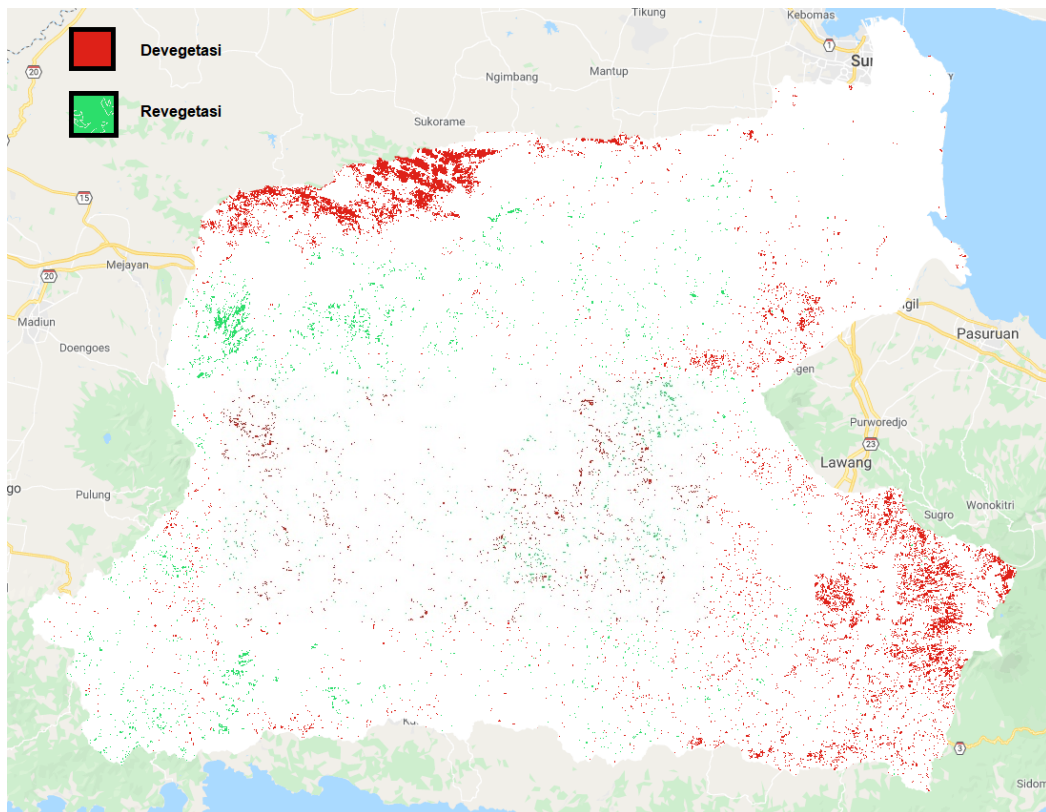


Figure 3-6: Revegetation and devegetation spatial information

In the study area, not all land-cover experienced revegetation or devegetation changes, as it includes cultivation and natural land. For example, rice fields are not considered to be devegetated or revegetated due to the growth of the rice plant phase, or changes in teak forests can be due to changes between the rainy season and dry season, so such change in land cannot be said to be devegetation or revegetation.

#### 4 CONCLUSION

Sentinel-2 MSI data with multi-temporal mosaic data can be used for monitoring changes in land cover dynamics, especially for tree cover loss. The results showed that revegetation can be determined by if  $\Delta \text{NDVI} > 0.0309$  and  $\Delta \text{NBR} < 0.0176$ , and devegetation if  $\Delta \text{NDVI} < -0.0206$  and  $\Delta \text{NBR} > 0.0314$ . Based on the NDVI and NBR threshold requirements set in this study, it is shown that devegetation is more widespread

than revegetation. Devegetation generally occurs in the barren highlands and revegetation in the low and high lands/mountains, which often experience rain. The weakness of using the Sentinel satellite is that the method cannot detect land that is narrow or steep.

### ACKNOWLEDGMENTS

This research was able to be carried out because of the collaboration of several parties. We would like to thank the INSINAS 2019 Program, the Ministry of Research and Technology/National Agency for Research and Technology and national research program 2020 LPDP for funding the research. Thanks also to the Remote Sensing Application Center and Remote Sensing Technology and Data LAPAN which provided us with facilities and input, as well as suggestions for the research.

### AUTHOR CONTRIBUTIONS

The main authors of the scientific work of this research are Samsul Arifin and Tatik Kartika, while Dede Dirgahayu and Gatot Nugroho are contributing members.

### REFERENCES

Aldrian and Sucahyono. (2013). Dictionary of climate change terms. BMKG

Arifin, S., Kartika, T., & Carolita, I. (2019) Application of geobiophysics NDVI model for forest identification in Lapan-A3 Satellite data. *Jurnal Penginderaan Jauh dan Pengolahan Data Citra Digital* 16(2), 91-100  
<http://dx.doi.org/10.30536/j.pjpdcd.2018.v0.a3109>

Barbosa, P.M., Pereira, J.M.C., & Grégoire, J. M. (1998). Compositing criteria for burned area assessment using multi-temporal low resolution satellite data, *Remote Sensing of Environment* 65(1), 38-49.

Chuvieco, E., Martin, M.P., & Palacios A. (2002). Assessment of different spectral indices in the red-near infrared spectral domain for

burned land discrimination, *International Journal of Remote Sensing* 23, 5103–5110.

Escuin, S., Navarro, R.M., & Fernandez, P. (2008). Fire severity assessment by using NBR (Normalized Burn Ratio) and NDVI (Normalized Difference Vegetation Index) derived from LANDSAT TM/ETM images. *International Journal of Remote Sensing*, 29(4), 1053–1073. DOI:10.1080/01431160701281072.

ESA-Sentinel-2. (2015) Mission Sentinel-2, <https://sentinel.esa.int/web/sentinel/missions/sentinel-2>, Europe.

Garcia, M.J.L., & Caselles, V. (1991). Mapping burns and natural reforestation using Thematic Mapper data. *Geocarto International*, 6(1), 31–37.

Horning, N., Robinson, J.A., Sterling E.J., Turning, W., Spector, S. (2010). *Remote Sensing for Ecology and Conservation*. New York: Oxford University Press.

Indratmoko S., & Rizqihandar N. (2019). Burn area detection using Landsat 8 OLI TIRS. *Southeast Asian Geography Association (SEAGA) 13th Conference IOP Conf. Series: Earth and Environmental Science* 338 012035 IOP Publishing doi:10.1088/1755-1315/338/1/012035  
1 of Geography, Faculty of Mathematic and Natural Science Universitas Indonesia Depok, Indonesia

Kartika, T., Arifin S., Sari I.L., Tosiani, A., Firmansyah, R., Kustiyo, Carolita, I., Adi, K., Daryanto, F., Said, Z. (2018), Analysis of vegetation indices using metric landsat-8 data to identify tree cover change in Riau Province. *Earth and Environmental Science* 280, 1-8. doi:10.1088/1755-1315/280/1/ 012013

Key, C.H., & Benson N. (1999). *Measuring and remote sensing of burn severity: the CBI and NBR*. <https://www.researchgate.net>

Lillesand, T.M., Kiefer R.W., & Chipman J.W. (2008). *Remote sensing and image interpretation* (Sixth Edition). New York: John Wiley & Sons, Inc.

Martín M.P., & Díaz-Delgado R. (2002). Burnedland mapping using NOAA-AVHRR

- and TERRA-MODIS. In: Viegas (Ed.). *Conference proceedings: Forest fire research & wildland fire safety*. Millpress, Rotterdam.
- Miettinen, J. (2007). *Burnt area mapping in insular Southeast Asia using medium resolution satellite imagery*. Academic dissertation. Department of Forest Resource Management Faculty of Agriculture and Forestry University of Helsinki.
- Nielsen, T.T., Mbow, C., & Kane R. (2002). A statistical methodology for burned area estimation using multi-temporal AVHRR data. *International Journal of Remote Sensing* 23(6), 1181-1196.
- Parwati, Zubaidah, A., Vetrira, Y., Yulianto, F., Ayu, K. DS, Khomarudin, M.R. (2012), Usage of Spot-4, Normalized Burn Ratio (NBR) and Normalized Difference Vegetation Index (NDVI) to identify burnt area. *Jurnal Ilmiah Geomatika* 18(1), 29-41.
- Philiani, I, Saputra, L, Harvianto, L., & Muzaki, A.A. (2016). Mapping of mangrove forest vegetation using method Normalized Difference Vegetation Index (NDVI). *Surya Octagon Interdisciplinary Journal of Technology*, 1(2), 211-222.
- Roy, D.P., Lewis, P.E., & Justice C.O. (2002). Burned area mapping using Multi-temporal moderate spatial resolution data - a bi-directional reflectance model-based expectation approach. *Remote Sensing and Environment* 83, 263- 286.
- Roy, D.P, Boschettm, L., & Triffm, S.N. (2006). Remote sensing of fire severity: assessing the performance of the normalized burn ratio. *IEEE Geoscience and Remote Sensing Letters*, 3(1), 112-116.
- Ryan, L. (1997). Creating a Normalized Difference Vegetation Index (NDVI) image using multispectral. University of New Hampshire.
- Silva, J.M.N, Cadima, J.F.C.L., Pereira, J.M.C. M. Grégoire. (2004), Assessing the feasibility of a global model for multi-temporal burned area mapping using SPOT-VEGETATION data. *International Journal of Remote Sensing* 25(22), 4889-4913. DOI: 10.1080/01431160412331291251.
- USGS-EROS. (2017). Comparison-Sentinel-2-And-Landsat, <https://www.usgs.gov/centers/eros/science/>.
- Weier, J, Herring, D, (2000), Measuring Vegetation (NDVI and EVI), NASA, <https://earthobservatory.nasa.gov/features>.





# INTERSEASONAL VARIABILITY IN THE ANALYSIS OF TOTAL SUSPENDED SOLIDS (TSS) IN SURABAYA COASTAL WATERS USING LANDSAT-8 SATELLITE DATA

Bela Karbela<sup>1\*</sup>, Pingkan Mayestika Afgatiani<sup>2</sup>, Ety Parwati<sup>2</sup>

<sup>1</sup>Geodesy Engineering Department Diponegoro University

Jl. Prof. Sudarto SH, Tembalang, Semarang, 50275, Indonesia

<sup>2</sup>Remote Sensing Applications Center–National Institute of Aeronautics and Space (LAPAN)

Jl. Kalisari No. 8 Kelurahan Pekayon Kecamatan Pasar Rebo Jakarta Timur, 13790, Indonesia

\*e-mail: belakarbela@students.undip.ac.id

Received: 25 September 2020; Revised: 17 December 2020; Accepted: 21 December 2020

**Abstract.** The spatial and temporal capabilities of remote sensing data are very effective for monitoring the value of total suspended solids (TSS) in water using optical sensors. In this study, TSS observations were conducted in the west season, transition season 1, east season, and transition season 2 in 2018 and 2019. Landsat 8 image data were used, extracted into TSS values using a semi-analytic model developed in the Mahakam Delta, East Kalimantan, Indonesia. The TSS data obtained were then analysed for distribution patterns in each season. The sample points were randomly scattered throughout the study area. The TSS distribution pattern in the west season showed a high concentration spread over the coastal area to the off sea, while the pattern in the east season only showed a high concentration in the coastal areas. Transitional seasons 1 and 2 showed different patterns of TSS distribution in 2018 and 2019, with more varied values. The distribution of TSS is strongly influenced by the season. Observation of each cluster resulted in the conclusion that human activity and the rainfall rate can affect the concentration of TSS.

Keywords: *Rainfall Rate, Total Suspended Solids, Seasonal Total Suspended Solids, Surabaya*

## 1 INTRODUCTION

Technological advances have completely changed human life and work. The digital world is increasingly helping people to do many things that were previously done manually in a more practical and effective way. Such advances have also taken place in earth observation satellite technology, which is used as a vehicle for remote sensing. The use of such technology can make work efficient both in terms of time and energy, allowing observation of large areas of study. Optical remote sensing systems are often used in monitoring natural resources and waters quality. Satellite recording technology can record electromagnetic waves outside the range of visible waves, which is very useful in

distinguishing the spectral pattern of objects being recorded; for example, land and water can be distinguished easily because they have spectral differences. The spectral pattern of water in visible waves can provide extensive effective information on matter in the air (Le, Li, Zha, Sun, Huang, & Zhang, 2011), meaning that water quality observation methods, such as total suspended solids (TSS), can be performed using digital images. Improved sensor spectra and various algorithms are continuously being developed, and TSS detection parameters can be determined more accurately and quickly. The use of Landsat-based sensors has been widely used in determining TSS parameters; for example, Arief et al. (2016) employed

Landsat-8 imagery to make TSS model estimation using a two-dimensional algorithm, with use of the green and red bands. In addition, Yanti et al. (2016) compared single Landsat-8 bands to map TSS distribution in Gajahmungkur Reservoir, Wonogiri City, Central Java, Indonesia, finding that the red band was the best to estimate TSS. Wang et al. (2017) and Jiyah et al. (2017) used QRLTSS model for TSS mapping, which used the red band and had a good ability to detect TSS with high dynamics. Using Landsat 5 TM, Landsat 7 ETM and Landsat 8, Parwati and Purwanto (2017) built a model based on one previously developed by Budhiman (2004), which also used the red band. Their results showed that TSS would increase if there was a change in land cover. Trisakti et al. (2015) also employed Landsat 8 to ascertain water clarity in Kerinci and Tondano Lakes, showing that Kerinci Lake (2m) had lower water clarity than Tondano Lake (2-3m).

TSS is the result of the reactions of heterogeneous materials, which then serve as the initial constituent material for sediment and inhibit the formation of organic substances in water (Tarigan & Edward, 2003). High TSS concentrations in water can cause other impacts, such as those found by Helfinalis et al. (2012), who demonstrated that high TSS concentrations can reduce the photosynthetic activity of marine biota, both micro and macro, which will result in decreased oxygen levels produced by plants, meaning fish will die due to a lack of oxygen. However, the level of TSS cannot determine what is happening in the water (Ainy et al., 2011; Doming et al., 2019). Waters that contain high TSS also tend to experience high sedimentation. TSS concentration measurements can be used as a determining indicator of water quality.

The coast of Surabaya is a busy area. The various activities that are conducted there show the importance of these waters. This entails the monitoring of water quality, namely the TSS content. Monitoring TSS concentrations can show the level of pollution in Surabaya waters (Hariyanto & Krisananda, 2019; Hariyanto *et al.*, 2014). Information on TSS concentration can be used as a parameter of water quality, so that action can be taken to prevent or deal with any water pollution that occurs. Pollution handling activities are conducted when the TSS content being monitored is at a dangerous level; namely, when the concentration is very high. Reducing TSS concentration can be achieved by avoided deforestation, especially of mangroves in the area around the water. Such concentration has been shown to decrease when there was an increase in the area of mangrove plants around the water (Parwati & Purwanto, 2017).

The territory of Indonesia is located in the tropics and is crossed by the equator. The pseudo motion of the sun crossing the equator cause the country experiences two seasons, namely the west season and the east season (Hutabarat, 2006). The west, or rainy season, occurs in December, January and February, while the east, or dry season occurs in June, July and August. The period between the west and east seasons, in March, April and May, is referred to as transitional season 1. While between the East Season to the West Season, in September, October and November, is referred to as transitional season 2 (Fadika et al., 2014).

In the west or rainy season, the TSS concentration (turbidity) will increase in the central area of the waters due to the high intensity of rain, which results in the process of material being moved from small rivers around the waters or from the coast to the middle of the water (deep

water) (Riswana *et al.*, 2017). Meanwhile, in the east or dry season, the TSS concentration will be low in the middle part of the water, but high in the coastal area. Baseline sediment resuspension is a major factor affecting TSS concentrations during the east season (Quang *et al.*, 2017).

The aim of this study is to determine the distribution pattern of TSS content in each observation season in order to establish the related TSS value range that was also matched with rainfall rate data.

## 2 MATERIALS AND METHODOLOGY

### 2.1 Location and Data

The research location was the Surabaya coastal region, East Java Province, Indonesia. Geographically, Surabaya is located to the south of the equator, at  $-7^{\circ}9'N$  to  $-7^{\circ}21'N$  and stretches from  $112^{\circ}36' E$  to  $112^{\circ}57' E$ . The area of Surabaya City is 52,087 Ha,

63.45% or 33,048 Ha of which is land, with the remaining 36.55% or 19,039 Ha being sea. The focus of this research is on the waters of the City of Surabaya, with the study area divided into three observation clusters, namely cluster 1 (waters of Lamong Bay Port), cluster 2 (waters around Suramadu Bridge) and cluster 3 (Wonorejo Mangrove area), as shown in Figure 2-1.

### 2.2 Data standardisation

Landsat 8 satellite spectral data, to be precise channels 1 to 7 in path/row 118/65, from the United States Geological Survey (USGS), were used in the process of extracting MPT concentration in water. The QGIS 3.14 and ArcGIS 10.4 open-source applications from the Environmental Systems Research Institute (ESRI) were employed to process the satellite image data. The layout of the MPT processing results used ArcGIS 10.4 tools.

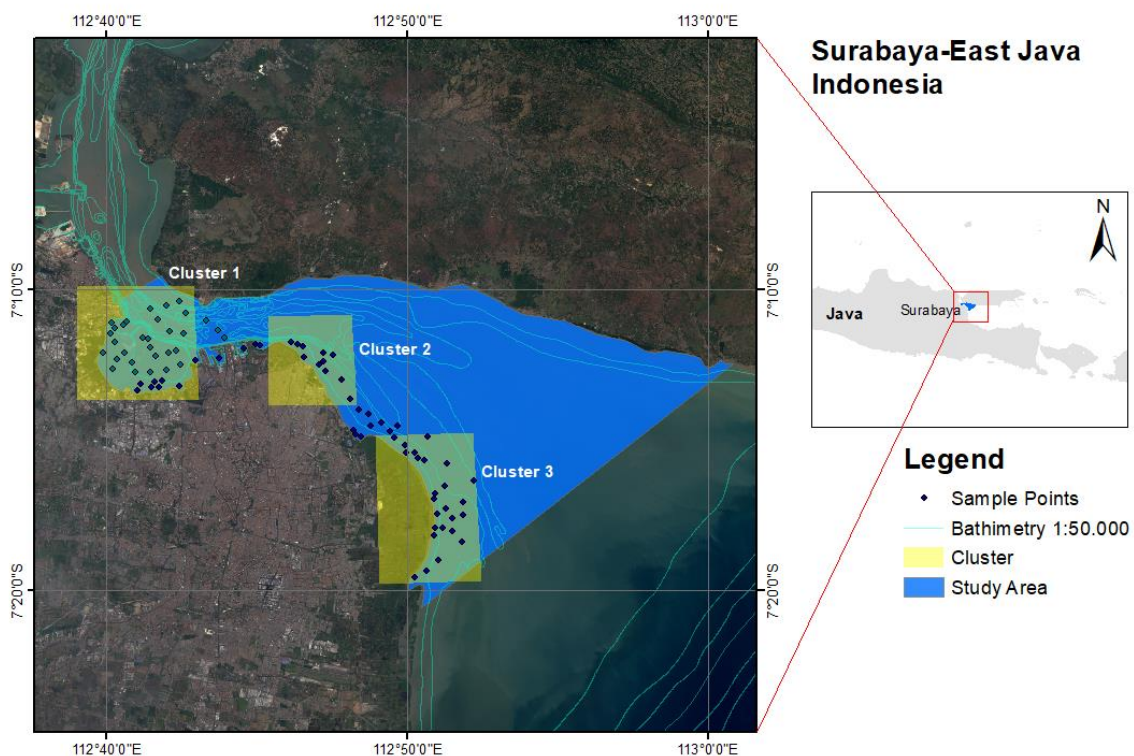


Figure 2-1. Study Area

### 2.3 Methods

The Landsat 8 satellite data used in the study comprised eight images representing each season: west season 2017, west season 2019 and transitional season 1, east season, and transitional season 2 in 2018 and 2019. It used data from 2017, 2018 and 2019 without any consideration of possible ENSO events during the season.

Table 2-1. Acquisition of Landsat Image Data

No.	Type of Data	Acquisition Date
1	West Season	30 December 2017
2	Transitional Season 1	7 May 2018
3	East Season	11 August 2018
4	Transitional Season 2	28 September 2018
5	West Season	18 January 2019
6	Transitional Season 1	26 May 2019
7	East Season	26 July 2019
8	Transitional Season 2	18 November 2019

The working stages in the research can be seen in the flow chart in Figure 2-2. The TSS information extraction process followed the stages described below.

1. The data collection required for the study was that of Landsat 8 imagery representing each season. At this stage, the number and distribution of the research sample points was also determined.
2. Performance of a cloud masking process. This was done manually using the QA channel on Landsat 8, which contains information about the quality of Landsat 8 images (USGS, 2013). The range of values in the QA channel detected as cloud will be eliminated, so the clouds in the scene image will disappear.

3. Image pre-processing, including radiometric correction, sun angle correction, and atmospheric correction using the DOS1 (Dark Object Subtraction) method. This process was performed using the pre-processing tools in QGIS 3.14 to produce surface reflectance data, the bottom of atmosphere reflectance.
4. Performance of the process of separating land and sea by running the normalized difference water index (NDWI) algorithm (McFeeters, 1996) with the equation:

$$NDWI = (A-B)/(A+B) \quad (2-1)$$

A : reflectance Green band  
 B : reflectance NIR band

5. Calculation of the TSS content using a semi-analytic model. This model was used as Afgatiani et al. (2020) showed that it produced lower error than the empirical model. The semi-analytic model of Budiman (2004) was employed, which has previously been used in the Porong River area (Budianto & Hariyanto, 2017; Indeswari et al, 2018) and has a high regression value, with the following formula:

$$MPT (mg/L) = X * (exp (Y * Z)) \quad (2-2)$$

X : 8.1529  
 Y : 23.704  
 Z : reflectance Red band

6. Extraction of the TSS value with a predetermined sample point on all the images resulting from the MPT processing. The sample point MPT data were used in the process of evaluating the MPT value in each cluster.
7. The rainfall rate used was based on data from the JAXA Global Rainfall

Watch (GSMAp). It was calculated according to each season.

8. Secondary data for validation were obtained from other papers and reports, as there are no in situ data.
9. Analysis of the TSS distribution data for each season, and analysis of the TSS sample data in each cluster by adding the rainfall rate and secondary data.

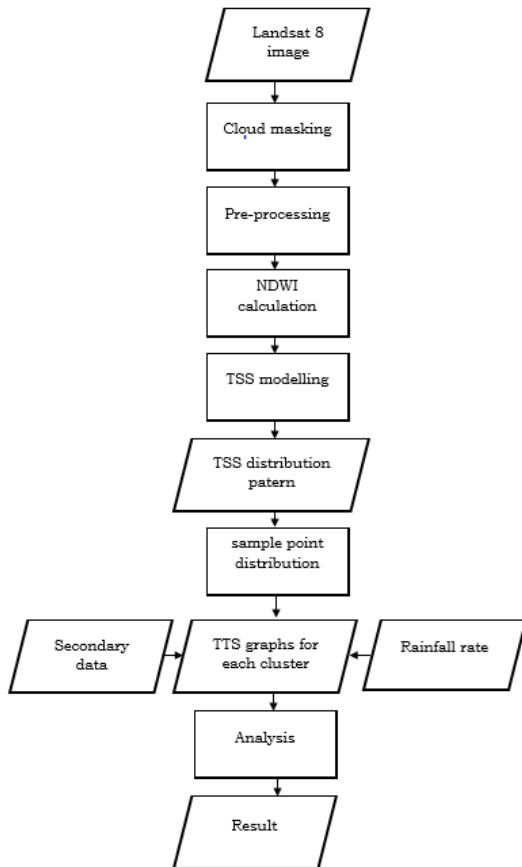


Figure 2-2. Flow diagram of data processing and analysis

### 3 RESULTS AND DISCUSSION

The TSS distribution shows dynamic fluctuations from season to season; that of 2018 can be seen in Figure 3-1. The distribution in the 2018 west season, which has a TSS concentration of 60.5 – 692.6 mg/L, indicates a high TSS concentration in the coastal (shallow) to middle (deep) waters. Transitional season 1 2018, with a TSS concentration of 29.6 – 97.2 mg/L, shows that the level had decreased in the coastal and mid-water areas. East

season 2018 had a TSS concentration of 45.9 – 144.9 mg/L, with high concentrations spread along the coastal area, while levels in the middle of the TSS waters experienced a decline. Transition Season 2 2018 had TSS concentrations of 35.6 – 281.6 mg/L, with high concentrations scattered in the middle of the water, while in the coastal areas the TSS concentration fell.

The distribution of TSS in the 2019 west season, with a concentration of 24.9 – 807 mg/L, indicates high TSS concentrations in the coastal to middle waters. The levels in transitional season 1 2019, with TSS concentrations of 23.8 – 115.4 mg/L, show that TSS with a high concentration decreases in both the coastal and middle water areas. The 2019 east season, with TSS concentrations of 34.2 – 122.9 mg/L, experienced a decrease in TSS concentrations in all the study areas, with no visible distribution of TSS at high concentrations. TSS concentrations in the coastal areas are higher than those in the middle of the water. Transition Season 2 2019 had TSS concentrations of 30.3 – 163 mg/L, with high concentrations scattered in the middle of the water, while in coastal areas the TSS concentration fell.

The distribution of TSS in the 2018 and 2019 west seasons shows high concentrations spread over the coastal area to the middle area. On the other hand, the distribution of TSS in transitional season 1 2018 and transitional season 1 2019 shows a decrease in concentration from the west season, both in the coastal and in mid-water areas. Regarding TSS distribution in east seasons 2018 and 2019, TSS distribution in the coastal areas shows a higher TSS concentration than in the middle water area, while the distribution of TSS in transitional seasons 2 of 2018 and 2019 shows an increase in the TSS

value from the east Season in the mid-water areas, but a decrease in coastal areas.

The distribution pattern of TSS in transitional seasons 1 and 2 does not show particular patterns, as is the case for the west and east seasons. TSS in each season in Surabaya displays the same pattern as in previous studies by Risuana et al. (2017) and Quang et al. (2017), with west season TSS concentrations high from the coastal area to the middle of the water. On the other hand, in the east season, TSS concentrations will be high in the coastal areas but will decrease in the middle of the water. Moko and Wiweka (2012) showed that the TSS concentration range in the east season was 24 – 402 mg/L. However, the resulting values from the image processing in the east season in both 2018 and 2019 were lower (34.2 - 144.9 mg/L) than in situ. Guntur et al. (2017) showed in situ data in transition season 1 of 9.9 - 131.7 mg/L. These values are almost similar to the TSS estimation results from the images of the 2018 and 2019 transition seasons, of 23.8 – 115.4 mg/L. Ma'arif and Hidayah

(2020) found in situ data in the west season of 250 – 470 mg/L.

By observing the variation in the TSS distribution in each season, it is clear that the distribution of TSS is strongly supported by the changing seasons, especially in the west and east seasons. In these seasons, the surface currents move in the direction of the monsoon wind. Surface currents in the west and east seasons are greatly influenced by the wind that blows over the season. In transition seasons 1 and 2, surface currents in the water are not dominated by the influence of the wind. This is because the wind speed above the sea level is too low. It is suspected that the surface currents that occur are caused by tidal influences (Fadika et al., 2014). Surface currents in water also affect the distribution and value of TSS; according to Fathiyah et al. (2017), strong surface currents affect the direction of TSS distribution, which will follow the direction of the sea surface currents. Krisna et al. (2012) also found that the direction of TSS distribution will be in the same direction as that of the wind in the area. Wind direction is also influenced by the seasons.



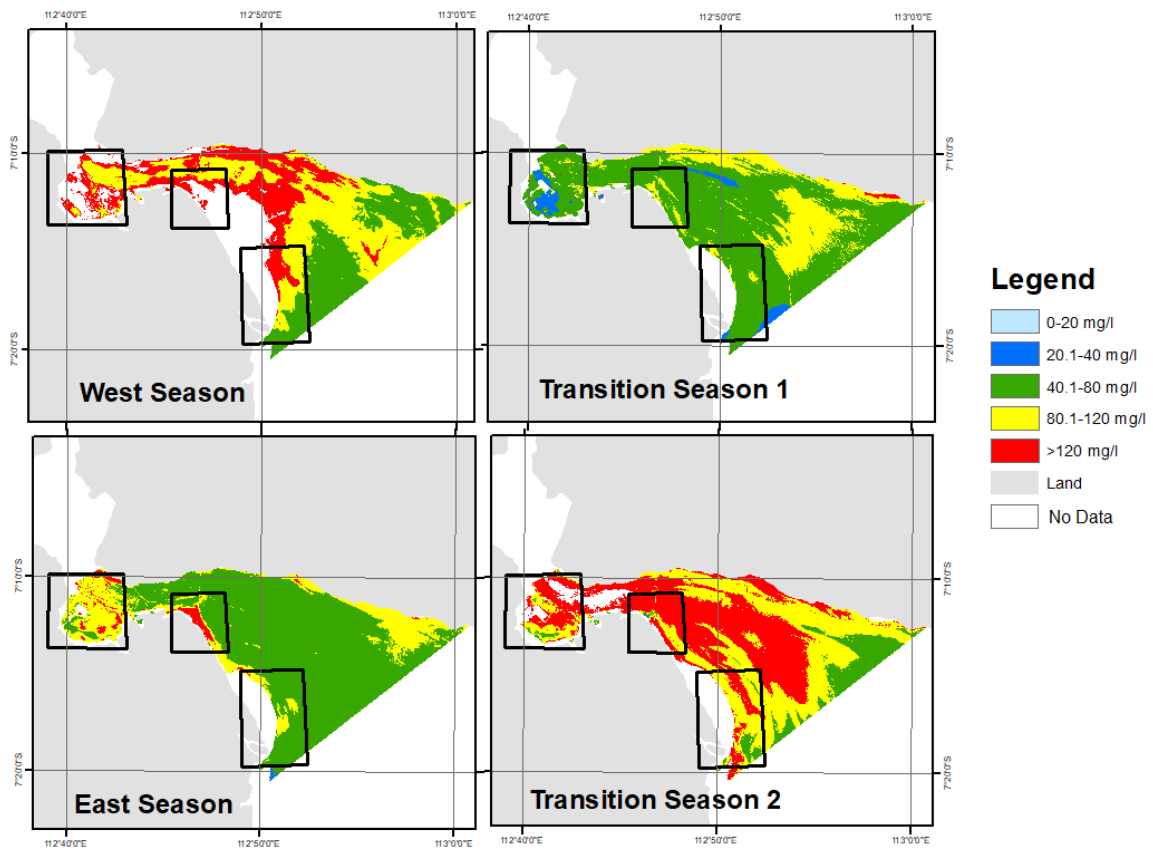


Figure 3-1. TSS distribution in 2018

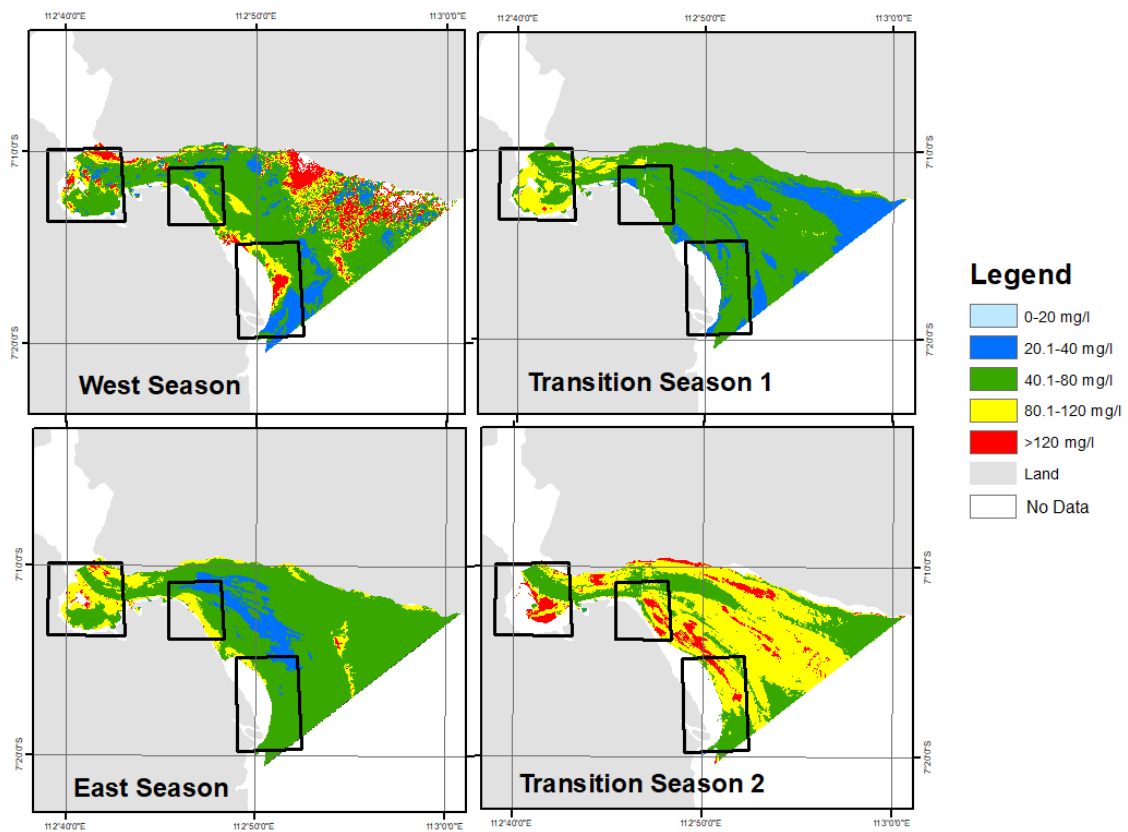


Figure 3-2. TSS distribution in 2019

Evaluation of the TSS values in each cluster was made by using six sample points. The selection of these took into account spatial distribution and avoided outlier values, as can be seen in Tables 3-1 to 3-3, which show the TSS values at each sample point. Figures 3-3 to 3-5 show the fluctuation of each sample in each season.

Cluster 1 was located in the Lamong Bay Port area, where the TSS values varied considerably from season to season, can be seen in Figure 3-3. Starting from the west season in 2018, the TSS value was relatively high, in the range of 100-200 mg/L, while in transition season 1 2018, the value dropped drastically. It increased again in east season 2018 and transitional season 2 2018. In west season 2019, the TSS value fell again, before successively increasing in transitional season 1 2019, east season 2019 and transitional season 2 2019. The average TSS value in cluster 1 was above 50 mg/L, which means that its concentration was quite high.

This high TSS value was due to the relatively high activity at Lamong Bay Port; moreover, the port is also near the other big port of Tanjung Perak. This directly increases the activity in cluster 1 waters. High activity in the waters causes considerable material to be carried into the waters, resulting in a high TSS value (Handoyo et al., 2017).

Cluster 2 in the Suramadu Bridge area also shows a variation in TSS values from season to season, as can be seen in Figure 3-4. Evaluation of the TSS values of the selected six cluster 2 sample points is shown in Table 3-2. The selection of sample points in each cluster must be free from clouds in each season so that the TSS value selected represents the actual situation.

Starting from the west season 2018, the TSS value was quite high, in the range of 100-200 mg/L, while in transition season 1 2018, it dropped drastically. The west season has the highest TSS value. This period is the peak of the rainy season at Indonesia, especially in the southern equator regions, such as Sumatra, Java, Bali and Nusa Tenggara. The amount of rainfall in the season is generally above 250 mm/month (Mulyana, 2002). This means there will be increasingly more water containing residue running off the land, resulting in an increment in TSS. The transition season is a time when there is a change from the west to the east seasons. In this season, the TSS values are irregular due to the changing wind direction (Siregar et al., 2017).

In east season 2018 and transitional season 2 2018, the TSS values increased again, then decreased in 2019 west and intermediate 1 season, before once again rising in 2019 east season and decreasing in transitional season 2 2019.

In the 2018 west season, 2018 east season, and transitional season 2 2018, the TSS value was in the range of 100-200 mg/L, with a high concentration. Meanwhile, for other seasons the TSS value was below 100 mg/L. In transition season 2 2019, four sample points had no TSS data because the areas were covered by cloud. Overall, the TSS value in cluster 2 was below that of cluster 1, which was because the activity in the waters around Surabaya Bridge was not as dense as that of Lamong Bay Port (cluster 1). Environmental factors such as wind speed, wind direction and tides have a relatively minor effect on increasing TSS concentrations compared to human activities in water areas (Noel et al., 1995). However, this paper does not include wind data.

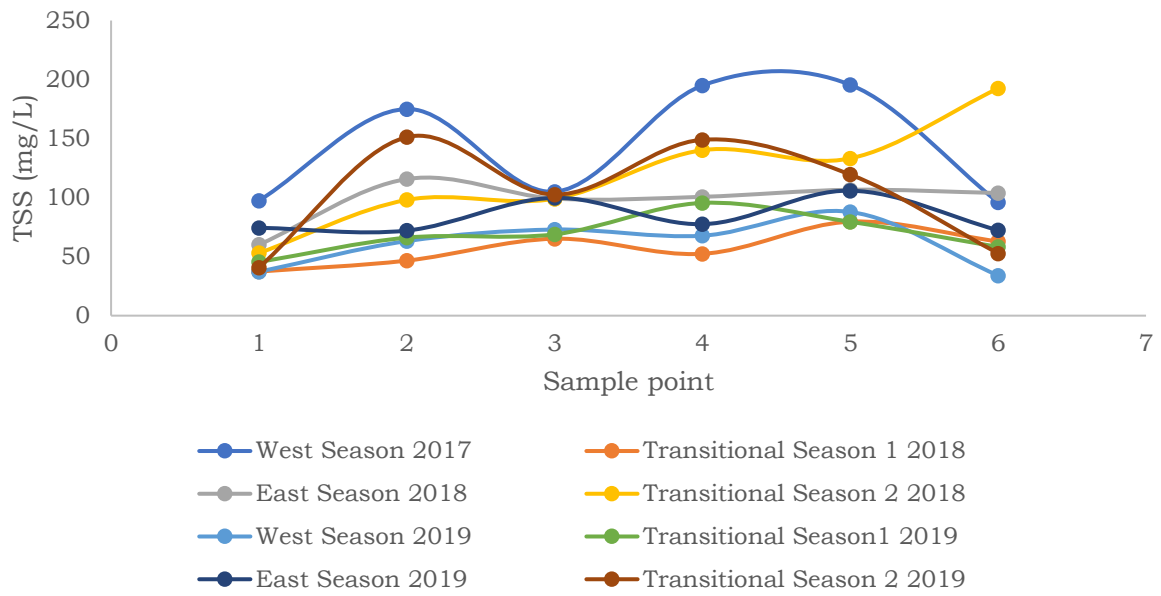


Figure 3-3. Graph of TSS values in cluster 1 (Lamong Bay Port).

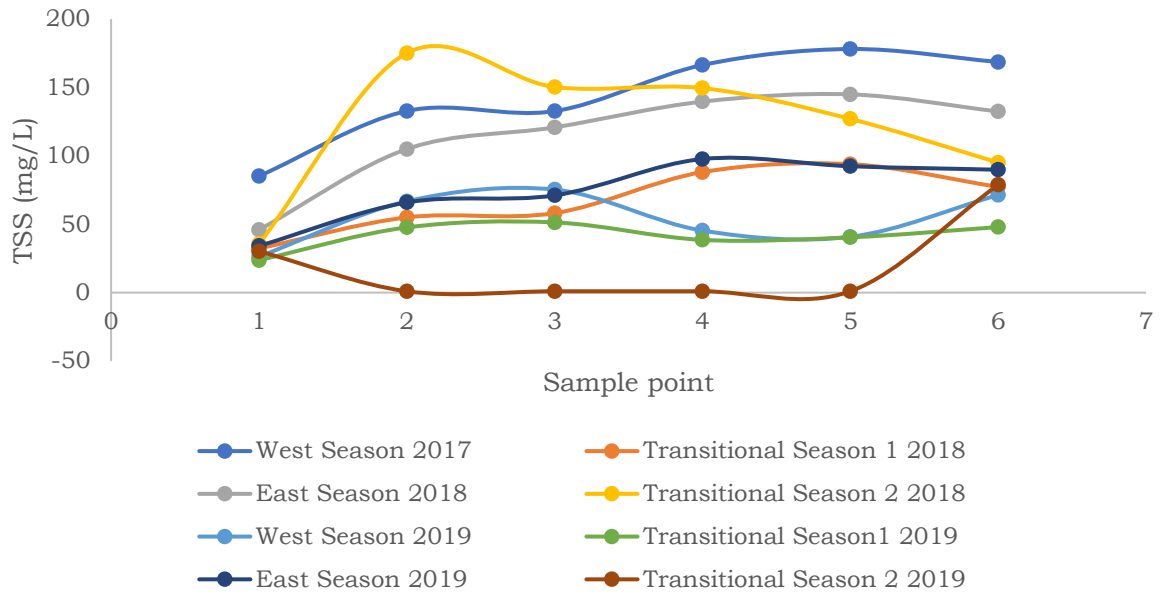


Figure 3-4. Graph of TSS values in cluster 2 (around Suramadu Bridge).

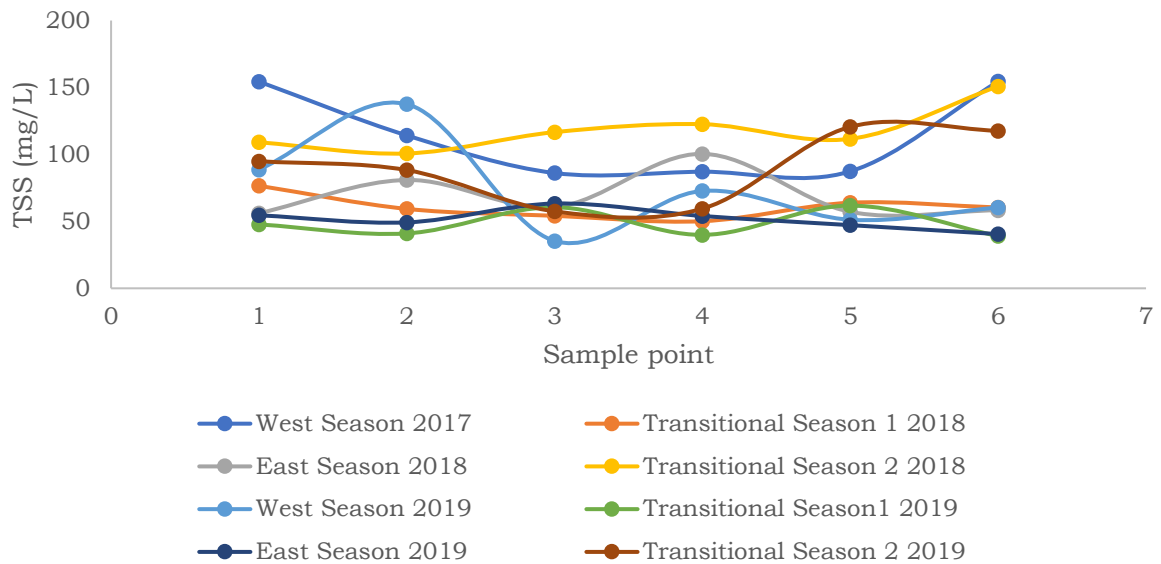


Figure 3-5. Graph of TSS values in cluster 3 (Wonorejo Mangrove area).

Table 3-1. TSS values (mg/L) of sample points, cluster 1

West Season 2018	Trans Season 1 2018	East Season 2018	Trans Season 2 2018	West Season 2019	Trans Season 1 2019	East Season 2019	Trans Season 2 2019
97.4	37.4	60.1	53.0	37.2	45.4	74.4	40.8
175.0	46.6	115.7	98.0	63.1	66.1	72.1	151.2
105.0	65.2	99.2	99.0	72.9	68.9	99.8	102.5
195.0	52.4	100.7	140.2	67.7	95.5	77.5	149.0
195.5	79.6	106.6	133.2	87.8	79.5	105.9	119.5
95.9	62.8	103.9	192.5	34.0	58.2	72.4	52.7

Table 3-2. TSS values (mg/L) of sample points, cluster 2

West Season 2018	Trans Season 1 2018	East Season 2018	Trans Season 2 2018	West Season 2019	Trans Season 1 2019	East Season 2019	Trans Season 2 2019
97.4	37.4	60.1	53.0	37.2	45.4	74.4	40.8
175.0	46.6	115.7	98.0	63.1	66.1	72.1	151.2
105.0	65.2	99.2	99.0	72.9	68.9	99.8	102.5
195.0	52.4	100.7	140.2	67.7	95.5	77.5	149.0
195.5	79.6	106.6	133.2	87.8	79.5	105.9	119.5
95.9	62.8	103.9	192.5	34.0	58.2	72.4	52.7

Table 3-3. TSS values (mg/L) of sample points, cluster 3

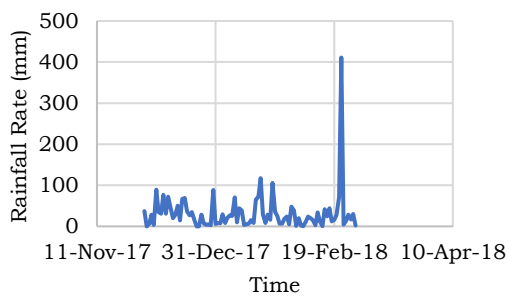
West Season 2018	Trans Season 1 2018	East Season 2018	Trans Season 2 2018	West Season 2019	Trans Season 1 2019	East Season 2019	Trans Season 2 2019
154.4	76.6	56.1	109.1	88.6	47.7	54.5	94.9
114.2	59.3	80.9	100.7	137.5	41.0	49.2	88.3
86.1	54.2	60.6	116.6	35.4	60.5	63.3	57.5
87.1	50.1	100.4	122.6	72.7	39.9	54.0	59.5
87.4	63.9	57.1	111.6	51.2	61.8	47.2	120.6
154.5	60.3	58.3	150.8	60.3	39.0	40.5	117.6

Cluster 3 was located in the Wonorejo Mangrove area, which shows that the TSS value varies from season to season, as seen in Figure 3-5. Evaluation of the TSS values for the selected six sample points in cluster 2 are shown in Table 3-3. The TSS values decreased between the 2018 west season and transition season 1 2018. In east season 2018 and transition season 2 2018, the TSS values then increased respectively. In west season 2019 and transitional season 1 2019, the values fell, before increasing again in east and transitional season 2 2019.

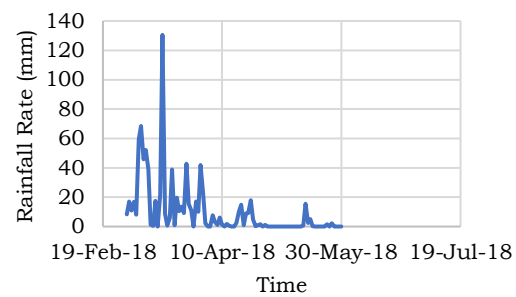
The monsoon season will affect rainfall. The rainfall data are shown in Figure 3-6, with the highest TSS values occurring in transition season 2 2018, with a concentration higher than 100 mg/L. On the other hand, in other seasons the value is below 100 mg/L. However, rainfall in this season tends to be high at the end of the period. Even though west and transition seasons 1 experience high rainfall with relatively high intensity, TSS levels are no higher than in transition season 2. Rainfall can affect TSS concentration; however, there is no correlation between first-flush loads of TSS and rainfall characteristics (He et

al., 2010). Therefore, it is likely that the end of transition season 2 will be a seasonal first flush event. Seasonal first flush is the release of a bigger mass off contaminants or higher concentration, compared with storms later in the season (Strenstrom & Kayhanian, 2005). Rainfall can be a medium for the transport of pollutants from the surface (Shehane et al., 2005). TSS variation is influenced by seasons, and any season can affect rainfall.

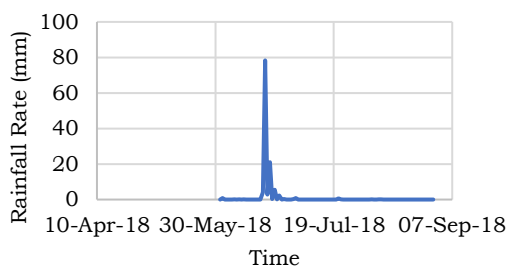
Based on the TSS value sample points in cluster 3, it can be said that cluster 3 has a lower level when compared to cluster 1 and cluster 2. The waters of cluster 3 have activities that are not as busy as cluster 1 or cluster 2. The cluster 3 area is used by fishermen- small fishermen from the surrounding area, not the center of large activity. Hasyim et al. (2009) explained that this area is dominated by *Euthymus spp.*, *Decapterus spp.*, *Ratsrellinger spp.*, *Trichiurus spp.* and *Sardinella lingiceps* during all seasons. Therefore, the TSS value is not too high when compared to the other two clusters. Human activities in and near coastal waters have great potential to increase TSS concentration (turbidity) in water (Nurjaya et al., 2019).



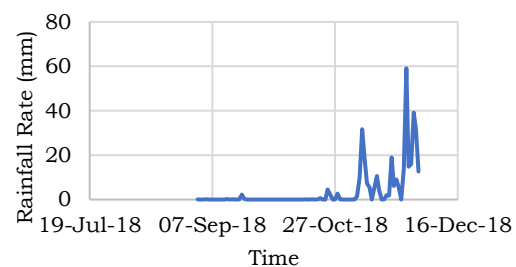
a.



b.



c.



d.

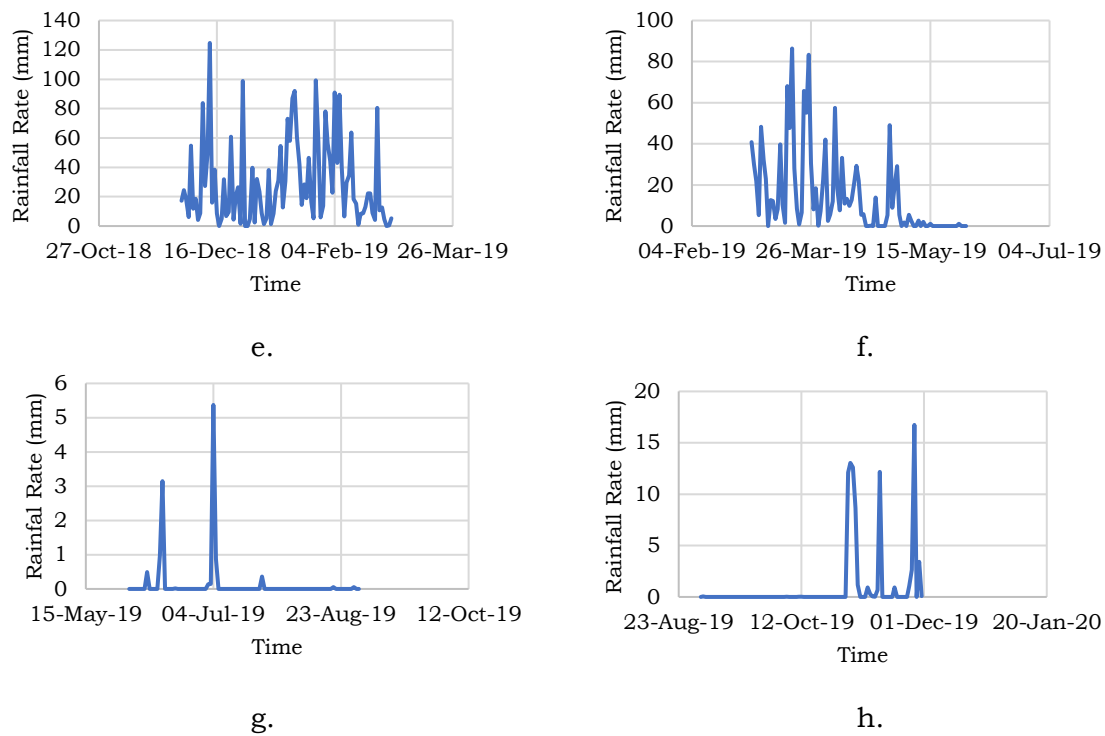


Figure 3-6. Rainfall Rate in Each Season: a. Rainfall Rate West Season 2018; b. Rainfall Rate Transitional Season 1 2018; c. Rainfall Rate East Season 2018; d. Rainfall Rate Transitional Season 2 2018; e. Rainfall Rate West Season 2019; f. Rainfall Rate Transitional Season 1 2019; g. Rainfall Rate East Season 2019; h. Rainfall Rate Transitional 2 Season 2019

#### 4 CONCLUSION

TSS distribution is highly influenced by the seasons. In the west season, TSS values with high concentrations will be scattered in the middle of the waters (deep waters), while in the east season they will only be seen in coastal areas. During transition seasons 1 and 2, the distribution of TSS is not influenced by seasons, only by tides, so that the distribution is more varied. Overall, TSS values in the west season will be higher than in the east season because of the higher rainfall.

As for the TSS values in the observation clusters, cluster 1 (Lamong Bay Port) shows different TSS distribution compared to the other locations. One of the factors that influences the distribution of TSS is seasonality.

#### ACKNOWLEDGEMENTS

The author would like to thank the Remote Sensing Application Center

LAPAN, which provided facilities for the study, and Lia Novianti N., a teammate on the Geodetic Engineering student internship team at Diponegoro University.

#### AUTHOR CONTRIBUTIONS

Interseasonal Variability in The Analysis of Total Suspended Solids (TSS) in Surabaya Coastal Waters Using Landsat-8 Satellite Data. Lead Author: Bela Karbela, Co-Author: Pingkan Mayestika Afgatiani and Ety Parwati. Author contributions are as follows:

1. Bela Karbela: image processing, map layouting, results analysis and prepare draft manuscripts
2. Pingkan Mayestika Afgatiani: Provision, writing and editing
3. Ety Parwati: Editing

#### REFERENCES

- Afgatiani, P.M., Hartuti M., & Budhiman S. (2020). Deteksi Sebaran Muatan Padatan Tersuspensi Dengan Model Empiris Dan

- Model Semi-Analitik Di Perairan Bekasi [Detection of the Distribution of Suspended Solids Using Empirical Models and Semi-Analytical Models in Bekasi Waters]. *Jurnal Ilmu dan Teknologi Kelautan Tropis*, 12(2), 341-351, DOI : <https://doi.org/10.29244/jitkt.v12i2.28138>.
- Ainy, K., Siswanto, A.D., & Nugraha, W.A. (2011). Sebaran total suspended solid (tss) di perairan sepanjang jembatan Suramadu Kabupaten Bangkalan [Distribution of total suspended solid (TSS) in the waters along the Suramadu bridge, Bangkalan Regency.]. *JURNAL KELAUTAN*, 4(2), 158-162. doi: <https://doi.org/10.21107/jk.v4i2.880>.
- Arief, M., Syifa, W., Hartuti, M. & Parwati E. (2016). Algoritma dua dimensi untuk estimasi muatan padatan tersuspensi menggunakan data satelit landsat-8 studi kasus Bay Lampung [The two-dimensional algorithm for estimating suspended solids loads uses the Landsat-8 satellite data case study: Lampung Bay]. *J Penginderaan Jauh*, 13(2), 109-120.
- Budhiman, S., Hobma, T., & Vekerdy, Z. (2004). Remote sensing for mapping tsm concentration in Mahakam Delta: an analytical approach. *The Thirteenth Workshop of OMISAR*, 1-14.
- Budianto, S., & Hariyanto T. (2017). Analisis Perubahan Konsentrasi Total Suspended Solids (TSS) Dampak Bencana Lumpur Sidoarjo Menggunakan Citra Landsat Multi Temporal (Studi Kasus: Sungai Porong, Sidoarjo) [Analysis of Changes in the Concentration of Total Suspended Solids (TSS) Impact of the Sidoarjo Mud Disaster Using Multi-Temporal Landsat Images (Case Study: Porong River, Sidoarjo)]. *Jurnal Teknik ITS*, 6(1), 130-135, DOI: [10.12962/j23373539.v6i1.21097](https://doi.org/10.12962/j23373539.v6i1.21097).
- Domining, A., Muskananfola, M.R., & A'in, C. (2019). Laju sedimentasi perairan Sungai Silandak, Semarang Barat [Sedimentation rate in Silandak River, West Semarang]. *Journal of Maquares*, 8(3), 126-132.
- Fadika, U., Rifai, A., & Rochaddi B. (2014). Arah dan percepatan angin musiman serta kaitannya dengan sebaran suhu permukaan laut di selatan Pangandaran Jawa Barat [The direction and acceleration of seasonal winds and their relation to sea surface temperature distribution in southern Pangandaran, West Java]. *Jurnal Oseanografi*, 3(3), 429-437.
- Fathiyah, N., Pin, T. G., & Saraswati, R. (2017). Pola Spasial dan Temporal Total Suspended Solid (TSS) dengan Citra SPOT di Estuari Cimandiri, Jawa Barat [Spatial Pattern and Temporal Total Suspended Solid (TSS) with SPOT Image in Estuary Cimandiri, West Java]. *8th Industrial Researc Workshop and National Seminar Politeknik Negeri Bandung July 26-27*.
- Guntur, G., Yanuar, A.T., Sari, S.H.J., & Kurniawana, A. (2017). Analisis Kualitas Perairan berdasarkan Metode Indeks Pencemaran di Pesisir Timur Kota Surabaya [Analysis of Water Quality based on the Pollution Index Method on the East Coast of Surabaya City]. *Depik Jurnal Ilmu-Ilmu Perairan, Pesisir dan Perikanan*, 6(1), 81-89, DOI : [10.13170/depik.6.1.5709](https://doi.org/10.13170/depik.6.1.5709).
- Handoyo, G., Subardjo, P, Suryoputro, A.A.D., & Sulaiman, M. (2017). The influence of ocean currents towards distribution of total suspended solid vertically in Cilalanang estuary, district Indramayu. *International Journal of Marine and Aquatic Resource Conservation and Co-existence Research*, 2(1), 23-30. doi: <https://doi.org/10.14710/ijmarcc.2.1.p>.
- Hariyanto, T., & Krisananda, H.R., (2019). Pemantauan perairan Bay lamong dengan pengembangan algoritma Total Suspended Solid (TSS) dari data citra satelit multitemporal dan data insitu [Monitoring the Bay Lamong waters with the development of a Total Suspended Solid (TSS) algorithm from multitemporal



- satellite imagery and in situ data]. *Geoid*, 14(2), 69-77. doi: <http://dx.doi.org/10.12962/j24423998.v14i2.3908>.
- Hariyanto, T., Cahyono, A.B., Krisna, T.C., & Hapsari, H.H. (2014). Identification of total suspended sediment (tss) distribution at surabaya east coast area in east java indonesia using tss algorithm implementation on multi temporal satellite images. *International Journal of Earth Sciences and Engineering*, 7(4), 1341-1346. doi: 10.13140/RG.2.1.3855.3049.
- Hasyim, B., Hartuti, M., & Sulma, S. (2009). Identification of Fishery Resources in Madura Strait Based on The Implementation of Potential Fishing Zone Information from Remote Sensing. *International Journal of Remote Sensing and Earth Sciences*, 6, 1-13. DOI: <http://dx.doi.org/10.30536/j.ijreses.2009.v6.a1234>.
- He, J., Valeo, C., Chu, A., & Neumann, N. F. (2010). Characteristics of Suspended Solids, Microorganisms, and Chemical Water Quality in Event-Based Stormwater Runoff from an Urban Residential Area. *Water Environment Research*, 82(12), 2333-2345.
- Helfinalis, Sultan & Rubiman. (2012). Padatan tersuspensi total di perairan selat Flores Boleng Alor dan selatan Pulau Adonara Lembata Pantar [Total suspended solids in the waters of the Flores Boleng Alor strait and south of Adonara Lembata Pantar Island]. *Ilmu Kelautan: Indonesian Journal of Marine Science*, 17(3), 148-153. doi:<https://doi.org/10.14710/ik.ijms.17.3.148-153>. Hutabarat, S., & Evans, S.M. (2006). Pengantar Oseanografi [Introduction to Oceanography]. UI pers Jakarta.
- Indeswari, L., Hariyanto, T., & Bekti, P.C. (2018). Pemetaan sebaran Total Suspended Solid (TSS) menggunakan citra landsat multitemporal dan data in situ (studi kasus: perairan muara Sungai Porong, Sidoarjo) [Mapping the distribution of Total Suspended Solid (TSS) using multitemporal landsat imagery and in situ data (case study: waters of the estuary of the Porong River, Sidoarjo)]. *Jurnal Teknik ITS*, 7(1), 2337-3520. <https://doi.org/10.12962/j23373539.v7i1.28698>.
- Jiyah, Sudarsono, B., & Sukmono, A. (2017). Studi distribusi total suspended solid (tss) di perairan pantai kabupaten Demak menggunakan citra Landsat [The study of the total suspended solid (TSS) distribution in the coastal waters of Demak Regency used Landsat imagery]. *Jurnal Geodesi Undip*, 6(1), 41-47

# A COMPARISON OF RAINFALL ESTIMATION USING HIMAWARI-8 SATELLITE DATA IN DIFFERENT INDONESIAN TOPOGRAPHIES

Nadine Ayasha<sup>1\*</sup>

<sup>1</sup>Indonesian Agency of Meteorology Climatology and Geophysics

\*e-mail: nadineayasha17@gmail.com

Received: 08 October 2020; Revised: 27 November 2020; Approved: 21 December 2020

**Abstract.** The Himawari-8 satellite can be used to derive precipitation data for rainfall estimation. This study aims to test several methods for such estimation employing the Himawari-8 satellite. The methods are compared in three regions with different topographies, namely Bukittinggi, Pontianak and Ambon. The rainfall estimation methods that are tested are auto estimator, IMSRA, non-linear relation and non-linear inversion approaches. Based on the determination of the statistical verification (RMSE, standard deviation and correlation coefficient) of the amount of rainfall, the best method in Bukittinggi and Pontianak was shown to be IMSRA, while for the Ambon region was the non-linear relations. The best methods from each research area were mapped using the Google Maps Application Programming Interface (API).

Keywords: *Rainfall Estimation, Himawari-8 Satellite, Google Maps API*

## 1 INTRODUCTION

Remote sensing is the science of obtaining information about the Earth's surface without having direct contact with it. This is done by sensing and recording the reflected energy and processing, analysing and applying the information (NRC, 2003). Nowadays, remote sensing for the observation of the atmosphere is very important. This is because not all areas on the earth's surface can be covered by in situ observations (Alfuadi, 2016). In addition, remote sensing has contributed greatly to various other fields and led to the development of various sensors (Lillesand et al., 2015). Remote sensing sensors themselves are divided into two types, namely remote sensing with active instruments sensors as found in weather radar and passive instrument sensors found in weather satellites (Stull, 2015).

Weather satellites can be used to identify cloud patterns and structures related to dynamic weather conditions. The development of weather satellite

systems has contributed greatly to their use in weather forecasts (Tan, 2014). In fact, observations using weather satellites can provide hourly weather information over a fairly wide area coverage. Such environmental and weather satellite data can be obtained real time, but their use remains very limited in the wider community (Suwarsono et al., 2009).

However, the most recent weather satellite and its data can be used by the wider community, namely the Japanese Himawari-8 satellite, which is a new generation of meteorological satellites with sophisticated optical sensors (Bessho et al., 2016). In addition, precipitation data can be derived from the Himawari-8 satellite data which can be useful in mitigating hydrometeorological disasters (Alfuadi, 2016).

Several studies using the Himawari-8 satellite have also been conducted to estimate rainfall in various areas. For example, Rani, et al. (2016) used the auto estimator method in Pangkalpinang Meteorological Station; the INSAT

Multispectral Rainfall Algorithm (IMSRA) method was employed by Alfuadi (2016) in Palangkaraya; and the non-linear relation method with non-linear inversion were used by Alfuadi and Wandala (2016) in Muara Teweh and Palangkaraya.

However, some of these studies only focus on one region topography. In fact, the latitude, slope and altitude in some areas will affect weather activities, such as cloud formation and rain, due to the uneven solar irradiation on the earth's surface (Sucahyono and Ribudiyanto, 2009). Therefore, it is necessary to conduct research into and test the methods used for different topography and weather systems. This study proposes to test the methods that are generally used in various topographies in Indonesia (highlands, lowlands and islands). Apart from testing the methods, the research will display rainfall estimation results into Google Maps Application Programming Interface (API) platform.

The Google Maps API platform allows users to integrate Google Maps into their respective websites by adding their own data points (Davis, 2006). The advantage of the API is that it is possible to modify maps according to user needs and integrate them with the data to be used (Akanbi and Agunbiade, 2013). Therefore, this study will utilise the Google Maps API to add data points in the form of rainfall estimation results (light, moderate, heavy and very heavy rain) into a map which interesting and easy to understand by users

## 2 MATERIALS AND METHODOLOGY

### 2.1 Location and Data

The locations of this research were in Bukittinggi (GAW Bukit Kototabang), Pontianak (Supadio Meteorological Station) and Ambon (Pattimura Meteorological Station) (as shown in red on the map in Figure 2-1).



Figure 2-1: Map of the research area

The data used were from Himawari-8 channel IR-1, obtained from ftp://202.90.199.115. IR-1 was used because IR-1 data can be converted into precipitation data (Alfuadi, 2016). The verification of the rainfall estimation was made using rainfall data from the AWS center BMKG. Rainfall date cases were employed in the research are shown in Table 2-1:

Table 2-1: Rainfall date cases (Source - BMKG, 2017 and 2018)

<b>Bukittinggi</b>	
15 April 2017	Heavy rainfall (60.8 mm/day)
25 June 2017	Moderate rainfall (36.9 mm/day)
28 June 2017	Moderate rainfall (46.5 mm/day)
<b>Pontianak</b>	
10 Sept 2017	Heavy rainfall (70.8 mm/day)
11 Nov 2017	Very Heavy rainfall (187.4 mm/day)
13 Oct 2018	Heavy rainfall (76.4 mm/day)
<b>Ambon</b>	
28 May 2018	Very heavy rainfall (100.2 mm/day)
29 June 2018	Very heavy rainfall (111 mm/day)
30 June 2018	Heavy rainfall (75 mm/day)

The tools used in the research were Python 3.7 to extract the value of the cloud top temperature (T) from the IR-1 data. These data are in netCDF (.nc) format, so Python 3.7 extracted the temperature in this format. JavaScript

was also used to prepare the script or the mapping of rainfall estimation, and the Google Maps API platform was used for mapping the best method of rainfall estimation result.

## 2.2 Methods

Two methods were employed, rainfall estimation equation and statistical verification of the rainfall estimation method

### 2.2.1 Rainfall Estimation Method

#### a. Auto Estimator

Based on Vicente et al (1998), the equation for auto estimator is :

$$R = 1.1183 \cdot 10^{11} \exp(-3.6382 \cdot 10^{-2} \cdot T^{1.2}) \quad (2-1)$$

where R is the rainfall estimation (mm/hour) and T is the cloud top temperature in Kelvin.

#### b. IMSRA

The equation used in the research of Gairola et al. (2011) was :

$$R = 8.613098 * \exp(-(T-197.97)/15.7061) \quad (2-2)$$

where R is the rainfall estimation (mm/hour) and T is the cloud top temperature in Kelvin.

#### c. Non-Linear Relation

The equation used in the research of Suwarsono et al. (2019) was :

$$R = 2 \cdot 10^{25} \cdot T^{-10.256} \quad (2-3)$$

Where R is rainfall estimation (mm/hour) and T is the cloud top temperature in Kelvin.

#### d. Non-Linear Inversion

Based on Octari et al (2015), the equation for non-linear inversion is :

$$R = 1.380462 \cdot 10^{-7} e^{3789.518/T} \quad (2-4)$$

Where R is rainfall estimation (mm/hour)

and T is the cloud top temperature in Kelvin.

### 2.2.2 Statistical Verification Method

After obtaining the results of the rainfall estimation described above, we verified the results using RMSE, correlation coefficient and standard deviation and incorporated them into a Taylor diagram. We also calculated the bias of the rainfall estimation.

#### a. RMSE

Based on Wang and Lu (2018), the RMSE equation is :

$$RMSE = \sqrt{\frac{\sum_{i=1}^N (x_i - y_i)^2}{N}} \quad (2-5)$$

where N is the amount of data,  $x_i$  is the rainfall estimation (mm) and  $y_i$  is the real observation of rainfall (mm).

#### b. Correlation Coefficient

In line with Saefuddin et al (2009), the correlation coefficient equation is :

$$r_{xy} = \frac{\sum (x_i - \bar{x})(y_i - \bar{y})}{\sqrt{\sum (x_i - \bar{x})^2} \sqrt{\sum (y_i - \bar{y})^2}} \quad (2-6)$$

where  $x_i$  is the rainfall estimation (mm) and  $y_i$  is the real observation of rainfall (mm).

#### c. Bias

Bias is used to establish whether the value of the data is underestimated or overestimated. The equation of bias based on Santos et al (2011) is :

$$Bias = \frac{1}{N} \sum_{i=1}^n (x_i - y_i) \quad (2-7)$$

where  $x_i$  is the rainfall estimation (mm) and  $y_i$  is the real observation of rainfall (mm).

#### d. Standard Deviation

Based on Supranto (2008), the equation of standard deviation is:

$$\sigma = \sqrt{\frac{\sum_{i=1}^N (x_i - \mu)^2}{N}} \quad (2-8)$$

where  $(x_i - \mu)^2$  is the deviation from the observation to the true mean.

### 3 RESULTS AND DISCUSSION

#### 3.1 Rainfall Estimation Results

Beside the statistical verification results, the determination of the best method was also based on the Taylor diagram results (the red point closest to the observation point being the best method).

##### a. GAW Bukit Kototabang Bukittinggi

Based on the statistical verification results (Table 3-1) and the Taylor diagram (Figure 3-1), out of three dates, two (25 and 28 June 2017) indicate that IMSRA is the best method. It has the best rainfall estimation when rain intensity is less than 5-6 mm/hour (Alfuadi, 2016), which

was the case on 25 and 28 June 2017. Furthermore, based on the rainfall bias graph (Figure 3-2), on 15 April 2017 there was an increased in rainfall bias (overestimation) in the auto estimator and non-linear relation methods. This is because of a time lag between the detected cloud top temperature and the real rainfall. On 25 June 2017, there was a drastic reduction (underestimation) at 12.00 UTC. This was due to 22.9 mm/hr of heavy rainfall resulting from cloud top temperature  $-6.435^{\circ}\text{C}$ . In other words, rain comes from cloud with warm cloud top temperature.

On the other hand, on 28 June 2017, the non-linear relation method tended to overestimate and there was a reduction at 13.00UTC, which was due to a time lag (on 12.00 UTC, the cloud top temperature was  $-52.5^{\circ}\text{C}$ , but the rain not falling directly to the earth. The heavy rain fell to the earth on 13.00 UTC when the cloud top temperature had increased).

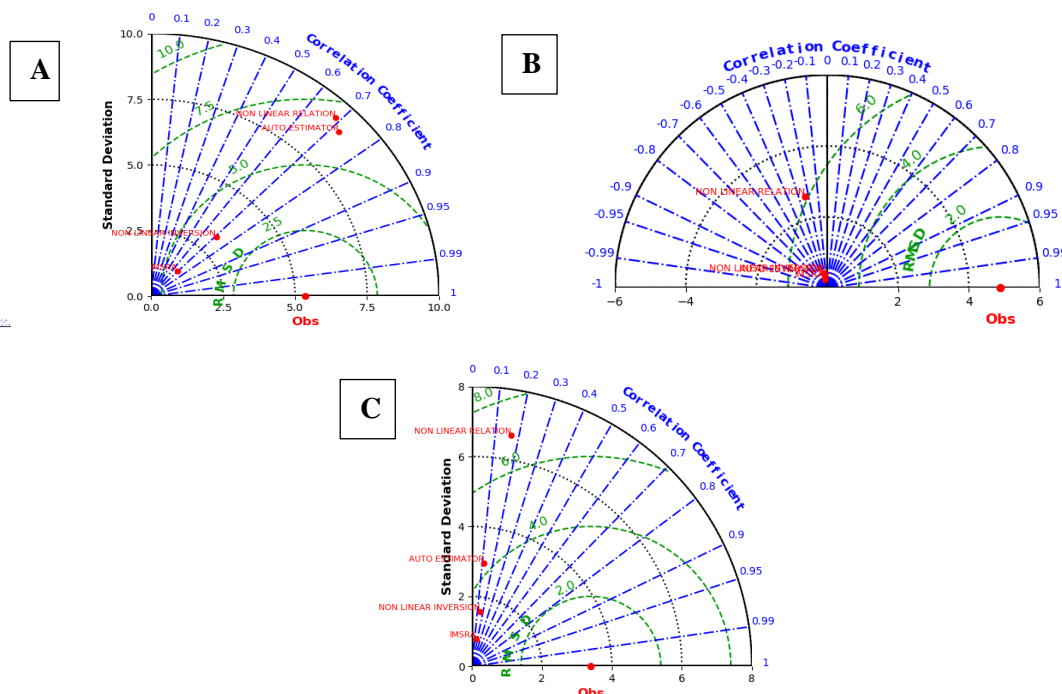


Figure 3-1: A. Taylor diagram on 15 April 2017; B. Taylor diagram on 25 June 2017; C. Taylor diagram on 28 June 2017

Table 3-1: Rainfall Estimation Results for GAW Bukit Kototabang, Bukittinggi

Dates	Methods	RMSE (mm/day)	Correlation	STDEV (mm/day)
15 April 2017	Auto Estimator	6.36	0.72	9.03
	IMSRA	4.54	0.69	1.32
	Non-Linear Relation	6.88	0.68	9.35
	Non-Linear Inversion	3.83	0.70	3.18
25 June 2017	Auto Estimator	4.98	-0.19	0.40
	IMSRA	4.95	-0.24	0.25
	Non-Linear Relation	6.08	-0.23	2.64
	Non-Linear Inversion	5.01	-0.23	0.43
28 June 2017	Auto Estimator	4.24	0.11	2.97
	IMSRA	3.37	0.15	0.79
	Non-Linear Relation	6.99	0.16	6.71
	Non-Linear Inversion	3.53	0.14	1.58

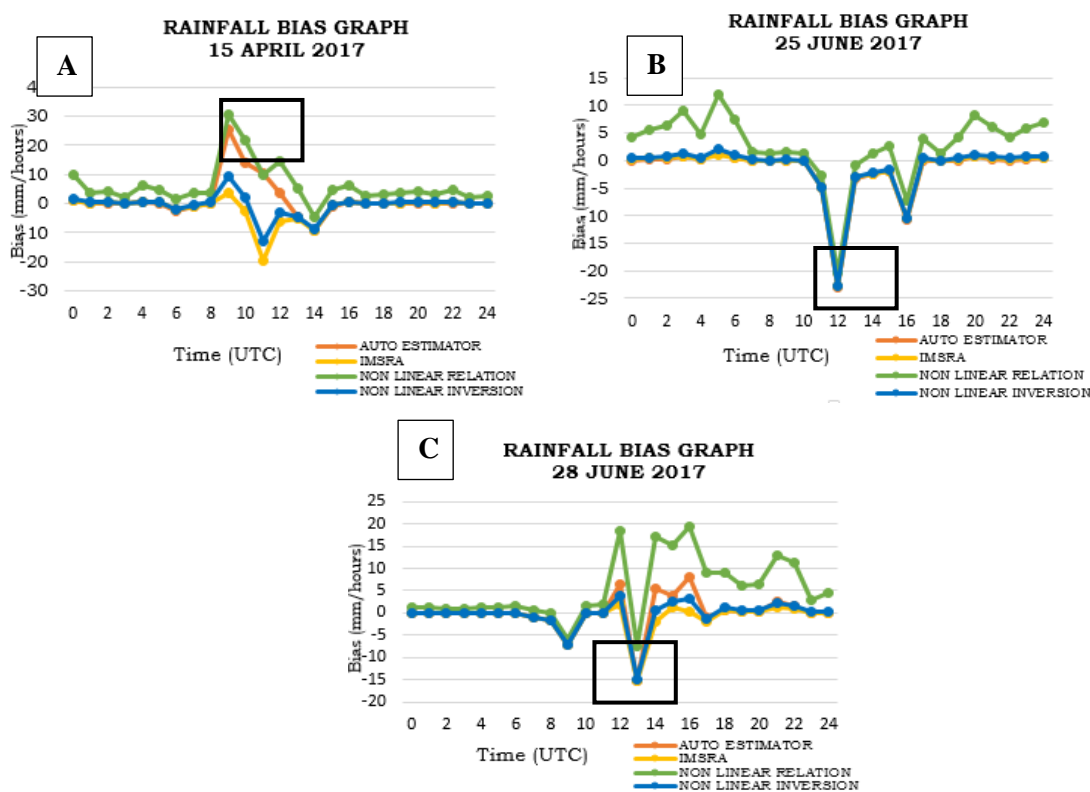


Figure 3-2: Rainfall Bias Graph for GAW Bukit Kototabang Bukittinggi (A. 15 April 2017; B. 25 June 2017; C. 28 June 2017)

**b. Supadio Meteorological Station Pontianak**

The statistical verification results (Table 3-2) and the Taylor diagrams (Figure 3-3) shows that IMSRA was the best method for the Supadio Meteorological Station. On 10 September 2017, 11 November 2017 and 13 October 2018, the method produced the best results because the dominant hourly rainfall (from AWS) had an intensity of

less than 5-6 mm / hour (Alfuadi, 2016). This was the same case as Bukittinggi, where the dominant hourly rainfall was also less than 5-6 mm / hour, so Bukittinggi and Pontianak have the same best rainfall estimation method. Moreover, one of the reasons why Bukittinggi and Pontianak have the same best rainfall estimation method is because both regions are in the equatorial rainfall category.

Generally, rainfall bias on 10 September 2017 showed that there was time lag between the detected cloud top temperature and the actual rainfall in Pontianak, which as shown in Figure 3-4 A. This was because the low temperature of the cloud tops, which in the mature

phase does not immediately produce heavy rainfall that falls to the Earth's surface. In addition, the influence of rapid cloud and wind movement affected the accuracy of rainfall in Pontianak and thus influencing the rainfall bias.

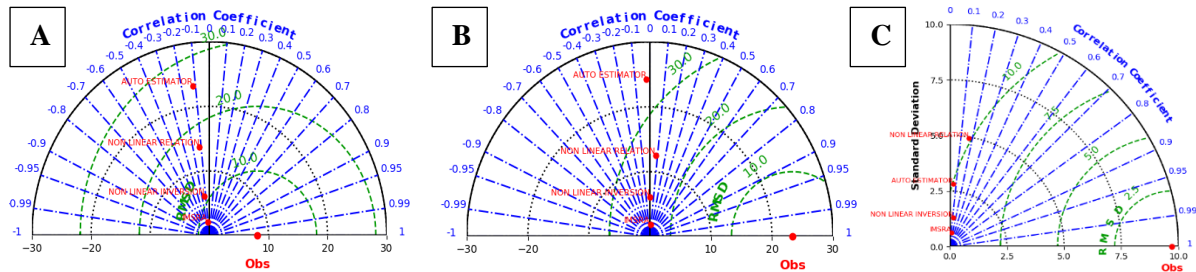


Figure 3-3: A. Taylor Diagram on 10 September 2017; B. Taylor Diagram on 11 November 2017; C. Taylor Diagram on 13 October 2018

Table 3-2 : Rainfall Estimation Results for Supadio Meteorological Station Pontianak

Dates	Methods	RMSE (mm/day)	Correlation	STDEV (mm/day)
<b>10 Sept 2017</b>	Auto Estimator	25.61	-0.12	23.31
	IMSRA	8.68	-0.13	2.09
	Non-Linear Relation	16.87	-0.12	13.82
	Non-Linear Inversion	10.84	-0.12	6.17
<b>11 Nov 2017</b>	Auto Estimator	34.06	-0.02	24.25
	IMSRA	23.36	0.04	1.92
	Non-Linear Relation	25.70	0.07	12.56
<b>13 Okt 2017</b>	Auto Estimator	9.97	0.05	2.83
	IMSRA	9.64	0.14	0.62
	Non-Linear Relation	10.12	0.16	4.94
	Non-Linear Inversion	9.65	0.11	1.30



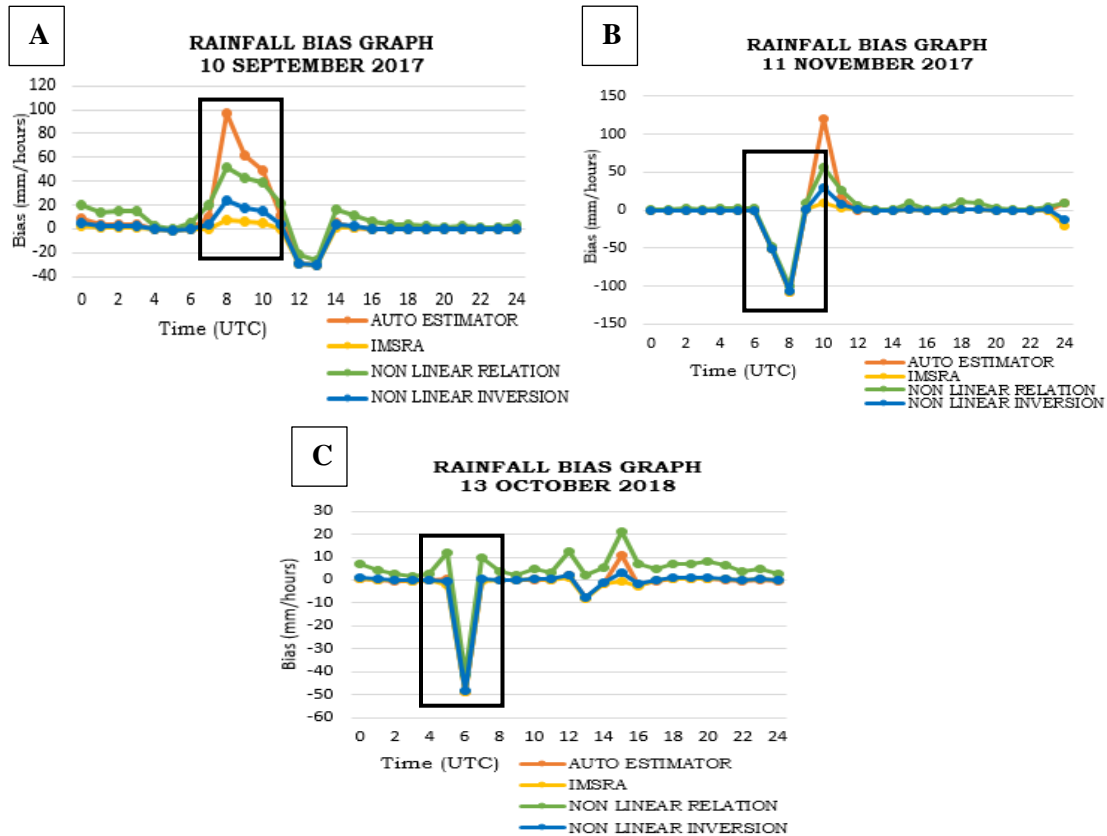


Figure 3-4: Rainfall Bias Graph for Supadio Meteorological Station Pontianak (A. 10 September 2017; B. 11 November 2017; C. 13 October 2018)

Furthermore, on 11 November 2017, there was a decrease in the bias value (Figure 3-4 B) at 08.00 UTC due to actual rainfall (from AWS) reaching 108.6 mm/hour, but the cloud top temperature was only  $-37.571^{\circ}\text{C}$ . In addition, there is an increase in the bias value at 10.00 UTC due to the low temperature of the top cloud of  $-75.289^{\circ}\text{C}$ , although the actual rainfall (from AWS) is 0 mm/hour. This was contrary to the principles that the lower the cloud top temperature, the higher it's potential to produce a rainfall. Rain events on this date indicate that low cloud top temperatures do not always produce heavy rains, and vice versa (Nurasniyati et al., 2018)

The rainfall bias graph of 13 October 2018 (Figure 3-4 C) shows that there was a significant decrease in the bias value at 06.00 UTC. This was because the cloud top temperature at 06.00 UTC was only  $-35.47^{\circ}\text{C}$ , but produces heavy rainfall up to 49.6 mm/hour (from AWS). This further reinforces the notion that the

cloud top temperature only played a minor role in the rainfall process on this date. The rainfall process is not only influenced by the cloud top temperatures, but can also be influenced by the conditions and composition of the atmosphere, circulation and local atmospheric dynamics (Avia & Haryanto, 2013) as well as by local convection currents (Marpaung, 2010) in Pontianak.

### c. Pattimura Meteorological Station Ambon

The statistical verification results (Table 3-3) and Taylor diagrams (Figure 3-5) show that the non-linear relation method was the best for Pattimura Meteorological Station Ambon.

The best dominant rainfall estimation method for the Ambon region is therefore different to that of the Pontianak and Bukittinggi areas. This could be a result of the topographical conditions of Ambon, which affect the process of rainfall formation. In addition,

Ambon has a local type of rainfall pattern characterised by the extent of the influence of local conditions, such as the presence of mountains, oceans, other water landscapes, and the occurrence of intensive local warming (Tukidi, 2010). The condition of Ambon, which has a local type of rainfall pattern and is heavily influenced by local characteristics (Tjasyono and Harijono, 2013) will affect the distribution of rain. The distribution of rain will affect the characteristics of rainfall in an area, meaning the estimation results will be affected

There was very intense rainfall reaching 100.2 mm / day on 28 May 2018. Rainfall bias graph at Figure 3-6 A shows that at 13.00, 14.00 and 16.00 UTC, the rainfall bias had decreased quite

dramatically (underestimated). This was because the rainfall fell to the earth's surface came from cloud tops with the temperatures of -36.279, -42.25 and -35.67<sup>o</sup> C. The hours of 13.00, 14.00 and 16.00 UTC are the time when peak rainfall occurs, with an intensity of 23, 17.4 and 16.4 mm/hour (from AWS). This shows that the cloud top temperature only makes a small contribution to the process of very heavy rain. This process can be influenced by local factors such as wind, humidity and water vapour (Nurasniyati et al., 2018). There is a gap in the rainfall bias data at 22.00 UTC, because the Himawari-8 satellite could not detect the cloud top temperature, so it could be converted into rainfall by the four methods.

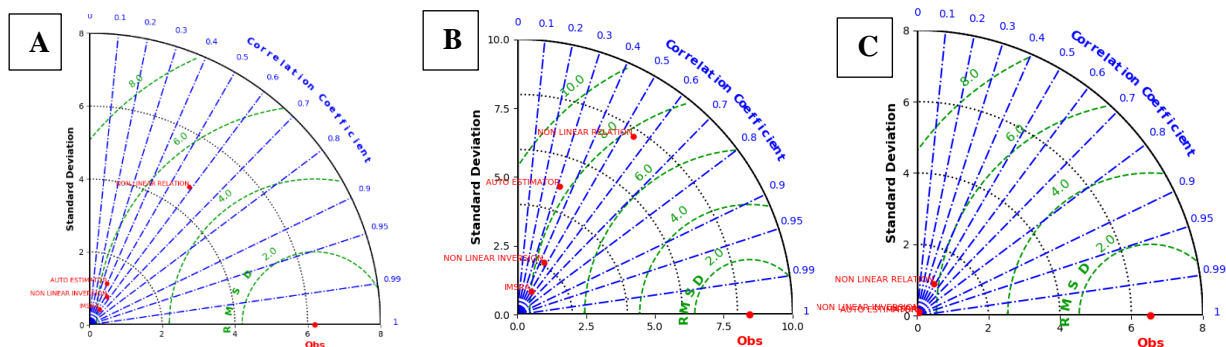


Figure 3-5: A. Taylor Diagram on 28 May 2018; B Taylor Diagram on 29 June 2018; C. Taylor Diagram on 30 June 2018

Table 3.3 Rainfall Estimation Result at Pattimura Meteteorological Station Ambon

Dates	Methods	RMSE (mm/day)	Correlation	STDEV (mm/day)
<b>28 May 2018</b>	Auto Estimator	5.81	0.39	1.23
	IMSRA	5.93	0.55	0.50
	Non-Linear Relation	5.13	0.58	4.67
	Non-Linear Inversion	5.77	0.52	0.91
<b>29 June 2018</b>	Auto Estimator	8.33	0.31	4.90
	IMSRA	7.99	0.50	0.98
	Non-Linear Relation	7.73	0.54	7.70
	Non-Linear Inversion	8.33	0.31	4.90
<b>30 June 2018</b>	Auto Estimator	6.52	0.30	0.04
	IMSRA	6.50	0.43	0.07
	Non-Linear Relation	6.13	0.47	1.00
	Non-Linear Inversion	6.48	0.43	0.12

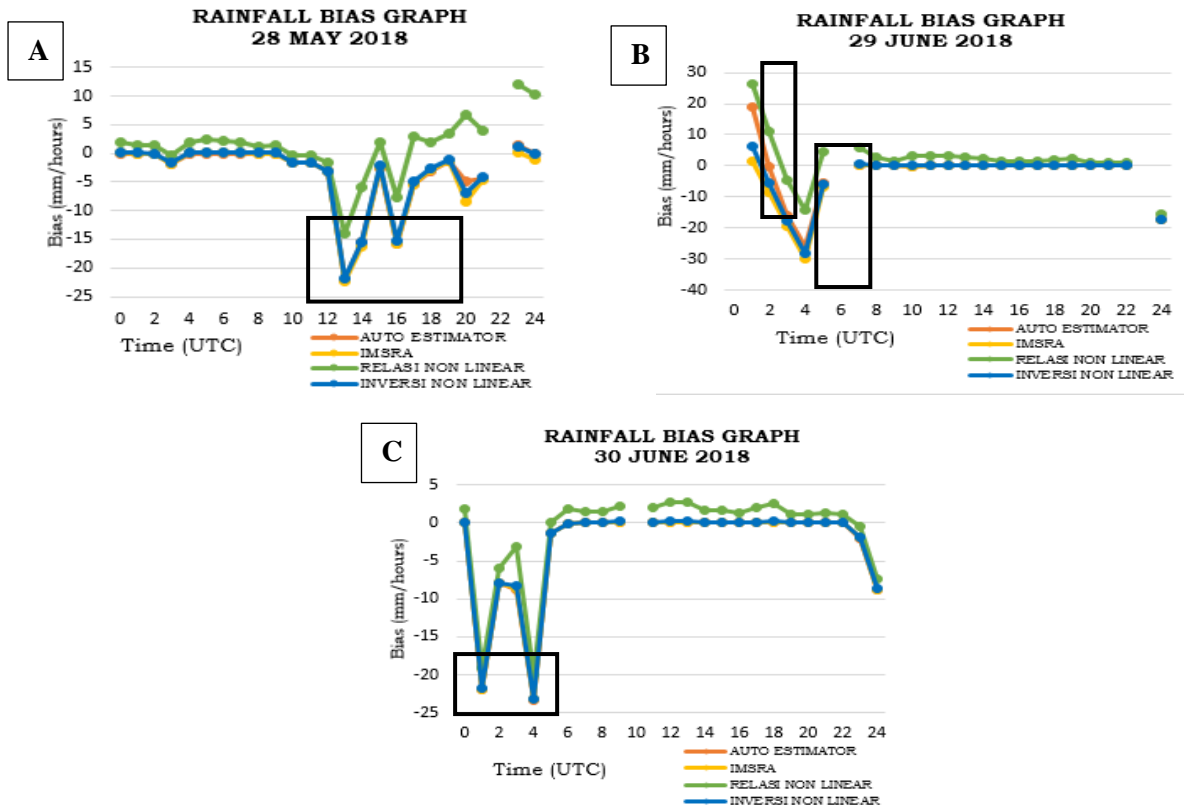


Figure 3-6: Rainfall Bias Graph in Pattimura Meteorological Station Ambon (A. 28 May 2018; B. 29 June 2018; C. 30 June 2018)

Furthermore, based on Figure 3-6 B, the time lag influenced the rainfall bias. There was an increase in this bias (overestimation) at 01.00 UTC, especially for the auto estimator and non-linear relation method. The different results in the bias were caused by the estimated rainfall results due to the low cloud top temperature ( $-61.53998^{\circ}\text{C}$ ), whereas the actual rainfall (based on AWS data) was only 2 mm/hour. In other words, this shows that a low cloud top temperature does not always produce heavy rain at that time. Likewise, at 04.00 UTC, there was a decrease in the rainfall bias (underestimation), because the rain fell heavily when the cloud top temperature gradually rose to  $-51.70801^{\circ}\text{C}$  from  $-61.53998^{\circ}\text{C}$ . There are a data gaps in the rainfall bias data at 00.00, 06.00 and 23.00 UTC, because the Himawari-8 satellite could not detect the temperature of the cloud tops, so it cannot be converted into rainfall by the four methods.

The rainfall bias graph on Figure 3-6 C shows that there was a decrease in the rainfall bias (underestimation). This was caused by heavy rainfall (22 and 23.4 mm/hour) at 01.00 and 04.00 UTC, although the detected cloud top temperatures were only  $-8.64404$  and  $-12.21997^{\circ}\text{C}$ . The cloud observations at Pattimura Meteorological Station showed Cumulus (Cu) clouds at 01.00 and 04.00 UTC. In other words, heavy rain is generated from Cu clouds, not Cumulonimbos (Cb) ones with low cloud top temperatures.

### 3.2 Visual Comparison Map of the Rainfall Estimation

In the rainfall estimation map, the blue colour shows light intensity rain, green shows moderate rain intensity, purple colour shows heavy intensity rain and red very heavy/ extreme rain. Mapping using Google Maps API only takes one date and a certain hour of rain events as an example.

**a. GAW Bukit Kototabang Bukittinggi**

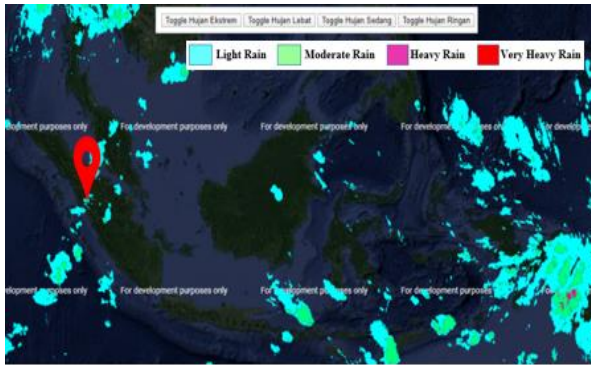


Figure 3-7: Mapping of Rainfall Estimation Results on 28 June 2017 at 12.00 UTC using Google Maps API

As the IMSRA method is the best method in Bukittinggi based on the results and discussion in section 3.1, the rainfall estimation result from the IMSRA method were mapped using Google Maps API for 28 June 2017. Based on the rainfall estimation results in Figure 3-7, it can be seen that the IMSRA method produced an estimate of light rainfall in GAW Bukit Kototabang at 12.00 UTC. In addition, the rainfall estimation from the IMSRA method produced the lowest amount of rainfall in comparison to the other three methods, but this was closer to the actual rainfall levels.

**b. Supadio Meteorological Station Pontianak**

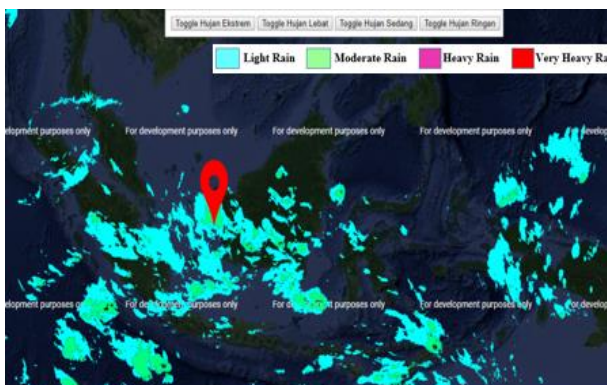


Figure 3-8 : Mapping of Rainfall Estimation Results on 10 September 2017 at 10.00 UTC using Google Maps API

As the IMSRA method is the best method in Pontianak based on the results and discussion in section 3, the rainfall

estimation results from the IMSRA method were mapped using Google Maps API for 10 September 2017. Based on the the rainfall estimation results in Figure 3-8, it can be seen that the IMSRA method produced an estimate of moderate rainfall at the Supadio Meteorological Station at 10.00 UTC.

**c. Pattimura Meteorological Station Ambon**

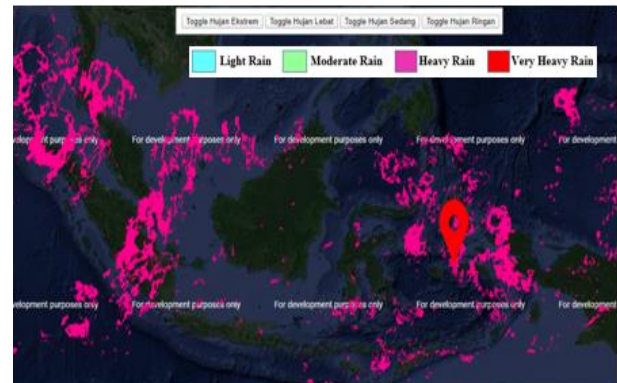


Figure 3-9 : Mapping of Rainfall Estimation Results on 29 June 2018 at 05.30 UTC using Google Maps API

As the non-linear relation method is the best method for Ambon based on results and discussion on section 3.1, the rainfall estimation results from non-linear relation method were mapped using Google Maps API for 29 June 2018. Based on Figure 3-9, it can be seen that the non-linear relation method produced as heavy rainfall estimation for Pattimura Ambon Station. Rainfall estimation using this method produced a high level of rainfall compared to the other three methods. This was influenced by the ability of the algorithm in the four methods to estimate rainfall.

**4 CONCLUSION**

Based on the results and discussion above, we can conclude that :

- a. The best method for estimating rainfall in Bukittinggi is the IMSRA method, with an RMSE of 3.37 to 4.95 mm/day, a correlation coefficient of -0.24 to 0.15 and a

- standard deviation of 0.25 to 0.79 mm/day.
- b. The best method for estimating rainfall in Pontianak is the IMSRA method, with an RMSE of 8.68 to 23.36 mm/day, a correlation coefficient of -0.13 to 0.14 and a standard deviation of 0.62 to 2.09 mm/day.
  - c. The best method for estimating rainfall in Ambon is the non-linear relation method, with an RMSE of 5.13 to 7.73 mm/day, a correlation coefficient of 0.47 to 0.58 and a standard deviation of 1.0 to 7.7 mm/day.
  - d. The conclusion from the visual comparison map of the rainfall estimation shows that it can clearly describe the types of cloud and the results of the estimated rainfall.
  - e. The physiographical conditions of Indonesian territory, such as its latitude, altitude, wind patterns (trade and monsoon winds), distribution of land and waters, and mountains have an effect on variations and types of rainfall in the country (equatorial, monsoon and local types), including rainfall estimation.
  - f. In further research, it will be necessary to process satellite data and considerable rainfall data (1-5 years), because this study investigates whether different topographies affect the results of rainfall estimation in each region.

#### ACKNOWLEDGEMENTS

This paper was written independently and I would like to thank Mrs. Fitria Puspitasari, SST, M.Sc for providing advice on the methods for estimating rainfall. I would also like to thank my senior Muhammad Ryan for providing advice regarding the programming for the paper.

#### REFERENCES

- Akanbi A.K., & Agunbiade, O.Y. (2013), Integration of a city GIS data with Google Map API and Google Earth API for a web-based 3D Geospatial Application. *International Journal of Science and Research (IJSR)* 2(11), 200-203.
- Alfuadi N. (2016). Interkomparasi Teknik Estimasi Curah Hujan. *Prosiding Seminar Nasional Sains Atmosfer*, 151-162.
- Alfuadi, N., & Wandala, A. (2016). Comparative Test of Several Rainfall Estimation Methods Using Himawari-8 Data. *International Journal of Remote Sensing and Earth Science* 3(2), 95-104.
- Avia, L.Q., & Haryanto, A. (2013). Penentuan Suhu Threshold Awan Hujan di Wilayah Indonesia Berdasarkan data satelit MTSAT dan TRMM. *Jurnal Sains Dirgantara* 10(2), 82-89.
- Bessho, K., Date K., Hayashi M., Ikeda A., Imai T., Inoue H., ...Yoshida, R. (2016). An Introduction to Himawari-8/9-Japan's New-Generation Geostationary Meteorological Satellites. *Journal of the Meteorological Society of Japan* 94(2), 151-183.
- Gairola, R.M., Varma A.K., Prakash, S., Mahesh, C., Pal, P.K. (2011). Development of Rainfall Estimation Algorithms for Monitoring Rainfall Events over India Using KALPANA-IR Measurements on Various Temporal and Spatial Scales. *38th Meeting of the Coordination Group of Meteorological Satellites (CGMS)*, New Delhi, India, 8-12 November.
- Lillesand, T.M., Kiefer R.W., & Chipman J.W. (2015). *Remote Sensing and Image Interpretation* (7<sup>th</sup> ed), USA: John Wiley & Sons, Inc.
- Marpaung, S. (2010). Pengaruh Topografi Terhadap Curah Hujan Musiman dan Tahunan di Provinsi Bali Berdasarkan data Observasi Resolusi Tinggi. *Prosiding Seminar Penerbangan dan Antariksa*, 104-110.



- NRC (2003). *Fundamentals of Remote Sensing*, A Canada Centre for Remote Sensing Remote Sensing Tutorial, Canada.
- Nurasniyati, Muliadi, & Adriat R. (2018). Estimasi Curah Hujan di Kota Pontianak Berdasarkan Suhu, Ketebalan dan Tekanan Puncak Awan. *Jurnal Prisma Fisika* 6(3), 184-189.
- Octari, G.R., Suhaedi D., & Noersomadi, (2015). Model Estimasi Curah Hujan Berdasarkan Suhu Puncak Awan Menggunakan Inversi Nonlinear. *Prosiding Penelitian SPeSIA 2015 Bid. Matematika* 1(1), 23-29.
- Rani, N.A., Khoir, A.N., & Afra S.Y. (2016). Rainfall Estimation Using Auto-Estimator Based On Cloud-Top Temperature Of Himawari 8 Satellite Compared To Rainfall Observation In Pangkalpinang Meteorological Station. *Proceedings The 6th International Symposium for Sustainable Humanosphere*, 1(1), 93-98.
- Saefuddin, A., Notodiputro K.A., Alamudi A., & Sadik, K. (2009). *Statistika Dasar*. Jakarta: PT Grasindo.
- Santos, C.A.C.D., Silva B.B.D., Rao T.V.R.R., Satyamurti P., & Manzi A.O. (2011). Downward Longwave Radiation Estimates For Clear Sky Conditions Over Northeast Brazil. *Revista Brasileira de Meteorologia* 26(3), 443-450.
- Supranto, J. (2008). *Statistik Teori dan Aplikasi*. Jakarta: Penerbit Erlangga.
- Stull, R. (2015). *Practical Meteorology-An Algebra-based Survey of Atmospheric Science*. University of British Columbia, Canada.
- Sucahyono, D., & Ribudiyanto, K. (2009). *Cuaca dan Iklim Ekstrim di Indonesia*. Puslitbang, Badan Meteorologi Klimatologi dan Geofisika.
- Suwarsono, P., Kusumaning A.D.S., & Kartasamita M. (2009). Penentuan Hubungan Antara Suhu Kecerahan dengan MTSAT dengan Curah Hujan Data QMORPH. *Jurnal Penginderaan Jauh* 6(1), 32-42.
- Tan, S.Y., (2014), *Meteorological Satellite Systems*. France : Springer.
- Tjasyono, B.H.K., & Harijono S.W.B. (2013). *Atmosfer Ekuatorial*, Puslitbang, Badan Meteorologi Klimatologi dan Geofisika.
- Tukidi (2010). Karakter Curah Hujan di Indonesia, *Jurnal Geografi* 7(2), 136-145.
- Wang, W., & Lu Y. (2018). Analysis of the Mean Absolute Error (MAE) and the Root Mean Square Error (RMSE) in Assessing Rounding Model. *IOP Conference Series: Materials Science and Engineering*, 324(1), 1-10.

# SHORELINE CHANGES AFTER THE SUNDA STRAIT TSUNAMI ON THE COAST OF PANDEGLANG REGENCY, BANTEN

Fandi Dwi Julianto<sup>1\*</sup>, Cahya Riski Fathurohman<sup>1</sup>, Salsabila Diyah Rahmawati<sup>1</sup>,  
Taufiq Ihsanudin<sup>1</sup>

<sup>1</sup>Geomatics Engineering, Universitas Pembangunan Nasional "Veteran" Yogyakarta

\*e-mail: fandidwij@yahoo.com

Received: 22 August 2021; Revised: 10 October 2021; Approved: 24 November 2021

**Abstract.** The Sunda Strait tsunami occurred on the coast of west Banten and South Lampung at 22<sup>nd</sup> December 2018, resulting in 437 deaths, with 10 victims missing. The disaster had various impacts on the environment and ecosystem, with this area suffering the greatest effects from the disaster. The utilisation of remote sensing technology enables the monitoring of coastal areas in an effective and low-cost manner. Shoreline extraction using the Google Earth Engine, which is an open-source platform that facilitates the processing of a large number of data quickly. This study used Landsat-8 Surface Reflectance Tier 1 data that was geometrically and radiometrically corrected, with processing using the Modification of Normalized Difference Water Index (MNDWI) algorithm. The results show that 30.1% of the coastline in Pandeglang Regency occurred suffered abrasion, 20.2% suffered accretion, while 40.7% saw no change. The maximum abrasion of 130.2 meters occurred in the village of Tanjung Jaya. Moreover, the maximum shoreline accretion was 43.3 meters in the village of Panimbang Jaya. The average shoreline change in Pandeglang Regency was 3.9 meters.

Keywords: *Landsat-8, Google Earth Engine, Abrasion, Tanjung Jaya, MNDWI*

## 1 INTRODUCTION

The tsunami disaster occurred on the coast of the Sunda Strait, including the coasts of Pandeglang, Serang and South Lampung Regency. The tsunami occurred on December 22<sup>th</sup>, 2018 at 21:27 local time (UTC + 7), the result of an underwater landslide after the eruption of Mount Anak Krakatau. At the same time, there was a high tide due to the influence of the full moon. According to BNPB (2019), the impact of the tsunami resulted in the deaths of 437 people, with 10 missing and 31,943 injured

Pandeglang Regency is located on the west coast of Banten in subduction zone. The zone originates from the meeting of the Indo-Australian plate and the Eurasian Plate. Besides earthquakes, there are active volcanoes that can cause damage, either man-made or natural. Mount Anak Krakatau is an active volcano in the Sunda Strait, located

directly opposite Pandeglang Regency. Therefore, there is a need for efforts to minimise the impact on and inventory changes to coastal areas in the management and protection of coastal ecosystems for sustainable development. Remote sensing techniques are currently being developed in various fields, enabling efficient and low-cost monitoring, including that of coastal zones. These are one of the most dynamic environments on the earth's surface because of natural and anthropogenic effects (Goncalves, Duro, Sousa & Figueiredo, 2015). The increasing volcanic activity of Anak Krakatau in 2018 raised concerns about a major disaster in the area around the Sunda Strait, with the potential to spread in all directions. Therefore, the shoreline faced a potential major impact from the volcanic activity in the area.

The increase and decrease in the coastal area each year can be calculated



and monitored. In most coastal areas, natural changes occur more rapidly than in other environments, apart from areas subject to earthquakes, floods and volcanoes. There are two kinds of shoreline change: forward changes (accretion) and backward changes (abrasion). The former is characterized by indications of deposition and/or merger. However, the coastline is said to be retreating if there is a process of abrasion and/or submergence (Sudarsono, 2011).

A shoreline is defined as a line of contact between land and a body of water. Although is easy to define, it is difficult to capture because of the natural variability of water levels (Bartlett, 2004). A shoreline which can be detected by remote sensing is tide-coordinated shoreline, which is an extraction from a specific tide water level. Water indices are mathematical models which enhance water signals for a given pixel in images obtained from visible/middle infrared scanning sensors (El-Asmar et al., 2010). Shoreline change can be determined by comparing two or more shorelines at different times. A significant change can result in changes to landscapes, which could have environmental and social impacts.

Google Earth Engine (GEE) is a cloud computing platform designed to store and process huge data sets (at petabyte-scale) for analysis and ultimate decision making (Mutanga, 2019). The platform allows users to create and run special algorithms and fast computations and is equipped with many open-source datasets that are linked to cloud computing engines, one of which is Landsat-8 medium resolution satellite imagery.

The mission of Landsat-8 has the primary objective of record an area of the earth's surface globally every 16 days. It

was launched in 2013. The satellite is equipped with an OLI sensor with eight different bands with a spectral resolution of 30 meters, one band with a spectral resolution of 15 meters, and a TIRS sensor with two bands of 100 meter resolution.

## 2 MATERIALS AND METHODOLOGY

### 2.1 Location and Data

This research on shoreline changes was conducted in Cigeulis and Panimbang districts, Pandeglang Regency, Banten Province, which were the areas affected by the Sunda Strait tsunami. The research area is directly adjacent to the Sunda strait and within  $\pm$  52 kilometers of the centre of the tsunami source, Mount Anak Krakatau.



Figure 2-1: Research location map

The data used in the study were administrative boundary data of Pandeglang Regency, obtained from <https://tanahair.indonesia.go.id/>.

Landsat 8 Surface Reflectance Tier 1 satellite image data from the database of the Google Earth Engine were used so that geometric and radiometric corrections were no longer needed. The satellite imagery used were from 16 July 2019 and 13 July 2018. The required data were tide prediction data, bathymetric data, and Digital Elevation Model (DEM) data, obtained from <http://tides.big.go.id/>.

## 2.2 Method

The method used in the research consisted of the preparation stage, the data processing stage, and the analysis stage.

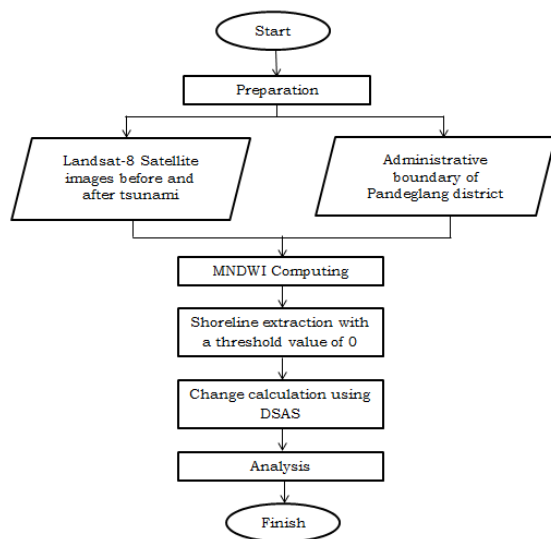


Figure 2-2: Research flow diagram

The first stage of the research was preparation, consisting of a literature review and data collection. The satellite image data used was Landsat-8 Surface Reflectance Tier 1 satellite imagery. These satellite image data are available from April 2013. The characteristic spectrals of Landsat-8 imagery are given in Table 2-1.

Table 2-1: Characteristic spectrals of Landsat-8 images

Spectral Characteristics	
Landsat 8	Length(µm)
Band 1	
Coastal/Aerosol	0.435 – 0.451
Band 2 Blue	0.452 – 0.512
Band 3 Green	0.533 – 0.590
OIL Band 4 Red	0.636 – 0.673
Band 5 NIR	0.851 – 0.879
Band 6 SWIR-1	1.566 – 1.651
Band 7 SWIR-2	2.107 – 2.294
Band 8 Panchromatic	0.503 – 0.676
Band 9 Cirrus	1.363 – 1.384
TIRS Band 10 TIRS-1	10.60 – 11.19
Band 11 TIRS-2	11.50 – 12.51

The data processing stage was performed using the Google Earth Engine, and included the importing of data on the boundaries of the research area and the Landsat-8 Surface Reflectance Tier 1 satellite image. The image was geometrically and radiometrically corrected (surface reflectance) and was cropped according to the research area of interest (AOI) for further analysis.

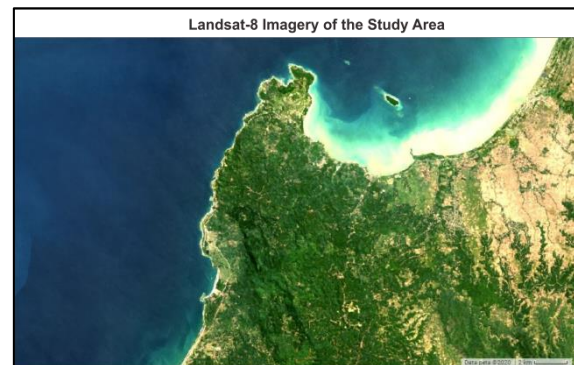


Figure 2-3: Landsat-8 imagery of the study area

Determination of the shoreline was made using the Modification of Normalized Difference Water Index (MNDWI) algorithm, which is more sensitive to water features mixed with vegetation than Normalized Difference Water Index (NDWI) algorithm due to its positive values (Singh et al., 2014). The algorithm uses Landsat TM and ETM+ images, as shown in equation (1) (Xu, 2006).

$$MNDWI = \frac{Green - MIR}{Green + MIR} \quad (2-1)$$

where: Green: Green band  
MIR: Medium infrared band

However, because the satellite imagery used was Landsat-8 Surface Reflectance satellite images which were processed from the Landsat-8 OLI/TIRS sensors, equation (2) was used (Ko et al., 2015):

$$MNDWI = \frac{Green - SWIR}{Green + SWIR} \quad (2-2)$$

where: Green: Green band  
SWIR1: Shortwave infrared 1 band

The bands used in this algorithm were band 3 (green), which has a wavelength of 0.533-0.590  $\mu\text{m}$ , and band 6 (SWIR1), which has a wavelength of 1.566-1.651  $\mu\text{m}$ . Both of bands have a spatial resolution of 30 meters. Using the MDWI algorithm, accurate classification of land and water can be made. MNDWI is a modification of NDWI using the Green band and the middle infrared (MIR) band. The MNDWI algorithm provides accurate extraction of open water features, as the built-up land, soil and vegetation are all negative values and thus are notably suppressed or even removed. Water classification using the MNDWI algorithm shown a high brightness value with a range between 0 and 1, with the value of non-water very low, within a range of between -1 and 0. Therefore, the algorithm could recognise the water bodies, the rocky coast and the shoreline.

Calculation of shoreline change can be made using the DSAS (Digital Shoreline Analysis System). This is a freely available software application that works within the ArcGIS software and computes rate-of-change statistics for a time series of shoreline vectors (Thieler et al., 2009), which is particularly useful for the evaluation of coastal retreat or accretion rates. A series of transects were cast at right angles from a defined baseline, and the points intersecting all the target lines were used for the calculation of distances and rates of shoreline changes (Gómez et al., 2014).

The results of the shoreline extraction obtained from the Google Earth Engine were exported and processed using DSAS. In this processing, a transect line that was perpendicular to the coastline was used at intervals of 50 meters. In DSAS, the method of calculating the distance change analysis for each coastline uses the Net Shoreline Movement (NSM) method, which measures the distance of the change in

the shoreline between the oldest and the newest shoreline (Thieler et al., 2009). The NSMs were calculated as the distance of the shoreline divided by the time elapsed between the baseline and the most recent shoreline. The results of this processing obtained the amount of change in the shoreline of each transect line.

The analysis stage was conducted by comparing the differences in the pattern and position of the coastline before and after the tsunami and based on processing data, predictive tide data, digital elevation model (DEM) data, and bathymetric data. The processed data was corrected for mean sea level (MSL). Correction was made from the difference between the water level and the MSL, divided by the tangent of the coastal slope angle. The coastal slope was obtained from the DEM and bathymetric data. The following was the correction formula for MSL (Prastyo, 2019).

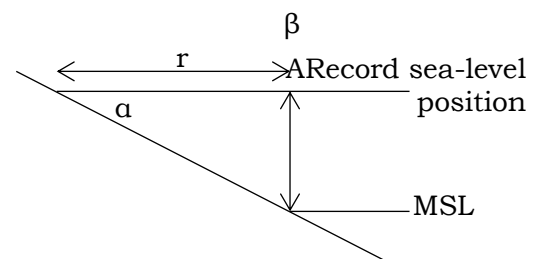


Figure 2-4: Tide correction

$$r = \frac{\beta}{\tan \alpha} \quad (2-3)$$

where:  $r$ : tide correction

$\beta$ : difference in the record sea level position and MSL

$\alpha$ : angle of the beach slope

### 3 RESULTS AND DISCUSSION

The research on shoreline changes resulting from the Sunda Strait tsunami using the Google Earth Engine was conducted in the coastal areas of Cigeulis and Panimbang districts, Pandeglang Regency, Banten Province. This area experienced the highest tsunami, a runup type of up to 14 meters.

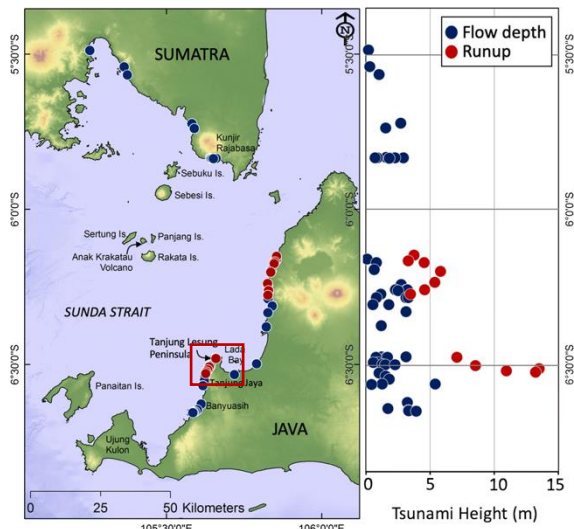


Figure 3-1: Distribution of the measured tsunami flow depth (blue) and runup (red) (Muhari et al., 2019)

In the study, shoreline extraction was conducted in 2018 and 2019 and compared so that the horizontal position differences from the coastline were ascertained. The coastline was identified from the Landsat-8 satellite imagery, analysed using the Google Earth Engine with the MNDWI algorithm, resulting in the different appearance of the extraction results, as shown in Figure 3-2.

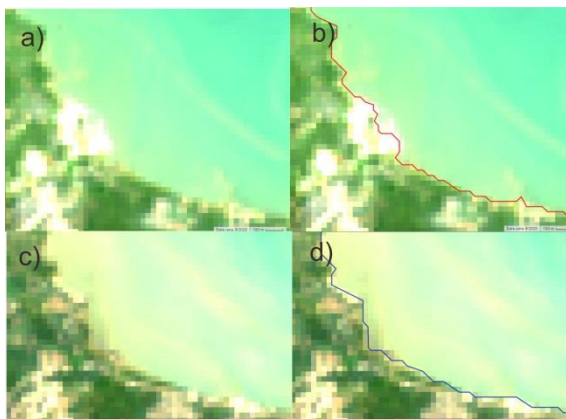


Figure 3-2: a) Satellite imagery from 2018; b) coastline extraction results from 2018; c) satellite imagery from 2019; d) shoreline extraction results from 2019.

In the shoreline extraction, there were differences between the extraction results of the 2018 and 2019 images. These were quite varied in each region. The following were figure. 3-3 shows the results of the 2018 and 2019 coastline overlay from the calculations using the

MNDWI algorithm in Tanjung Jaya village.



Figure 3-3: Shoreline extraction overlay, 2018 and 2019

Shoreline changes were observed from the coastline overlay from 2018 and 2019. The changes that occurred at the research location due to the Sunda Strait tsunami varied not only in abrasion but also accretion. Tsunami waves hitting land can damage the coast and cause deformation to it, so abrasion can occur. However, tsunamis can also carry and drag land material, causing sedimentation in coastal areas and accretion. Shoreline changes occur more easily on a gentle slope, where the water level tends to move horizontally. In the study area, the slope of coastal tended to gently, with a slope of below  $30^\circ$ .

The water level at the time the image was taken was 0.095 m in the 2018 image and 0.077 m for the 2019 image. The result of tide correction made showed that did not have a significant impact compared to the spatial resolution of the image, which was 30 meters. This caused the tide corrections to be excluded from the study. The difference in shoreline position before and after the tidal correction could be ignored because visually the difference was only 0.018 m, which is not significant. Changes to the shoreline identified by DSAS found that the study area had experienced abrasion, accretion and constant on the shoreline. DSAS processing used the NSM method with 909 transect lines. The shoreline changes are illustrated in Figure 3-5.



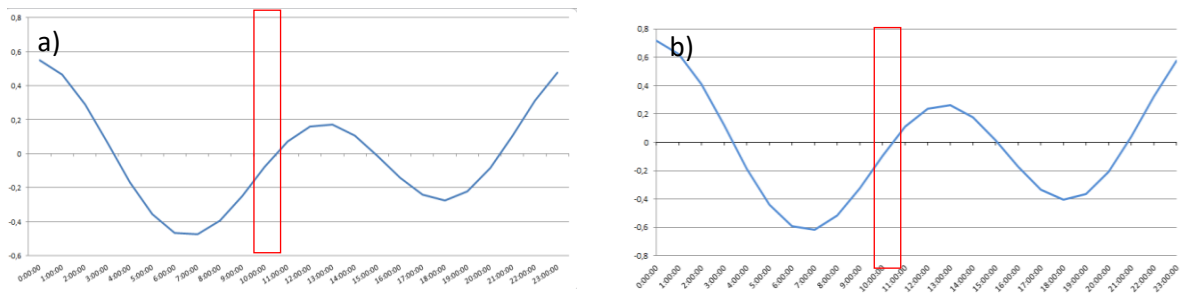


Figure 3-4: a) graph of tide prediction in the study area on 13 July, 2018; b) graph of tide prediction in the study area on 16 July 2019

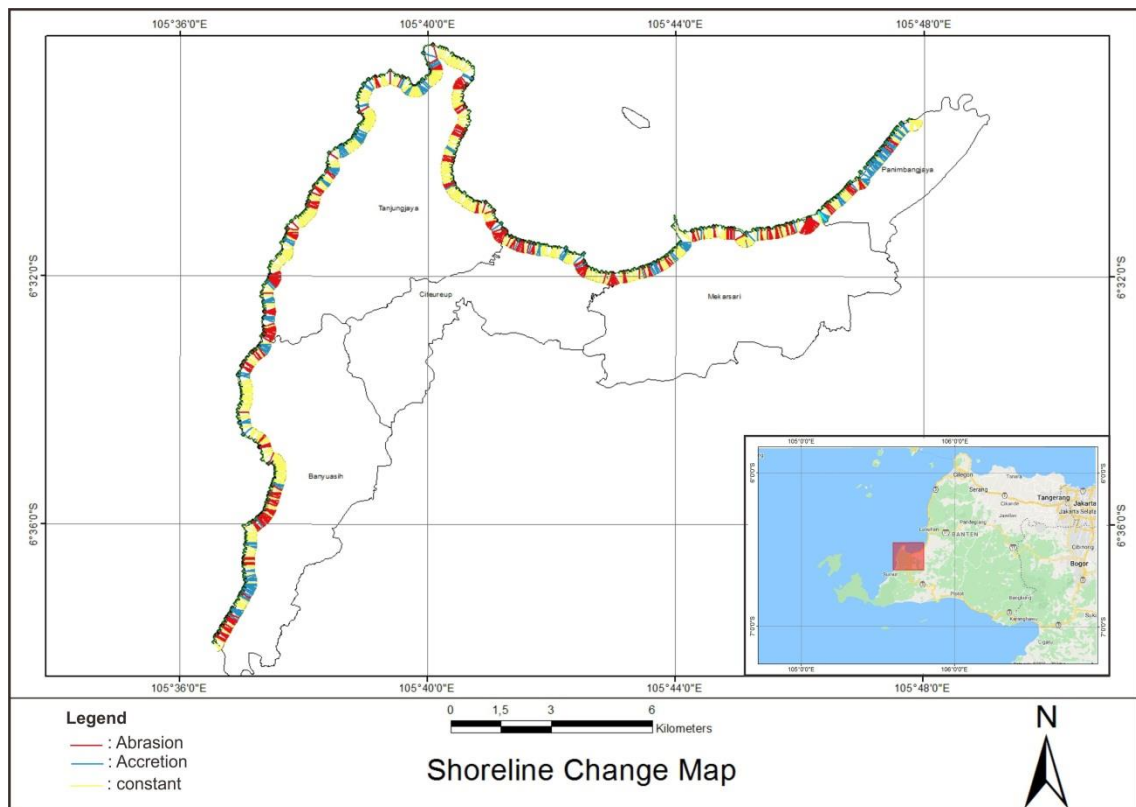


Figure 3-5: Shoreline change map

Changes to the shoreline identified by DSAS found that the study area had experienced abrasion, accretion and constant on the shoreline. DSAS processing used the NSM method with 909 transect lines. The shoreline changes are illustrated in Figure 3-5.

In Pandeglang Regency, there was a change in the coastline of 30.1% from abrasion and 20.2% from accretion, while the remaining area did not have any change. A maximum abrasion of 130.2

meters occurred in the village of Tanjung Jaya, while a maximum accretion of 43.3 meters was experienced in the village of Panimbang Jaya.

In Banyuasih village, the average change in the shoreline was -1.2 meters, while Tanjung Jaya village experienced an average change of -5.3 meters, Citeureup village of -8.0 meters, Mekarsari village of -9.4 meters, and Panimbang Jaya of 8.0 meters.

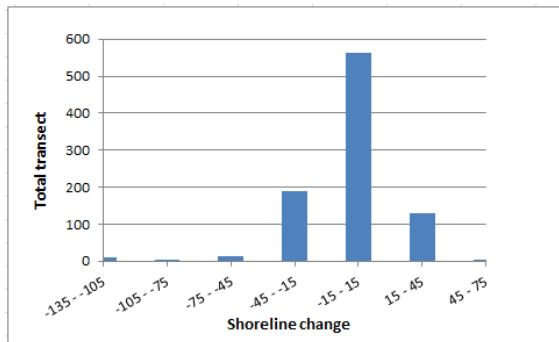


Figure 3-6: Chart of the total transect with the distance of change in the shoreline.

The shoreline changes were dominated by less significant changes, with 564 transect lines on values ranging from -15 to 15 meters. This was followed by classes -45 to -15 with 190 transect lines and classes 15 to 45 meters with 130 transect lines. In Pandeglang Regency, the change in the coastline due to the Sunda Strait tsunami was an average of 3.9 meters of abrasion

From these results, it is clear that there is the need for effective land cover management to take steps to minimise damage to coastal areas. In areas that occurred abrasion, it is necessary to plant mangrove trees as a measure for coastal conservation. It is also important to monitor changes to coastal areas as a basis for taking action in those that require attention. These efforts are important to maintain the resource wealth of coastal areas.

#### 4 CONCLUSION

The analysis found that 30.1% of the coastline on the coast of Pandeglang Regency suffered abrasion and 20.2% suffered accretion, while 40.7% did not change. A maximum abrasion of 130.2 meters occurred in the village of Tanjung Jaya, while maximum accretion of 43.3 meters was experienced in the village of Panimbang Jaya. The average change in the shoreline in Pandeglang Regency was 3.9 meters. Therefore, a good land cover arrangement, such as planting mangrove

trees in areas of abrasion, and monitoring to maintain resources in coastal areas are necessary.

#### ACKNOWLEDGEMENTS

Thanks to the Google Earth engine, USGS and Banten Provincial Government for providing the platform and data, and to all the parties who supported the research.

#### AUTHOR CONTRIBUTIONS

Main Contributor: Fandi Dwi Julianto. Contributing Members: Cahya Riski Fathurohman, Salsabila Diyah Rahmawati, Taufiq Ihsanudin.

#### REFERENCES

- Bartlett D., & Smith J. (2004). GIS for coastal zone management. Boca Raton, Fla: CRC.
- Bouchahma M., & Yan W. (2013). Monitoring shoreline change on Djerba Island using GIS and multi-temporal satellite data. *Arabian Journal of Geosciences*, 7, 3705-3713. doi: 10.1007/s12517-013-1052-9
- El-Asmar H., & Hereher M., (2010). Change detection of the coastal zone east of the Nile Delta using remote sensing. *Environmental Earth Sciences*, 62, 769-777. doi:10.1007/s12665-010-0564-9
- Gómez, C., Wulder, M. A., Dawson, A. G., Ritchie, W., & Green, D. R. (2014). Shoreline Change and Coastal Vulnerability Characterization with Landsat Imagery: A Case Study in the Outer Hebrides, Scotland. *Scottish Geographical Journal*, 130(4), 279-299. doi: 10.1080/14702541.2014.923579
- Gonçalves G., Duro N., Sousa E., & Figueiredo I. (2015). Automatic Extraction of Tide-Coordinated Shoreline Using Open Source Software and Landsat Imagery. *International Archives of the*



- Photogrammetry, Remote Sensing and Spatial Information Sciences 40(7), 953-957. doi: 10.5194/isprsarchives-xl-7-w3-953-2015
- Himmelstoss, E.A., Henderson, R.E., Kratzmann, M.G., & Farris, A.S. (2018). Digital Shoreline Analysis System (DSAS) version 5.0 user guide. U.S. Geological Survey.2018(1179),1-110 doi: 10.3133/ofr20181179.
- Ihlen, V (2019). Landsat Data(L8) Data User Handbook version 5. Landsat Science Official Website, USGS. Digital Shoreline Analysis System (DSAS) in [https://prd-wret.s3.us-west2.amazonaws.com/assets/palladium/production/atoms/files/LS\\_DS1574\\_L8\\_Data\\_Users\\_Handbook-v5.0.pdf](https://prd-wret.s3.us-west2.amazonaws.com/assets/palladium/production/atoms/files/LS_DS1574_L8_Data_Users_Handbook-v5.0.pdf) (Accessed September 3rd, 2020)
- Ko B., Kim H., & Nam J. (2015). Classification of Potential Water Bodies Using Landsat 8 OLI and a Combination of Two Boosted Random Forest Classifiers. *Sensors*, 15, 13763-13777. doi:10.3390/s150613763
- Muhari, A., Heidarzadeh, M., Susmoro, H., Nugroho, H. D., Kriswati, E., Wijarnato, A. B., & Arikawa, T.. (2018), Anak Krakatau Volcano Tsunami as Inferred from Post-Tsunami Field Surveys and Spectral Analysis. *Pure and Applied Geophysics*, 176, 5219–5233, doi: 10.1007/s00024-019-02358-2
- Mutanga O., & Kumar L. (2019). Google Earth Engine Applications. *Remote Sensing*, 11(5), 591(1-4), doi:10.3390/rs11050591
- Ozturk D., & Sesli F., (2015). Shoreline change analysis of the Kizilirmak Lagoon Series. *Ocean & Coastal Management*, 118, 290-308. doi: 10.1016/j.ocecoaman.2015.03.009
- Prastyo W. D., Gaol J. L., & Nurjaya I. W. (2019). Perubahan Garis Pantai Pasca Tsunami di Pesisir Barat Banten dengan Menggunakan Data Citra Landsat 8 OLI (Operational Land Imager) [Post Tsunami Shoreline Changes In The West Coast Of Banten Using OLI Landsat Satellite Image Data]. Undergraduate, Institut Pertanian Bogor
- Singh, K. V., Setia, R., Sahoo, S., Prasad, A., & Pateriya, B. (2015). Evaluation of NDWI and MNDWI for assessment of waterlogging by integrating digital elevation model and groundwater level. *Geocarto International*, 30(6), 650-661, doi: 10.1080/10106049.2014.965757
- Sudarsono, B. (2011). Inventarisasi Perubahan Wilayah Pantai Dengan Metode Penginderaan Jauh (Studi Kasus Kota Semarang)[Inventory Changes In Coastal Area Using Remote Sensing Method (A Case Study Of Semarang City)]. *Teknik*, 32(2), 163-170.
- Suwarsono N., Prasasti I., Nugroho J. T., Sitorus J., & Triyono D. (2019). Detecting the lava flow deposits from 2018 Anak Krakatau eruption using data fusion Landsat-8 optic and Sentinel-1 SAR. *International Journal of Remote Sensing and Earth Sciences (IJReSES)*, 15(2), 157-166, DOI: 10.30536/j.ijreses.2018.v15.a3078
- Syahrani L., & Triyatno T., (2019) Analisis Perubahan Garis Pantai Kabupaten Padang Pariaman dan Kota Pariaman Tahun 1988-2018 Menggunakan Digital Shoreline Analysis System

# BATHYMETRIC EXTRACTION USING PLANETSCOPE IMAGERY (Case Study: Kemujan Island, Central Java)

Asih Sekar Sesama<sup>1\*</sup>, Kuncoro Teguh Setiawan<sup>2</sup>, Atriyon Julzarika<sup>2,3</sup>

<sup>1</sup>Faculty of Fisheries and Marine Sciences, Brawijaya University

<sup>2</sup>Remote Sensing Applications Center–National Institute of Aeronautics and Space (LAPAN)

<sup>3</sup>Department of Geodesy and Geomatics Engineering, Universitas Gadjah Mada (UGM)

\*e-mail: sekarsesama@student.ub.ac.id

Received: 13 October 2020; Revised: 3 November 2020; Approved: 24 November 2020

**Abstract.** Bathymetry refers to the depth of the seabed relative to the lowest water level. Depth information is essential for various studies of marine resource activities, for managing port facilities and facilities, supporting dredging operations, and predicting the flow of sediment from rivers into the sea. Bathymetric mapping using remote sensing offers a more flexible, efficient, and cost-effective method and covers a large area. This study aims to determine the ability of PlanetScope imagery to estimate and map bathymetry and to ascertain its accuracy using the Stumpf algorithm on the in-situ depth data. PlanetScope level 3B satellite imagery and tide-corrected survey data are employed; satellite images are useful in high-precision bathymetry extraction. The bathymetric extraction method used the Stumpf algorithm. The research location was Kemujan Island, Karimunjawa Islands, Central Java. The selection of this region was based on its water characteristics, which have a reasonably high variation in depth. Based on the results of the data processing, it was found that the PlanetScope image data were able to estimate depths of up to 20 m. In the bathymetric results, the  $R^2$  accuracy value was 0.6952, the average RMSE value was 2.85 m, and the overall accuracy rate was 71.68%.

Keywords: *marine resources activity, Stumpf algorithm, Karimun Jawa Island, remote sensing, water characteristics*

## 1 INTRODUCTION

Nowadays, bathymetric technology development is becoming well known in mapping for scientific purposes, including fisheries management, tsunami propagation modeling, and in the oil-gas industries. Previously, bathymetric data were only used for navigation purposes because of the very high cost of the research equipment (such as multibeam and single-beam echosounders and side scan sonar), survey vessels and personal expertise as well as the length of time involved. However, some coastal areas cannot be accessed by the survey vessels because the water depth is shallow, making that type of measurement inefficient.

One of the technological developments in bathymetric measurement is that of remote sensing using a multispectral or hyperspectral sensor. This type of satellite imagery helps obtain information in areas that are difficult to access by survey vessels. The depth information obtained by analysing satellite imagery is known as Satellite-Derived Bathymetry (SDB). Using multispectral sensors, some studies have employed satellite imagery with a high spatial resolution of more than 30 m, such as that from Landsat, SPOT, IKONOS, and WorldView. Satellite images are useful in high-precision bathymetric extraction.

This study uses PlanetScope satellite imagery with a 3 m spatial resolution to extract water depth. There are three levels of PlanetScope imagery: basic scene (Level 1B), ortho scene (Level 3B), and ortho tile (Level 3A) (Planet Lab Inc., 2020). An orthorectified scene is shown visually (RGB) and analytically as a digital number (DN), radiance, and surface reflectance (SR). Poursanidis, Traganos, Chrysoulakis, & Reinartz (2019) were the first to attempt to employ Planet data in SDB for fine and accurate bathymetric prediction. The basic concept of SDB is that light transmission depends on the exponential wavelength, penetration and attenuation in the water in relation to the depth. According to Pe'eri et al. (2014), 350 nm (ultra-violet) - 700 nm (red) is the range of the light wavelength that is less capable of being attenuated in seawater. However, wavelengths greater than 700 nm (near-infrared) are less sensitive in seawater and are suitable for reflecting land and water boundaries.

The novelty of this research is the use of PlanetScope imagery with the Stumpf algorithm for bathymetric extraction in the Karimunjawa islands. PlanetScope satellite imagery data is rarely used in Indonesia, two of the few previous examples being the studies of Gabr et al. (2020) and Waskito dan Wicaksono (2019). This study was conducted in Kemujan Island waters, Karimunjawa Islands, using the Stumpf algorithm method. Stumpf et al. (2003) developed a ratio model comparing two bands of water reflectance factors. They assumed that using a two band comparison would decrease the albedo effect of water, a problem found in bathymetric mapping. This study aims to determine the ability of PlanetScope multispectral satellite imagery in estimating and mapping bathymetry and to establish the accuracy of water

bathymetry using the Stumpf algorithm and PlanetScope imagery on the in-situ depth data. The results of the research will be very useful for the management of coastal areas and small islands, especially the Karimunjawa Islands. Furthermore, bathymetric information can be used to assist in determining ideal zones for marine tourism, conservation zones and other zoning in an effort to improve the sustainability of coastal resources.

## 2 MATERIALS AND METHODOLOGY

### 2.1 Location and Data

The research area was Kemujan Island, located in the Karimunjawa Islands. Administratively, it is included in Jepara District, Central Java, Indonesia (Figure 2-1).

The data used was PlanetScope Level 3B imagery. This is an analytic ortho scene, on which orthorectification has been conducted and projected into the Universal Transverse Mercator (UTM). Level 3B was also conducted on surface reflectance (SR) so as not to need atmospheric correction. The imagery data were acquired on August 25, 2019, and the band information is presented in Table 2-1.

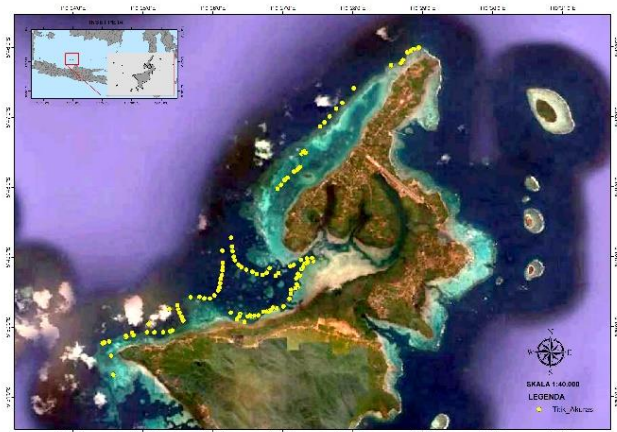


Figure 2-1: Study Site: Satellite image of Karimunjawa islands. The yellow dots show the depth measurement data.

Table 2-1: PlanetScope image band information. (Source: Planet Lab Inc., 2020)

Band Number	Description	Wavelength (µm)	Spatial Resolution
Band 1	Blue	0.455–0.515	3 m
Band 2	Green	0.500–0.590	
Band 3	Red	0.590–0.670	
Band 4	Near-infrared	0.780–0.860	

## 2.2 Data Standardisation

PlanetScope imagery that has been converted becomes SR, which is followed by a masking process. This process is conducted to cover the land area, and radiometric correction is performed to reduce the radiometric distortion in the image. Water masking is performed using band 2 (Green) and band 4 (NIR) to focus on the study and reduce the imagery process load. Both bands are also designed to maximise the reflectance of the water body in the green band and to minimise it in the NIR band (Sun et al., 2012).

## 2.3 Methods

### 2.3.1 Bathymetric Estimation

According to Muzirafuti et al. (2020), the ability of satellite sensors to collect water information in multispectral bands allows for research on bathymetry. A methodological bathymetric approach using two spectral bands (blue and green) in conjunction with in situ bathymetry, taking into account the quality of water and the propagation of light through the water column has been proposed by Stumpf et al (2003). Although most near infrared light is absorbed by clear water, it is still a useful parameter for the land/water boundary extraction process (Jensen, 2007). Green and blue light penetrate the water column and are exponentially attenuated as the water depth increases, leading to the principle of bathymetric extraction (Gao et al., 2007).

The method of water depth estimation through PlanetScope imagery uses an algorithm developed by Stumpf et

al. (2003). This method applies the basic principle that each band has a different absorption rate in the water column. These different rates will generate ratios between the bands, which will consistently change simultaneously when the depth changes. Bands with a high absorption rate will continue to decrease as the depth increases. Equation (2-1) shows the Stumpf algorithm:

$$Z = m_1 \frac{\ln(nR(\lambda_2))}{\ln(nR(\lambda_1))} - m_0 \quad (2-1)$$

where  $Z$  = depth estimation;  $m_1$ ,  $m_0$  = the constant coefficients of the regression results;  $n$  = constant;  $R(\lambda_1,2)$  = radiant for the  $\lambda_1$  and  $\lambda_2$  spectra.

Therefore, to obtain the estimated depth from the regression results of the reflectance value ratio in each band used, equation (2-1) can be re-written according to the linear regression equation to become:

$$Y = aX + b \quad (2-2)$$

Where  $a$  = coefficient  $m_1$ ;  $b$  = coefficient  $m_0$ ; and  $X$  = the ratio results of the band reflectance value.

Calculation of the Stumpf algorithm produces the bathymetry of Kemujan Island in a raster (2D). ArcScene is a tool from ArcGIS that specialises in 3D visualisation; using it, bathymetry in a 2D raster can be displayed in 3D.

### 2.3.2 Accuracy Test

Accuracy assessment is an essential step in the data processing of remote sensing, generating data informatively. An accuracy test of the

depth estimation value is conducted by measuring the Root Mean Square Error (RMSE) and the Confusion Matrix.

RMSE is generated from the average root of the error square number between field value differences and imagery processing result values, and is expressed in meters (m). A lower RMSE value shows a better equation model of depth estimation (Nurkhayati, 2013). RMSE is defined as the error rate in the prediction results; as it becomes lower (close to 0), the prediction results will be more accurate (Suprayogi et al., 2013). RMSE can be calculated using equation (2-3):

$$RMSE (m) = \sqrt{\sum_{i=1}^n \frac{(100e - V_{ti})^2}{n}} \quad (2-3)$$

where e is the difference between the imagery depth value (V<sub>ti</sub>) and the field depth value (V<sub>ai</sub>), and n is the number of depth points used for the validation.

The confusion matrix puts the values from the in-situ data into columns and the estimation data into rows. The diagonal part of the matrix displays the correct classified pixel value. One of the bases for the accuracy test is overall accuracy (OA) by calculating the number of correct pixel divisions compared to the total number. Besides OA, individual class classification accuracy can be calculated by producer accuracy (PA) and user accuracy (UA). PA is obtained by dividing the number of correct pixels in a class by the number of pixels obtained from the in-situ data (column total). When the pixels in the estimation data are correct, a class is divided by the total number of estimation data pixels (row total), a calculation which is known as user accuracy (UA) (Banko, 1998).

### 3 RESULTS AND DISCUSSION

The combination of the Blue and Green bands in the PlanetScope imagery is used to calculate the depth estimation. The use of the Blue/Green band ratio is to normalise the primary reflection effect change due to the water column. In the PlanetScope imagery, the Blue/Green bands are on bands 1 and 2. Figure 3-1 shows the relative depth ratio generated from the imagery data processing, obtaining a ratio value of 14.38 to 67.13. In the colour distribution in the map, light blue is assumed to represent shallow water, and dark blue quite deep water. The low-value distribution is located near the land, which is then surrounded by the high-value distribution.

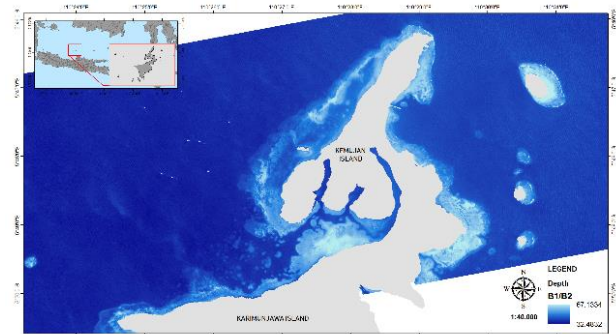


Figure 3-1: Relative depth results using b1/b2

The relative depth results were entered into the in-situ data, and then the regression calculation was made. The ratio of the regression value of both bands and the in-situ data form the regression graph in Figure 3-2.

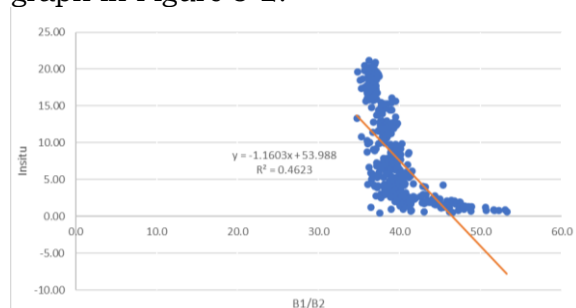


Figure 3-2: Regression model graph from the relative depth results

The function of the regression is used to determine the depth value using the regression equation:

$$Y = -1.1603x + 53.988 \quad (3-1)$$

The equation results are then entered into the Stumpf algorithm to obtain absolute bathymetric values. Bathymetric data from the processing results in satellite imagery cannot be used directly because the data are lacking. The data regarding absolute depth were entered into the in-situ data. The corrected data were then compared with the in-situ measurement data to observe the accuracy value. The bathymetry estimation results generated negative values under 0, with a maximum value generated of 13.8 m. Therefore, depth values under 0 (zero) were eliminated from the bathymetry map because it is a depth value with a high error rate. This is confirmed by Nurkhayati (2013), who states that depth

values under 0 should be eliminated because they are values with relatively high bias. The bathymetry map is shown in Figure 3-3.

The bathymetry map classification is oriented towards the results of absolute depth, resulting in four classes. The regression results (Figure 3-4) obtained a determination coefficient value ( $R^2$ ) of 0.6952, showing that absolute depth could explain 69% of the in-situ depth values. R-Square ( $R^2$ ) is between 0 and 1; a number closer to 1 is better.

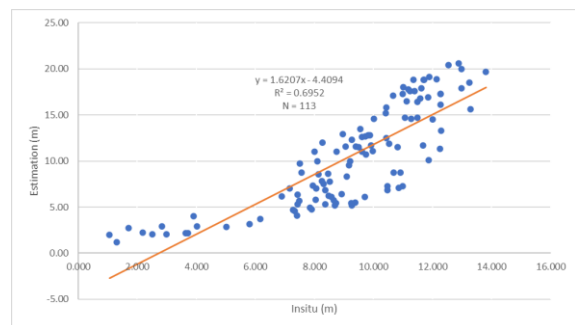


Figure 3-4: Regression model graph from the absolute depth results

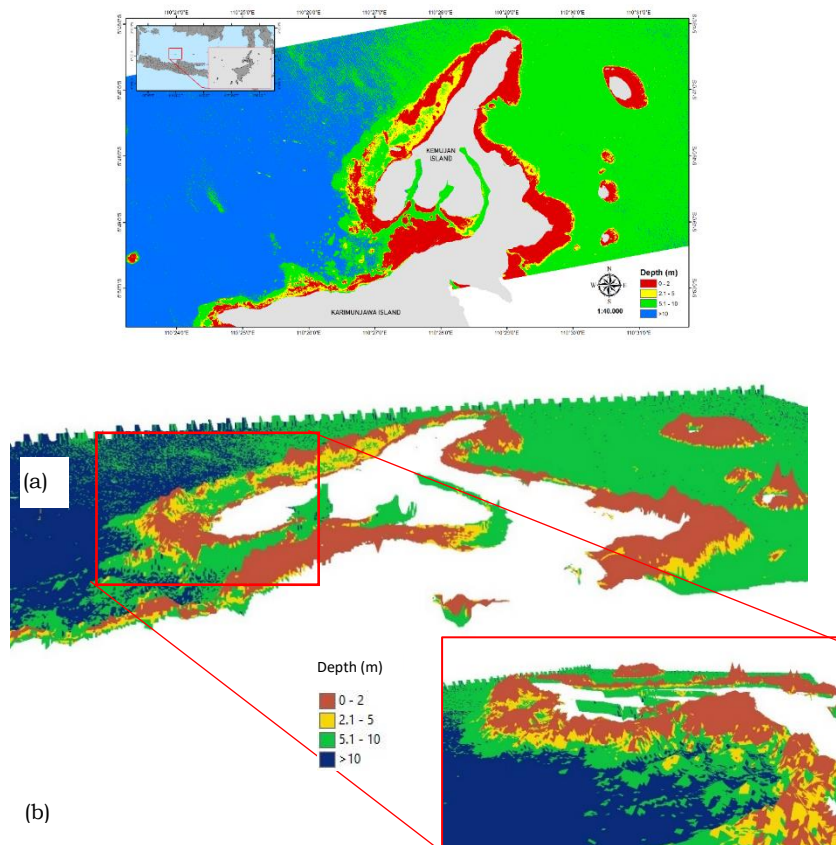


Figure 3-3: Absolute depth results using the Stumpf algorithm: (a) 2D and (b) 3D



Table 3-1. Accuracy test calculations using the confusion matrix

Extraction(m) \ Insitu(m)	Insitu(m)				Total	User Accuracy (%)
	0 - 2	2.1 - 5	5.1 - 10	>10		
0 - 2	2	1			3	67
2.1 - 5		8			8	100
5.1 - 10		8	31	17	56	55
>10			6	40	46	87
Total	2	17	37	57	113	
Producer Accuracy (%)	100	47	84	70		71.68%

An accuracy test was conducted to establish the accuracy of the bathymetric data generated by the imagery processing. Such tests are generally performed to compare data generated from the analysis of remote sensing and from field surveys (Siregar et al., 2008).

Table 3.1 shows that the matrix of theoretical confusion (the error matrix) of the bathymetric estimation uses PlanetScope satellite imagery. Columns in the matrix show the pixel class and the actual value (in-situ), while rows represent the pixel class of the estimation results by image. The diagonal part of the table shows the correct pixel classification.

The highest accuracy based on the producer and user accuracy values was 100% at depths of 0 - 2 m and 2.1 - 5 m respectively. In contrast, the overall accuracy (OA) value reaches a good level of 71.68%. The OA value is obtained by dividing the number of correct pixels (on the diagonal) by the total number.

#### 4 CONCLUSION

The study has illustrated the depth of Kemujan Island waters in 2D and 3D. The Stumpf algorithm in the PlanetScope image data processing can estimate depths of 0 to 20 m. In the accuracy test calculation, the  $R^2$  value was 0.6952; if this figure approaches 1, the estimation results are better. Based on the results, PlanetScope imagery is suitable and recommended for use to extract

bathymetric information. The accuracy test with the confusion matrix calculation was classified into four bathymetry classes, with an overall accuracy value of 71.68%.

#### ACKNOWLEDGEMENTS

We are grateful to the remote sensing applications center, LAPAN, for aiding the process of completing the reports and manuscripts of this research. Thanks too to Universitas Gadjah Mada (UGM) for providing in situ data and to Planet.com providing the PlanetScope imagery data for the study.

#### AUTHOR CONTRIBUTIONS

A.S.S conceived the research idea, proposed the methodology, conducted the analysis and prepared the manuscript. K.T.S coordinated the satellite imagery, participated in the methodology and analysis and contributed to the manuscript. J.A coordinated the in-situ data and contributed to the manuscript.

#### REFERENCES

- Banko, G. (1998). A Review of Assessing the Accuracy of Classifications of Remotely Sensed Data and of Methods Including Remote Sensing Data in Forest Inventory. INTERIM REPORT IR-98-081
- Gabr, B., Ahmed, M., & Marmoush, Y. (2020). PlanetScope and Landsat 8 Imageries for Bathymetry Mapping. *Journal of Marine Science and Engineering* 8, 143

- Gao, B.C., Montes M.J., Li R.R., Dierssen H.M. and Davis C.O. (2007). An Atmospheric Correction Algorithm for Remote Sensing of Bright Coastal Waters Using MODIS Land and Ocean Channels in the Solar Spectral Region. *IEEE Transactions on Geoscience and Remote Sensing* 45, 1835–1843
- Jensen, J.R. (2007). *Remote Sensing of the Environment: An Earth Resource Perspective*. (2nd ed). Upper Saddle River, NJ: Prentice Hall.
- Muzirafuti, A., Barecca, G., Crupi, A., Faina, G., Paltrinieri, D., Lanza, S., & Randazzo, G. (2020). The Contribution of Multispectral Satellite Image to Shallow Water Bathymetry Mapping on the Coast of Misano Adriatico, Italy. *Journal of Marine Science and Engineering* 8, 126, 1-21.
- Nurkhayati, R. (2013). Pemetaan Batimetri Perairan Dangkal Menggunakan Citra Quickbird di Perairan Taman Nasional Karimunjawa, Kabupaten Jepara, Jawa Tengah (Bathymetry Mapping of Shallow Waters Using Quickbird Images in the Waters of Karimunjawa National Park, Jepara Regency, Central Java). *Jurnal Bumi Indonesia* 2(2), 140-148.
- Pe'eri, S., Parrish, C., Azuik, C., Alexander, L., & Armstrong, A.. (2014). Satellite Remote Sensing as Reconnaissance Tool for Assessing Nautical Chart Adequacy and Completeness. *Marine Geodesy* 37, 293–314.
- Pike, S., Traganos, D., Poursanidis, D., Williams, J., Medcalf, K., Reinartz, P., Chrysoulakis, N.. (2019). Leveraging Commercial High-Resolution Multispectral Satellite and Multibeam Sonar Data to Estimate Bathymetry: The Case Study of the Caribbean Sea. *Remote Sensing* 11, 1830, 1-16.
- Planet Lab Inc. (2020). Planet Imagery Product Specification. Retrieved July 20, 2020, from <https://assets.planet.com/docs/combined-imagery-product-spec-april-2019.pdf>.
- Poursanidis, D., Traganos, D., Chrysoulakis, N., & Reinartz P. (2019). Cubesats Allow High Spatiotemporal Estimates of Satellite-Derived Bathymetry. *Remote Sens.* 11, 1299
- Said, N.M., Mahmud M.R., & Hasan R.C. (2017). Satellite-Derived Bathymetry: Accuracy Assessment on Depths Derivation Algorithm for Shallow Water Area. *The International Archives of the Photogrammetry, Remote Sensing and Spatial Information Sciences XLII-4/W5*, 159-164
- Siregar, V.P. & Selamat, M.B. (2008). Interpolator Dalam Pembuatan Kontur Peta Batimetri (Interpolator in Bathymetric Map Contouring). *E-Jurnal Ilmu dan Teknologi Kelautan Tropis* 1(1), 39-47
- Stumpf, R. P., Holderied K., & Sinclair M., (2003). Determination of Water Depth with High-Resolution Satellite Imagery over Variable Bottom Types. *Limnology Oceanography* 48, 547-556
- Sun, F.D., Sun, W.X., Chen, J., & Gong, P. (2012). Comparison and improvement of methods for identifying waterbodies in remotely sensed imagery. *Int. J. Remote Sens* 33, 6854–6875
- Suprayogi, I., Trimaijon & Mahyudin (2013). Model Prediksi Liku Kalibrasi Menggunakan Pendekatan Jaringan Saraf Tiruan (JST) (Studi Kasus: Sub AS Siak Hulu) (*Calibration Twist Prediction Model Using Artificial Neural Network (ANN) Approach (Case Study: Sub AS Siak Hulu)*)
- Waskito, R. & Wicaksono, P. (2019). Aplikasi Citra WorldView-2 untuk Pemetaan Batimetri di Pulau Kemujan Taman Nasional Karimunjawa. (WorldView-2 Image Application for Bathymetry Mapping in Kemujan Island, Karimunjawa National Park) *Jurnal Penginderaan Jauh Indonesia* 1(1): 32-38



## AUTHORS INDEX

<b>A</b>		<b>P</b>	
Abdullah Ali	65,72 [17,1]	Panji Mahyatar	115,123 [17,2]
Anang Dwi Purwanto	9,23,25,33 [17,1]	Pingkan Mayestika Afgangiani	175,186 [17,2]
Argo Galih Suhada	9,23 [17,1]	<b>R</b>	
Argo Galih Suhadha	25,33 [17,1]	Rafika Minati Devi	45,53 [17,1]
Asih Sekar Sesama	209 [17,2]	Rahma Nafila Fitri Sabrina	160,149 [17,2]
Atriyon Julzarika	209 [17,2]	Rian Nurtyawan	35,42 [17,1]
<b>B</b>		Rizky Faristyawan	25,33 [17,1]
Bayu Elwantyo Bagus Dewantoro	115,123 [17,2]	Rosaria Damai	127, 147 [17,2]
Bela Karbela	175,186 [17,2]	<b>S</b>	
<b>C</b>		Salsabila Diyah Rahmawati	201 [17,2]
Cahya Riski Fathurohman	201 [17,2]	Samsul Arifin	163,172 [17,2]
<b>D</b>		Sartono Marpaung	9,23,25,33 [17,1]
Dede Dirgahayu	75,82 [17,1]	Sri Harini	75,82 [17,1]
	163,172 [17,2]	Sudaryatno	160,149 [17,2]
Desak Putu Okta Veanti	85,96 [17,1]	Supriatna	57,63 [17,1]
Diah Indriani	45,53 [17,1]	Suwarsono	1,7,57,63 [17,1]
Dony Kushardono	75,82 [17,1]	<b>T</b>	
Dzikrullah Akbar	85,96 [17,1]	Tatik Kartika	163,172 [17,2]
<b>E</b>		Taufiq Ihsanudin	201 [17,2]
Eko Kusratmoko	57,63 [17,1]	Teguh Prayogo	9,23,25,33 [17,1]
Ety Parwati	175,186 [17,2]	Tofan Agung Eka Prasetya	45,53 [17,1]
<b>F</b>		<b>U</b>	
Fajar Yulianto	1,7 [17,1]	Udhi Catur Nugroho	1,7 [17,1]
Fandi Dwi Julianto	201 [17,2]	<b>V</b>	
<b>H</b>		Viv Djanat Prasita	127, 147 [17,2]
Hana Listi Fitriana	1,7,57,63 [17,1]	<b>W</b>	
Hermanto Asima Nainggolan	85,96 [17,1]	Wafiq Nur Hayani	115,123 [17,2]
<b>I</b>		Wikanti Asriningrum	25,33 [17,1]
Iddam Hairuly Umam	65,72 [17,1]	<b>J</b>	
<b>J</b>		Jansen Sitorus	25,33 [17,1]
<b>K</b>		<b>K</b>	
Komang Iwan Suniada	99 [17,2]	Komang Iwan Suniada	99 [17,2]
Kuncoro Teguh Setiawan	127, 147,209 [17,2]	Kuncoro Teguh Setiawan	127, 147,209 [17,2]
Kusumaning Ayu Dyah Sukowati	1,7 [17,1]	Kusumaning Ayu Dyah Sukowati	1,7 [17,1]
<b>M</b>		<b>M</b>	
Made Parsa	75,82 [17,1]	Made Parsa	75,82 [17,1]
Muhammad Rokhis Khomarudin	1,7 [17,1]	Muhammad Rokhis Khomarudin	1,7 [17,1]
<b>N</b>		<b>N</b>	
Nadia Fiscarina	35,42 [17,1]	Nadia Fiscarina	35,42 [17,1]
Nadine Ayasha	189 [17,2]	Nadine Ayasha	189 [17,2]

## KEYWORDS INDEX

<b>A</b>		<b>G</b>	
Abrasion	201, 202, 205, 206, 207 [17,2]	GHRSSST	9, 12, 15, 17, 19, 20, 21, 22, 23 [17,1]
Accuracy	2, 35, 36, 37, 38, 39, 40, 41, 42, 57, 59, 61, 65, 66, 71, 75, 76, 80, 81, 82 [17,1]	Google Earth Engine	76 [17,1] 117, 118, 201, 202, 203, 204, 205, 207 [17,2]
<b>B</b>		Google Maps API	189, 190, 191, 197, 198 [17,2]
Banda Sea	25, 26, 28, 29, 32, 33 [17,1] 110 [17,2]	<b>H</b>	
Beralas Pasir Island	127, 128, 131, 132, 133, 135, 137, 138, 139, 140, 141, 142, 143, 144, 145, 146, 147 [17,2]	Himawari-8 Satellite	189, 196, 197 [17,2]
Burnt Area	57, 58, 59, 60, 61, 63 [17,1] 164 [17,2]	Hotspots	85, 86, 87, 88, 90, 91, 92, 93, 94, 95, 96 [17,1]
<b>C</b>		Hovmoller Diagram	25, 27, 28, 29, 30, 31 [17,1]
Chlorophyll-a	9, 11, 12, 13, 14, 15, 16, 17, 18, 19, 22, 25, 26, 27, 28, 29, 30, 31, 32, 33 [17,1] 149, 150, 151, 152, 153, 154, 155, 156, 157, 158, 159, 160 [17,2]	<b>K</b>	
Cirata Dam	1, 3, 4, 5, 7 [17,1]	Karimun Jawa Island	209 [17,2]
Climate Change	45, 46, 49, 52, 53 [17,1] 110, 111, 115, 116 [17,2]	<b>L</b>	
Coastal ZPPI	9, 11, 12, 13, 14, 16, 17, 18, 19, 20, 21, 22 [17,1]	Land Cover	45, 46, 50, 52 [17,1] 115, 117, 120, 121, 122, 163, 164, 167, 168, 171, 176, 207 [17,2]
Conditional Probability	85, 87, 89, 91 [17,1]	Land Surface Temperature	45, 46, 47, 48, 49, 50, 51, 53 [17,1] 115, 116, 117, 119, 122, 123 [17,2]
Coral Reefs	19 [17,1] 127, 128, 129, 131, 133, 134, 135, 136, 138, 141, 146, 147 [17,2]	Landsat 8	5, 57, 58, 59, 60, 61, 62, 63, 76 [17,1] 117, 118, 120, 123, 167, 175, 176, 177, 178, 202, 203 [17,2]
Cubic Spline	45, 46, 48, 50, 51, 52, 53 [17,1]	Landsat-8	2, 5, 75, 76, 81, 82 [17,1] 123, 175, 176, 186, 201, 202, 203, 205 [17,2]
<b>D</b>		<b>M</b>	
Density	25, 26, 27, 28, 32, 66, 72, 85, 86, 87, 93, 94, 95, 96 [17,1] 115, 164 [17,2]	Marine Resources Activity	209 [17,2]
Devegetation	163, 164, 167, 170, 172 [17,2]	Mean Field Bias Method	65 [17,1]
Digital Elevation Model	35, 36, 39 [17,1] 202, 204 [17,2]	MNDWI	2, 4, 5, 6 [17,1] 201, 203, 204, 205 [17,2]
<b>E</b>		<b>Model</b>	1, 5, 6, 9, 10, 11, 14, 17, 22, 35, 36, 37, 39, 40, 45, 46, 48, 49, 51, 52, 58, 65, 66, 75, 76, 80, 81, 82 89 [17,1] 102, 120, 149, 150, 152, 153, 154, 155, 156, 157, 163, 164, 175, 176, 178, 202, 204, 209, 210, 212, 213 [17,2]
ENSO	25, 26, 30, 31, 32 [17,1] 99, 100, 101, 102, 103, 108, 109, 110, 111, 178 [17,2]		
EVI	75, 76, 77, 78, 79, 80, 81, 82 [17,1]		
<b>F</b>			
FMA 715	99, 101, 102, 103, 109 [17,2]		
Forest Fires	57, 58, 60, 61, 63, 85, 86, 87, 91, 92 [17,1]		
Freshwater Lakes	149 [17,2]		
FWI	85, 86, 87, 88, 89, 90, 91, 92, 93, 94, 95, 96 [17,1]		

Monitoring	1, 3, 26, 36, 57, 76 [17,1] 102, 115, 116, 127, 147, 163, 164, 165, 171, 175, 176, 201 [17,2]	SST	9, 12, 15, 17, 18, 19, 20, 22 [17,1] 99, 100, 101, 102, 103, 104, 105, 106, 107, 108, 109, 110, 111, 199 [17,2]
Monsoon	26, 29, 30, 32 [17,1] 99, 100, 101, 102, 103, 104, 105, 106, 108, 109, 110, 111, 128, 180, 185, 199 [17,2]	Stereo	35, 36, 37, 38, 42 [17,1]
Multi-Temporal	75, 76, 78, 82 [17,1] 165 [17,2]	Stumpf Algorithm	209, 210, 211, 213, 214 [17,2]
<b>N</b>		Sulfur Bursts	149, 153, 159, 160 [17,2]
NDWI	1, 2, 4, 5, 6 [17,1] 178, 203, 204 [17,2]	Surabaya	45, 65, 66, 67 [17,1] 128, 175, 176, 177, 180, 182 [17,2]
New Britain Island	45, 46, 47, 49, 50, 51, 52, 53 [17,1]	Surface Urban Cool Island	115, 117, 120, 123 [17,2]
Nias Island	9, 11, 12, 14, 15, 17, 18, 19, 20, 21, 22, 23 [17,1]	Surface Water Area	1, 2, 4, 5, 6, 7 [17,1]
<b>O</b>		<b>T</b>	
OBIA	57, 58, 59, 60, 61, 63 [17,1]	Tanjung Jaya	201, 205, 206, 207 [17,2]
Optimization	75, 76 [17,1]	Thermal Remote Sensing	115 [17,2]
<b>P</b>		Threshold	12, 75, 76, 79, 80, 81, 82 [17,1] 100, 115, 119, 120, 121, 123, 163, 167, 170, 171 [17,2]
PFZ Point	25, 26, 27, 28, 32 [17,1]	Tomini Bay	99, 101, 102, 103, 107, 108, 109, 110, 111 [17,2]
Pleiades	35, 36, 37, 39, 40, 41, 42 [17,1]	Total Suspended Solids	175, 186 [17,2]
Potential Fishing Zones	9, 10, 11, 18, 23 [17,1]	TSI Carlson	149, 156, 158 [17,2]
<b>Q</b>		<b>U</b>	
Quantitative Precipitation Estimation	65, 72 [17,1]	Ultraoligotrophic	149, 155, 156, 157, 158, 160 [17,2]
<b>R</b>		Upstream Citarum	1, 3, 4, 7 [17,1]
Radar–Gauge Merging	65 [17,1]	Urban Microclimate	115, 119 [17,2]
Rainfall Estimation	189, 190, 191, 192, 193, 194, 195, 196, 197, 198, 199 [17,2]	<b>W</b>	
Rainfall Rate	175, 177, 178, 179, 186 [17,2]	Water Characteristics	209 [17,2]
Remote Sensing	1, 5, 7, 9, 10, 11, 22, 25, 26, 33, 35, 47, 57, 58, 63, 65, 82, 86, 89 [17,1] 115, 116, 122, 127, 128, 135, 147, 149, 150, 152, 163, 164, 172, 175, 186, 189, 201, 202, 209, 211, 214 [17,2]	Water Productivity	25, 26, 27, 28, 29, 30, 31, 32, 33 [17,1]
Revegetation	163, 164, 167, 170, 171, 17 [17,2]		
<b>S</b>			
Seasonal Total Suspended Solids	175 [17,2]		
Sentinel-2	1, 3, 4, 5, 6, 7 [17,1] 163, 164, 165, 166, 171 [17,2]		
Single Image Edge Detection (SIED)	9, 12, 27 [17,1]		
SPOT 4	127, 128, 131, 132, 133, 134, 135, 147 [17,2]		
SPOT 7	127, 128, 129, 131, 132, 133, 134, 135, 136, 147 [17,2]		



# INTERNATIONAL JOURNAL OF REMOTE SENSING AND EARTH SCIENCES

## Instruction for Authors

### Scope

**International Journal of Remote Sensing and Earth Sciences (IJReSES) publishes research results on remote sensing and earth sciences, with special interest in Asian region.**

### Manuscript Submission

Manuscripts submission to the IJReSES must be original with a clear definition of the objective(s), material used (data), methods applied, results, and should not have been published or offered for publication or submitted elsewhere. The manuscript should be written in English, using single line spacing on single-sided A4 size paper with 2.5 cm left and right margins, 2.5 cm upper and lower margins. The author(s) is (are) also required to submit original version of figures embedded in the paper along with their captions. All figures should be in tiff or jpeg format with high resolution (300 or 600 dpi). Submit your paper in Word to IJReSES secretariat via: jurnal.lapan.go.id.

### Manuscript Preparation

- Title should be concise and informative and not exceeding 15 words.
- The author name(s) and affiliation(s) should be written in the footnotes at the bottom of the title page.
- Abstract should contain a summary of the paper including brief introduction, the objective(s), method, and principal conclusions. Abstract should not exceed 250 words. Keywords are between 3 to 5 words and must be relevant to the subject. Do not use any sub-headings.
- Materials and methods used should clearly and concisely describe the experiment with sufficient details for independent repetition.
- Results should be presented with optimum clarity and without unnecessary detail. Results should also be presented in figures or tables but not duplicated in both format. Tables should be typed with same font size as the text and given consecutive Arabic number.
- Discussion should explain the significant findings and other important aspects of the research. Do not repeat material and methodology.
- Citation should be written in the text by the author's last name and year in one or two forms: Field *et al.* (1996) or (Field *et al.*, 1996). For references with more than two authors, list the first author plus *et al.*
- Conclusion should be concise and answer the objective(s).
- Acknowledgment, if any, should be kept at minimum (less than 40 words)
- References should be in alphabetical order. It should be written as follows:  
Field, C.B., M.J. Behrenfeld, J.T. Randerson, and P. Falkowski, 1998, Primary production of the biosphere: integrating terrestrial and oceanic components. *Science*, 281(5374):237-240.
- Acronym or uncommon abbreviations must be given in full at the first text mentioned. New abbreviation should be coined only for unwieldy names and should not be used at all unless the names occur frequently.
- Latin name and family of the species should be given besides its common name at the first mention in the manuscript, and the common name only for subsequent mentions.
- International Standard unit system (kg, m, s, etc) should be used for all manuscripts.

**International Journal of  
Remote Sensing and Earth Sciences**

December 2020

Published by:



**National Institute of Aeronautics and Space of Indonesia (LAPAN)**

**Secretariat:**

**National Institute of Aeronautics and Space of Indonesia (LAPAN)**

Jl. Kalisari No. 8, Pekayon, Pasar Rebo, Jakarta 13710, INDONESIA

Telp. (021) 8710065, Fax. (021) 8722733

[Pukasi.lapan@gmail.com](mailto:Pukasi.lapan@gmail.com)

**INTERNATIONAL JOURNAL OF  
REMOTE SENSING AND EARTH SCIENCES  
Vol. 17 No. 2 December 2020  
P-ISSN 0216-6739; E- ISSN 2549-516X  
Accreditation No. 30/E/KPT/2018**

**Contents**

Editorial Committee Preface .....	ii
Editorial Committee Members .....	iii
<b>VARIABILITY OF SEA SURFACE TEMPERATURE AT FISHERIES MANAGEMENT AREA 715 IN INDONESIA AND ITS RELATION TO THE MONSOON, ENSO AND FISHERY PRODUCTION</b>	
<b>Komang Iwan Suniada .....</b>	<b>99</b>
<b>DETECTION AND ANALYSIS OF SURFACE URBAN COOL ISLAND USING THERMAL INFRARED IMAGERY OF SALATIGA CITY, INDONESIA</b>	
<b>Bayu Elwanto Bagus Dewantoro, Panji Mahyatar, Wafiq Nur Hayani.....</b>	<b>115</b>
<b>MONITORING CHANGES IN CORAL REEF HABITAT COVER ON BERALAS PASIR ISLAND USING SPOT 4 AND SPOT 7 IMAGERY FROM 2011 AND 2018</b>	
<b>Rosaria Ria Damai, Viv Djanat Prasita, Kuncoro Teguh Setiawan.....</b>	<b>127</b>
<b>MULTITEMPORAL ANALYSIS FOR TROPHIC STATE MAPPING IN BATUR LAKE AT BALI PROVINCE BASED ON HIGH-RESOLUTION PLANETSCOPE IMAGERY</b>	
<b>Rahma Nafila Fitri Sabrina, Sudaryatno Sudaryatno.....</b>	<b>149</b>
<b>MONITORING MODEL OF LAND COVER CHANGE FOR THE INDICATION OF DEVEGETATION AND REVEGETATION USING SENTINEL-2</b>	
<b>Samsul Arifin, Tatik Kartika, Dede Dirgahayu, and Gatot Nugroho.....</b>	<b>163</b>
<b>INTERSEASONAL VARIABILITY IN THE ANALYSIS OF TOTAL SUSPENDED SOLIDS(TSS) IN SURABAYA COASTAL WATERS USING LANDSAT-8 SATELLITE DATA</b>	
<b>Bela Karbela, Pingkan Mayestika Afgatiani, Ety Parwati.....</b>	<b>175</b>
<b>A COMPARISON OF RAINFALL ESTIMATION USING HIMAWARI-8 SATELLITE DATA IN DIFFERENT INDONESIAN TOPOGRAPHIES</b>	
<b>Nadine Ayasha.....</b>	<b>189</b>
<b>SHORELINE CHANGES AFTER THE SUNDA STRAIT TSUNAMI ON THE COAST OF PANDEGLANG REGENCY, BANTEN</b>	
<b>Fandi Dwi Julianto, Cahya Rizki Fathurohman, Salsabila Diyah Rahmawati, Taufiq Ihsanudin.....</b>	<b>201</b>
<b>BATHYMETRIC EXTRACTION USING PLANETSCOPE IMAGERY (CASE STUDY: KEMUJAN ISLAND, CENTRAL JAVA)</b>	
<b>Asih Sekar Sesama, Kuncoro Teguh Setiawan, Atriyon Julzarika.....</b>	<b>209</b>
Instruction for Authors .....	
Index.....	

Published by:

**National Institute of Aeronautics and Space of Indonesia (LAPAN)**